Proper Motions in the Local Group

Dissertation

zur

Erlangung des Doktorgrades (Dr. rer. nat.)

der

Mathematisch-Naturwissenschaftlichen Fakultät

der

Rheinischen Friedrich-Wilhelms-Universität Bonn

vorgelegt von

Andreas Brunthaler

aus

Köln

Bonn, Mai 2004

Angefertigt mit Genehmigung der Mathematisch-Naturwissenschaftlichen Fakultät der Rheinischen Friedrich-Wilhelms-Universität Bonn

1. Referent: Prof. Dr. H. Falcke
2. Referent: Prof. Dr. U. Klein

Tag der Promotion:

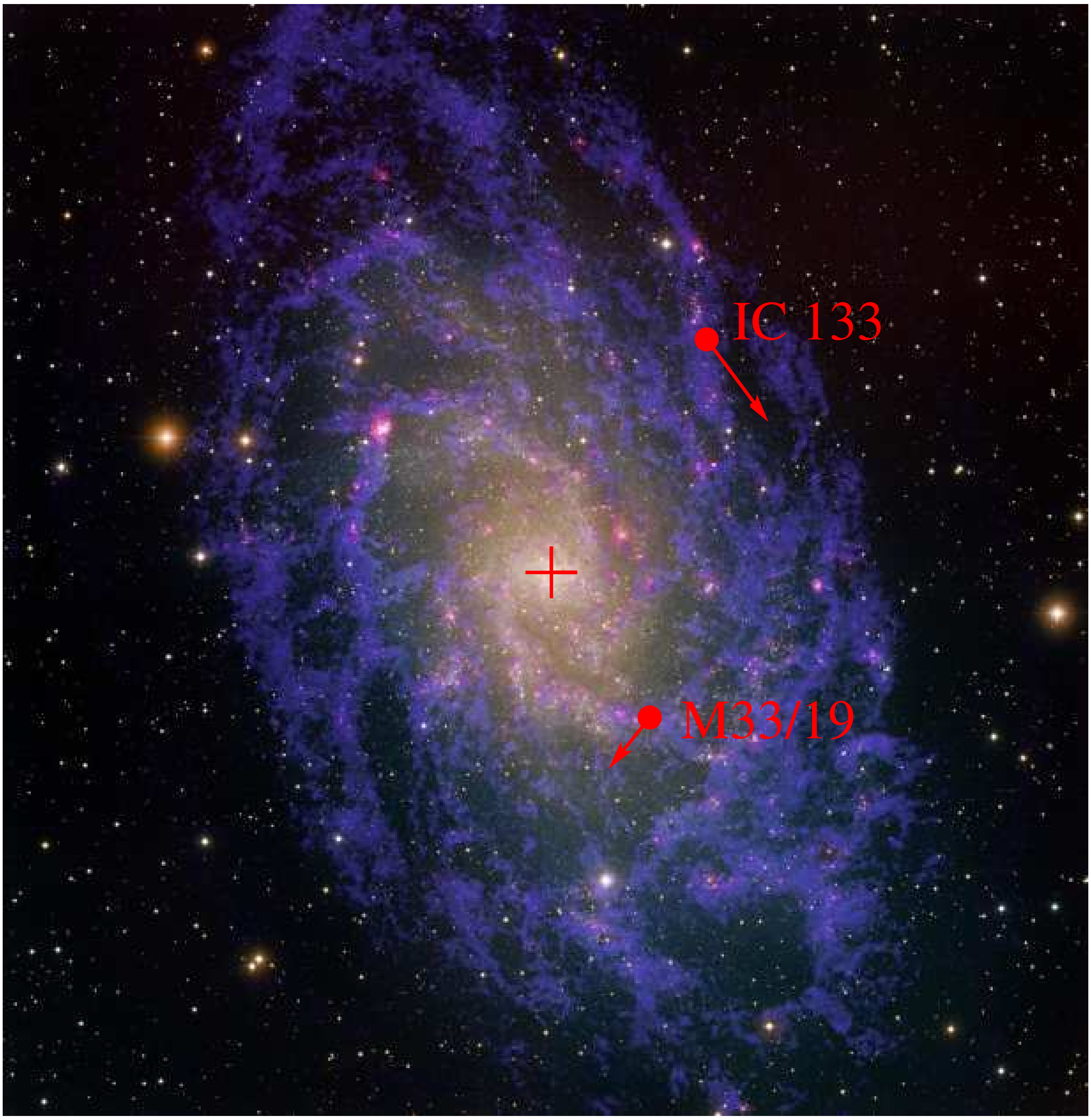

The positions of two regions of maser activity (IC 133 and M33/19) and their proper motion relative to the nucleus of M33 as measured by the VLBA in this thesis.

The image of the Triangulum Galaxy was created by combining optical data from the National Science Foundation's 0.9-meter telescope on Kitt Peak in Arizona with radio data from the National Science Foundation's Very Large Array (VLA) telescope in New Mexico and the Westerbork Synthesis Radio Telescope (WSRT) in the Netherlands.
T.A.Rector (NRAO/AUI/NSF and NOAO/AURA/NSF) and M.Hanna (NOAO/AURA/NSF)

Contents

1

Introduction

1.1 Geometric Distances

The nature of spiral nebulae like M33 was the topic of an intense discussion in the 1920's. While van Maanen favored a Galactic origin, Hubble was convinced of the extragalactic nature. The Galactic nature was supported in a paper by van Maanen (1923). He claims an apparent rotation of M33 from photographic plates separated by ≈ 12 years. These measurements yielded rotational motions of ≈ 10-30 mas yr^{-1}, clearly indicating a close distance to M33.

Today, we know that Hubble was right and M33 is indeed an extragalactic object. The expected proper motions from the rotation of M33 are only ≈ 30 μas yr^{-1}, and 3 orders of magnitude smaller than the motions claimed by van Maanen. The source of error in van Maanens observations was never identified. However, the idea behind the experiment to measure the rotation of galaxies remains interesting until today. These measurements can yield in combination with the galaxy inclination and known rotation speed from spectral line observations (e.g. H I) a direct geometric distance.

Currently, the calibration of most standard candles used for extragalactic distances, are tied in one way or another to the distance to the Large Magellanic Cloud (LMC) (e.g., Freedman 2000; Mould et al. 2000). However, two relatively new methods suggest a "short distance" to the LMC, about 10 to 20% smaller than from Cepheids. These methods involve the emission from "red clump" stars using Hipparcos distance calibrations (Stanek, Zaritsky, & Harris 1998), and analysis of light and radial velocity curves for the eclipsing binary HV 2274 (Guinan et al. 1998; Udalski et al. 1998). If the short distance is correct, then indirectly measured distances to other objects would shrink, increasing estimates of H_0 by 10 to 20%.

Hence, a geometric distance would allow an independent re-calibration of extragalactic distance indicators. This would lead not only to more accurate distances, and corresponding changes in many physical parameters, but it would lead to revised estimates of the expansion rate and age of the Universe.

1.2 Proper Motions

Another important astrophysical question is the nature and existence of dark matter in the universe, which had been inferred originally from the flat rotation curves of galaxies (e.g. Fich & Tremaine 1991). The closest place to look for dark matter halos is the Milky Way and Andromeda in the Local Group. Various attempts have been made to weigh the galaxies in the Local Group and determine size and mass of the Milky Way and its not very prominent dark matter halo (Kulessa & Lynden-Bell 1992; Kochanek 1996). Other attempts use Local Group dynamics in combination with MACHO data to constrain the universal baryonic fraction (Steigman & Tkachev 1999).

The problem when trying to derive the gravitational potential of the Local Group is that usually only radial velocities are known and hence statistical approaches have to be used. Kulessa & Lynden-Bell (1992) introduced a maximum likelihood method which requires only the line-of-sight velocities (Hartwick & Sargent 1978), but it is also based on some assumptions (eccentricities, equipartition).

Clearly, the most reliable way of deriving masses is using orbits, which requires the knowledge of three-dimensional velocity vectors obtained from measurements of proper motions. The usefulness of proper motions was impressively demonstrated for the Galactic Center where the presence of a dark mass concentration, presumably a black hole, has been unambiguously demonstrated by stellar proper motion measurements (Eckart & Genzel 1996; Schödel et al. 2002; Schödel et al. 2003 and Ghez et al. 2003).

However, measuring proper motions of members of the Local Group to determine its mass is difficult. For the LMC Jones, Klemola, & Lin (1994) claim a proper motion of 1.2 ± 0.28 mas yr^{-1} obtained from comparing photographic plates over a timespan of 14 years. Schweitzer et al. (1995) claim 0.56 ± 0.25 mas yr^{-1} for the Sculptor dwarf spheroidal galaxy from plates spanning 50 years in time. Kochanek (1996) shows that inclusion of these marginal proper motions can already significantly improve the estimate for the mass of the Milky Way, since it reduces the strong ambiguity caused by Leo I, which can be treated as either bound or unbound to the Milky Way. The same work also concludes that if the claimed optical proper motions are true, the models also predict a relatively large tangential velocity of the other satellites of the Galaxy.

The dynamics of nearby galaxies are also important to determine the solar motion with respect to the Local Group to help define a standard inertial reference frame (Courteau & van den Bergh 1999). And again, as Courteau and van den Bergh point out, "interpretation errors for the solar motion may linger until we obtain a better understanding of the true orbital motion of Local Group members".

Despite the promising start, the disadvantage of the available optical work is obvious: a further improvement and confirmation of these measurements requires an additional large time span of many decades and will still be limited to only the closest companions of the Milky Way. Future optical space astrometric missions such as SIM or GAIA will have the necessary atrometric accuracy, but it is not clear whether they have the sensitivity to detect single stars out to a distance of 800 kpc.

1.3 Proper Motions with VLBI

On the other hand, the expected proper motions for galaxies within the Local Group, ranging from 0.02 – 1 mas yr^{-1}, can be seen with Very Long Baseline Interferometry (VLBI) using the phase-referencing technique. A good reference point is the motion of Sgr A* across the sky reflecting the Sun's rotation around the Galactic Center. This motion is well detected between epochs separated by only one month with the VLBA (Reid et al. 1999). New observations increased the time span to 8 years. The position of Sgr A* relative to the background quasar J1745-283 is shown in Figure 1.1 (taken from Reid & Brunthaler 2004).

The motion of Sgr A* is 6.379 ± 0.026 mas yr^{-1} and almost entirely in the plane of the galaxy. This gives, converted to Galactic coordinates a proper motion of -6.379 ± 0.026 mas yr^{-1} in Galactic longitude and -0.202 ± 0.019 mas yr^{-1} in Galactic latitude. If one assumes a distance to the Galactic Center (R_0) of 8 ± 0.5 kpc (e.g. Reid 1993, Eisenhauer et al. 2003), these motions translate to a velocity of -241 ±15 km s^{-1} along the Galactic plane and -7.6 ± 0.6 km s^{-1} out of the plane of the Galaxy. This motion can be entirely explained by a combination of a circular rotation of the Local Standard of Rest (LSR) Θ_0 and the deviation of the motion of the Sun from the motion of the LSR. After removing the Solar motion relative to the LSR as measured by Hipparcos data by Dehnen & Binney (1998) (5.25 ± 0.62 km s^{-1} in longitude and -7.17 ± km s^{-1} in latitude) yields an estimate of Θ_0=236±15 km s^{-1}. Here the error is dominated by the uncertainty in the distance R_0

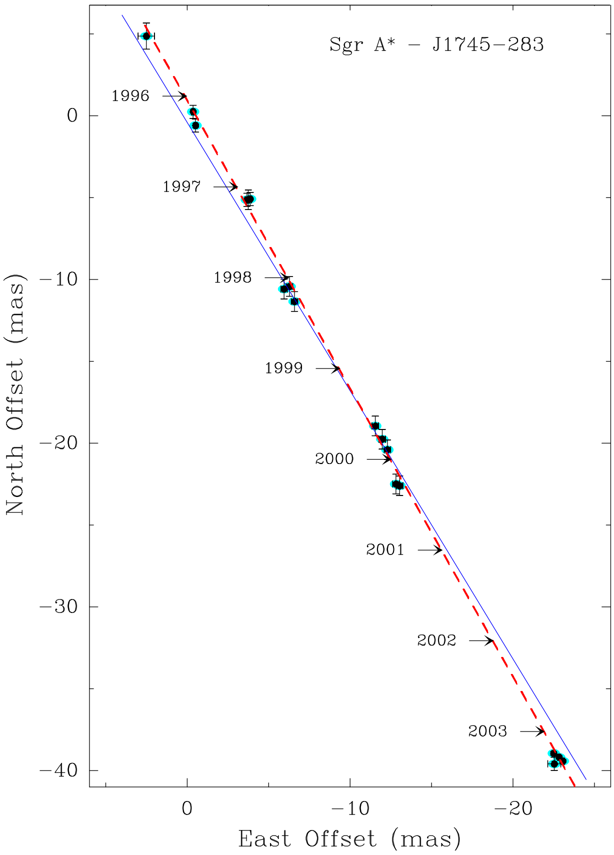

FIGURE 1.1— Apparent motion of Sgr A* relative to the background quasar J1745-283. The blue line indicates the orientation of the Galactic plane and the dashed line is the variance-weighted best-fit proper motion.

to the Galactic Center. The motion of Sgr A* out of the plane of the Galaxy is only -0.4 ± 0.8 km s^{-1}. This lower limit can be used to put tight constrains for the mass of Sgr A* (for details see Reid & Brunthaler 2004).

With the accuracy obtainable with VLBI one could in principle measure very accurate proper motions for most Local Group members within less than a decade. The main problem so far is finding appropriate radio sources. Useful sources would be either compact radio cores or strong maser lines associated with star forming regions. Fortunately, in a few galaxies bright masers are already known. Hence the task that lies ahead of us, if we want to significantly improve the Local Group proper motion data and mass estimate, is to make phase-referencing observations with respect to background quasars of known Local Group galaxies with strong H_2O masers to test this method and to provide a baseline for future measurements.

1.4 Useful Local Group galaxies

The most suitable candidates for such a VLBI phase-referencing experiment are the strong H_2O masers in IC 10 ($\sim$ 10 Jy peak flux in 0.5 km s^{-1} line, the brightest known extragalactic maser; Becker et al. 1993) and IC 133 in M33 ($\sim$ 2 Jy, the first extragalactic maser discovered). Both masers have been observed successfully with VLBI (e.g. Argon et al. 1994, Greenhill et al. 1990, Greenhill et al. 1993). Additional fainter masers also exist in M33.

The two galaxies belong to the brightest members of the Local Group and are thought to be associated with M31. In both cases a relatively bright phase-referencing source is known to exist within a degree. In addition their galactic rotation is well known from H I observations. Consequently, M33 and IC 10 seem to be the best known targets for attempting to measure Local Group proper motions with the VLBA.

The proper motion vectors of the observed masers will consist of various contributions, which we list in the following (with numbers for M33 roughly valid also for IC 10):

a) solar motion around the Galactic Center: 220 km s^{-1} ($\sim$60 μas yr^{-1}at a distance of 800 kpc times the sine of the angle between the solar motion vector and the line-of-sight to the galaxy);

b) motion of M31 with respect to the Milky Way: predicted to be $\sim$60 km s^{-1} (16 μas yr^{-1});

c) orbital motion of M33 (or IC 10) around M31: 100-200 km s^{-1} (25-50 μas yr^{-1});

d) internal galactic rotation: 110 km s^{-1} (25 μas yr^{-1});

e) velocity of individual components: $\sim$20-50 km s^{-1} ($\sim$5-13 μas yr^{-1}).

The vector (a) is competely constrained by the rotation of the Sun around the Galactic Center and the distance to the galaxies. The proper motion vectors (b-c) basically depend on the mass of M31 and the Milky Way and the distance to the galaxies, hence parameters we want to constrain with our observations. The galactic rotation (d) is very well determined from HI observations. For the intrinsic velocity of maser components (e) we note that though individual maser components can have velocities of several tens of km s^{-1}, the average velocity (79 components in IC 133) is just a few km s^{-1} and hence negligible.

Depending on how the vectors add up, we can conservatively expect a measurable motion of 50-100 μas yr^{-1}. With an expected astrometric precision of 30-50 μas yr^{-1}a 1σ proper motion result should be achieved within a year. Roughly half of this detectable motion is due to the astrophysically interesting vectors (b-c). For a simple model of the Local Group with two dominant galaxies and a fixed mass ratio between Milky Way and Andromeda (usually assumed to be 1:1.5) our two proper motion measurements would already significantly constrain any mass model for the Local Group. In a more elaborate approach, which takes the full data set of radial and proper motions in the Local Group into account (see Kochanek 1996), the constraints would be even stronger leading to significantly improved mass estimates and distances.

A possible pitfall for such a project is that individual maser components could be short lived and lost with time. However, in IC 133 the stronger maser components are known to exist for now two decades.

1.5 Aim and structure of the dissertation

The concept of Very Long Baseline Interferometry will be introduced in Chapter 2. Then the basics of astrometry with VLBI will be explained before a new technique will be presented to estimate and correct phase errors caused by errors in the atmospheric model of the correlator.

In Chapter 3 initial observations to search for extragalactic test sources with a small angular separation from IC 10 and M33 will be described. The results of test observations to verify the feasibility of the observation technique are also shown. Chapters 4 and 5 contain the observations and results of the H_2O masers in IC 10 and M33 respectively.

The high resolution and astrometric accuracy of VLBI can be used not only to measure the relative positions and motions of different radio sources but to measure the motions of different components within one source (e.g. jet components in quasars). Chapter 6 describes high resolution VLBI and low resolution VLA observations of the Seyfert I galaxy III Zw 2 to monitor the structural and spectral evolution of an outburst of this source. As a by-product of the monitoring, the VLA was also used to detect circular polarized emission in the galaxy M81 (Chapter 7).

Finally, a short summary will be given in Chapter 8.

2

Very Long Baseline Interferometry and Astrometry

The diffraction limited resolution of a telescope is proportional to the ratio of the observed wavelength λ and the diameter D of the telescope. Thus, one can increase the resolution by observing at shorter wavelength or by increasing the size of the telescopes. However, the telescope sizes are limited due to technical and financial reasons. The techniques of interferometry and aperture synthesis can be used to avoid these problems. Here, the signals from individual telescopes are combined to simulate an instrument with a resolution of a telescope with a diameter similar to the largest distance – or baseline – between two telescopes.

The concept of interferometry was first used in astronomy in the early 1920s by Michelson & Pease (1921) to measure the diameter of the star α Orionis. It was introduced almost 30 years later to radio astronomy by Martin Ryle and led to the development of Very Long Baseline Interferometry (VLBI). Nowadays, this techniques is used in a large number of existing (e.g. VLA, VLBA, BIMA) and future (e.g. ALMA, LOFAR, SKA) instruments in radio astronomy. In this chapter we give a brief introduction into the fundamentals of interferometry, VLBI and astrometry. For a detailed introduction into these topics see Thompson, Moran, & Swenson (1986), Zensus, Diamond, & Napier (1995) and Taylor, Carilli, & Perley (1999).

2.1 VLBI

2.1.1 Spatial Coherence Function

An astronomic object emits electromagnetic waves, which can be detected by astronomers on Earth. The object at a position $\boldsymbol{R}$ (variables printed in bold face denote vectors) creates a time-dependent electric field $\boldsymbol{E}(\boldsymbol{R}, t)$. This field can be expressed by coefficients of a Fourier series, the *quasi-monochromatic components* $\boldsymbol{E}_\nu(\boldsymbol{R})$. The time-dependent electric field generates an electromagnetic wave which propagates through space and can be measured with a telescope at position $\boldsymbol{r}$. Because of the linearity of Maxwell's equations we can superpose the fields at location $\boldsymbol{r}$ which are produced by all source points $\boldsymbol{R}$. This gives us

$$\boldsymbol{E}_\nu(\boldsymbol{r}) = \iiint P_\nu(\boldsymbol{R}, \boldsymbol{r}) \boldsymbol{E}_\nu(\boldsymbol{R}) \mathrm{d}x \, \mathrm{d}y \, \mathrm{d}z \quad (2.1)$$

where we integrate over all source points $\boldsymbol{R}$. $P_\nu(\boldsymbol{R}, \boldsymbol{r})$ is called *propagator* and describes the effect of the electric field at position $\boldsymbol{R}$ on the electric field at position $\boldsymbol{r}$. Now we assume that the source is far away from the observer and the information about the third dimension is lost. This implies that we observe only a surface brightness which is located on the surface of a *celestial sphere* of radius $|\boldsymbol{R}|$. Then the propagator takes a simple form according to Huygens' Principle, and we can write

$$E_\nu(\boldsymbol{r}) = \int \mathcal{E}_\nu(\boldsymbol{R}) \frac{\mathrm{e}^{\frac{2\pi \mathrm{i}\nu}{c}|\Delta \boldsymbol{R}|}}{|\Delta \boldsymbol{R}|} \mathrm{d}S \tag{2.2}$$

Here $\mathrm{d}S$ is the element of surface area, $\mathcal{E}_\nu(\boldsymbol{R})$ is the distribution of the electrical field on the celestial sphere, $\Delta \boldsymbol{R} = \boldsymbol{R} - \boldsymbol{r}$ and c is the speed of light. For further simplification we neglect polarization effects and treat the electric field as a scalar field instead of a vector field.

The correlation of a field measured with two telescopes at the locations $\boldsymbol{r}_1$ and $\boldsymbol{r}_2$ is defined as the expectation of the product $V_\nu(\boldsymbol{r}_1, \boldsymbol{r}_2) = \langle E_\nu(\boldsymbol{r}_1) E^*_\nu(\boldsymbol{r}_2)\rangle$. The raised asterisk denotes the complex conjugate. Using Equation 2.2, one gets

$$\begin{aligned} V_\nu(\boldsymbol{r}_1, \boldsymbol{r}_2) = \langle \iint & \mathcal{E}_\nu(\boldsymbol{R}_1) \mathcal{E}^*_\nu(\boldsymbol{R}_2) \frac{\mathrm{e}^{\frac{2\pi \mathrm{i}\nu}{c}|\Delta \boldsymbol{R}_1|}}{|\Delta \boldsymbol{R}_1|} \\ & \times \frac{\mathrm{e}^{-\frac{2\pi \mathrm{i}\nu}{c}|\Delta \boldsymbol{R}_2|}}{|\Delta \boldsymbol{R}_2|} \mathrm{d}S_1 \, \mathrm{d}S_2 \rangle. \end{aligned} \tag{2.3}$$

We can assume that the radiation from astronomical objects is not spatially coherent, i.e. $\langle \mathcal{E}_\nu(\boldsymbol{R}_1) \mathcal{E}^*_\nu(\boldsymbol{R}_2)\rangle = 0$ for $\boldsymbol{R}_1 \neq \boldsymbol{R}_2$. We can also exchange the integration and the expectation and write

$$\begin{aligned} V_\nu(\boldsymbol{r}_1, \boldsymbol{r}_2) = \int & \langle |\mathcal{E}_\nu(\boldsymbol{R})|^2 \rangle |\boldsymbol{R}|^2 \frac{\mathrm{e}^{\frac{2\pi \mathrm{i}\nu}{c}|\boldsymbol{R} - \boldsymbol{r}_1|}}{|\boldsymbol{R} - \boldsymbol{r}_1|} \\ & \times \frac{\mathrm{e}^{-\frac{2\pi \mathrm{i}\nu}{c}|\boldsymbol{R} - \boldsymbol{r}_2|}}{|\boldsymbol{R} - \boldsymbol{r}_2|} \mathrm{d}S. \end{aligned} \tag{2.4}$$

Now we introduce the unit vector in the direction of the source $\boldsymbol{s} = \boldsymbol{R}/|\boldsymbol{R}|$ and define the observed *intensity* $I_\nu(\boldsymbol{s}) = |\boldsymbol{R}|^2 \langle |\mathcal{E}_\nu(\boldsymbol{s})|^2 \rangle$. Replacing the surface element $\mathrm{d}S$ by the solid angle $|\boldsymbol{R}|^2 \mathrm{d}\Omega$ then yields

$$V_\nu(\boldsymbol{r}_1, \boldsymbol{r}_2) \approx \int I_\nu(\boldsymbol{s}) \mathrm{e}^{-\frac{2\pi \mathrm{i}\nu}{c} \boldsymbol{s} \cdot (\boldsymbol{r}_1 - \boldsymbol{r}_2)} \mathrm{d}\Omega. \tag{2.5}$$

The distance to astronomical objects is usually much larger than the separation of the telescopes. Hence terms of order $|\boldsymbol{r}/\boldsymbol{R}|$ are small and were neglected. This assumption is justified for most cases. Only cases in which objects in the solar system are observed, have to consider these effects. One example is the attempt to track the Huygens probe during its descent to the surface of the Saturn moon Titan on 2005 January 14 (for a reference, see JIVE Research note #4).

One sees that this *spatial coherence function* $V_\nu(\boldsymbol{r}_1, \boldsymbol{r}_2)$ depends only on the relative position $\boldsymbol{r}_1 - \boldsymbol{r}_2$, the so called *baseline*, of the two telescopes.

2.1.2 uv-Plane and Visibilities

Now we consider that the radiation comes only from a small part of the sky, i.e. all points $\boldsymbol{s} = \boldsymbol{s}_0 + \boldsymbol{\sigma}$ with small $\boldsymbol{\sigma}$ and introduce a coordinate system where $\boldsymbol{s}_0 = (0, 0, 1)$. Then we can rewrite Equation 2.5 as

$$\begin{aligned} V'_\nu(u, v, w) = \mathrm{e}^{-2\pi \mathrm{i} w} & \iint I_\nu(l, m) \\ & \times \mathrm{e}^{-2\pi \mathrm{i}(ul + vm)} \mathrm{d}l \, \mathrm{d}m. \end{aligned} \tag{2.6}$$

Here the baseline vector $\boldsymbol{r}_1 - \boldsymbol{r}_2 = \lambda \cdot (u, v, w)$ is given in units of the wavelength λ and the components of $\boldsymbol{s}$ are equal to $(l, m, 1)$. If we multiply this equation with $\mathrm{e}^{2\pi \mathrm{i} w}$, the right hand side of the equation becomes independent of w and we can replace $\mathrm{e}^{2\pi \mathrm{i} w} V'_\nu(u, v, w)$ with $V_\nu(u, v)$ and write

$$V_\nu(u, v) = \iint I_\nu(l, m) \mathrm{e}^{-2\pi \mathrm{i}(ul + vm)} \mathrm{d}l \, \mathrm{d}m. \tag{2.7}$$

$V_\nu(u, v)$ is the coherence function relative to the *phase center* $\boldsymbol{s}_0$. One can see that this coherence function is a Fourier transform of the intensity $I_\nu(l, m)$. Hence, one can calculate the intensity by inversion of the Fourier transform in Equation 2.7 if the coherence function is measured by an interferometer.

The elements of an interferometer are usually antennas which have different sensitivity in different directions. Because of this *primary beam*, one has to include a factor $\mathcal{A}_\nu(l, m)$ into Equation 2.7 which gives

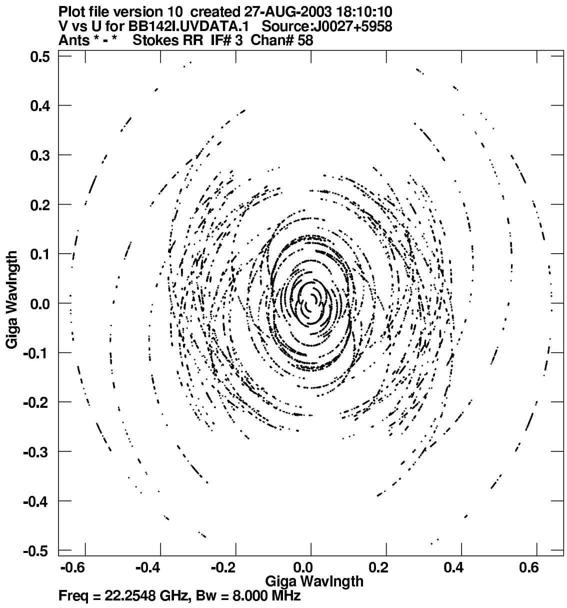

FIGURE 2.1— UV-coverage of an 8 hour observation with the VLBA.

$$V_\nu(u,v)=\iint \mathcal{A}_\nu I_\nu \mathrm{e}^{-2\pi \mathrm{i}(ul+vm)}\mathrm{d}l\,\mathrm{d}m. \quad (2.8)$$

The $V_\nu(u,v)$ defined by Equation 2.8 is called the *complex visibility*. An interferometer can be used to measure the visibility of a source, which contains information about the source structure and position.

2.1.3 Earth Rotation and Sampling

A two element interferometer with one baseline will measure the visibility function only at one point in the uv-plane. An interferometer with n antennas will have $n(n-1)/2$ baselines that yield as many measurements of the visibility function. Since the earth rotates during the observation, the orientation of the baselines change with respect to the source. This results in a track of measurements in the uv-plane from each baseline. Figure 2.1 shows the uv coverage of an 8 hour observation with the Very Long Baseline Array (VLBA), an array of 10 radio telescope in the USA.

This incomplete uv coverage can be described by a sampling function $S(u,v)$ which is one for all data points and zero for the rest. Then the *dirty image* is

$$I_\nu^D(l,m)=\iint V_\nu(u,v)S(u,v)\mathrm{e}^{2\pi \mathrm{i}(ul+vm)}\,\mathrm{d}l\mathrm{d}m. \quad (2.9)$$

This dirty image is connected to the true intensity distribution I_ν by a convolution

$$I_\nu^D(l,m) = I_\nu * B, \quad (2.10)$$

where B is the *synthesized beam* or the *point spread function*

$$B(l,m) = \iint S(u,v)\mathrm{e}^{2\pi \mathrm{i}(ul+vm)}\mathrm{d}u\mathrm{d}v. \quad (2.11)$$

This convolution can not be inverted directly and special algorithms like *CLEAN* (see Högbom 1974, Clark 1980, or Schwab 1984) are needed to reconstruct the true intensity distribution.

2.1.4 Correlation

If the signal of an astronomical object in direction of the unit vector $\boldsymbol{s}$ is observed with two telescopes separated by the baseline $\boldsymbol{b}$, the wavefront will arrive at one antenna at a time τ_g later than at the other. This *geometric delay* is given by

$$\tau_g = \frac{\boldsymbol{b}\cdot\boldsymbol{s}}{c}. \quad (2.12)$$

The signals from the antennas are then amplified and combined in the *correlator* where the signals are multiplied and averaged over time. The input voltage can be represented by quasi-monochromatic Fourier components of frequency ν which have the form $V_1(t) = v_1\cdot\cos 2\pi\nu(t-\tau_g)$ and $V_2(t) = v_2\cdot\cos 2\pi\nu t$. In a very simplified version, the correlator output is then

$$r(\tau_g)=\langle V_1(t), V_2(t)\rangle=v_1 v_2\cdot\cos 2\pi\nu\tau_g \quad (2.13)$$

It can be shown that the correlator output is connected with the true visibility by the relation

$$r \propto \Delta\nu |V| \cos\left(\frac{2\pi\nu \boldsymbol{b}\cdot\boldsymbol{s}_0}{c} - \phi_v\right), \quad (2.14)$$

where $|V|$ is the visibility amplitude and ϕ_v the visibility phase. A proper calibration of the data allows us to determine the visibility.

2.1.5 Calibration

Goal of the calibration is to determine the true visibilities from the correlator output. The *observed visibilities* $\tilde{V}_{ij}$ of the baseline $i - j$ and the true visibility are related by

$$\tilde{V}_{ij}(t) = \mathcal{G}_{ij}(t)V_{ij}(t) + \epsilon_{ij} + \eta_{ij}(t). \quad (2.15)$$

Here $\mathcal{G}_{ij}(t)$ is the complex gain of the baseline, ϵ_{ij} a baseline-based offset and $\eta_{ij}(t)$ a stochastic complex noise. The complex gain of the baseline is composed of two antenna-based complex gains

$$\begin{aligned}\mathcal{G}_{ij}(t) &= g_i(t)g_j^*(t) \quad (2.16)\\ &= a_i(t)a_j(t)\mathrm{e}^{\mathrm{i}(\phi_i(t)-\phi_j(t))}\end{aligned}$$

where $a_i(t)$ and $a_j(t)$ are the amplitude corrections and $\phi_i(t)$ and $\phi_j(t)$ are the phase corrections of the antennas. If the observed sources are strong enough, one can use the data of the source itself to do a *self-calibration* (e.g., Cornwell & Fomalont 1999). However, during the self-calibration the information about the position of the source is lost. If the sources are too weak for self-calibration, or if one goal of the observation is to measure the position of the target source the *phase-referencing* technique, which will be introduced in the next section, has to be used.

2.2 Astrometry

Astrometry is the precise measurement of the absolute and relative positions of celestial objects. The measured visibility phase contains all information about the position of a source. Hence, the phase calibration has do be done very carefully in astrometry. Here we will follow the descriptions by Beasley & Conway (1995) and Fomalont (1999).

2.2.1 Total Phase Delay

As seen in Equation 2.13, the output of an interferometer is a quasi-sinusoidal response

$$r(t) = A \cdot cos(\phi_T) \quad (2.17)$$

where ϕ_T is the total phase delay. It is given by the path-length differences of the signals from the two telescopes as well as the visibility phase and has various contributions:

$$\phi_T = 2\pi\nu(\tau_g + \tau_n) + \phi_d + \phi_v. \quad (2.18)$$

Here τ_g is the geometric delay defined in Equation 2.12. It depends only on the relative positions of the telescopes, i.e. the baseline $\boldsymbol{b}$ and the source position $\boldsymbol{s}_0$. The term τ_n includes all non-dispersive delays which are not frequency dependent. This includes tropospheric refraction, clock errors at the telescopes and path length changes in the telescope electronics. The dispersive phase changes which are caused by effects that do not depend linearly on frequency are represented by ϕ_d. One example is the effect of the ionosphere on the signal. The final contribution to the total phase delay is the visibility phase ϕ_v for extended sources.

The correlator calculates a model phase ϕ_M. This correlator model takes into account a large number of effects. It includes the geometry of the interferometer like the positions of the source and the telescopes, the nutation and precession of the earth as well as the tectonic motion, and tidal effects. The effect of light deflection in the gravitational potential of the Sun and the planets are also included.

VLBI usually uses the *fringe phase* which is the fractional part of the difference between the model phase delay and the true total phase delay.

2.2.2 Astrometric Equation

The position of a source with coordinates (α, δ) on the sky at a siderial time t_s can be described by the declination δ and the hour angle $H = t_s - \alpha$. Using the declination δ and the hour angle H, one can define a Cartesian coordinate system by three unit vectors $\boldsymbol{i}, \boldsymbol{j}, \boldsymbol{k}$ where $\boldsymbol{i}$ points to $\delta = 0, H = 0$, $\boldsymbol{j}$ points to $\delta = 0, H = -\pi/2$, and $\boldsymbol{k}$ points to $\delta = \pi/2$. In this coordinate system, the baseline $\boldsymbol{b}$ and source direction $\boldsymbol{s_0}$ are

$$\begin{aligned} \boldsymbol{b} &= \boldsymbol{i}L_x + \boldsymbol{j}L_y + \boldsymbol{k}L_z \qquad (2.19) \\ \boldsymbol{s_0} &= \boldsymbol{i}\cos H \cos\delta - \boldsymbol{j}\sin H \cos\delta + \boldsymbol{k}\cos\delta. \end{aligned}$$

Then the geometric phase delay is given by

$$\begin{aligned} \phi &= \frac{2\pi\nu}{c}(L_x \cos\delta \cos H \qquad (2.20) \\ &- L_y \cos\delta \sin H + L_z \sin\delta), \end{aligned}$$

where the baseline components L_x, L_y and L_z are given in meters. Since each geometric model has a limited accuracy, a residual phase delay ϕ_R will be observed in the fringe phase. This leads to the fundamental astrometric equation:

$$\begin{aligned} \phi_R &= \frac{2\pi\nu}{c}(A\cos H + B\sin H + C) \qquad (2.21) \\ A &= \Delta L_x \cos\delta + \Delta\alpha L_y \cos\delta - \Delta\delta L_x \sin\delta \\ B &= -\Delta L_y \cos\delta + \Delta\alpha L_x \cos\delta + \Delta\delta L_y \sin\delta \\ C &= \Delta L_z \sin\delta + \Delta\delta L_z \cos\delta + \Delta T. \end{aligned}$$

Here ΔL_i is the difference between the true and model antenna separations on the i-axis. The errors of the source position are given by $\Delta\alpha$ and $\Delta\delta$. ΔT denotes a clock offset between two antennas. Figure 2.2 show the resulting fringe phase for an 8 hour observation on two VLBA baselines for a position offset of the source of 0.5 mas.

Hence, a measurement of the residual phase delay would yield a direct estimation of the source position if the locations of the telescopes are known. This is the fundamental concept of astrometry. The inversion of this problem is used in geodesy. If the source position is known, one can measure the positions and motions of the telescopes from the residual phase delay.

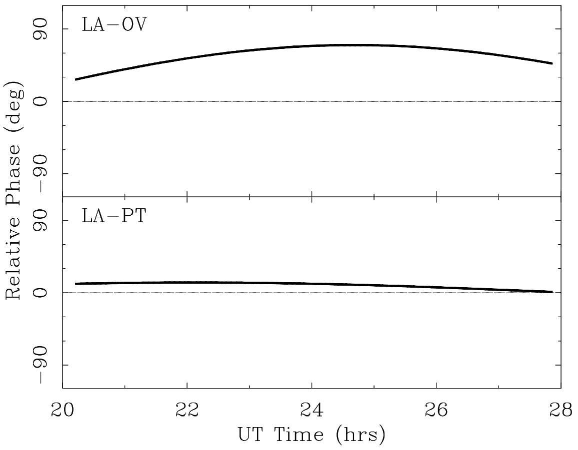

FIGURE 2.2— Fringe phase induced by a 0.5 mas position offset for a 1088 km baseline Los Alamos (LA) to Ovens Valley (OV) (top) and a 236 km baseline Los Alamos to Pie Town (PT) (bottom).

2.2.3 Phase Referencing

In addition to the geometric errors the other parameters of the correlator model are also known only to a certain accuracy. This will result in residuals in the observed fringe phase. These residuals can be written as

$$\begin{aligned} \phi(t) = \phi_v(t) + \phi_{ins}(t) + \phi_{pos}(t) \qquad (2.22) \\ +\phi_{ant}(t) + \phi_{atm}(t) + \phi_{ion}(t). \end{aligned}$$

Here the residual phase delay from equation 2.21 is separated into position errors of the source ϕ_{pos} and antenna position errors ϕ_{ant}. Further contributions are the visibility phase ϕ_v, phase errors caused by instrumental effects ϕ_{ins}, the neutral atmosphere ϕ_{atm} and the ionosphere ϕ_{ion}.

These residual phases are self-calibrated using the data of the source itself if the target source is strong enough and its absolute position is not needed. For weak sources or if the goal of the observation is to determine the position of the source the technique of phase-referencing can be used to correct this errors by using a bright and nearby calibrator source to calibrate the data. The concept of phase-referencing is based on the assumption that the phase errors of two sources with a small angular separation on the sky are similar. One observes the target source between two scans on the calibrator. Then one can interpolate the calibration between the two scans and apply this interpolated phase corrections ϕ^i to the phase of the target source ϕ^t.

$$\begin{aligned} \phi^t - \phi^i = \phi^t_v + (\phi^t_{ins} - \phi^i_{ins}) \\ +(\phi^t_{pos} - \phi^i_{pos}) + (\phi^t_{ant} - \phi^i_{ant}) \\ +(\phi^t_{atm} - \phi^i_{atm}) + (\phi^t_{ion} - \phi^i_{ion}) \end{aligned} \qquad (2.23)$$

Here we assume that the calibrator source is unresolved, i.e. $\phi^i_v = 0$. Now we assume that the errors are similar for both sources, i.e. $\phi^t_{ins} \approx \phi^i_{ins}$, $\phi^t_{ant} \approx \phi^i_{ant}$, $\phi^t_{atm} \approx \phi^i_{atm}$, and $\phi^t_{ion} \approx \phi^i_{ion}$. Then we can write

$$\phi^t - \phi^i \approx \phi^t_v + (\phi^t_{pos} - \phi^i_{pos}). \qquad (2.24)$$

This means that the phase-referenced difference phase contains only the information about the target source structure and its position relative to the calibrator together with noise from interpolation errors.

2.2.4 Residual Phase Errors

There will be residual phase errors after the interpolation and the phase-referencing that will degrade the image quality of the phase-referenced source. These errors can have various causes.

One source of errors are inaccuracies in the geometric model. These include errors in the antenna positions as well as errors in the absolute position of the calibrator. An error in the absolute position of the calibrator will shift the target source to first order by the same amount. However, second-order effects will introduce phase errors that will degrade the phase-referenced image and limit its dynamic range. This error scales with the angular separation between calibrator and target source. Thus, it is important to know the absolute position of the calibrator and use calibrators as close as possible to the target source.

The second source of phase errors are short term fluctuations of the total path length in the turbulent atmosphere. These variations constrain the switching time (the time between two scans on the calibrator) of the phase-referencing observation. The path length changes between two calibrator scans has to be much smaller than $\lambda/2$ or the phase interpolation will become ambiguous. The required switching time depends on the frequency, with a few minutes at 5 GHz and less than one minute at 22 GHz for VLBI observations. The only ways to reduce these phase errors are to use shorter switching times or use dual beam receiver systems which observe the calibrator and the target source continously. The second option was chosen in the VLBI Exploration of Radio Astronomy (VERA) project which is currently under construction in Japan (see e.g. Kobayashi et al. 2001).

Further sources of errors arise from the different atmosphere in front of the two sources. These errors can be separated in a static and a dynamic component. A tropospheric zenith delay error $\delta\tau_z$ in the correlator model is responsible for the static component. These errors will not be removed completely by phase referencing because of the angular separation between the calibrator and the target source. This will be discussed in more detail in the next section where a method is presented to correct these errors. The dynamic component of the troposphere moves very rapid through the line of sight of the antennas and constrains the switching time more than the switching angle.

2.3 Atmospheric Corrected Phase-Referencing

One major problem of phase-referencing observations is the unknown tropospheric zenith delay at each antenna. The VLBA correlator model uses a seasonally averaged and latitude-dependent atmospheric model (Niell 1996) which can misestimate the zenith delay by a few centimeters. This section will describe the effect of the neutral atmosphere on the signal and a method to correct the introduced errors.

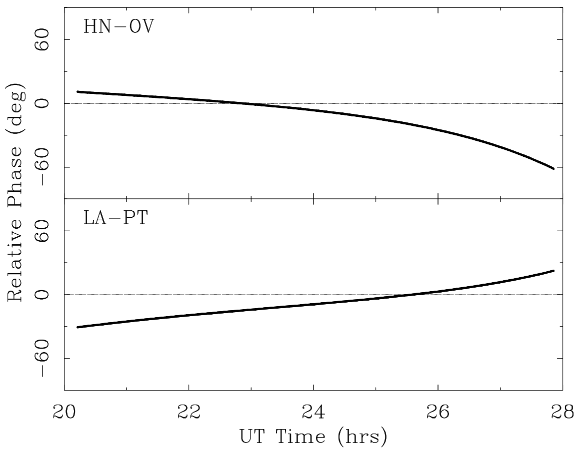

FIGURE 2.3— Phase error introduced by a zenith delay error of 5 cm at the antennas Hancock (HN) and Pie Town (PT) during an 8 hour observation.

2.3.1 Neutral Atmosphere

An electromagnetic wave in a dielectric medium with refractive index n will travel with a phase velocity of c/n. Hence, the wave will have a delay $\Delta t = \int (n-1)/c \, \mathrm{d}x$ compared to a wave in vacuum. This time delay can be interpreted as an excess path length $c\Delta t$, or

$$l = 10^{-6} \int N(x) \, \mathrm{d}x. \qquad (2.25)$$

where N is the refractivity, defined by $N = 10^6(n-1)$. The refractivity of moist air is given by the Smith-Weintraub Equation

$$N = 77.6\frac{p_D}{T} + 64.8\frac{p_V}{T} + 3.776{\times}10^5\frac{p_V}{T^2} \qquad (2.26)$$

where T is the temperature in Kelvin, p_D is the partial pressure of the dry air and p_V is the partial pressure of water vapor in millibars.

Using that a parcel of gas is in static equilibrium between pressure and gravity, it can be shown that the dry excess path length in zenith direction can be written as

$$l_D \approx 0.228\frac{\mathrm{cm}}{\mathrm{mb}} \, P_0, \qquad (2.27)$$

where P_0 is the surface pressure (e.g. Thompson, Moran, & Swenson 1986). Hence, the dry excess path length for a pressure of 1013 mb is 231 cm. The wet component of the excess path length can be approximated by

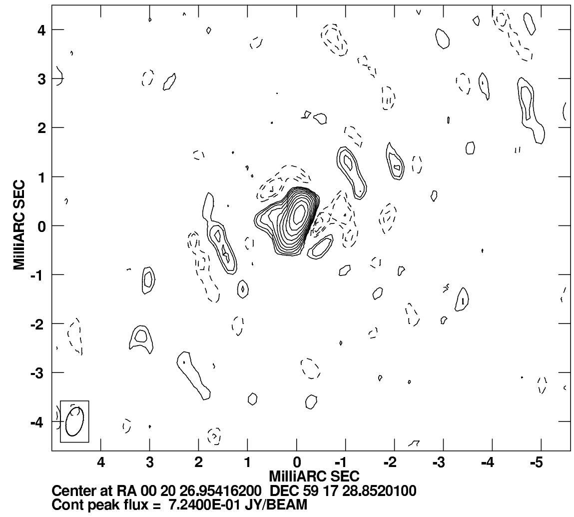

FIGURE 2.4— Phase-referenced image of a H_2O maser spot in IC 10. The contour levels start at 25 mJy and increase by a factor of $\sqrt{2}$. The peak-to-noise ratio is 77.

$$l_V \approx 7.6 \times 10^4 \frac{p_{V_0}}{T^2}, \qquad (2.28)$$

where p_{V_0} is the partial pressure of water vapor at the surface.

The simplest atmospheric model is a uniform flat slab. Here the signal from a source at zenith angle Z will see an excess path length of $l_0\mathrm{sec}(Z)$ if l_0 is the zenith excess path length. In a more realistic case, where the refractivity is exponentially distributed with a scale height h_0, the excess path length can be written as

$$\begin{aligned} l &\approx 0.228 P_0 \,\mathrm{sec}Z(1 - 0.0013\tan^2 Z) \qquad (2.29)\\ &+ \frac{7.5{\times}10^4 p_{V_0} \,\mathrm{sec}Z}{T^2}(1 - 0.0003\tan^2 Z) \end{aligned}$$

where the scale height of the dry and wet atmosphere were 8 km and 2 km respectively.

If the zenith delay of the dry atmosphere is misestimated in the correlator model by δl_0, the signal from a source at zenith angle Z will have a delay error of

$$\delta l(Z) \approx \delta l_0 sec(Z)(1 - 0.0013\tan^2 Z). \qquad (2.30)$$

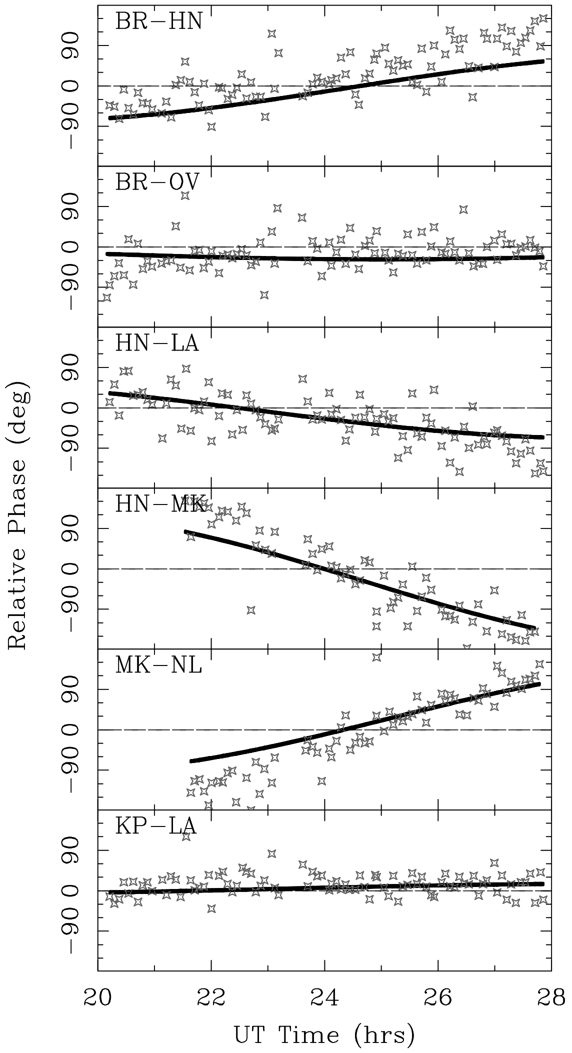

FIGURE 2.5— Phase data and best model-fit with a position offset only. The data and the model disagree during the beginning and end of the observation.

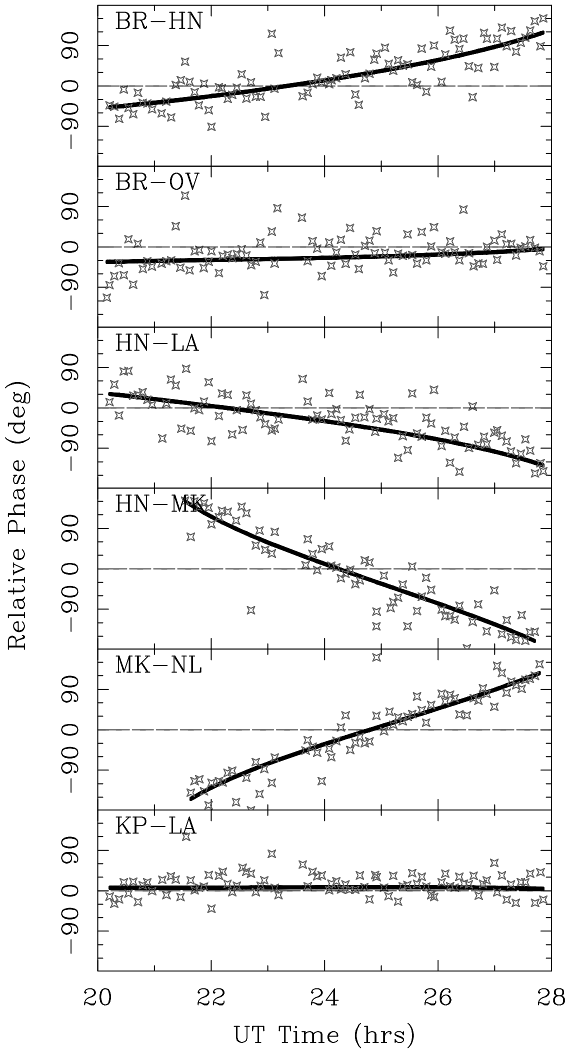

FIGURE 2.6— Phase data and best model-fit with a position offset and a zenith delay error at each antenna. The model agrees with the model during the whole observation.

This error will be different for the calibrator and the target source since both sources usually have different zenith angles Z_c and Z_t. A fringe-fit on the calibrator will correct both sources for the same value $\delta l(Z_c)$. Hence, a residual error of $\delta l(Z_c) - \delta l(Z_t)$ will remain after phase-referencing for the target source. If the correlator model misestimates the zenith delay l_0 by 3 cm ($\approx$ 0.1 ns), one would expect delay errors of 0.2 cm for zenith angles of $\approx 60^\circ$ and source separations of $\approx 1^\circ$. Figure 2.3 shows the phase errors for two baselines with a zenith delay error of 5 cm at one antenna. These phase errors will degrade the quality of the phase-referenced image of the target source. Figure 2.4 show the phase-referenced image of a H_2O maser spot in IC 10. The image shows asymmetric errors close to the source which are typical for phase errors. These errors can be corrected if the true zenith delay is known.

2.3.2 Phase Fitting

Equation 2.24 shows that the phase-referenced phase of the target source contains the infor-

TABLE 2.1— Fit parameters for the observation on 2002 January 12: Zenith delay offset ($\tau_{0,p}$) from the fit to the phase data, zenith delay offset (τ_0) and rate ($\dot{\tau}_0$), and clock offset (Δt) and rate ($\dot{\Delta t}$) from the geodetic-like observations. The errors are the formal errors of the least-squares fit.

Antenna	$\tau_{0,p}$ [cm]	τ_0 [cm]	$\dot{\tau}_0$ [cm h^{-1}]	Δt[ns]	$\dot{\Delta t}$[ns d^{-1}]
BR	2.5±0.6	1.6±0.1	0.4±0.03	-0.24±0.01	-1.52±0.03
FD	4.4±0.3	1.7±0.05	0.3±0.01	-0.08±0.01	-0.84±0.02
HN	7.0±0.2	6.4±0.1	0.3±0.03	0.37±0.01	0.47±0.04
KP	1.0±0.3	-0.1±0.05	0.3±0.01	–	–
LA	-0.4±0.4	-1.7±0.07	0.3±0.02	-0.12±0.01	-0.17±0.02
MK	-3.3±0.1	-4.0±0.06	0.3±0.01	-0.93±0.01	-0.97±0.03
NL	9.4±0.4	7.8±0.1	0.2±0.02	0.42±0.01	0.51±0.03
OV	4.7±0.4	2.2±0.07	0.3±0.01	0.00±0.01	-0.62±0.02
PT	-0.2±0.4	-1.8±0.07	0.2±0.01	0.08±0.01	1.05±0.02

mation about the position and structure of the target source as well as interpolation errors. Now we assume that the largest interpolation error comes for the inaccurate zenith delay of the atmosphere. If the source structure is negligible or if the structure is known (e.g., from self-calibration) and the visibility phase is subtracted from the observed phase, the phase of the target source is a sum of the position offset and the effects of the zenith delay error. The phase induced by the position offset shows a simple 24 hour cosine behavior as seen in Figure 2.2 for two baselines, while the phase errors from the zenith delay error follow a more complex dependence of the zenith angle (e.g., Figure 2.3). Because of the different behavior of the two contributions, it is possible to separate both effects and estimate the position offset as well as the zenith delay error. One can compute a model phase with a position offset using equation 2.21 (two parameters) and a zenith delay error at each antenna according to equation 2.30 (one parameter for each antenna) and perform a least-squares fit to the phase data.

Figure 2.5 shows the referenced phase data of a strong H_2O maser component in IC 10 from an observation on 2002 January 12 together with the best model-fit to the data points using only a position offset. One can see two different effects in the data. The phase data shows a scatter on short timescales. This scatter is mainly due to short term fluctuations of the water vapor content in the line of sight of the individual telescopes. Additionally, there are systematic differences between model and data that change only slowly during the observation. The differences are largest at the beginning and end of the observation, when the elevation of the source is low and the corresponding airmass in the line of sight is high. This elevation dependency is a clear sign of an atmospheric effect. Hence, the observed phase can not be explained by a pure position offset.

The least squares fit resulted in a position offset of $\mathrm{d}x = -33$ μas and $\mathrm{d}y = 181$ μas. This agrees with the position of the source in Figure 2.4. A fit of a single Gaussian to the image yielded a position offset of $\mathrm{d}x = -26$ μas and $\mathrm{d}y = 186$ μas.

The agreement between phase-data and model becomes much better if one adds a zenith delay error at each antenna to the model. The best model-fit of a model with position offset and zenith delay errors can be seen in Figure 2.6. The model can reproduce the data, except the scatter on short timescales, now on all baselines for the whole observation.

The position offset of the best model-fit was $\mathrm{d}x = -4$ μas and $\mathrm{d}y = 112$ μas while the zenith delay errors were of the order of a few centimeters at each station and are shown in the second column of Table 2.3.2.

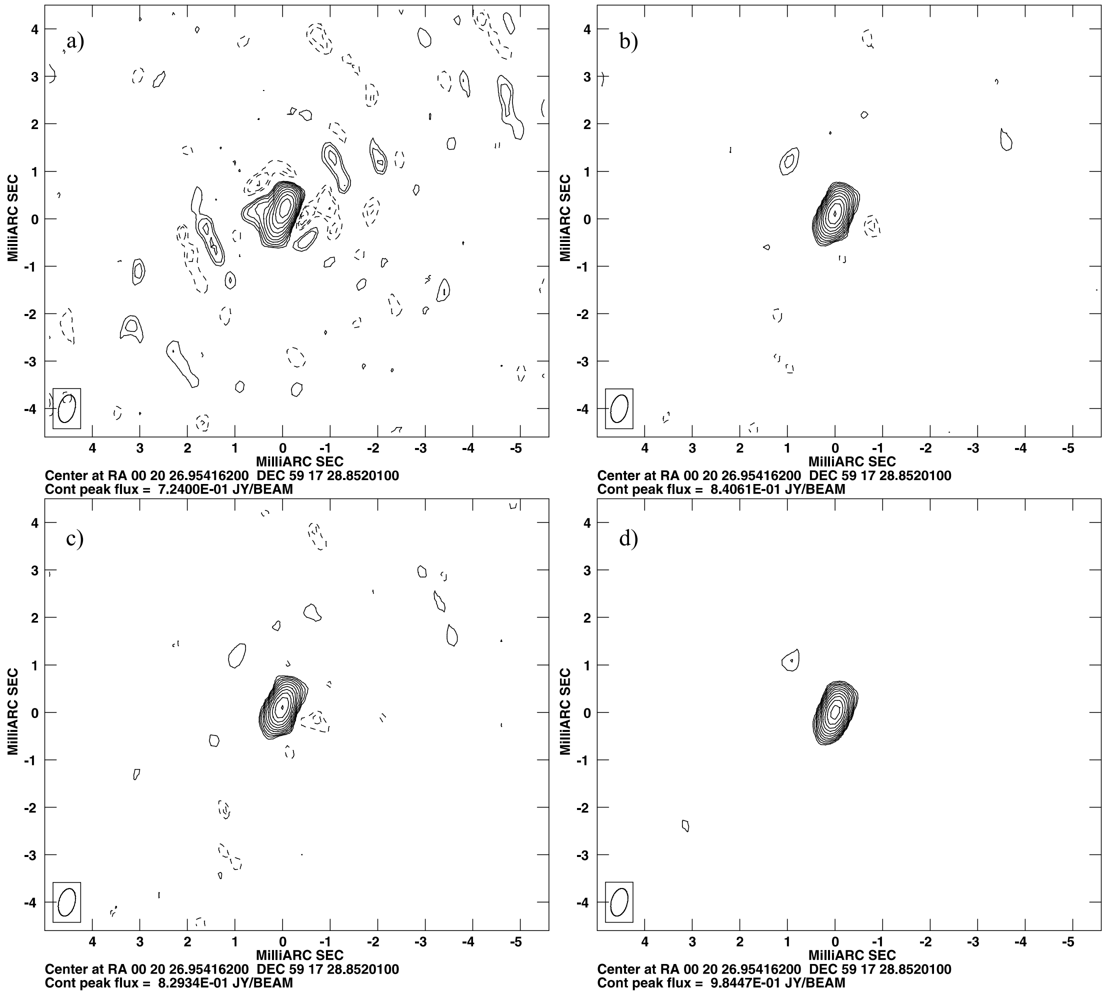

FIGURE 2.7— Phase-referenced image of a H_2O maser spot in IC 10 without correction a), with atmosphere correction from the fit to the phases b), with corrections from the geodetic-like observations c) and after phase-self-calibration d). The contour levels start at 25 mJy and increase by a factor of $\sqrt{2}$ in all images. The peak-to-noise ratios are 77, 101, 100 and 151 respectively.

2.3.3 Geodetic-like Observations

A second, independent method to estimate the zenith delay offset is to use *geodetic-like* observations. Here one observes a number of bright and compact radio sources with positions known to 1 mas at different elevations. The sources were observed with a frequency setup of 8 IFs spread over 450 MHz. A fringe-fit yielded then a multi-band delay (i.e. one solution for all 8 IFs combined) and a rate for each baseline and source. These multi-band delays and rates were then fit with a model that consisted of a zenith delay offset and drift at all antennas as well as a clock offset and drift at all antennas except the reference antenna. The parameters of the best model-fit for the observation on 2002 January 12 are given in Table 2.3.2. The differences between the observed multi-band delays and the model are less than 0.1 ns.

The zenith delay offsets obtained from the fit to the phases and from the geodetic-like observations are in general comparable although they can be different for some antennas. The differences between the two methods are not surprising, since the model in the geodetic-like observations includes not only a zenith delay offset but also a drift, a clock offset and a clock drift and should yield more reliable results.

2.3.4 Phase Corrections

The errors in the uv-data of the reference and target sources caused by the zenith delay offset can be calculated. Hence, it is possible to correct the uv-data of all sources for these errors. After suggesting this method to NRAO, Leonid Kogan provided a new version of the AIPS task CLCOR with OPCODE='ATMO'. This task reads in the zenith delay offsets, calculates the delays of the source at their zenith angle $\delta l(Z)$ and corrects the corresponding calibration table entries. The corrections are applied to all sources before the fringe-fit on the calibrator.

These corrections cause an improvement in the quality of the phase-referenced image. This can be seen in Figure 2.7, where the phase-referenced image of a H_2O maser component in IC 10 is shown without any corrections a) (same as Figure 2.4), with the corrections obtained from the fit to the phases b), with the corrections from the geodetic-like observations c), and a phase self-calibrated image d). The image looks much cleaner and the large phase errors are removed. The noise in the corrected images is reduced while the peak fluxes increased. The peak-to-noise ratios are 77, 101, 100 and 151 respectively.

The position of the source in the map that was corrected with the zenith delay offsets from the fit to the phases is $\mathrm{d}x = -1$ μas and $\mathrm{d}y = 103$ μas. This is consistent with the positions from the fit to the phases. This agreement is not surprising, since the two methods are not independent. In both cases, the data on the target sources was used to estimate the zenith delay offset and the position. However, it is a consistency check for the method.

The position in the phase-referenced image using the correction from the geodetic-like observations is $\mathrm{d}x = 13$ μas and $\mathrm{d}y = 101$ μas. This is again in good agreement to the positions estimated by the fit to the phases. This method is an independent check, since here the zenith delay offsets were estimated from completely different data, i.e. the geodetic-like observations.

A further check of consistency is a new fit of the corrected data. The corrected phase-data can be fitted again with a model consisting of an position offset and a zenith delay offset at each antenna. This fit results in the same position and the residual zenith delay offsets are typical < 0.5 cm.

The geodetic-like data can also be corrected by CLCOR. A new fit to the corrected data yields also zenith delay offsets < 0.5 cm and clock offsets < 0.02 ns.

2.4 Summary

In this chapter, the concepts of interferometry, Very Large Baseline Interferometry, astrometry and phase-referencing were introduced.

A technique was presented to correct phase-referencing observations for inaccurate zenith delays in the correlator model. The quality of the atmosphere-corrected phase-referenced images can be improved by this technique. The peak-to-noise ratios in the corrected images increased by $\approx 30\%$.

Two independent methods were presented to estimate the zenith delay offsets at each antenna. The images obtained from the correction with the zenith delay offsets from the fit to the phases and for the geodetic-like observations are very similar and the positions measured from these images are consistent. This is a proof of concept for the technique. The atmosphere-corrected phase-referencing can now be applied to the observations of IC 10 and M33.

3

Calibrator Search and Test Observations

The phase errors in a phase-referencing experiment scale with the angular separation on the sky between the calibrator and the target source. Hence it is important to observe calibrator sources as close as possible to the target source. This chapter will present the search for closer calibrator sources with the VLA and the VLBA and results of initial test observations to verify the feasibility of phase-referencing observations at 22 GHz.

3.1 Calibrator Search

The sources J0027+5958 and J0137+3122 from the VLBA calibrator survey with flux densities between 100 and 200 mJy at 22 GHz were already known within one degree from IC 10 and M33 respectively. The use of closer calibrators would reduce the systematic errors (e.g. from atmospheric mismodelling). Radio sources with a smaller angular separation from the target source would also allow a check of the obtained positions. Hence, the first step of this work was to find useful check sources near the masers in M33 and IC 10 for phase-referencing observations.

3.1.1 Sample selection

To find useful check sources a sample of radio sources with a small angular separation from the target sources in IC 10 and M33 was observed with the VLA and the VLBA. Since no all-sky survey exists at high frequencies, we had to take sources from the NVSS (**N**RAO/**V**LA **S**ky **S**urvey) at 1.4 GHz and the WENSS (**We**sterbork **N**orthern **S**ky **S**urvey) at 325 MHz. The sources were selected if they satisfied each of the following conditions:

- Angular separation to target < 30 arcmin
- Relatively flat spectrum ($\alpha \geq -0.8$)
- Unresolved in NVSS
- Flux density at 1.4 GHz > 5 mJy

This criteria yield a list of nearby check source candidates which is given in Table 3.1 and Table 3.2 for IC 10 and M33 respectively. The position uncertainty of the NVSS is between 1 and 7 arcseconds depending on the source strength. To get a more accurate position for VLBA follow-up observations and to check the compactness, the candidates were first observed with the VLA in B-configuration.

3.1.2 VLA observations

The sources A1 – A10 and B1 – B9 were observed on 2000 March 9 with the VLA in B configuration at 8.4 GHz with an total observing time of two hours. The source 3C 48 was used as the primary flux density calibrator. Since 3C 48 is resolved with the VLA on the longer baselines one cannot directly determine the amplitude calibration of all antennas. One has to use secondary calibrators which are unresolved on all baselines. However, sources which are compact enough have variable flux densities which must be determined during the observation. The method is to calibrate the inner VLA antennas with

Table 3.1— Calibrator candidates from NVSS and WENSS for IC 10. Listed are names, angular separation from IC 10, flux density at 1.4 GHz, major and minor axis of the source and flux density at 325 MHz.

	Name	Separation	$S_{1.4\ GHz}$	Major	Minor	$S_{325\ MHz}$
		[$arcsec$]	[mJy]	[arcsec]	[arcsec]	[mJy]
A1	J002017+591841	90.6	20.8	<21.4	<17.5	30
A2	J002100+591659	279	10.9	<30.7	<22.6	26
A3	J002108+591132	493	13.6	<20.3	<20.3	21
A4	J002057+590122	1000	12.6	<28.3	<21.1	32
A5	J002144+590329	1043	10.0	<37.9	<32.8	28
A6	J002102+585427	1413	72.0	<17.7	<15.5	242
A7	J002342+592507	1580	47.5	<19.4	<16.1	123
A8	J002035+584807	1765	12.9	<27.9	<22.7	42
A9	J002253+592838	1316	32.2	26.3	<22.7	93
A10	J001843+585722	1436	27.4	<19.0	<16.3	96

Table 3.2— Calibrator candidates from NVSS and WENSS for M33. Listed are names, angular separation from IC133, flux density at 1.4 GHz, major and minor axis of the source and flux density at 325 MHz.

	Name	Separation	$S_{1.4\ GHz}$	Major	Minor	$S_{325\ MHz}$
		[$arcsec$]	[mJy]	[arcsec]	[arcsec]	[mJy]
B1	J013326+305000	225	15.4	<22.2	<19.3	44
B2	J013329+304538	477	17.8	<18.3	<18.3	32
B3	J013414+305406	759	7.7	<35.7	<26.5	–
B4	MG3 J013224+3043	870	169.6	<16.8	<16.0	68
B5	J013247+310741	951	6.4	<51.1	<29.7	–
B6	J013236+311417	1374	16.4	<23.0	<19.5	27
B7	J013159+311038	1444	17.2	<24.5	<20.7	31
B8	J013507+310529	1622	16.5	<25.1	<18.9	24
B9	J013230+310854	1115	20.7	18.9	<20.6	51
B10	J013328+303306	1208	12.4	27.4	<22.2	30
B11	87GB 013140.5+304709	1123	44.5	<19.7	<18.0	131

3C 48 and use them to measure the flux density of the secondary calibrators. These calibrators can then be used to calibrate the rest of the antennas.

The sources 0059+581 and 0116+319 from the VLA calibrator list were used as secondary calibrators for the sources near IC 10 and M33 respectively. Each scan of the target sources was done between two scans of the secondary calibrator. 3.5 minutes were spent on each target source and 2 minutes on the secondary calibrators. Unfortunately, the data of the first 30 minutes of this observation were lost due to a tape problem at the VLA. This included the scans on A1, A2, A3, and A4. The remaining sources were then mapped. All sources except B3 were detected in this observation and the results are shown in Figures 3.1, 3.2, and 3.3.

The sources A5 and B5 were rejected from further investigations, because of their low flux densities. A9, B7, and B9 were also rejected because they appear to be extended. This left the sources A6, A7, A8, A10, B1, B2, B4, B6, and B8 as good candidates for VLBA follow-up observations. The sources A1 – A4 were the best candidates because of their

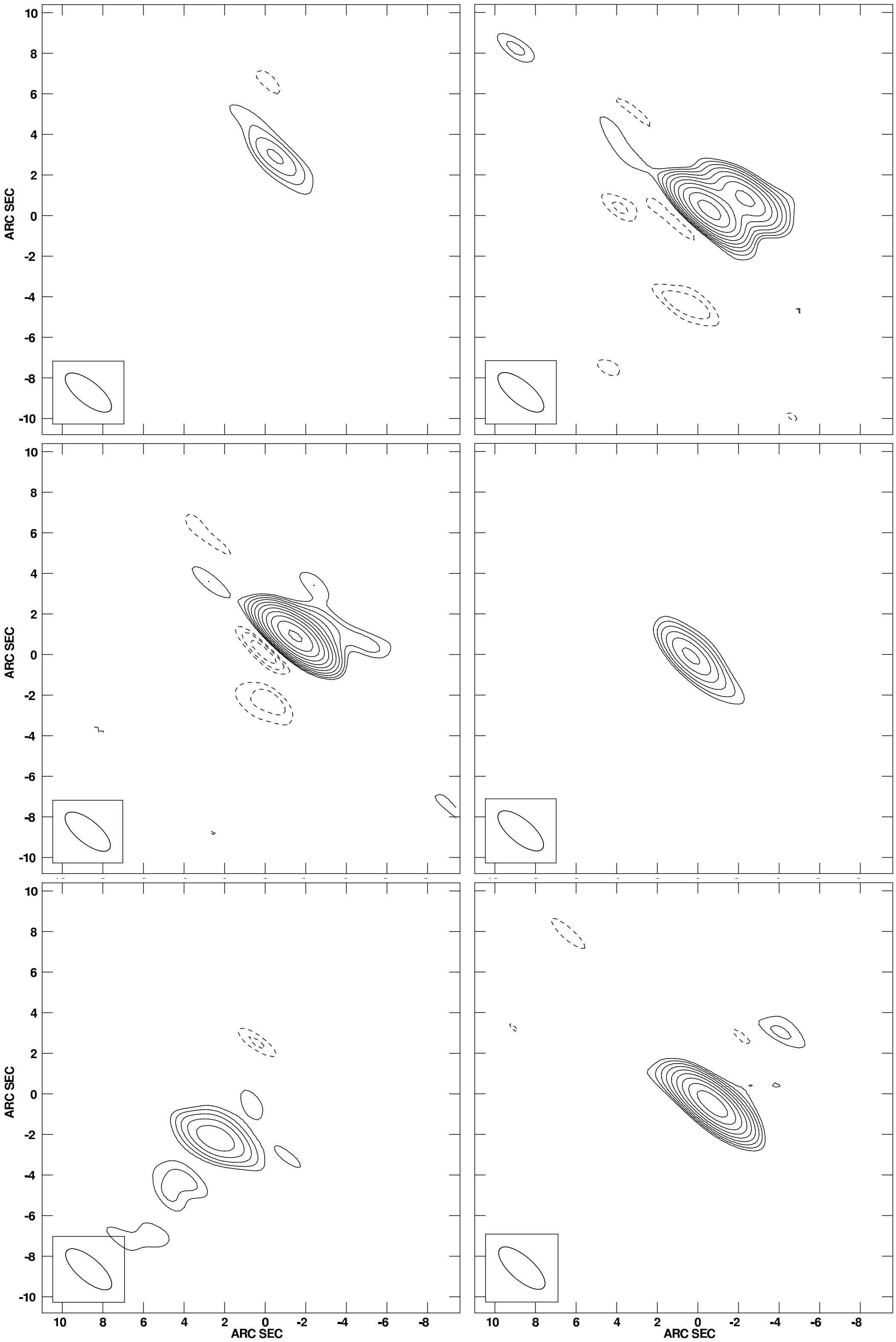

FIGURE 3.1— 8.4 GHz VLA maps of A5 – A10 (from top left to bottom right). The contours start at 0.3 mJy and increase by factors of $\sqrt{2}$. The peak fluxes are 0.92 mJy, 8.0 mJy, 10.2 mJy, 1.9 mJy, 1.6 mJy, and 6.2 mJy.

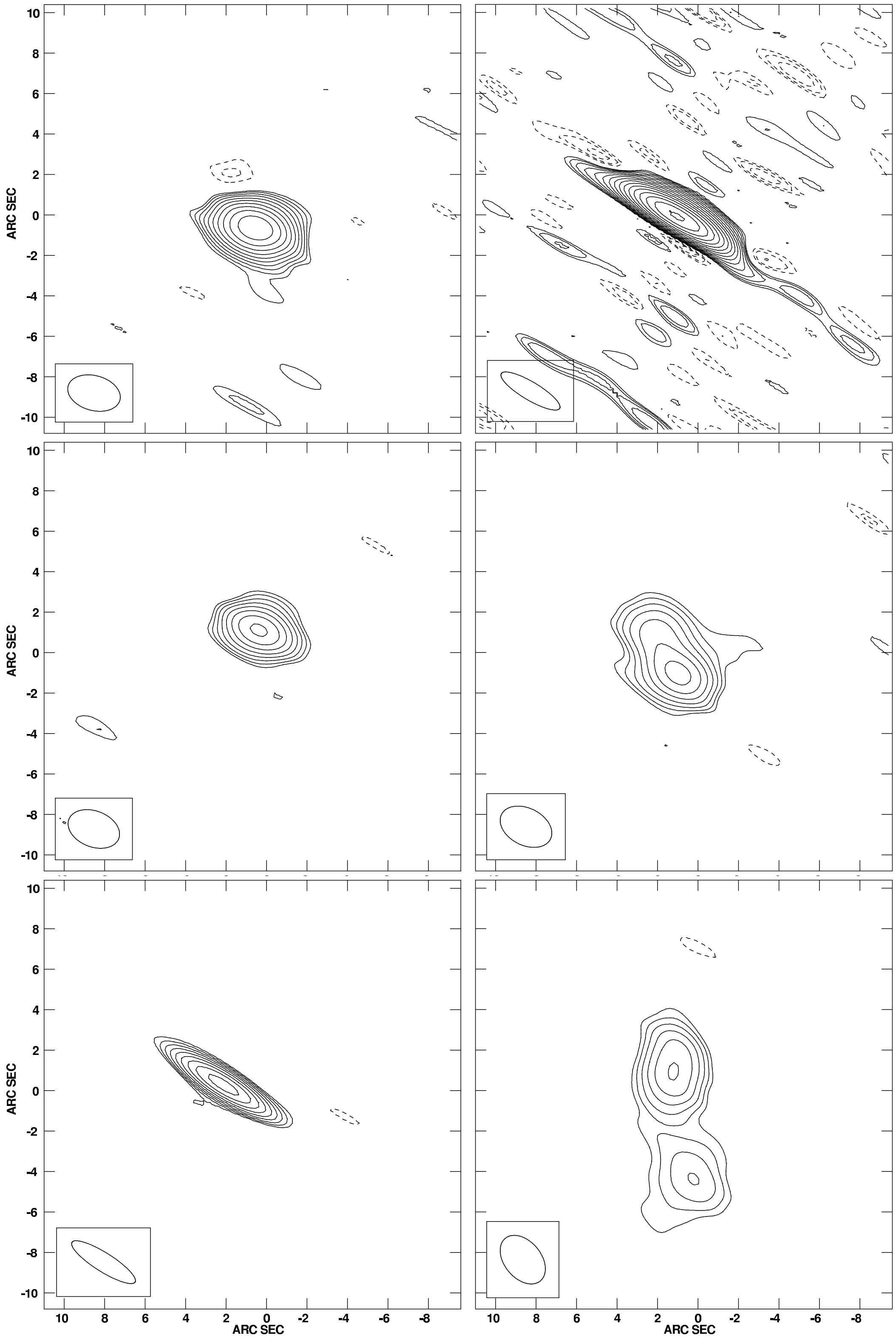

FIGURE 3.2— 8.4 GHz VLA maps of B2, B4, B6 – B9 (from top left to bottom right). The contours start at 0.3 mJy and increase by factors of $\sqrt{2}$. The peak fluxes are 9.2 mJy, 57.5 mJy, 3.6 mJy, 2.8 mJy, 5.7 mJy, and 1.7 mJy.

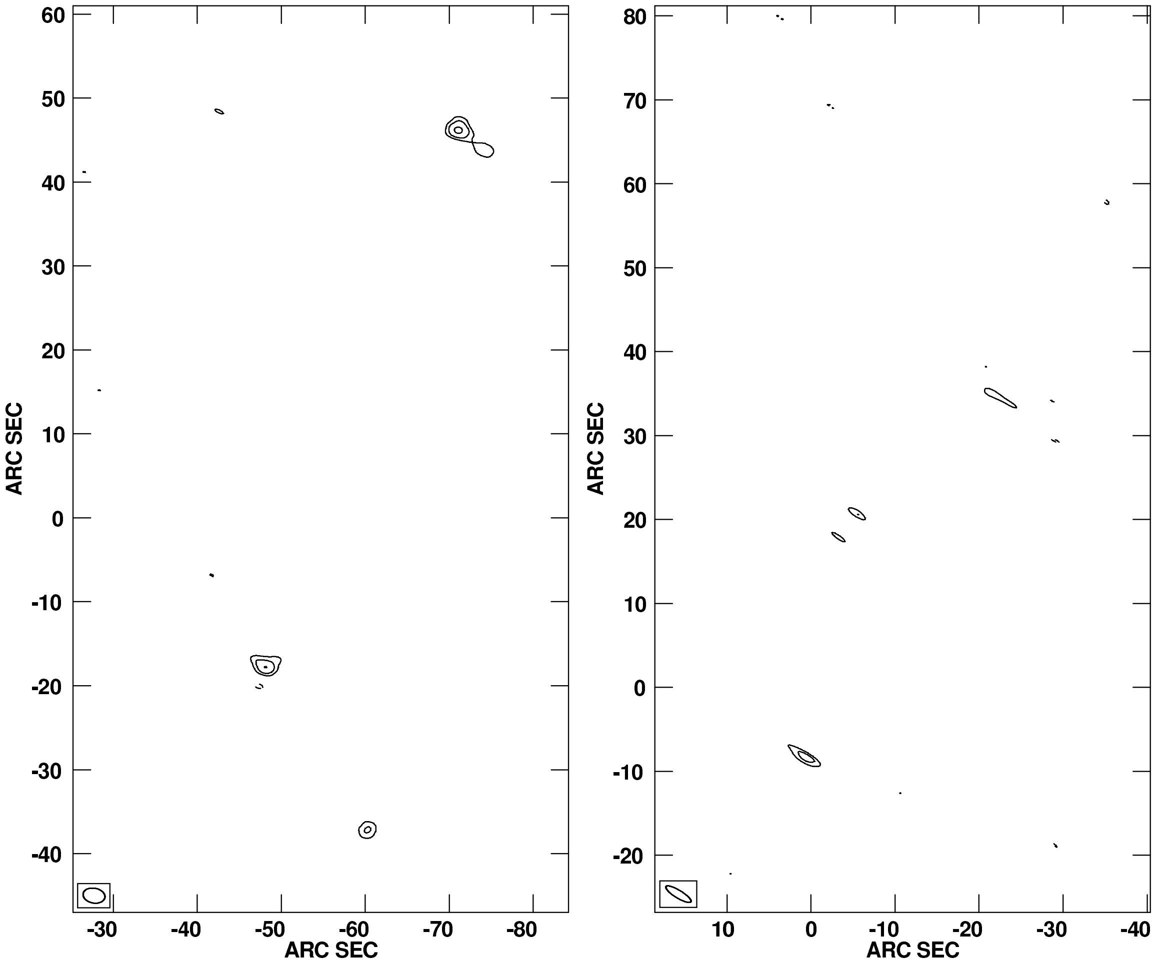

FIGURE 3.3— 8.4 GHz VLA maps of B1 (left) and B5 (right). The contours start at 0.3 mJy and increase by factors of $\sqrt{2}$. The peak fluxes are 0.6 mJy and 0.5 mJy.

small angular separation to the maser in IC 10. Hence, they were also included although the VLA data of their scans was lost. The source B3, B10 and B11 were also included. This resulted in a set of 8 candidate sources for each of our target galaxies for further VLBA observations.

3.1.3 VLBA observations

The sixteen remaining candidate sources were observed with the VLBA on 2000 March 21 at 15 GHz. The intermediate frequency was chosen because the detection of weak sources using phase-referencing is easier than at 22 GHz. The sensitivity of the VLBA is higher at 15 GHz than at 22 GHz and the atmosphere is also more stable at lower frequencies. Most sources are also brigther at lower frequencies. We observed with four 8 MHz bands, each at right and left circular polarization. The total observing time was 4 hours. All sources were phase-referenced to J0027+5958 or J0137+3122 with 20 second scans on the calibrators and 30 second scans on the target sources. The data were calibrated with standard techniques using the AIPS software package. A priori amplitude calibration was applied using system temperature measurements and standard gain curves. A fringe-fit was performed on J0027+5958 and J0137+3122 and the solutions were applied to the candidate sources near IC 10 and M33 respectively. All sources were then mapped.

From all sixteen sources only B4 was de-

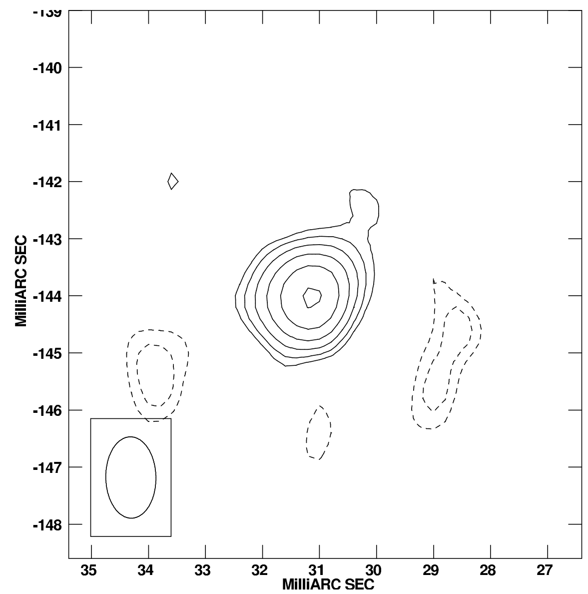

FIGURE 3.4— VLBA maps of B4 at 15 GHz. The contours start at 2 mJy and increase by factors of $\sqrt{2}$. The peak flux is 11.8 mJy.

tected. It appeared compact and had a peak flux density of 11.8 mJy (see Figure 3.4). With its close distance of less than 15 arcminutes from IC 133 and its flux density of 12 mJy, B4 is a good source for phase-referencing. Unfortunately, no check source was detected near IC 10. One reason for the non-detection of A1 – A4 could be an inaccurate position, because the VLA observations of these sources failed. Thus, a re-observation of these sources with the VLA would be important to get a better position.

3.2 Test observations

To verify the feasibility of phase-referencing observations at 22 GHz initial test observations were performed. IC 133 in M33 was observed on 2000 June 20 with the VLBA and the phased VLA while IC 10 was observed on 2000 July 2 with the VLBA and the Effelsberg 100 m-telescope. The VLA and Effelsberg were included to increase the sensitivity of the array (Effelsberg and the phased VLA have alone more collecting area than the all VLBA antennas together.) to detect as many maser features as possible. However, including Effelsberg or the phased VLA has two disadvantages:

- The slew time to switch between two sources is much larger for Effelsberg and the VLA antennas compared to the VLBA antennas. Hence one has to use longer switching times for the phase-referencing.
- Effelsberg and the VLA cannot be included in the dynamic scheduling for the VLBA and the observations have to be on a fixed date regardless of the weather conditions.

Each observation was made with four 8 MHz bands, each at right and left circular polarization. The 128 spectral channels in each band yield a spectral resolution of 62.5 kHz, equivalent to 0.84 km s^{-1}.

In the observation of M33, IC 133 was phase-referenced to J0137+3122 with 30 seconds on each source for 9 minutes. Then B4 was phase-referenced to IC 133 with 40 seconds on each source also for 9 minutes. This continued for 12 hours with a few scans on strong calibrator sources in between.

Since no useful secondary check source could be found in the calibrator search, a second calibrator from the VLBA calibrator survey was included in the observation of IC 10. J0007+5706 is separated by 1.2° from IC 10 and has a flux density of 30 mJy at 8.4 GHz. Here IC 10 was phase-referenced to J0027+5958 with 45 seconds on each source for 10 minutes, before IC 10 was phase-referenced to J0007+5706 with 45 seconds on each source for another 10 minutes. This continued for 11 hours with a few scans on strong calibrator sources in between.

Due to an unfortunate oversight, the frequency setup for the two observations did not include the velocity information for the maser sources and the maser lines were outside our observed bands. Hence, none of the maser features were detected. However, the test observations showed that phase-referencing at 22 GHz is possible. Figures 3.5 and 3.6 show

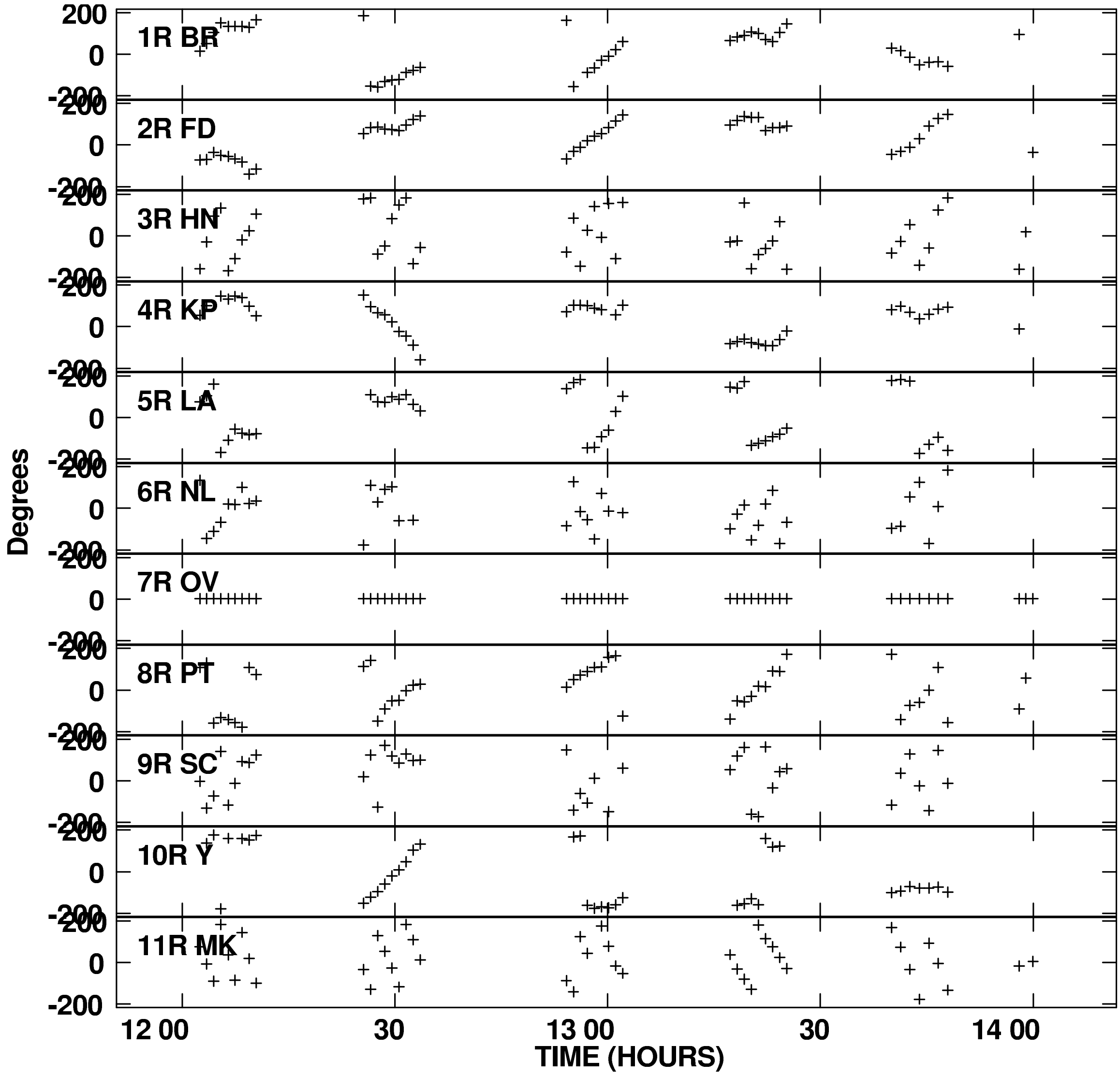

Figure 3.5— Phase solutions on J0137+3122 on a two hour period for all antennas.

the phase solutions from the fringe-fits on J0137+3122 and J0027+5958. One sees that the phases behave very nicely and it is very easy to connect the phases between two adjacent scans. The high fringe rates at the longer baselines to Mauna Kea (MK), St. Croix (SC) and Hancock (HN) are consistent with the expected fringe rate for a position error of ~ 0.05 arcseconds.

Another important lesson learned from these observations is that the primary phase calibrators J0027+5958 and J0137+3122 could be easily detected even without Effelsberg or the phased VLA.

3.3 Summary

The initial calibrator search found one good secondary calibrator with a flux density of 12 mJy with a separation to the masers in IC 133 of less than 15 arcmin. Unfortunately, a secondary calibrator near IC 10 was not found due to the lost data during the VLA observation. However, a later VLA observation of the sources A1 – A4 at 15 GHz resulted in a clear detection and a better position measurement of the source A3 (Reid, private communica-

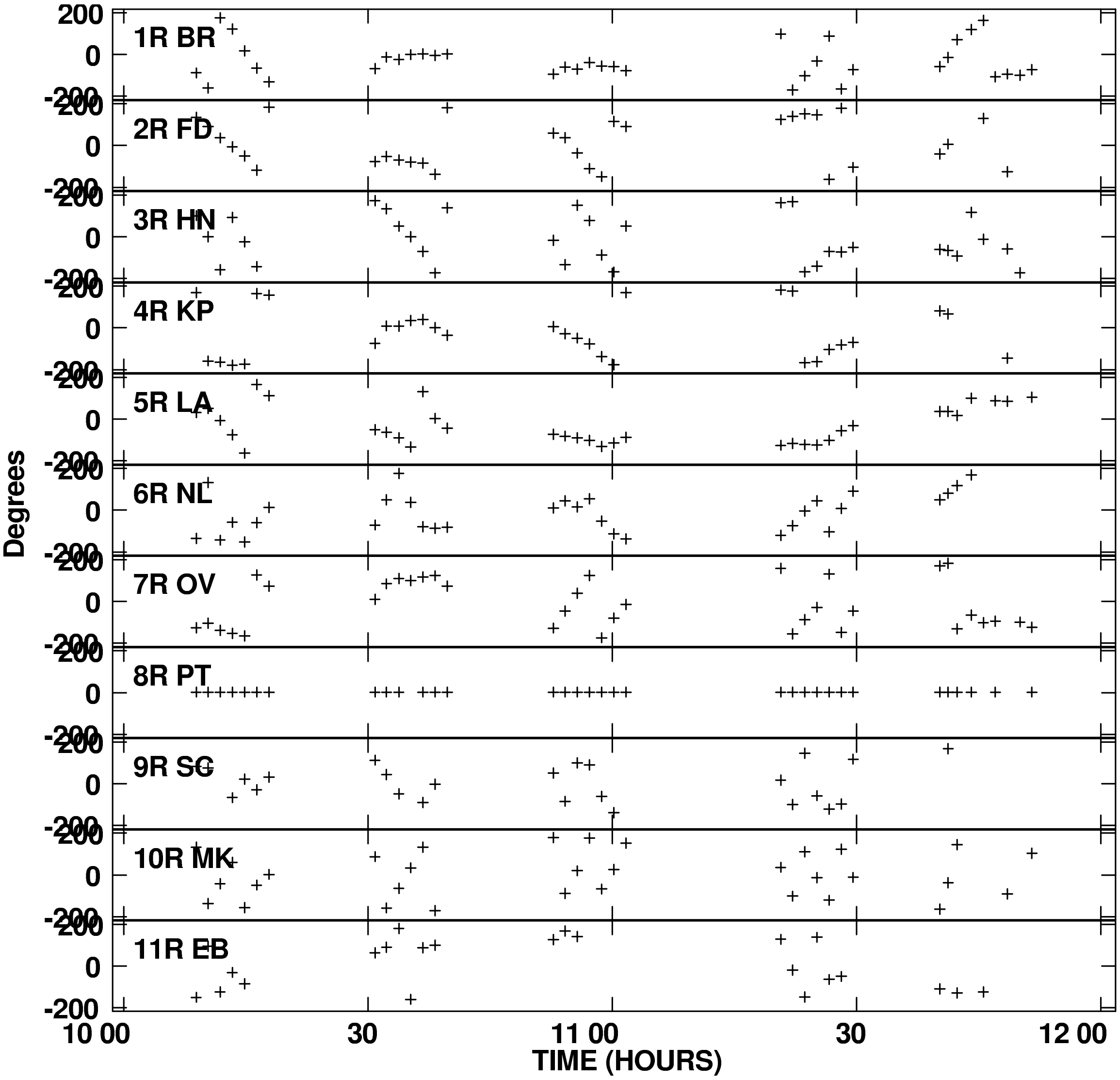

FIGURE 3.6— Phase solutions on J0027+5958 on a two hour period for all antennas.

tion).

The test observations clearly demonstrated that phase connections at 22 GHz are possible with a switching time between sources of 30 seconds. It was also shown that the larger antennas like Effelsberg and the phased VLA are not necessary. Hence, the first epoch of observations were done with the VLBA only using the dynamic scheduling to wait for good weather conditions.

4

VLBA Observations of IC 10

After the calibrator search and the initial test observations, the first epoch of phase-referencing observations of IC 10 and M33 were performed. The idea is to observe each source at least twice in closely spaced observations to verify the true relative positional accuracy. The separation of the observations should be large enough that the weather conditions are uncorrelated, but small enough that proper motions are negligible during this time. Hereafter, the term *epoch* is used for a set of two or three observations within a few weeks.

TABLE 4.1— List of sources and positions for the first observation with references:[1] VLBA calibrator survey; [2] Argon et al. (1994); [3] VLA observations.

Name	RA	DEC
J0027+5958[1]	00:27:03.291	+59:58:52.983
IC 10[2]	00:20:26.962	+59:17:28.850
A3[3]	00:21:08.808	+59:11:33.432

4.1 IC 10

The extragalactic nature of IC 10 was first recognized by Mayall (1935). Hubble (1936) proposed that it was likely a member of the Local Group and described it as "one of the most curious objects in the sky". However, observations of IC 10 have been always difficult because of the low Galactic latitude of 3°. IC 10 has been classified as Ir IV galaxy (e.g. van den Bergh 1999), and Richer et al. (2001) argue that it has more properties of a blue compact dwarf galaxy. It is also the nearest starburst galaxy because of its large number of Wolf-Rayet stars (Massey, Armandroff, & Conti 1992) and the discovery of 144 H II regions (Hodge & Lee 1990). Observations of H I with the Westerbork Synthesis Radio Telescope by Shostak & Skillman (1989) revealed that IC 10 has a regularly rotating disk surrounded by a counter-rotating outer distribution of gas.

The distance to IC 10 was subject to many discussions because of the difficulties caused by the low Galactic latitude. Early estimates claim a distance of 1-1.5 Mpc Roberts (1962), 3 Mpc (Bottinelli, Gouguenheim, & Heidmann 1972, Sandage & Tammann 1974). Huchtmeier (1979) argued for a closer distance of 1 Mpc. Sakai, Madore, & Freedman (1999) obtained a distance of 660±66 kpc to IC 10 from multi-wavelength observations of Cepheid variable stars. If this distance is correct, then IC 10 is probably a free-floating member of the Local Group (van den Bergh 1999). In this work we will adopt this most recent distance estimate of 660 kpc.

Strong H_2O maser emission in IC 10 was detected near one of the brightest H II region in IC 10 at a distance of $\approx$ 104 arcseconds from the kinematic center of the galaxy by Henkel, Wouterloot, & Bally (1986). Another known region of maser activity exists, but the emission from this region is much weaker. Thus, we will consider in this work only the region of strong emission.

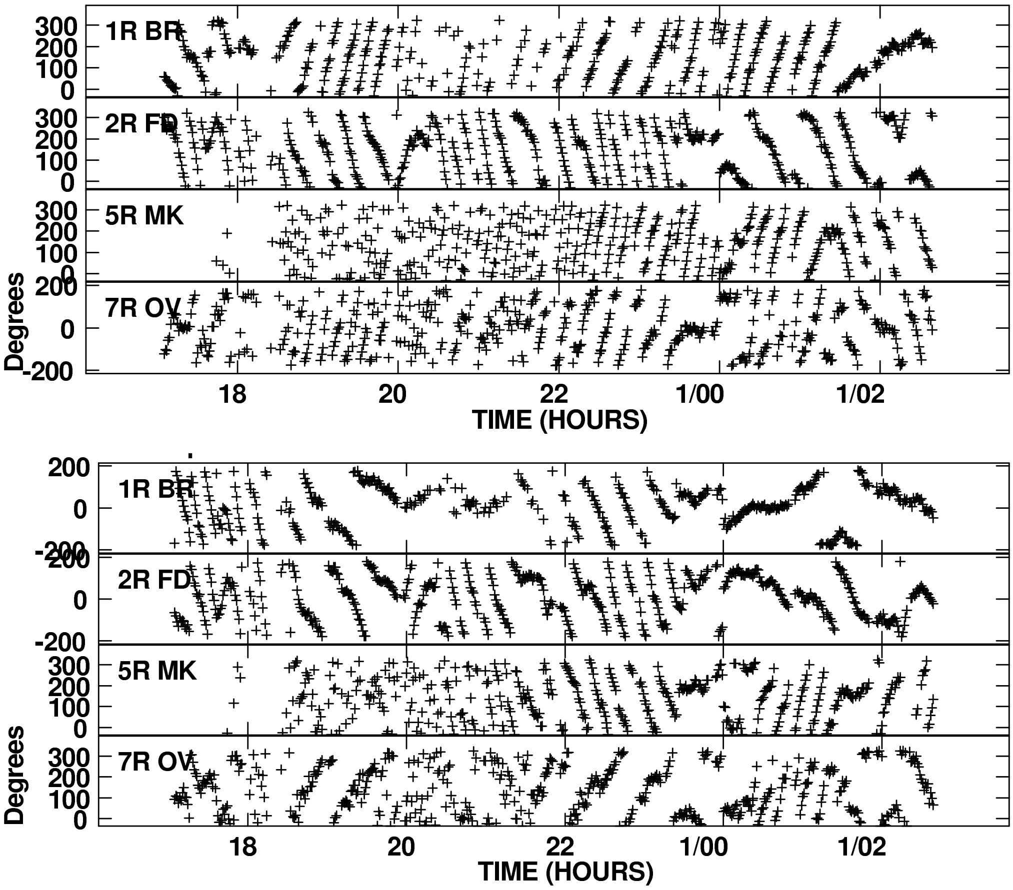

FIGURE 4.1— Phase solutions from fringe-fit on J0027+5958 before (upper) and after (lower) position shift. The phase varies slower after the position shift.

4.2 First Epoch

4.2.1 Observations

In the first epoch, we observed the H_2O masers in IC 10 three times with the VLBA on 2001 February 09, 2001 March 28 and 2001 April 12. We observed four 8 MHz bands, each at right and left circular polarization. The 128 spectral channels in each band yield a spectral resolution of 62.5 kHz, equivalent to 0.84 km s^{-1}, and cover a velocity range of 107.5 km s^{-1}. The third band was centered at -330 km s^{-1} and covers all of the known maser emission as well as the systematic velocity of the galaxy.

The observations involved rapid switching and we went through the cycle J0027+5958 – IC 10 – J0027+5958 – A3 – J0027+5958. The sources were changed every 30 seconds with ≈ 22 seconds on source for each scan. The remaining ≈ 8 seconds include the actual movement and the setteling time of the antennas. Each hour we observed J0102+5824 or J0136+475, two strong calibrators with flux densities of roughly 2 Jy, for 270 seconds. The total observing time was 10 hours for each observation. In the first epoch, no geodetic-like observations as described in Section 2.3.3 were made.

4.2.2 Absolute Positions

The positions of the sources which were used in the first observation are shown in Table 4.1. They were taken from the VLBA calibrator survey for J0027+5958, earlier VLBI observations by Argon et al. (1994) for IC 10 and VLA observations for A3. The uncertainties of the

TABLE 4.2— List of sources and positions for the second and third observation of the first epoch. The positions are taken from the first observation.

Name	RA	DEC
J0027+5958	00:27:03.28569	59:58:52.9634
IC 10	00:20:26.95332	59:17:28.8561
A3	00:21:08.80359	59:11:33.4196

absolute positions were $\approx 20-100$ milliarcseconds. An absolute position error of the reference source will shift the target sources and degrade the image quality. Hence, it is important to have a very accurate absolute position of the calibrator.

The data were first calibrated with the standard techniques in the Astronomical Image Processing System (AIPS). After the initial amplitude calibration using system temperatures and gain curves, a manual phase-cal was performed on J0136+475. Then we did a fringe-fit on J0027+5958. The phase solutions of the fringe-fit showed high fringe-rates which are consistent with an absolute position error of ≈ 50 milliarcseconds (Figure 4.1, upper panel). To get a better absolute position of J0027+5958, we tried to *phase-reference* J0027+5958 towards the strong calibrator J0102+5824, which has a position known to one milliarcsecond. We made a fringe-fit on J0102+5824, applied the solutions to J0027+5958 and imaged J0027+5958. The map looked horrible with extremely strong phase errors. This is expected because the calibrator J0102+5824 was only observed once each hour and the interpolations were very inaccurate. But J0027+5958 could be detected ≈ 45 milliarcseconds from the map center and a better absolute position could be derived with an uncertainty of ≈ 10 milliarcseconds. The new position is given in Table 4.2.

This better position allowed us to correct the data using the AIPS task CLCOR. This task calculates the phase, delay and rate corrections to shift a source and writes this corrections into a CL-table. The data after the correction should be equivalent to data which was correlated at the shifted position. After these corrections, we conducted a new fringe-fit on J0027+5958 and the fringe-rates are much smaller now (Figure 4.1, lower panel), as expected due to a more accurate absolute position. The solutions of the fringe-fit using the corrected position were then applied to all sources.

TABLE 4.3— List of sources and positions for the observations of the second and third epochs. The absolute position of J0027+5958 is taken from the updated VLBA calibrator survey. The positions of IC 10 and A3 are taken from the first epoch.

Name	RA	DEC
J0027+5958	00:27:03.286532	59:58:52.95931
IC 10	00:20:26.954162	59:17:28.85201
A3	00:21:08.804432	59:11:33.41551

After the calibration, A3 and the masers in IC 10 were imaged. A3 and many maser features in IC 10 were easily detected and it was possible to derive a position of the sources. The positions of A3 and of the strongest maser feature in IC 10 are given in Table 4.2. The positions of IC 10 and A3 relative to J0027+5958 are accurate to less than 1 milliarcsecond, but the accuracy of the absolute position is limited by the knowledge of the absolute position of J0027+5958.

Since the data of this first observation on 2001 February 09 was analyzed before the second observation has been correlated, it was possible to correlate the second and third observations of the first epoch with the new and better positions.

On 2001 August 21 the positions of many of the VLBA calibrator sources were updated from a typical accuracy of 20 milliarcseconds to less than 1 milliarcsecond. The position improvements were made by the NASA Goddard Space Flight Center VLBI Group which used the software package Calc/Solve to analyze ten 24-hour VLBA calibrator observations at 13cm/3.6cm. The true position of J0027+5958 differs by 7 milliarcseconds from our rough estimate derived from the *phase-*

referencing towards J0102+5824 as described above. The positions of all sources were updated by this 7 milliarcseconds in the observations of the second and third epochs and are given in Table 4.3. To have all observations as similar as possible, all sources of the observations in the first epoch were shifted with CLCOR to the new and more accurate positions that were also used in the second and third epoch. Thus, the datasets of all observations have the same phase-center now.

4.2.3 Imaging

All three observations of the first epoch were re-analyzed after the correct position of the calibrator J0027+5958 was known. The data reduction was similar to the procedure described above. After the initial amplitude calibration, the sources were shifted using CLCOR to their best known positions from Table 4.3.

Pulse-calibration tones are injected into the VLBA receivers and can be used to measure and track instrumental variations in delay and phase between separate IFs. The application of this data in the PC table using the task PCCOR eliminates instrumental phase and delay offsets between individual IFs. Then the two strong calibrators J0136+475 and J0102+5824 were fringe-fitted and the solutions were applied to all sources. This allows a rough delay calibration.

Finally, the calibrator J0027+5958 was fringe-fitted and the solutions were applied to IC 10 and A3. The solutions for most antennas showed relatively small fringe-rates and it was easy to connect the phases. Only the solutions for the antenna in St. Croix were very noisy and a phase connection was not possible. This behavior was seen in all three observations. The antenna in St. Croix is located very close to the Atlantic Ocean on the Virgin Islands. The relative humidity is very high and the total water vapor content in the line of sight varies very rapid. Hence, the data from this antenna were discarded in all observations. The antenna in North Liberty yielded no data at the first observation. The data from Hancock for the third observation were also discarded due to bad weather. The data on the baselines Brewster to Fort Davis and Brewster to Pie Town on the second observations showed occasional unusual high amplitudes. The corresponding data were also discarded.

Then the sources were imaged. For the continuum source A3, all channels and IFs

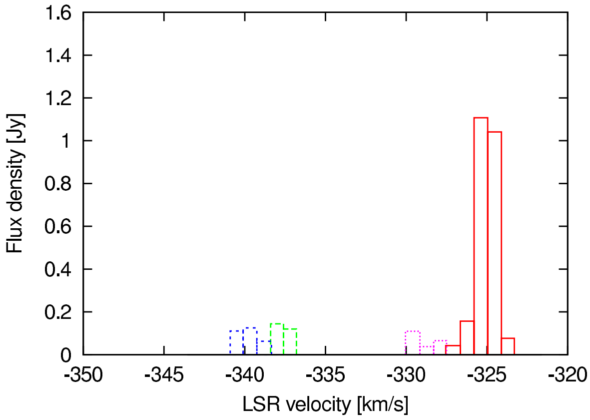

FIGURE 4.2— VLBI-spectrum of IC 10 on 2001 February 09.

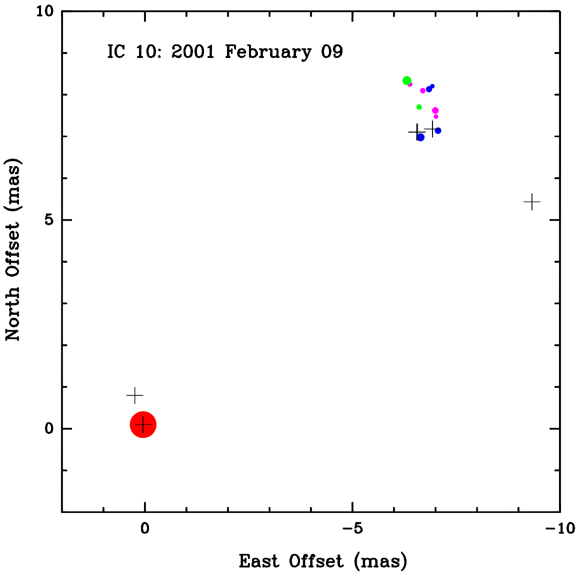

FIGURE 4.3— Composite map of the H_2O masers in IC 10. The area of the circles is proportional to the flux density of the components and the colors are as in Figure 4.2. The black crosses mark the positions of maser emission detected by Argon et al. (1994).

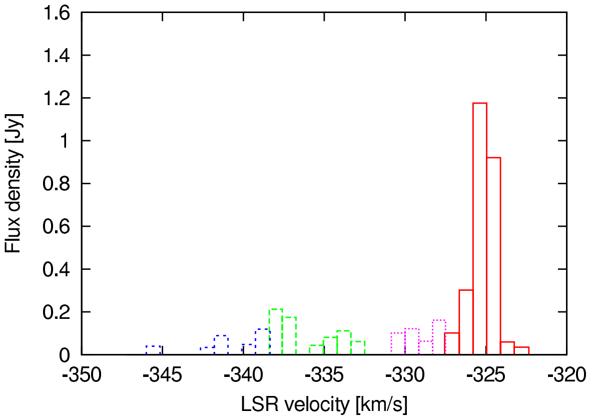

FIGURE 4.4— VLBI-spectrum of IC 10 on 2001 March 28.

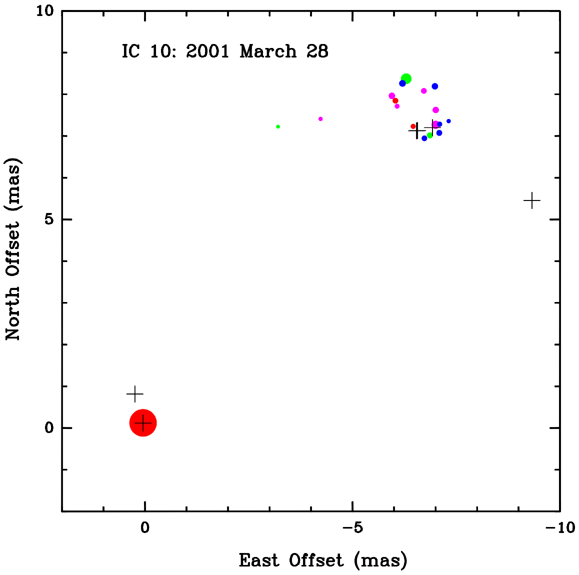

FIGURE 4.5— Composite map of the H_2O masers in IC 10. The area of the circles is proportional to the flux density of the components and the colors are as in Figure 4.2. The black crosses mark the positions of maser emission detected by Argon et al. (1994).

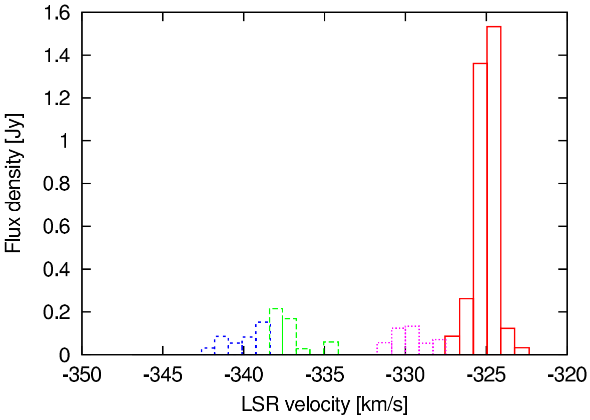

FIGURE 4.6— VLBI-spectrum of IC 10 on 2001 April 12.

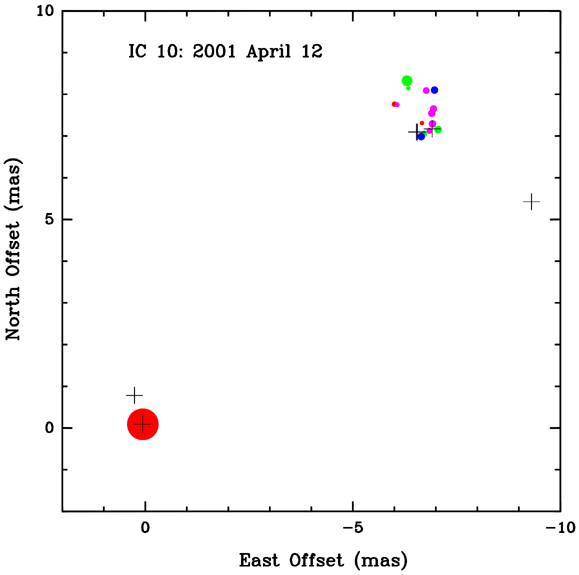

FIGURE 4.7— Composite map of the H_2O masers in IC 10. The area of the circles is proportional to the flux density of the components and the colors are as in Figure 4.2. The black crosses mark the positions of maser emission detected by Argon et al. (1994).

were averaged and imaged, while for IC 10 all channels of the IF containing the masers were imaged separately. The beam sizes for the three observations were 0.53×0.33 mas, 0.55×0.36 mas, 0.63×0.37 mas for the observations in February, March and April respectively. Maser emission could be detected in 21 channels spread over $\approx$ 23 km s^{-1}. The spectra of IC 10 for the three observations of the first epoch can be seen in Figures 4.2, 4.4 and 4.6. The spectra were made by summing up the flux densities of all detected components in the maps of the individual channels. All spectra include one strong component at a LSR velocity of ≈ -324 km s^{-1} which could be detected in 6 channels as well as some weaker components. The strong component was first detected by Henkel, Wouterloot, & Bally (1986) and the whole spectrum of IC 10 showed strong variability since its discovery

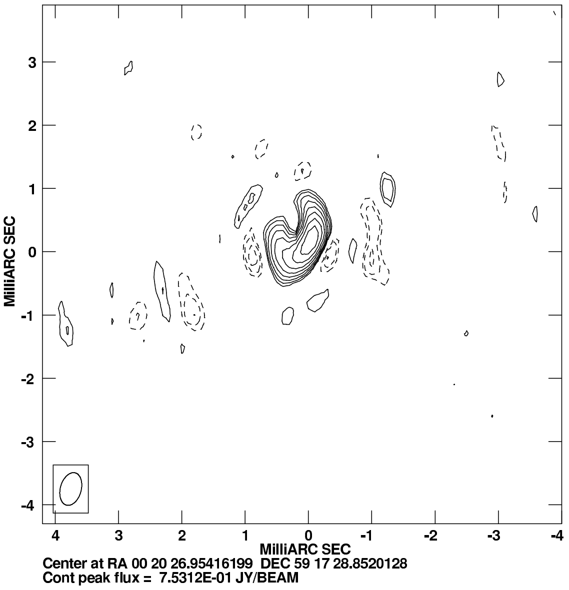

FIGURE 4.8— Phase-referenced image of the H_2O maser spot in IC 10 with an LSR velocity of -324.5 km s^{-1} for the observation on 2001 February 09. The contour levels start at 50 mJy and increase by a factor of $\sqrt{2}$. The peak-to-noise ratio is 53.

(e.g. Baan & Haschick 1994). Even intraday variability has been reported by Argon et al. (1994), but the strong component at ≈ -324 km s^{-1} is persistent until now. The strong variability can already be seen between the three observations. The flux density in channel 58, corresponding to -324.5 km s^{-1} LSR velocity increased from 1.0 to 1.5 Jy between February and April. The weaker components are also very variable and they can appear or disappear from one observation to the next.

The spatial distribution of the masers in the three observations can be seen in Figures 4.3, 4.5 and 4.7. The strong component is separated by ≈ 10 mas or 10^{17} cm from the weaker components. This suggests that the emission is associated with a single object if the maser emission is similar to H_2O maser emission in galactic star forming regions like W3(OH), W49 or Sgr B2 (e.g. Reid et al. 1995, Walker et al. 1977 and Kobayashi et al. 1989 respectively). The weaker maser components form an apparent ring-like structure with an projected size of $\approx$ 1.6 mas or 1000 AU.

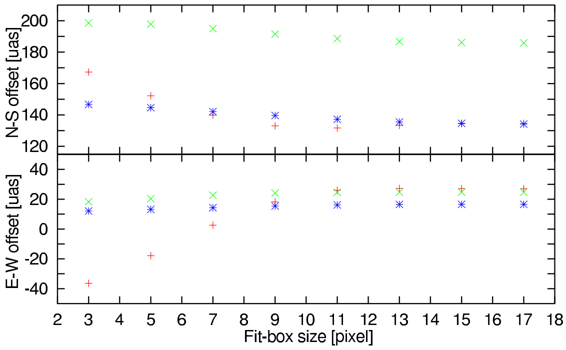

FIGURE 4.9— East-West and North-South offset as a function of the fit-box size for the the observations of the first epoch. The observation on 2001 February 09, 2001 March 28 and 2001 April 12 are represented by (+), (x) and (*) respectively.

Since the astrometric accuracy depends strongly on the source strength, we will concentrate in the following on the two channels with the strongest emission. Figure 4.8 shows the phase-referenced image of the maser component in IC 10 with an LSR velocity of -324.5 km s^{-1} for the first observation on 2001 February 09. The image shows large errors which are caused by phase calibration errors. The phase errors have the effect that the point source is spread out over a larger area. This makes the estimate of the position very difficult. If one fits a single elliptical Gaussian component to the image, the outcome depends very strongly on the size of the fit-box, i.e. the part of the image which is included in the fit. This can be seen in Figure 4.9, were the position offset from the map center in north-south and east-west directions are shown as a function of the size of the used fit-box for all three observations. Here the fit-box was centered at the pixel of the peak emission. The measured positions change by up to ≈ 70 μas if the fit-box size is changed. This can be explained by a closer look to the corresponding map of the observation on 2001 February 09. If the fit-box is small at the position of the peak, the fit will discard all the extended emission in the map. However, if the fit-box grows, the emission south-east of the peak will be included in the fit. This will move the measured position

TABLE 4.4— Epoch 1: Position offset in right ascension $\Delta\alpha$, declination $\Delta\delta$ and peak flux S of IC 10 from imaging.

	-324.5 km s^{-1}			-325.4 km s $^{-1}$		
Date	$\Delta\alpha$ [μas]	$\Delta\delta$ [μas]	S [mJy]	$\Delta\alpha$ [μas]	$\Delta\delta$ [μas]	S [mJy]
2001/02/09	27	135	725	25	138	780
2001/03/28	25	186	831	25	190	1082
2001/04/12	17	134	1531	20	134	1393
Mean	23±4	152±24		23±2	154±26	

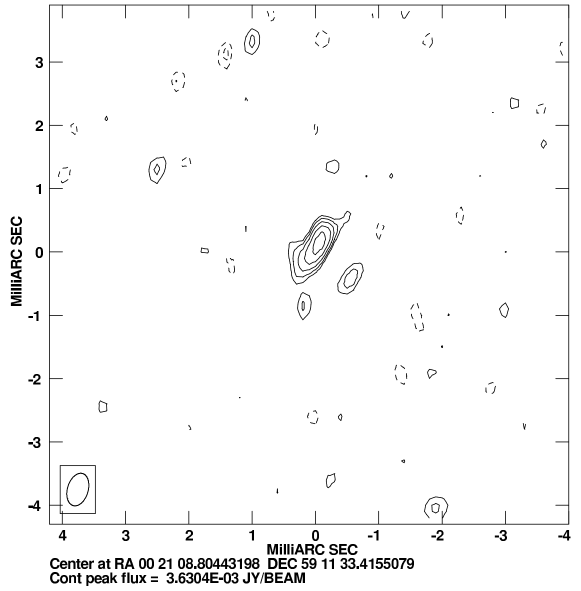

FIGURE 4.10— Phase-referenced image of the check source A3 for the observation on 2001 February 09. The contour levels start at 0.75 mJy and increase by a factor of $\sqrt{2}$. The peak-to-noise ratio is 11.

TABLE 4.5— Epoch 1: Position offsets in right ascension $\Delta\alpha$, declination $\Delta\delta$ and peak flux S of A3 from imaging.

Date	$\Delta\alpha$ [μas]	$\Delta\delta$ [μas]	S [mJy]
2001/02/09	-15	87	3.5
2001/03/28	1	103	5.9
2001/04/12	-6	89	7.0
Mean	-7±7	93±7	

in south-east direction, which is seen in Figure 4.9. Because of this large differences, it is not trivial to measure a position from this map.

Figure 4.9 also shows that the positions do not change significant for fit box sizes larger than 11 pixel, corresponding to 1.1 mas. The positions of the maser in the two channels with the strongest emission from all three observations are given in Table 4.4. Here fit-boxes with a size of 17 pixels, i.e. the last points in Figure 4.9, were used. The agreement of the positions for the three observations is already very good with a standard deviation of 4 and 2 μas in right ascension and 24 and 26 μas in declination for the two channels respectively. This standard deviation is only a formal statistical error. This formal error has to be treated carefully due to the small number of observations. The largest deviation in declination comes from the second observation, which differs by ≈ 50 μas from the other two observations. The reason for this deviation is probably caused by atmospheric effects.

The phase-referenced image of the check source A3 for the observations of 2001 February 09 can be seen in Figure 4.10. The apparent elongation of the source is caused – as seen later – by the same phase errors that distort the image of the H_2O maser in IC 10. The source is unresolved in the second and third observation. The position of A3 on the images of the three observations were determined also by a fit of a single Gaussian component to the map. The resulting positions and peak fluxes are shown in Table 4.5. The agreement of the positions between the three observations is also very good. The largest deviation in declination comes – similar to IC 10 – from the second observation.

TABLE 4.6— Epoch 1: Position offset of IC 10 from phase fitting and zenith delay offsets at each antenna in cm.

	-324.5 km s^{-1}		-325.4 km s $^{-1}$	
Date	$\Delta\alpha$ [μas]	$\Delta\delta$ [μas]	$\Delta\alpha$ [μas]	$\Delta\delta$ [μas]
2001/02/09	40	102	40	108
2001/03/28	42	121	45	122
2001/04/12	51	100	52	108
Mean	44±5	108 ± 9	46±5	113± 7

Date	BR	FD	HN	KP	LA	MK	NL	OV	PT	SC
2001/02/09	0.54	4.59	1.16	3.72	2.48	-6.03	–	4.88	3.03	–
2001/03/28	0.05	1.31	5.48	0.14	1.22	-1.33	3.68	-1.84	-0.61	–
2001/04/12	1.20	1.93	–	-0.47	-2.28	-1.49	1.64	-1.60	-1.69	–

4.2.4 Phase-fitting

Instead of imaging the sources to get the position, one can look directly at the calibrated phase data of the target source. One can fit a model including a position offset and a constant zenith delay offset at each antenna as described in section 2.3.2. Since we got two channels with strong maser emission, the data from both channels were fit simultaneously. The resulting position offsets and zenith delay errors for the best model-fit can be seen in Table 4.6. The agreement between the three observations is again very good. The standard deviation in right ascension is 5 μas for both channels, which is comparable to the results from the imaging. A large improvement could be made in the accuracy of the position offset in declination, where the standard deviation is only 9 and 7 μas for the two channels. This is a factor 3-4 better than the accuracy from the imaging. The largest deviation in declination is now only $\approx$ 20 μas instead of $\approx$ 50 μas from the imaging. This is a clear sign that the large error from the imaging comes indeed from the contribution of the atmosphere. The fitted zenith delay offsets are of the order of a few centimeters for all stations.

The position from the fit show also a systematic offset from the positions from the imaging, which is 10-30 μas in right ascension and 30-70 μas in declination. This position shift can be also explained by the zenith delay errors. As seen in section 2.3.2, the delay errors after phase-referencing for a zenith delay error of 3 cm, zenith angles of 60° and source separations of 1° are $\approx$ 0.2 cm. Since these errors are uncorrelated for different antennas, one expects an error of $\sqrt{2} \times 0.2$ cm on one baseline. This corresponds at a wavelength of 1.3 cm to a position shift of $\approx$ 20 % of a fringe spacing, or 80 and 130 μas in right ascension and declination respectively. If one considers, that this effect will cancel partially due to the different baselines, it is of the right order of magnitude to explain the position shift between the images and the phase fit.

The phase data of the check source A3 is extremely noisy, because of the low flux density of the source. Hence, a fit to the phases makes no sense, and no position offset could be obtained by this method.

4.2.5 Phase Correction

The zenith delay offsets from Table 4.6 can now be used to correct the uv-data itself with the AIPS task CLCOR as described in section 2.3.4. The masers were imaged after the correction and the atmosphere-corrected phase-referenced image of the maser component with an LSR velocity of -324.5 km s^{-1} can be seen in Figure 4.11. The quality of the image is much better than the uncorrected image in Figure 4.8. The strong image distortions caused by phase errors have almost completely disappeared and the source is more compact and point-like. The peak-to-noise ra-

TABLE 4.7— Epoch 1: Position offset of IC 10 from atmosphere-corrected imaging.

	-324.5 km s^{-1}			-325.4 km s^{-1}		
Date	$\Delta\alpha$ [μas]	$\Delta\delta$ [μas]	Peak Flux [mJy]	$\Delta\alpha$ [μas]	$\Delta\delta$ [μas]	Peak Flux [mJy]
2001/02/09	44	104	926	44	108	974
2001/03/28	42	124	898	42	130	1159
2001/04/12	56	94	1556	58	97	1424
Mean	47± 6	107±13		48±7	112±14	

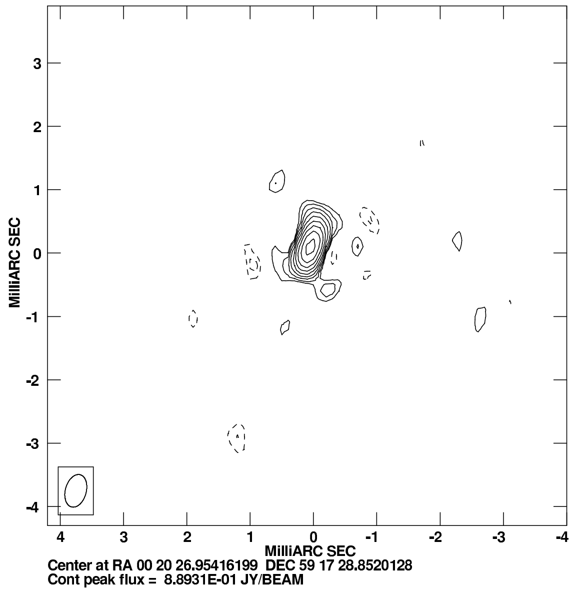

FIGURE 4.11— Atmosphere-corrected phase-referenced image of the H_2O maser spot in IC 10 with an LSR velocity of -324.5 km s^{-1} for the observation on 2001 February 09. The contour levels start at 50 mJy and increase by a factor of $\sqrt{2}$.

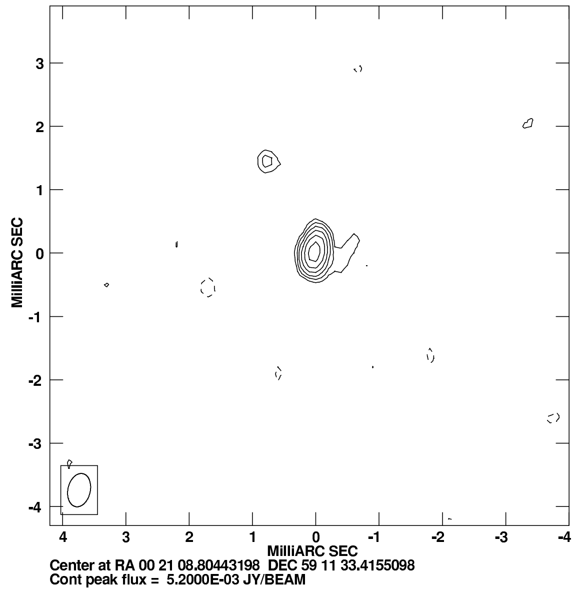

FIGURE 4.12— Atmosphere-corrected phase-referenced image of the check source A3 for the observation on 2001 February 09. The contour levels start at 0.75 mJy and increase by a factor of $\sqrt{2}$.

tio increased from 53 to 76, an increase of 43%. For the other two observations, the peak-to-noise ratio increased by ≈ 10-20%.

The positions in the images can be obtained again by a fit of a single Gaussian component to the map. The resulting positions from all three observations are given in Table 4.7. The positions agree very good with the positions from the fit to the phases, but the deviations are slightly larger. This good agreement and the improved image quality and astrometric accuracy are a clear sign that the largest source of error in the uncorrected maps is indeed caused by an inaccurate zenith delay in the correlator model.

TABLE 4.8— Epoch 1: Position offsets in right ascension $\Delta\alpha$, declination $\Delta\delta$ and peak flux S of A3 from atmosphere-corrected imaging.

Date	$\Delta\alpha$ [μas]	$\Delta\delta$ [μas]	S [mJy]
2001/02/09	13	17	4.9
2001/03/28	17	35	6.0
2001/04/12	15	60	7.0
Mean	15±2	37±18	

Since the corrections were applied to all sources, the check source A3 was also imaged using the corrected data. The resulting im-

Table 4.9— Epoch 2: Position offset of IC 10 from imaging.

	-324.5 km s^{-1}			-325.4 km s $^{-1}$		
Date	$\Delta\alpha$ [μas]	$\Delta\delta$ [μas]	Peak Flux [mJy]	$\Delta\alpha$ [μas]	$\Delta\delta$ [μas]	Peak Flux [mJy]
2002/01/12	-26	185	740	-22	182	593
2002/01/17	-22	214	810	-26	215	553
Mean	-24±2	200±15		-24±2	199±17	

age of A3 for the first observation is shown in Figure 4.12. The elongated structure seen in the uncorrected image disappeared and the source is unresolved. The peak-to-noise ratio increased from 11 in the uncorrected map to 19 in the corrected map, an increase by 72%. For the other two observations, the peak-to-noise ration increased only by ≈ 10%.

Here, the positions of the source in the map can be obtained also by a fit to the map. The positions of A3 in the atmosphere-corrected maps are given in Table 4.8. The agreement in right ascension is very good, while the deviations in declination became larger by the correction. However, the good agreement on the uncorrected maps is probably caused by a coincidence. The expected error from the signal-to-noise ratio of the uncorrected maps is ≈ 30 μas, more than a factor of 3 larger than the value in Table 4.5.

4.3 Second Epoch

4.3.1 Observations

The second epoch of IC 10 was observed with the VLBA on 2002 January 12 and 2002 January 17. The experimental setup was identical to the observations in the first epoch, except for the inclusion of geodetic-like observations as described in section 2.3.3 before and after the phase-referencing observations. During the geodetic-like observations, we observed with eight 8 MHz bands at left circular polarization. The eight bands were set to frequencies which were 0.0, 25.0, 87.5, 187.5, 350.0, 400.0, 437.5 and 450.0 MHz offset from the reference frequency. For the geodetic-like observations nine strong sources from the VLBA calibrator list were observed for 5 minutes each. The positions of these sources were chosen to cover all elevation ranges at all telescopes. The total observing time was 10 hours, 8.5 hours were spent on the phase-referencing and 45 minutes were spent on the geodetic-like observations before and after the phase-referencing. The sources were observed at the best known positions listed in Table 4.3.

Table 4.10— Epoch 2: Position offsets in right ascension $\Delta\alpha$, declination $\Delta\delta$ and peak flux S of A3 from imaging.

Date	$\Delta\alpha$ [μas]	$\Delta\delta$ [μas]	S [mJy]
2002/01/12	-28	107	5.9
2002/01/17	-40	108	6.6
Mean	-34±6	108±1	

4.3.2 Imaging

The data reduction was identical to the data reduction of the first epoch. After the initial amplitude calibration using the system temperatures and gain curves, the task PCCOR was used to eliminate instrumental phase and delay offsets between individual IFs. A fringe-fit was performed on the two strong calibrators J0102+5824 and J0136+475 for a rough delay calibration. Then the calibrator J0027+5958 was fringe-fitted and the solutions were applied to IC 10 and A3. The data of the antenna in St. Croix were discarded in both observations due to the large phase noise on all baselines to this telescope.

Then all sources were imaged. The beam sizes were 0.6×0.34 mas and 0.58×0.33 mas for the two observations. Maser emission was detected in a velocity range from -323.7 to -

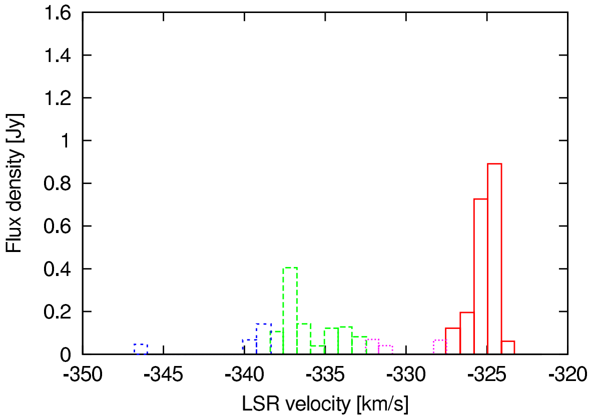

FIGURE 4.13— VLBI-spectrum of IC 10 on 2002 January 12.

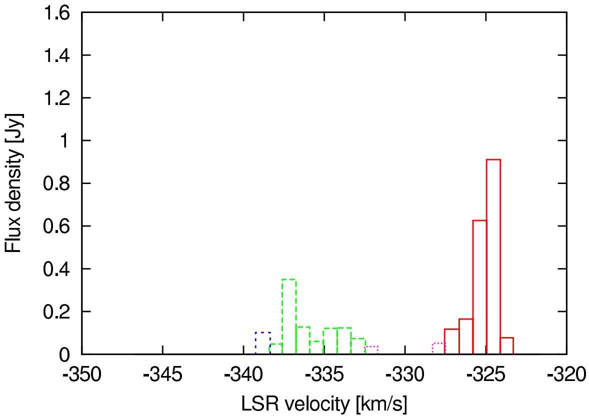

FIGURE 4.15— VLBI-spectrum of IC 10 on 2002 January 17.

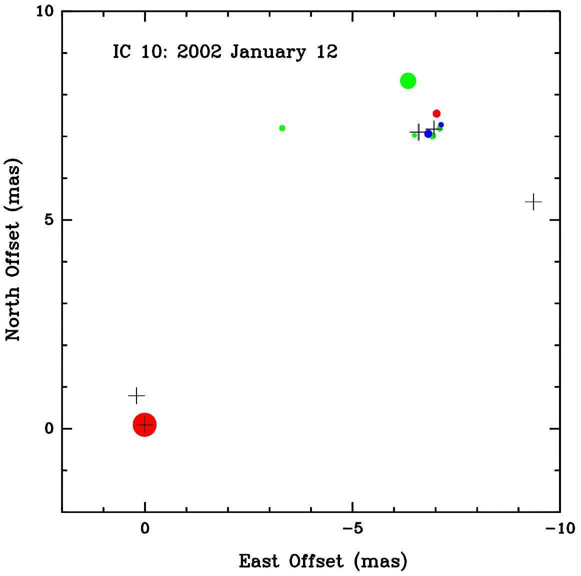

FIGURE 4.14— Composite map of the H_2O masers in IC 10. The area of the circles is proportional to the flux density of the components and the colors are as in Figure 4.13. The black crosses mark the positions of maser emission detected by Argon et al. (1994).

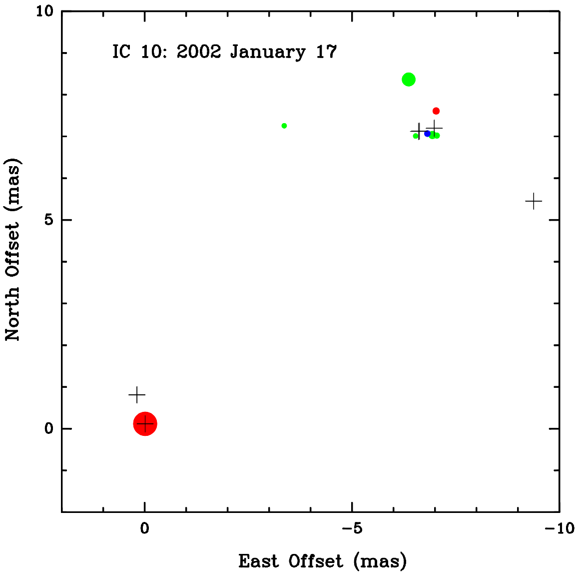

FIGURE 4.16— Composite map of the H_2O masers in IC 10. The area of the circles is proportional to the flux density of the components and the colors are as in Figure 4.13. The black crosses mark the positions of maser emission detected by Argon et al. (1994).

346.4 km s^{-1}. The spectra of IC 10 for the two observations can be seen in Figures 4.13 and 4.15. The spectra show the same features as the spectra from the first epoch, but the flux density of the strong component at ≈ -324 km s^{-1} decreased to less than 1 Jy compared to over 1.5 Jy in the last observation of the first epoch. A component at ≈ -337 km s^{-1} got significantly brighter. The spectra show also some variability between the two observations, e.g. a different ratio between the two strongest channels.

The spatial distribution of the masers in the two observations can be seen in Figures 4.14 and 4.16. The overall picture looks similar to the distribution in the first epoch. The strong maser component at a LSR velocity of ≈ -324 km s^{-1} is separated from the weaker features

Table 4.11— Epoch 2: Position offset of IC 10 from phase fitting and zenith delay offsets at each antenna in cm.

	-324.5 km s^{-1}		-325.4 km s^{-1}	
Date	$\Delta\alpha$ [μas]	$\Delta\delta$ [μas]	$\Delta\alpha$ [μas]	$\Delta\delta$ [μas]
2002/01/12	0	110	1	114
2002/01/17	-11	136	-14	141
Mean	-6±6	123±13	-7±8	128±14

Date	BR	FD	HN	KP	LA	MK	NL	OV	PT	SC
2002/01/12	1.87	4.15	6.93	0.80	-0.40	-3.54	9.35	4.47	-0.32	–
2002/01/17	6.91	-0.03	9.54	4.85	4.43	-1.38	9.12	7.06	2.85	–

by a distance of ≈ 10 mas. The ring-like structure from the first epoch is still visible, although fewer components were detected.

The positions of the two strongest maser components in the images are again obtained by a fit of a single elliptical Gaussian to the maps and given in Table 4.9. The positions of the two observations agree again very well. The position difference between the two observations is, like in the first epoch, larger in declination than in right ascension.

The continuum check source A3 is unresolved in both observations. The positions of A3 from the maps are shown in Table 4.10. Here the agreement is also very good.

4.3.3 Phase-fitting

We also looked directly at the calibrated data of the observations of the second epoch. We fitted a model including a position offset and a constant zenith delay offset at each antenna to the data as described in section 2.3.2. The data of the two strongest channels were fit simultaneously. The resulting position offsets and zenith delay offsets for the best model-fit are shown in Table 4.11. The agreement between the two observations is again very good. The difference between the two observations is comparable to the difference in the images, while the positions changed by ≈ 20 μas in right ascension and ≈ 75 μas in declination.

The phase data of the check source A3 was again too noisy and could not be used to determine a position of the source.

4.3.4 Phase Correction

The zenith delay offsets from the fit to the phases in Table 4.11 were then used to correct the uv-data using the task CLCOR. Then the masers and the check source A3 were imaged again. The quality of the atmosphere-corrected maps increased. The peak-to-noise ratios of the uncorrected maps of the strongest maser in IC 10 were 77 and 84 for the two observations on January 12 and 17 respectively. These ratios increase after the corrections to 101 and 90, an increase of 31% and 7%. The positions of the masers in the corrected maps are shown in Table 4.12. They agree within 10 μas with the positions obtained by the fit to the phase data.

The peak-to-noise ratios in the maps of the check source A3 increased also from 22 and 26 in the uncorrected maps to 26 and 28 in the corrected maps, an increase of 18% and 8%. The positions of A3 in the corrected maps are given in Table 4.13 and show again a very good agreement. The position shifted here by ≈ 15 μas in right ascension and ≈ 50 μas in declination compared to the uncorrected maps.

The geodetic-like observations were used to determine a zenith delay offset and drift at each station and a clock offset and rate at each antenna except the reference antenna. The values for the zenith delay offsets were in general comparable to the zenith delay offsets derived by the fit to the phase data. These values could then also be used to correct the uv-data. The images made with this corrected

TABLE 4.12— Epoch 2: Position offset of IC 10 from atmosphere-corrected imaging.

	-324.5 km s^{-1}			-325.4 km s^{-1}		
Date	$\Delta\alpha$ [μas]	$\Delta\delta$ [μas]	Peak Flux [mJy]	$\Delta\alpha$ [μas]	$\Delta\delta$ [μas]	Peak Flux [mJy]
2002/01/12	3	100	837	5	98	675
2002/01/17	-16	122	836	-19	126	569
Mean	-7±10	111±11		-7±12	112 ±14	

TABLE 4.13— Epoch 2: Position offsets in right ascension $\Delta\alpha$, declination $\Delta\delta$ and peak flux S of A3 from atmosphere-corrected imaging.

Date	$\Delta\alpha$ [μas]	$\Delta\delta$ [μas]	S [mJy]
2002/01/12	-14	48	6.8
2002/01/17	-24	54	7.1
Mean	-19±5	51 ±3	

data were very similar to the images corrected by the zenith delay offsets from the fit to the phases and the positions were also in good agreement with the positions obtained by the fit to the phase data. Hence, both methods to determine the zenith delay errors are equivalent and yield similar results.

Since the fist epoch was observed without the geodetic-like observations, we will consider here only the results from the maps corrected with the zenith delay offsets from the fit to the phases. However, the geodetic-like observations will play an important role in the observations of M33, where the masers are weaker and a model fit to the phase data becomes more difficult.

4.4 Third Epoch

4.4.1 Observations

The third epoch of IC 10 was observed with the VLBA on 2002 October 01 and 2002 October 11. The experimental setup was identical to the observations of the second epoch with a total observing time of 10 hours. Here also 8.5 hours were spent on the phase-referencing observations while 45 minutes were spent on the geodetic-like observations before and after the phase referencing. All sources were observed at the positions listed in Table 4.3.

4.4.2 Imaging

The data reduction was identical to the data reduction in the first epochs. The amplitude was calibrated by system temperatures and gain curves. Then PCCOR was performed before a fringe fit on J0102+5824 and J0136+475 was done. Then the phase-calibrator J0027+5958 was fringe-fitted. This fringe-fit yielded only a very small number of good solutions compared to the earlier epochs. A comparison with the solutions of the earlier epochs showed that the signal-to-noise ratio of the solutions in the two new observations of the third epoch were significantly lower than in the observations before. This indicates that the flux density of the calibrator was lower than in the earlier observations. To get a higher number of good solutions, the signal-to-noise cutoff, used to discriminate between good and bad solutions, was lowered from 5 to 4. The solutions of the fringe-fit were then applied to all sources. The data of the antenna in St. Croix were discarded.

Then all sources were imaged. The beam sizes were 0.65×0.33 mas and 0.63×0.36 mas for the two observations. Maser emission was detected only in the two strongest channels from the previous observations. The flux density in this two channels is only 150-300 mJy. This is much lower than flux densities in the previous observations. The check source A3 was only barely detected with a flux density of only 2.5 mJy. This is also much lower than in the previous epochs. The phase-reference J0027+5958 was also mapped and its flux density was also lower than in earlier epochs.

TABLE 4.14— Epoch 3: Position offset of IC 10 from imaging.

	-324.5 km s^{-1}			-325.4 km s^{-1}		
Date	$\Delta\alpha$ [μas]	$\Delta\delta$ [μas]	Peak Flux [mJy]	$\Delta\alpha$ [μas]	$\Delta\delta$ [μas]	Peak Flux [mJy]
2002/10/01	2	40	203	-21	51	156
2002/10/11	-14	101	297	-24	-11	212
Mean	-6±8	71± 31		-23±2	20 ±31	

TABLE 4.15— Epoch 3: Position offsets in right ascension $\Delta\alpha$, declination $\Delta\delta$ and peak flux S of A3 from imaging.

Date	$\Delta\alpha$ [μas]	$\Delta\delta$ [μas]	S [mJy]
2002/10/01	36	0	2.5
2002/10/11	-6	17	4.1
Mean	15±21	9±9	

The quality of the phase-referencing will be affected if the flux density of the calibrator source is too low. This will then reduce the quality of the phase-referenced images. Hence, the peak flux of the target sources will also decrease. This can explain the lower flux density of A3. Single dish observations of the masers in IC 10 with the 100 m telescope in Effelsberg indicate indeed a sudden drop in flux density just days before our observations (Henkel, private communication).

Despite the low quality of the data it was possible to map the sources and measure its positions by a fit of a single Gaussian component to the map. The positions of the maser components in the two detected channels are given in Table 4.14. The deviation between the positions in two observations is surprisingly good in right ascension, given the poor data quality. The positions of the check source A3 are shown in Table 4.15. Here the agreement between the positions in the two observations is also fairly good.

4.4.3 Phase-fitting

A fit to the phase data failed for both observations, due to the low flux density of the maser. The geodetic-like observations yield also no useful zenith delay corrections. Hence, we can not correct the data of the two observations and are restricted to the positions from the uncorrected maps. But these positions have to be treated very carefully.

4.5 Discussion

We presented three different methods to estimate the positions of the observed maser positions. The positions of the maser sources on the images from the corrected uv-data are in very good agreement with the positions obtained by the fit to the phases, but differ significantly from the positions on the uncorrected maps. The image quality and the agreement of the positions in closely spaced observations have also increased by the phase corrections. However, the phase corrections in the first two epoch always yielded a small position shift in the same direction. This could lead to a bias, if one compares the corrected positions of the first two epochs with the uncorrected positions from the last epoch.

4.5.1 Astrometric accuracy

To get the astrometric accuracy of each epoch the standard deviation of the positions in the individual observations within each epoch was calculated. This is given by

$$\sigma_N = \sum_{i=1}^{N} \sqrt{\frac{(x_i - \bar{x})^2}{N}}, \tag{4.1}$$

where x_i are the individual measurements and $\bar{x}$ is the arithmetic mean. Usually, a standard deviation is reliable only for a large number of measurements N. In our case the number of observations is very small, and we are dealing with very small number statistics. Thus, the derived standard deviations can be misleading. Two measurements that are by coincidence very close together, would yield a very small error, even if their intrinsic error is much larger. However, the fact that the standard deviation of the positions in the uncorrected maps is always less than ≈ 30 μas clearly indicates that the true astrometric accuracy is better than 30 μas.

The astrometric accuracy is always better in right ascension than in declination. The position errors in the uncorrected maps were usually 2-5 μas in right ascension and 15-30 μas in declination. This can be only partly explained by the elongated beam of the VLBA. The beam sizes were typically 0.33-0.38 mas in right ascension and 0.55-0.65 in declination. The phase errors which are induced by the atmosphere also increase the position error in declination. This can be seen by the fact that the position error in declination is reduced by the fit to the phases and the resulting corrections to the uv-data to only 10-15 μas.

The fit to the phases and the correction of the phase errors caused by the zenith delay errors increase the astrometric accuracy in general, but the error can increase in some cases due to the low number statistics (e.g. A3 in the first epoch). However, the large improvement in the image quality as well as the increased astrometric accuracy clearly justifies this method. The excellent agreement between the positions from the fit to the phases and from the corrected images is a further verification of the method.

4.5.2 Proper Motion of IC 10

The position offsets from the phase center of the strong maser components change significantly between the epochs. First, one can compare the positions obtained by the fit to the phases and the corrected images. Here, the strong maser moved from $\Delta\alpha_{\rm IC\,10} = 44 \pm 5$ and $\Delta\delta_{\rm IC\,10} = 108 \pm 9$ μas in the first epoch to $\Delta\alpha_{\rm IC\,10} = -6 \pm 6$ and $\Delta\delta_{\rm IC\,10} = 123 \pm 13$ μas in the second epoch. This would result in a motion of $\dot\alpha_{\rm IC\,10}$=-67±10 and $\dot\delta_{\rm IC\,10}$=+20±21 μas yr^{-1}.

The position of the check source A3 in the corrected maps was $\Delta\alpha_{\rm A3} = 15 \pm 2$ and $\Delta\delta_{\rm A3} = 37 \pm 18$ μas in the first epoch. In the second epoch, the source was detected at a position of $\Delta\alpha_{\rm A3} = -19 \pm 5$ and $\Delta\delta_{\rm A3} = 51 \pm 3$ μas. This would result in a motion of $\dot\alpha_{\rm A3} = -45 \pm 7$ μas yr^{-1} $\dot\delta_{\rm A3} = +14 \pm 18$ μas yr^{-1}. This motion of the check source is completely unexpected, since it was believed to be a background quasar which should show no motion. Please note that the motions of A3 and IC 10 are both in the same direction.

There are three possible explanations for the motion of the source A3.

- No optical counterpart for A3 and hence no redshift is known. The only information available about A3 is its radio flux. It is possible, that the source A3 is not a background quasar, but a source in the outer regions of IC 10 that moves with the galaxy. However, in this case the nature of this object would be completely unclear. The radio emission of A3 is also to bright to be a X-ray binary (see Fender 2001; Falcke, Körding, & Markoff 2004).

- The apparent motion of the check source A3 could be caused by unknown systematic errors. The phase calibrator J0027+5958 can have an unresolved structure, e.g. a core-jet structure. The observed image of J0027+5958 is the convolution of the source structure and the synthesized beam of the VLBA. Flux density variations of the individual components could move the position of the observed image by a fraction of the beam size. Since the phase calibrator is assumed to be stationary, this would shift the positions of all target sources by the same amount.

- The observed motion of A3 could also be caused by some errors in the geometry of the correlator model. These errors would be similar for closely spaced observations, but different for observations

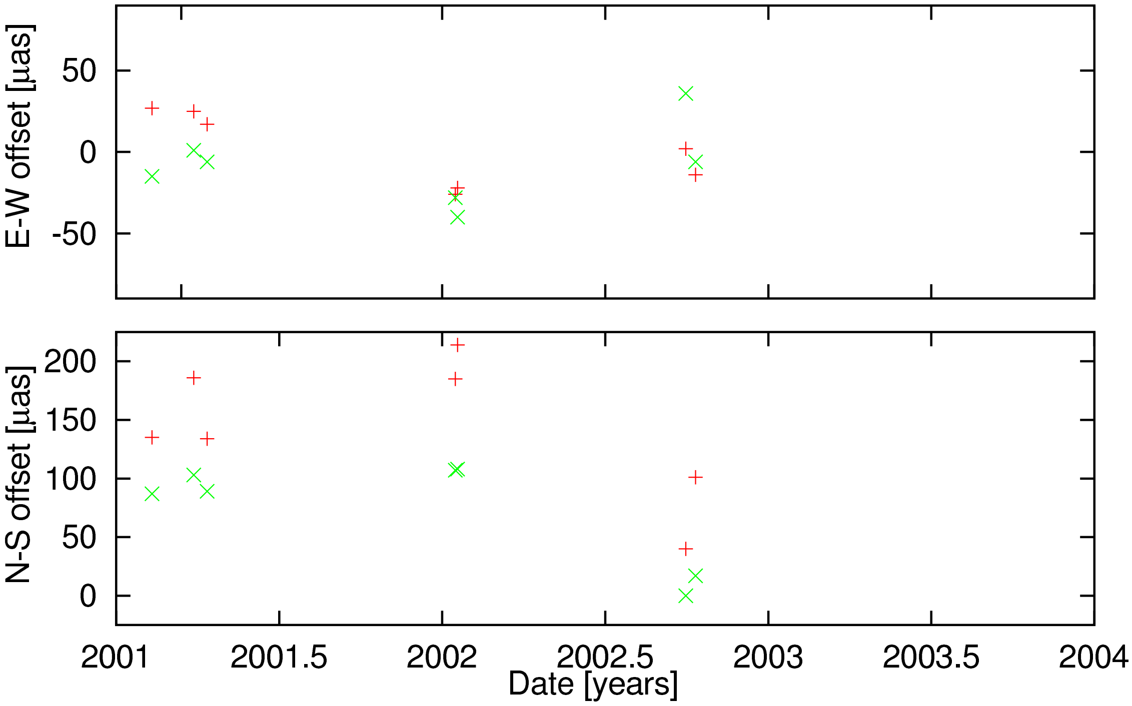

FIGURE 4.17— Position offsets of the masers in IC 10 (+) and the check source A3 (x) in right ascension (upper) and declination (lower) from the uncorrected maps.

separated by several months. The angular separation between IC 10 and A3 (8') is much smaller than the separation between IC 10 and J0027+5958 (1°), and the position shift induced by geometric errors would be similar for IC 10 and A3. This could explain the similar motion of A3 and IC 10.

Further observations are necessary to understand the observed position shift of A3. Unfortunately, the fit to the phases for the observations of the third epoch yield no useful results. The correction of the zenith delay errors in the first two epochs have always resulted in a similar position shift in the same direction. To include the third epoch, one has to compare only the positions of the uncorrected maps. Figure 4.17 shows the position offsets of the masers in IC 10 and the check source A3. It can be seen that the apparent motion of the masers in IC 10 and the check source A3 follow not a straight line. Both sources seem to 'jump' between the epochs. One can also see that both sources always 'jump' in the same direction.

If the systematic errors of the observations are indeed similar for both sources, the relative position of IC 10 to A3 should not be affected. If one assumes that A3 is stationary, one can correct the systematic errors. Any motion of IC 10 relative to A3 would then represent the true motion of IC 10. This is done in Figure 4.18, where the relative position of IC 10 to A3 for all observations is plotted. Here the masers in IC 10 move in right ascension with a constant velocity. The motion in declination is consistent with zero. The best fit to the data points yield a measured proper motion of:

$$\begin{aligned} \dot{\alpha}_{prop} &= \; -32 \pm 7 \quad \mu\text{as yr}^{-1} \qquad (4.2) \\ \dot{\delta}_{prop} &= \; 6 \pm 16 \quad \mu\text{as yr}^{-1}. \end{aligned}$$

To increase the accuracy, one should use the positions from the fit to the phases or from the corrected maps. The phase correction in

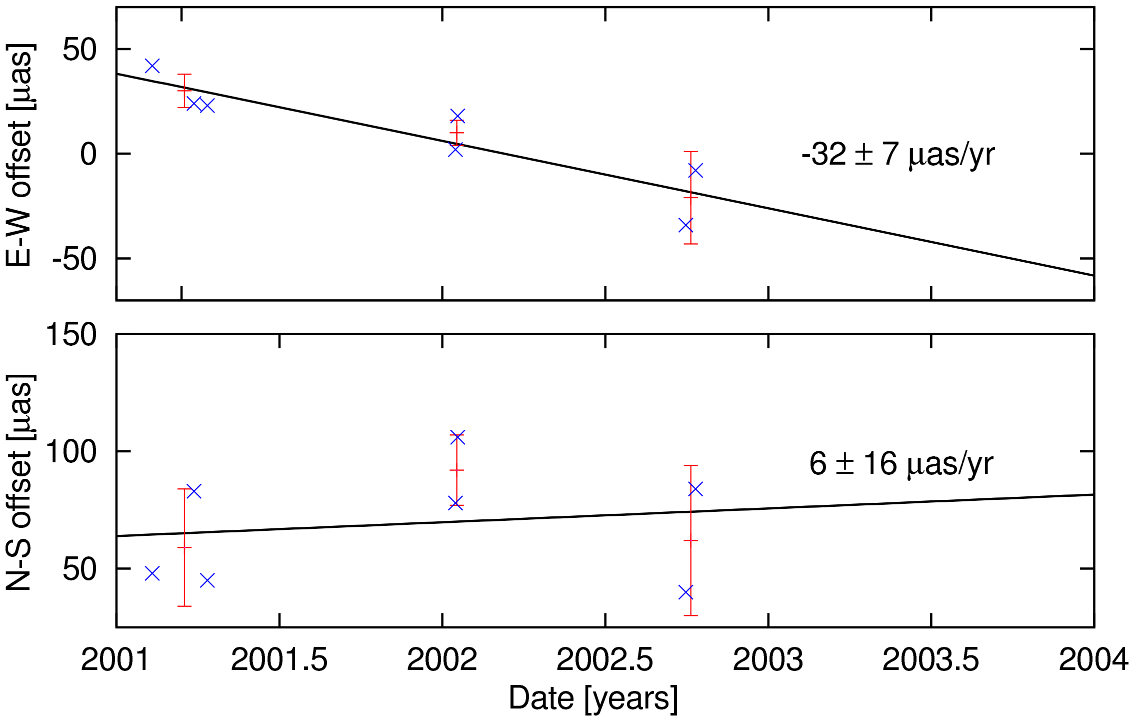

FIGURE 4.18— Position of IC 10 relative to A3 for the individual observations (x) in right ascension (upper) and declination (lower). The errorbars represent the average position for each epoch. The lines are the best fit to the data.

the first two epochs shift the sources always to higher right ascensions and lower declinations. Thus, one could introduce systematic errors if one compares the phase-corrected positions in the first two epochs with the results from the third epoch. However, if one uses the corrected positions form the first two epochs and the uncorrected from the third epoch, one gets motions of $\dot{\tilde{\alpha}} = -33 \pm 7$ μas yr^{-1} and $\dot{\tilde{\delta}} = -7 \pm 14$ μas yr^{-1}, consistent with the results mentioned above.

There is no proof that the apparent motion of IC 10 relative to A3 in Figure 4.18 reflects the true proper motion of IC 10. Although it is not very likely that the positions in the three epochs could lie only by coincidence on a line. If this is correct, the jumps in Figure 4.17 may indicate some unknown systematic errors. A fit to the data in Figure 4.17 would yield a proper motion of -22 ± 10 μas yr^{-1} in right ascension and -42 ± 33 μas yr^{-1} in declination for IC 10.

Further observations are needed to confirm the detected motion. Three more epochs of two observations each will be observed within the next two years. Since proper motion measurements improve with time as $t^{3/2}$ and one can use the more accurate positions from the fit to the phases, these new observations will increase the accuracy dramatically.

4.5.3 Space velocity of IC 10

The measured proper motion $\tilde{\boldsymbol{v}}_{prop}$ of IC 10 can be decomposed into a sum of several components:

$$\tilde{\boldsymbol{v}}_{prop} = \boldsymbol{v}_{rot} + \boldsymbol{v}_{pec} + \boldsymbol{v}_{\odot} + \boldsymbol{v}_{prop} \qquad (4.3)$$

Here $\boldsymbol{v}_{rot}$ is the motion of the masers due to the internal galactic rotation in IC 10, $\boldsymbol{v}_{pec}$ is the deviation of the motion of the masers from the internal galactic rotation and $\boldsymbol{v}_{\odot}$ is the apparent motion of IC 10 caused by the rotation of the Sun about the Galactic Center. The last contribution $\boldsymbol{v}_{prop}$ is the true proper motion of IC 10.

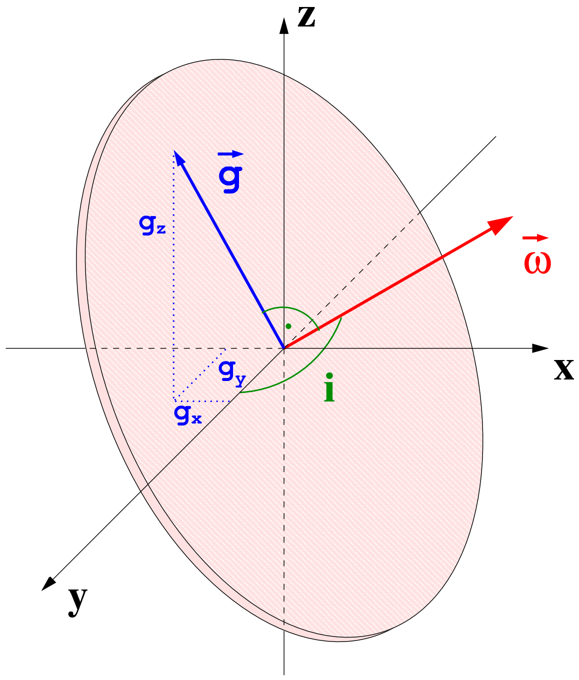

FIGURE 4.19— 3-dimensional orientation of a disk of a galaxy. The x and z axes are on the plane of the sky, and the y axis points towards the observer. $\boldsymbol{\omega}$ is the rotation vector and $\boldsymbol{g}$ points towards a point in the galaxy.

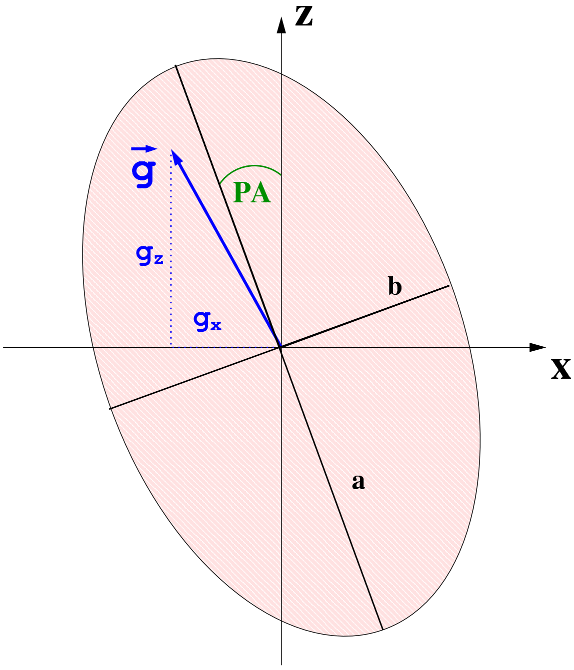

FIGURE 4.20— Projection of a disk of a galaxy on the sky as seen by an observer. The observables are the major and minor axes of the ellipse (a and b) and the position angle (PA) of the major axis. The inclination is then given by cos $i = b/a$.

Observations of the neutral hydrogen in IC 10 with the Westerbork Synthesis Radio Telescope by Shostak & Skillman (1989) revealed a central rotating disk which is rotating oppositely to an outer hydrogen envelope discovered by Cohen (1979) and Huchtmeier (1979). The H_2O masers are located within a massive H I cloud in the central disk. If one assumes that the masers are rotating with the disk, one can calculate its expected proper motion.

The rotation of the disk can be described by the rotation vector $\boldsymbol{\omega}$ (see Figure 4.19). This vector is parallel to the axis of rotation and its length is equal to the rotation speed. An observer will see a projection of the disk on the sky (see Figure 4.20) and the orientation of this ellipse is given by two observables. The inclination of the disk is defined as the angle between the rotation axis and the line of sight, i.e. 90° for an edge-on and 0° for a face-on galaxy. The second observable is the position angle of the major axis measured east of north, where east is on the left for an astronomical map. One can define a three dimensional Cartesian coordinate system (x,y,z) with the origin at the center of the disk. The x and z axes are in direction of negative right ascension and positive declination, respectively. The y axis is then towards the observer. In this coordinate system, the rotation vector $\boldsymbol{\omega}$ is related to the inclination i and the position angle PA by:

$$\boldsymbol{\omega} = \omega_0 \begin{pmatrix} \cos PA \ \sin i \\ -\cos i \\ \sin PA \ \sin i \end{pmatrix}, \tag{4.4}$$

where ω_0 is the rotation speed. One can now construct a vector $\boldsymbol{g}$ which lies in the plane of the disk and points from the origin towards the maser. The x- and z-components of $\boldsymbol{g}$ are given by the offset of the masers from the center of the disk on the sky. The y-component of $\boldsymbol{g}$ is constrained by the fact that $\boldsymbol{\omega}$ and $\boldsymbol{g}$ are orthogonal by definition:

$$\boldsymbol{\omega}.\boldsymbol{g} = \omega_x g_x + \omega_y g_y + \omega_z g_z = 0. \tag{4.5}$$

This leads to

$$g_y = -\frac{\omega_y}{(\omega_x g_x + \omega_z g_z)} \tag{4.6}$$

The velocity vector $\boldsymbol{v}$ at the position $\boldsymbol{g}$ is now orthogonal to $\boldsymbol{g}$, since it moves on a circular orbit. It is also orthogonal to $\boldsymbol{\omega}$, since it is in the plane of the galaxy. Then $\boldsymbol{v}$ is given by

$$\boldsymbol{v} = \frac{1}{|\boldsymbol{g}|}\boldsymbol{\omega} \times \boldsymbol{g}. \tag{4.7}$$

Shostak & Skillman (1989) measure an inclination of 45° from the ellipticity of the H I distribution. The masers are 33 arcseconds (106 pc) east and 99 arcseconds (317 pc) south of the kinematic center. Unfortunately no position angle of the major axis was given. Wilcots & Miller (1998) used higher resolution VLA observations of the H I content of IC 10 to fit a tilted ring model to the velocity field of the disk of IC 10. This model has a separate rotation speed, inclination and position angle for each ring. Unfortunately, the radius for each ring in the paper is given in arcseconds. This leads to confusion for an inclined disk since a given angular distance along the major axis gives a different radius than the same distance along the minor axis of the disk. Here, we assume that the authors used the distance along the major axis of the disk. They find a highly inclined disk in the inner 110 arcseconds with a position angle of $\approx 75°$ and a rotational velocity of ≈ 30 km s^{-1}. The position of the kinematic center of their tilted ring model was not given. If one combines the kinematic center of Shostak & Skillman (1989) and the inclination and position angle of Wilcots & Miller (1998), one gets a proper motion of 29 and 9 km s^{-1} in right ascension and declination. The masers are very close to the kinematic center. Hence, a small error in the position of the kinematic center can already change the expected motions. Hence, the combination of two papers by two different groups which observed IC 10 with two different telescopes is a possible source of error.

However, if one calculates the expected motion for different realistic scenarios, one get always proper motions between 20-30 km s^{-1} in right ascension and 5-15 km s^{-1} in declination. Hence, we adopt values of 25 ± 5 and 10 ± 5 km s^{-1} in right ascension and declination, respectively. This translates to $\dot{\alpha}_{rot} = 8 \pm 2$ and $\dot{\delta}_{rot} = 3 \pm 2$ μas yr^{-1} at a distance of 660±60 kpc.

The deviation of the motion of the masers from the galactic rotation is unknown. This motion should be small compared to the galactic rotation and the error should not be larger than the uncertainty of the internal galactic rotation in IC 10. Thus we assume $\boldsymbol{v}_{pec}$ to be zero.

The rotation of the Sun about the Galactic Center causes an apparent motion of IC 10. The motion of the Sun can be decomposed into a circular motion of the local standard of rest (LSR) and the peculiar motion of the Sun. The peculiar motion of the Sun has been determined from Hipparcos data by Dehnen & Binney (1998) to be in km s^{-1} U$_0$=10.00±0.36 (radially inwards), V$_0$=5.25±0.62 (in the direction of Galactic rotation) and W$_0$=7.17±0.38 (vertically upwards). The LSR moves with at a velocity of 220 km s^{-1} towards a Galactic longitude of $l = 90°$ and latitude of $b = 0°$ (Kerr & Lynden-Bell 1986). This value has been confirmed by Reid et al. (1999) and Backer & Sramek (1999). New VLBI measurements of the proper motion of SgrA*, the compact radio source at the Galactic Center, indicate a slightly higher circular velocity of 236±15 km s^{-1} (Reid & Brunthaler 2004), where the uncertainty is dominated by the uncertainty in the distance to the Galactic Center.

This motion of the Sun causes at a distance of 660 kpc and the Galactic coordinates of IC 10 ($l = 118.96°$, $b = -3.32°$) an apparent proper motion of 38 ± 3 μas yr^{-1} in Galactic longitude and -6±1 μas yr^{-1} in Galactic latitude. Converted to equatorial coordinates, one gets $\dot{\alpha}_{\odot} = 37 \pm 3$ μas yr^{-1} and $\dot{\delta}_{\odot} = -10 \pm 1$ μas yr^{-1}.

The true proper motion of IC 10 is then given by

$$\begin{aligned}
\dot{\alpha}_{prop} &= \dot{\tilde{\alpha}}_{prop} - \dot{\alpha}_{rot} - \dot{\alpha}_{\odot} \\
&= (-32 \pm 7 - 8 \pm 2 - 37 \pm 3)\frac{\mu\text{as}}{\text{yr}} \\
&= -77 \pm 8\ \frac{\mu\text{as}}{\text{yr}} = 241 \pm 25\frac{\text{km}}{\text{s}} \\
\text{and} & \qquad\qquad\qquad\qquad\qquad\qquad (4.8) \\
\dot{\delta}_{prop} &= \dot{\tilde{\delta}}_{prop} - \dot{\delta}_{rot} - \dot{\delta}_{\odot} \\
&= (6 \pm 16 - 3 \pm 2 + 10 \pm 1)\frac{\mu\text{as}}{\text{yr}} \\
&= 13 \pm 16\ \frac{\mu\text{as}}{\text{yr}} = 41 \pm 50\frac{\text{km}}{\text{s}}
\end{aligned}$$

The measured systematic heliocentric velocity of IC 10 (-344±3 km s^{-1}, de Vaucouleurs et al. 1991) is the sum of the radial motion of IC 10 towards the Sun and the component of the solar rotation about the Galactic Center towards IC 10 which is -192±18 km s^{-1}. Hence IC 10 is moving with 152±18 km s^{-1} towards the Sun.

The proper motion and the radial velocity combined give the three-dimensional space velocity of IC 10. The total velocity is 288±59 km s^{-1} relative to the Milky Way. This velocity vector is shown in the a schematic view of the Local Group in Figure 4.21.

4.5.4 Motion relative to M31

The systematic heliocentric velocity of M31 is -297±1 km s^{-1} (e.g., Huchra, Vogeley, & Geller 1999). This can be also decomposed into the component caused by the motion of the Sun and the motion of M31 towards the Sun. The component of the solar motion at the Galactic coordinates of M31 ($l = 121.17°, b = -21.57°$) is -172±16 km s^{-1}. Hence, the motion of M31 towards the Sun is 125±16 km s^{-1}. The tangential motion of M31 is unknown and we assume that it is zero. This assumption is probably justified, since no other large galaxies except the Milky Way and M31 exist in the Local Group that could create angular momentum through tidal torques (Evans & Wilkinson 2000). Hence, M31 is probably falling directly towards the Milky Way. This has been already argued by Kahn & Woltjer (1959). This motion is also plotted in Figure 4.21. Possible similar VLBI observations of radio sources in M31 may test this in the future. Unfortunately, no H_2O maser emission could be detected yet in M31 despite intensive searches. The nucleus of M31 with flux densities between 30 and 100 μJy is also too weak to be detected with VLBI. However, recent developments using higher bandwidths in VLBI have increased the sensitivity and an image rms noise of only 9μJy was reached (Garrett, Wrobel, & Morganti 2003). This has the potential to detect and measure the motion of the nucleus of M31. Here we will assume a zero proper motion of M31. Then the motion of IC 10 relative to M31 is then almost completely perpendicular to the connecting line between the two galaxies.

The distance of IC 10 to M31 is with 247 kpc much less than the distance of IC 10 to the Milky Way (660 kpc). Thus, the gravitational force of M31 on IC 10 will be almost one order of magnitude larger than the gravitational force of the Milky Way on IC 10.

If IC 10 is gravitationally bound to M31 and on a circular orbit about M31, one can get a rough estimate of the mass of M31. On a circular orbit, the gravitational force equals the centrifugal force

$$\frac{mv^2}{R} = G\frac{mM}{R^2}, \tag{4.9}$$

where v is the rotation speed, R is the radius of the orbit, m and M are the masses of the moving particle (IC 10) and the central mass (M31) and G is the gravitational constant. This gives

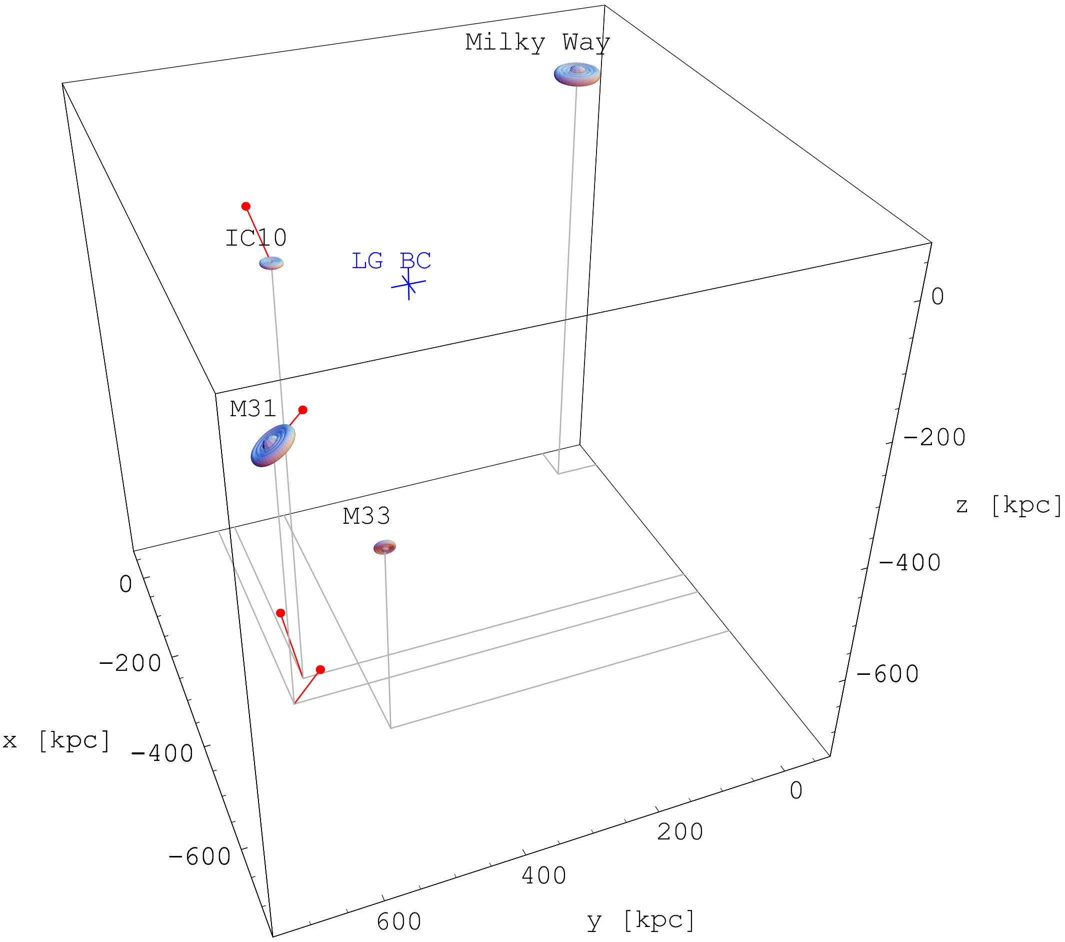

FIGURE 4.21— Schematic view of the Local Group of Galaxies. The Sun is located at (0,0,0), the Galactic Center at (8,0,0). Plotted are also the velocities if IC 10 and M31 and the position of the Local Group barycenter (LGBC), taken from van den Bergh (1999).

$$M = \frac{v^2 R}{G}. \tag{4.10}$$

If one uses the values of the orbit of IC 10 with R=247 kpc and v=243 km s^{-1}, one gets a mass of

$$M_{M31} = (3.4 \pm 1.9) \times 10^{12}\ \mathrm{M}_\odot, \tag{4.11}$$

and IC 10 would need $\approx 6 \times 10^9$ yr for one full orbit. The most recent estimate by Evans & Wilkinson (2000), who used the radial velocities of 10 satellite galaxies, 17 distant globular clusters and nine halo planetary nebulae of M31 gives a mass of $12.3^{+18}_{-6} \times 10^{11}$ M$_\odot$. The two measurements are consistent, given their large errorbars.

However, this mass is only a very rough estimate and based on several assumptions. IC 10 would not be on a circular orbit if the distances to M31 or IC 10 are not correct. A significant tangential velocity of M31 would also change the picture. Furthermore, we assumed that IC 10 is bound to M31 and not a free-floating member of the Local Group as suggested by van den Bergh (1999).

5

VLBA Observations of M33

For M33, the same observing strategy as for IC 10 was used. Two observations were made within a short time to verify the positions.

5.1 M33

The Sc II-III spiral galaxy M33 is the third-brightest member of the Local Group. A review on the properties of M33 is given in van den Bergh (1991). Two regions of strong maser activity, namely IC 133 and M33/19, are known in this galaxy and were observed in this project. The galactic rotation of M33 is also very well known from observations of H I (e.g. Corbelli & Schneider 1997). Distance estimates for M33 range from 794 ± 23 kpc (McConnachie et al. 2004) to 916 ± 55 kpc (Kim et al. 2002). In this work we will assume a distance of 790 kpc (van den Bergh 1999).

5.2 First Epoch

5.2.1 Observations

The first epoch on M33 was observed on 2001 March 27 and 2001 April 05. The observations were identical to the observations of IC 10 with four 8 MHz band, each right and left circular polarization and 128 spectral channels in each band that yield a spectral resolution of 62.5 kHz, equivalent of 0.84 km s^{-1}.

The observations also involved rapid switching and we went through the cycle J0137+312 – IC 133 – J0137+312 – B4 – J0137+312 – M33/19 – J0137+312. The sources were changed every 30 seconds. Each hour we observed J0136+475 or J0152+2207, two strong calibrators with flux densities of roughly 2 Jy, for 270 seconds. The total observing time was 10 hours for each observation and no geodetic-like observations were made.

TABLE 5.1— List of sources and positions for the first observation with references:[1] VLBA calibrator survey; [2] Greenhill et al. (1990); [3] VLBA observations.

Name	RA	DEC
J0137+312[1]	01:37:08.73270	+31:22:35.7890
IC133[2]	01:33:16.54500	+30:52:50.0000
M33/19[2]	01:33:29.43000	+30:31:55.4200
B4[3]	01:32:22.67099	+30:44:07.2003

5.2.2 Absolute Positions

Like in the observations of IC 10, the absolute positions of the sources were not known very accurate in the beginning. Table 5.1 shows the positions used in the first epoch. They were taken from the VLBA calibrator survey for J0137+312, earlier VLBI observations by Greenhill et al. (1990) for IC 133 and M33/19, and our VLBA calibrator search for B4. The uncertainties of the positions were again $\approx 20 - 100$ milliarcseconds.

The data were calibrated with the same standard techniques as the data of IC 10. An initial amplitude calibration using system temperatures and gain curves and a manual phase-cal on J0136+475 were done before J0137+312 was fringe-fitted. The solution were then applied to all sources and IC 133, M33/19 and B4 were imaged. B4 and many maser features in IC 133 and M33/19 could be detected and we could derive the positions of B4 and the strongest maser features in IC 133 and M33/19.

The position of J0137+312 was also updated on 2001 August 21 by the NASA Goddard Space Flight Center VLBI Group. The new position, accurate to 1 milliarcsecond, is given in Table 5.2 together with the positions of the other sources. These new positions were used in the second and third epochs. The data of the first epoch was shifted to these positions using the task CLCOR and re-analyzed. Thus, the data sets of all observations have the same phase-center now.

5.2.3 Imaging

Both observations of the first epoch were re-analyzed after the corrected position of J0137+312 was known. The data reduction was identical to the procedures described for the observations of IC 10. After the initial amplitude calibration, the sources were shifted using CLCOR to their best known positions from Table 5.2. Then PCCOR was used to eliminate instrumental phase and delay offsets between separate IFs. Then the two strong calibrators J0136+475 and J0152+2207 were fringe-fitted for a rough delay calibration and the solutions were applied to all sources.

Finally, the phase-calibrator J0137+312 was fringe-fitted and the solutions were applied to IC 133, M33/19 and B4. Here, the antenna in St. Croix yields no useful data and all data from this antenna was discarded.

Then all sources were imaged. For the continuum source B4, all channels and IFs were averaged and imaged, while for IC 133 and M33/19 all channels of the IF containing the maser emission were imaged separately. The beam sizes were 0.88×0.41 mas at position angle 164° and 0.86×0.39 at position angle 169° for the observations in March and April, respectively. The beam for these observations is much more elongated than for the observations of IC 10, due to the lower declination of M33 (+31°, compared to +60° for IC 10).

TABLE 5.2— List of sources and positions for the second and third epochs. The position of J0137+312 is taken from the updated VLBA calibrator survey. The positions of IC 133, M33/19 and B4 are taken from the first epoch.

Name	RA	DEC
J0137+312	01:37:08.733637	+31:22:35.85551
IC133	01:33:16.540877	+30:52:49.99491
M33/19	01:33:29.431047	+30:31:55.40191
B4	01:32:22.671857	+30:44:07.26721

IC133:

Maser emission could be detected in IC 133 over a range of ≈ 35 km s^{-1}. The spectra of IC 133 in the first two observations, made by summing up the flux densities of all detected components in the maps of the individual channels, can be seen in Figures 5.1 and 5.3. The emission in IC 133 is, unlike IC 10, not dominated by one strong component but shows a broader distribution. Most features of the single dish discovery spectrum of IC 133 by Churchwell et al. (1977) are also present in our observations 25 years later. Only the emission at velocities < -240 km s^{-1} was not detected by the VLBI observations.

The spatial distribution of the maser emission can be seen in in Figures 5.2 and 5.4. Most maser components cluster in two regions, IC 133M (main) and IC 133SE (southeast), following the notation of Greenhill et al. (1990), hereafter G90. These two regions are separated by ≈ 30 mas, which translates at an assumed distance of 790 kpc to 3.5×10^{17}cm. The emission in both regions is spread over ≈ 4 mas, corresponding to ≈ 3200 AU. Two additional maser components are located ≈ 7 mas from IC 133M. This is again similar to water maser emission in Galactic star-forming regions. Emission in a second region of activity IC 133W, displaced by ≈ 0.3 arcseconds (Greenhill et al. 1993) was not detected in our data.

The masers in IC 133 show significant variability between the two observations separated by one week. New components appear or

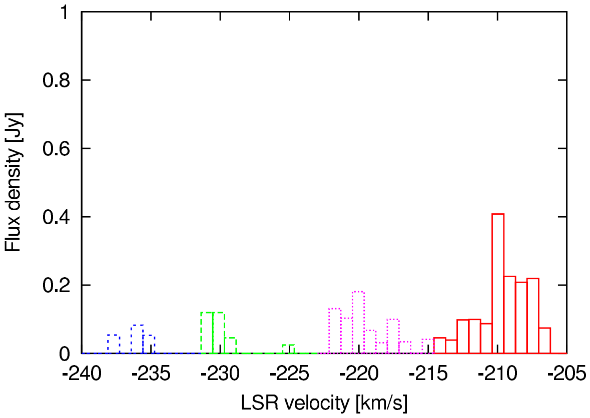

FIGURE 5.1— VLBI-spectrum of IC 133 on 2001 March 27.

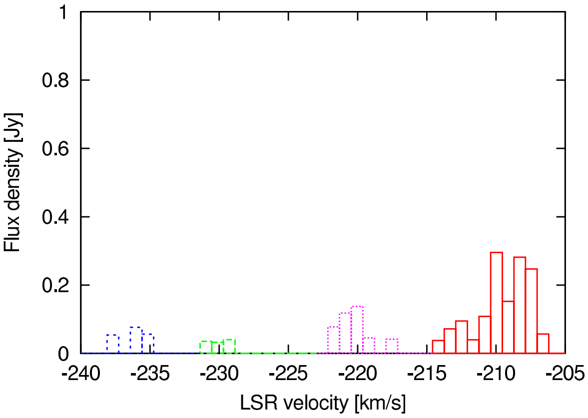

FIGURE 5.3— VLBI-spectrum of IC 133 on 2001 April 05.

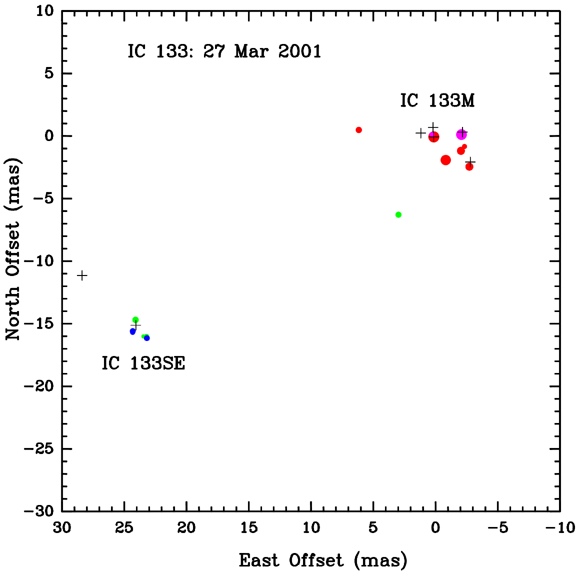

FIGURE 5.2— Composite map of the H_2O masers in IC 133. The area of the circles is proportional to the flux density of the components and the colors are as in Figure 5.1. The crosses mark the positions of maser emission detected by Greenhill et al. (1990) (features 1, 2, 3, 8, 11, 13 and 14).

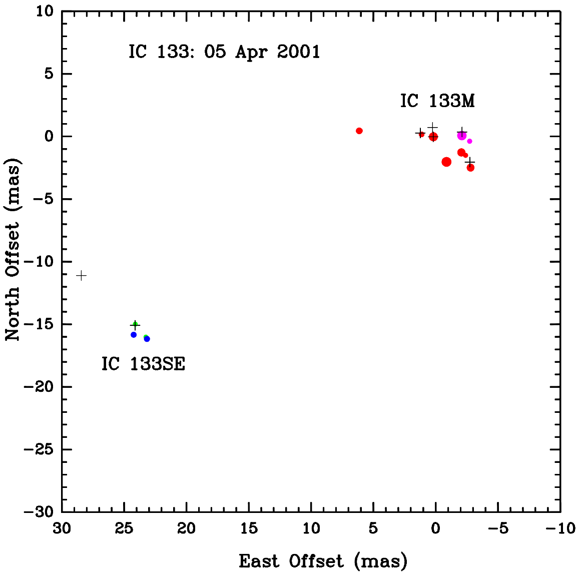

FIGURE 5.4— Composite map of the H_2O masers in IC 133. The area of the circles is proportional to the flux density of the components and the colors are as in Figure 5.3. The crosses mark the positions of maser emission detected by Greenhill et al. (1990) (features 1, 2, 3, 8, 11, 13 and 14).

brighten while other components fade. However, six features (I1 to I6) in IC 133M can be seen in all epochs. The positions of these six stable maser components are shown in Figure 5.5.

A single elliptical Gaussian component was fitted to each detected feature of maser emission. The positions, peak and integrated flux densities, sizes and position angles of all components are given in Tables A.1 and A.2 for the two observations of the first epoch. The errors are the formal uncertainties from the fit to the map. Most components are unresolved and their apparent size (≈ 0.9 × 0.4 mas) and position angle (≈ 173°) resemble the beam of the observation. Only one component in the first observation (I11) shows a significant different position angle. However, this compo-

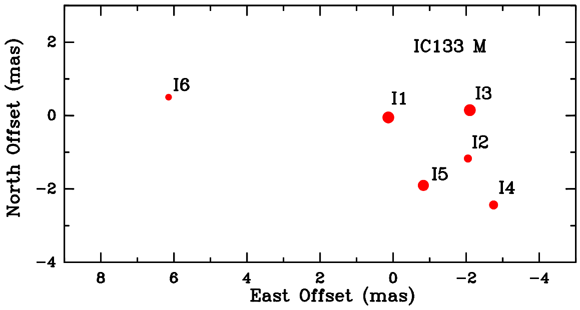

FIGURE 5.5— Zoom of IC 133M with the six stable components I1 to I6.

nent is very weak (peak flux density ≈ 25 mJy beam^{-1}) and only barely detected.

The variability of the emission in IC 133 can have several reasons. A scaling error in the amplitude calibration would affect all channels and can not explain the different behavior of the different components. Changes in the quality of the phase-referencing due to different external conditions (e.g. weather) would also affect all frequency channels in the same way. One source of error is the detection threshold of ≈ 30 mJy. The spectra in Figures 5.1 and 5.3 contain only the emission of components which were detected in the maps. A weak component which was barely detected in the first (≈ 35 mJy) but not in the second observation (≈ 25 mJy) would change the flux in this channel by ≈ 35 mJy, although the real variability is much less. Hence, one has to look for variability of each component separately. Figure 5.6 shows the relative flux density change m between the two observations for all components defined by:

$$m = \frac{f_2 - f_1}{mean(f_1, f_2)}, \qquad (5.1)$$

where f_1 and f_2 are the flux densities in the first and second observation respectively and $mean(f_1, f_2)$ is the average of both flux densities. Here, only components which were detected in both observations were used. Although the majority of components get weaker by up to 50% ($m < 0$) some components brighten by also up to 50% ($m > 0$). While the decrease by ≈ 25% in most components

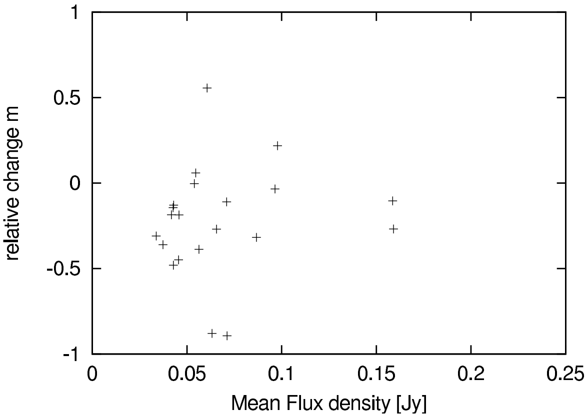

FIGURE 5.6— IC 133: Relative flux density changes between the first and second observation.

can be explained by pure instrumental effects, intrinsic variations of the source play a role for the stronger varying features.

Most components can be detected in multiple channels and the positions in these different channels agree in general within ≈ 0.1 mas. A closer look at the components I1 and I3 shows that the emission in different channels can have slightly different positions. Most of the emission in I1 can be separated into I1$_a$ and I1$_b$, while the emission denoted by I1$_?$ can not be attributed to I1$_a$ or I1$_b$. I1$_a$ and I1$_b$ are displaced by ≈ 0.1 mas, or 79 AU and 2.5 km s^{-1} in velocity. The component I3 can be also separated into I3$_a$ and I3$_b$, separated by ≈ 0.2 mas (≈ 158 AU) and 2.5 km s^{-1}.

The average position of one component over different channels could then lead to a false detection of motion if the emission in one channel becomes more dominant over the other. Thus, one has to measure the motions of each component in each channel separately and then average all the motions.

Figure 5.7 shows the position difference between the two observations for all components which were detected in both observations as a function of the component flux density. Here, the weaker flux density of both observations was chosen. One can clearly see a trend towards lower position differences at higher flux densities. Also shown is the theoretical

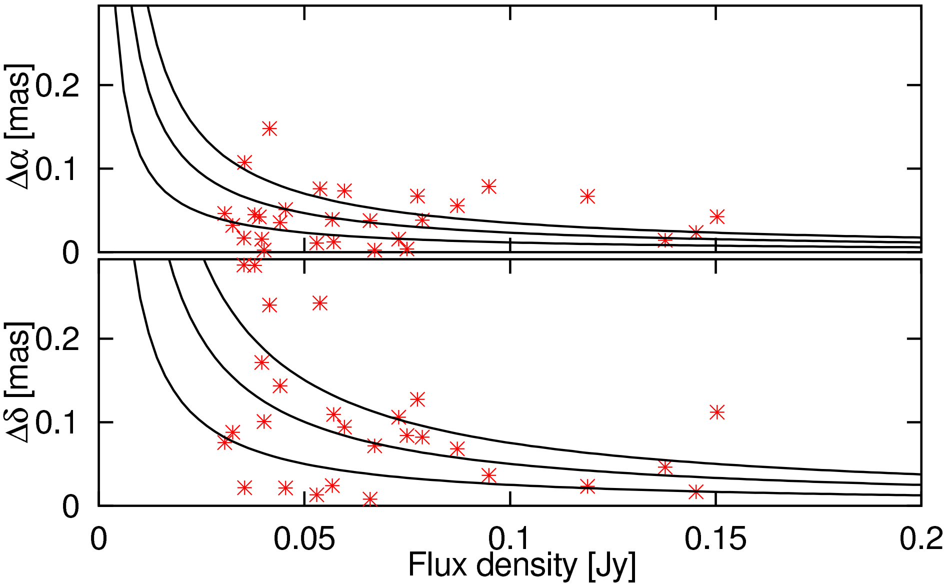

FIGURE 5.7— IC 133: Position difference between the first and second observation as a function of component flux density in right ascension (upper) and declination (lower). The solid lines are the theoretical limit from Equation 5.2 (1, 2 and 3σ).

limit for the astrometric accuracy, given by the beam size θ_b and the signal-to-noise ratio SNR:

$$\sigma \approx \frac{\theta_b}{2 \times SNR}. \tag{5.2}$$

The position agreement for all points below this line is better than the theoretical expectation. This can be explained by a coincidental agreement of the two observations. The average difference is 43 μas in right ascension and 111 μas in declination. This larger difference in declination is mainly caused by the larger beam size of the VLBA in this direction. Thus, an astrometric accuracy of $\approx$ 20 μas can be reached also for M33 even without one strong ($\approx$ 1 Jy) component like in IC 10. In IC 133, one can also average the motions of several maser components to increase the accuracy.

Figures 5.2 and 5.4 show also the positions of components detected by G90. The positions were aligned on the component I1$_b$ (or component 3 in G90) at a velocity of -210 km s^{-1}. Component I3$_b$ (at $\approx$ -220 km s^{-1}) and I4 (at $\approx$ -212.5 km s^{-1}) can be identified by position and velocity with components 13 and 8 from G90. Comparing the relative positions of I3$_b$ and I4 towards I1$_b$ in our observations with the relative positions of components 13 and 8 towards 3 in G90, yields relative transverse velocities of $\approx$ 6-7 μas yr^{-1} or $\approx$ 20-25 km s^{-1} in right ascension. These are similar to proper motion reported in IC 133 by Greenhill et al. (1993) from observations over a period of 479 days. These proper motions are comparable with the differences in radial velocity. The apparent motions in declination are much larger. However, the uncertainty in declination is much larger due to the larger beam in declination in the observation of G90 (0.25×1.25 mas, PA=173°). The component identification is also not very certain due to the long time between the G90 observations and our data.

However, a comparison of the relative proper motions of different maser components with their radial velocity dispersion can be

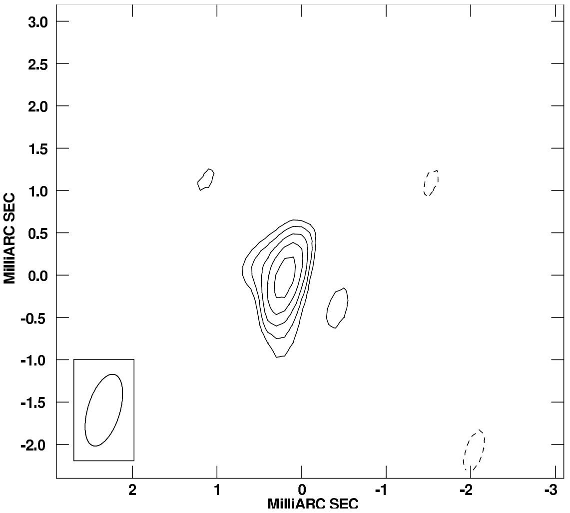

FIGURE 5.8— Phase-referenced image of the check source B4 for the observation on 2001 March 27. The contour levels start at 1 mJy and increase by a factor of $\sqrt{2}$. The peak-to-noise ratio is 15.

TABLE 5.3— Epoch 1: Position offsets in right ascension $\Delta\alpha$, declination $\Delta\delta$ and peak flux S of B4 from imaging.

Date	$\Delta\alpha$ [μas]	$\Delta\delta$ [μas]	S [mJy]
2001/03/27	207	-46	4.7
2001/04/05	210	-38	3.2
Mean	209±2	-42±4	

used to estimate a distance to M33. Argon et al. (1998) used 7 epochs between 1987 and 1993 and yield a distance of 820±250 kpc. The inclusion of our new data presented in this work has the potential to increase the accuracy of this method (Argon et al. in prep).

The strongest component of maser emission in IC 133 has a flux density of only ≈ 200 mJy. This is much weaker than the strongest component in IC 10, and a fit to the phase-data of this component as described in section 4.2.4 is unfortunately not possible. Hence, it was not possible to improve the phase-referencing by correcting for a zenith delay offset.

Check Source B4

The phase-referenced image of the check source B4 for the observation on 2001 March 27 can be seen in Figure 5.8. The source was clearly detected with a peak-to-noise ratio of 15 and very compact with a possible extension to the east. This extension is also seen in the image of the second observation on 2001 April 05.

The position of B4 was then obtained by a fit of a Gaussian component to the image. The positions for the two observations are given in Table 5.3 and agree within a few μas. The flux density of B4 decreased by ≈ 30% between the two observations. This is similar to the flux density variations of many maser components in IC 133 and can be explained by instrumental effects.

M33/19:

Maser emission in M33/19 could be detected over a range of ≈ 10 km s^{-1}. The spectra of M33/19 for the first two observations, made by summing up the flux densities of all detected components in the maps for the individual channels, can be seen in Figures 5.9 and 5.11. G90 observed a few scans on M33/19 and found one single spectral component at an LSR velocity of ≈ -135 km s^{-1}with a width of ≈ 1.5 km s^{-1} and a correlated flux density of ≈ 1 Jy. Here, the spectra consist of at least two weaker and broader components, separated by ≈ 2.5 km s^{-1}.

The spatial distribution of the maser emission can be seen in Figures 5.10 and 5.12. All emissions comes from five maser features M1 – M5 spread over ≈ 5 mas or ≈ 4000 AU. The components M1, M2 and M3 are seen in both observations, while the components M4 and M5 are seen only in the first observation. While the component M1 is unresolved, the emission from the components M2 and M3 can not be clearly separated into two distinct components. The emission is unresolved in right ascension but forms an elongated structure with a length of ≈ 2 mas or 1600 AU in declination.

A single elliptical Gaussian component was fitted to each detected feature of maser emission. The positions, peak and integrated flux densities, sizes and position angles of all com-

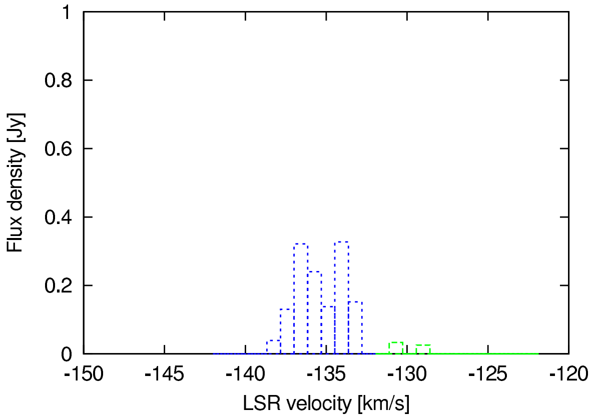

FIGURE 5.9— VLBI-spectrum of M33/19 on 2001 March 27.

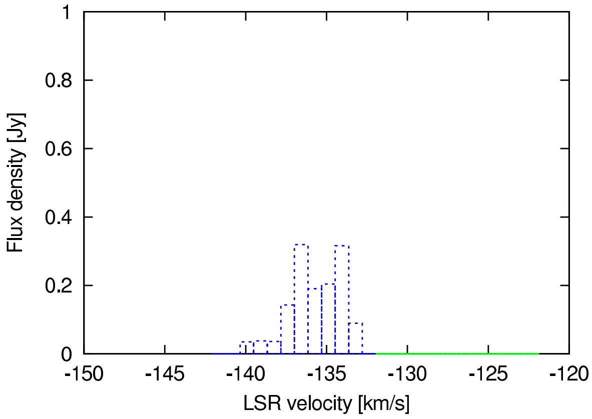

FIGURE 5.11— VLBI-spectrum of M33/19 on 2001 March 27.

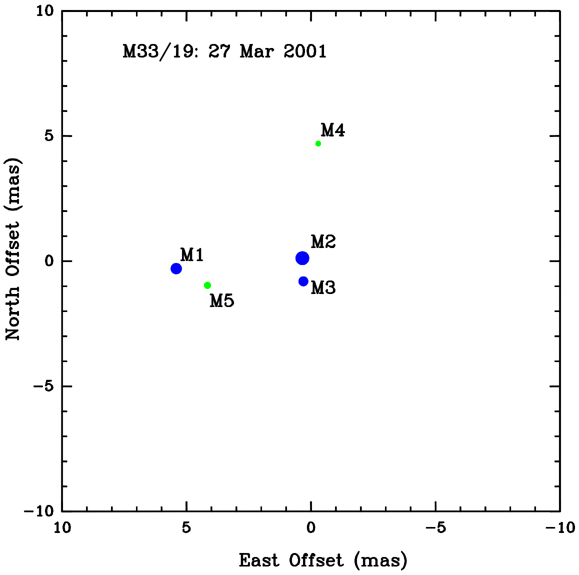

FIGURE 5.10— Composite map of the H_2O masers in M33/19. The area of the circles is proportional to the flux density of the components and the colors are as in Figure 5.9.

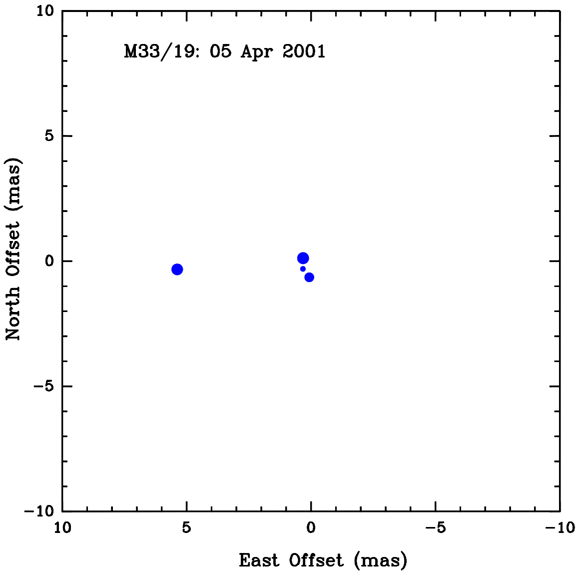

FIGURE 5.12— Composite map of the H_2O masers in M33/19. The area of the circles is proportional to the flux density of the components and the colors are as in Figure 5.11.

ponents are given in Tables A.9 and A.10. The extended nature of M2 and M3 strongly affects the fitted positions and introduces large deviations. While the position of the components in right ascension is roughly consistent for the different channels, the positions in declination differ by up to 0.7 mas. The apparent size of the two components in declination is with 1-1.8 mas also much larger than the beam size. This makes the position measurement of these two components very uncertain. Hence, these positions, especially the declinations, have to be treated very carefully. However, component M1 should yield reliable results for M33/19.

The relative flux density changes m of all components of M33/19 as defined in Equation 5.1 is plotted in Figure 5.14. Here, most components show some variability of ± 50%, but no systematic changes like in IC 133 and

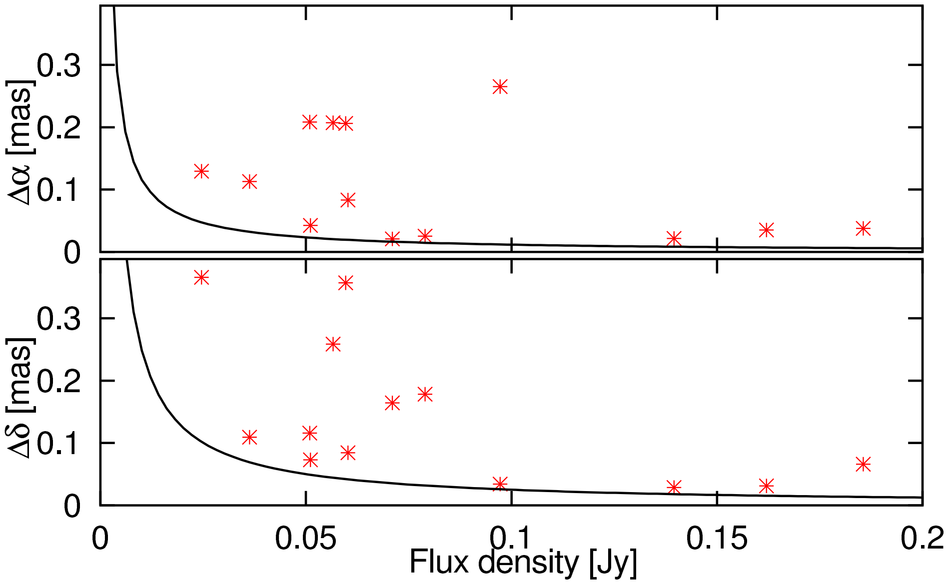

FIGURE 5.13— M33/19: Position difference between the first and second observation as a function of component flux density in right ascension (upper) and declination (lower). The solid line is the theoretical limit from Equation 5.2.

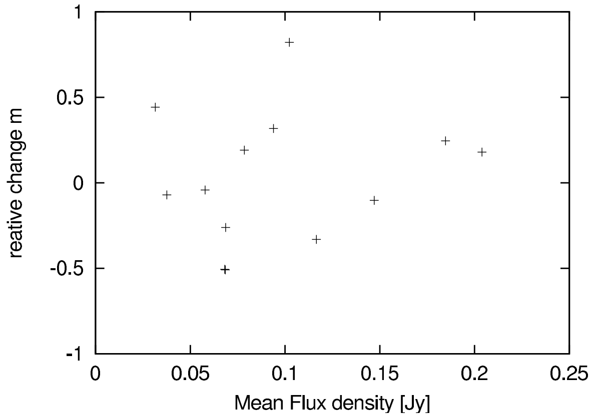

FIGURE 5.14— M33/19: Relative flux density changes between the first and second observation.

B4 are seen.

Figure 5.13 shows the position difference between the two observations for the three components M1 – M3 as a function of the component flux density together with the theoretical noise limit. Here, the differences between the two observations are larger than for IC 133. This is caused by the complicated structure of the components M2 and M3. If one considers only component M1, one gets agreements of better than 50 and 100 μas in right ascension and declination respectively. This is again comparable to IC 133.

All components of M33/19 were also to weak to fit the phase data directly. Since no geodetic observations were made, the data of M33 from the first epoch could not be corrected for zenith delay offsets.

5.3 Second Epoch

5.3.1 Observations

The second epoch on M33 was observed with the VLBA on 2002 January 28 and 2002 February 03. The setup of the experiment was identical to the observations of the first epoch, except the inclusion of geodetic-like observation as described in section 2.3.3 before and after the phase-referencing observations. All sources were observed at the updated posi-

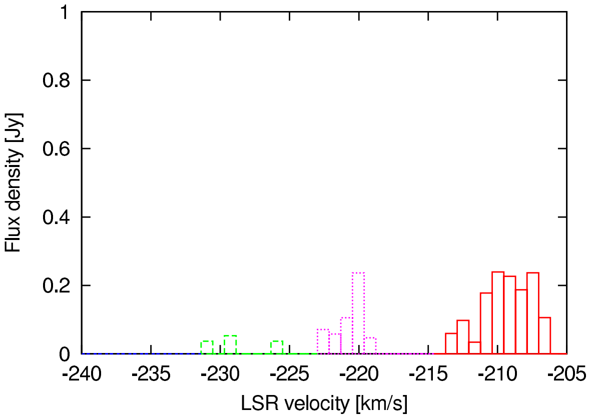

FIGURE 5.15— VLBI-spectrum of IC 133 on 2002 January 28.

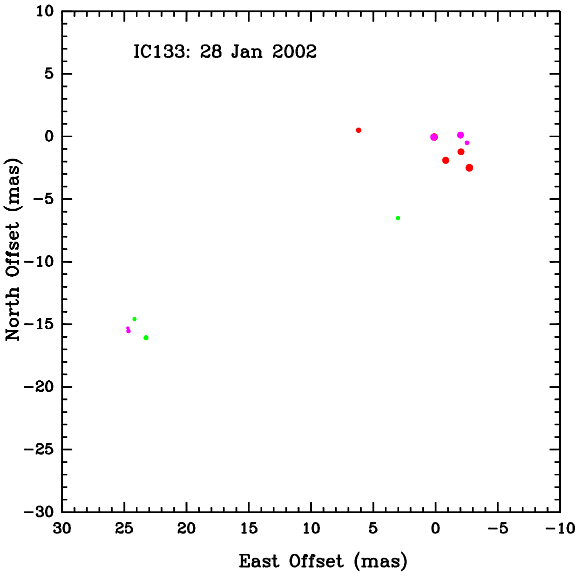

FIGURE 5.16— Composite map of the H_2O masers in IC 133. The area of the circles is proportional to the flux density of the components and the colors are as in Figure 5.15.

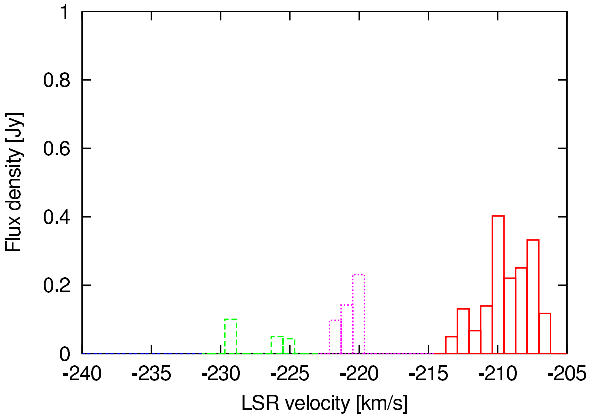

FIGURE 5.17— VLBI-spectrum of IC 133 on 2002 February 03.

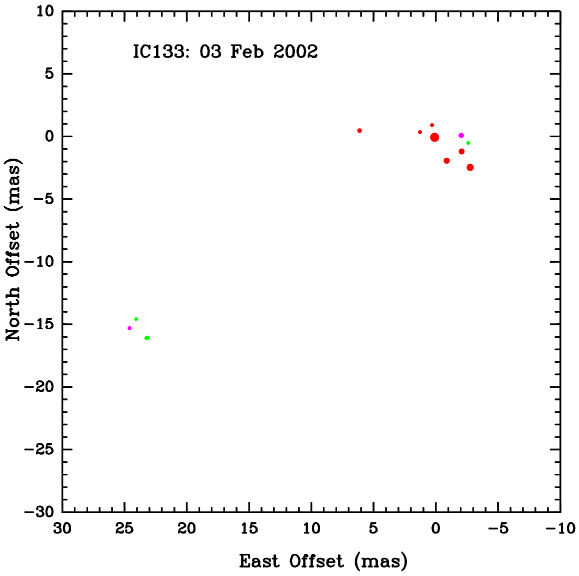

FIGURE 5.18— Composite map of the H_2O masers in IC 133. The area of the circles is proportional to the flux density of the components and the colors are as in Figure 5.17.

tions in Table 5.2. During the geodetic-like observations, we observed with eight 8 MHz bands at left circular polarization. The eight bands were set to frequencies which were 0.0, 25.0, 87.5, 187.5, 350.0, 400.0, 437.5 and 450 MHz offset from the reference frequency. Nine strong sources from the VLBA calibrator list were observed for 5 minutes each. The positions of the sources were chosen to cover all elevation ranges at all telescopes. The total observing time was 10 hours, 8.5 hours were spent on the phase-referencing and 45 minutes were spent on the geodetic-like observations before and after the phase-referencing.

5.3.2 Imaging

The data reduction was identical to the data reduction of the first epoch. After the initial amplitude calibration using the system temperatures and gain curves, the task PCCOR

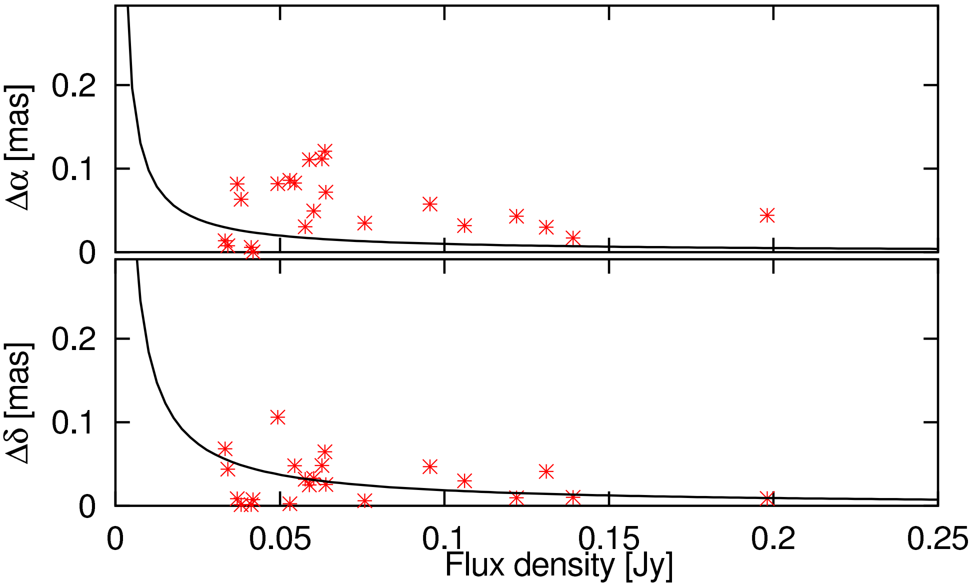

FIGURE 5.19— IC 133: Position difference between the first and second observation as a function of component flux density in right ascension (upper) and declination (lower). The solid line is the theoretical limit from Equation 5.2.

was used to eliminate instrumental phase and delay offsets between individual IFs. A fringe fit was performed on the two strong calibrators J0136+475 and J0152+2207 for a rough delay calibration. Then the phase-calibrator J0137+312 was fringe-fitted and the solutions were applied to IC 133, M33/19 and B4. The data of the antenna in St. Croix were discarded in both observations. In the first observation on 2002 January 28, the antenna in Pie Town observed only for the first half of the experiment.

Then all sources were imaged. The beam sizes for the two observations were 0.62×0.33 mas at a position angle of 176° and 0.71×0.33 at position angle 175°.

IC 133

Maser emission could be detected in IC 133 over a range of $\approx$ 25 km s^{-1}. The spectra of all detected emission in the two observations can be seen in Figures 5.15 and 5.17. The spectra are similar to the spectra of the first epoch, but the emission around 235 km s^{-1} is not detected.

The spatial distribution of the maser emission can be seen in Figures 5.16 and 5.18. The maser features cluster again in the two separate regions IC 133M and IC 133SE. All six stable components I1 – I6 in IC 133M from the first epoch are clearly detected in the second epoch. In IC 133SE, only one component (I12) from the first epoch could be also detected in the second epoch. All other components disappeared (e.g. the emission around -235 km s^{-1}) while new components appeared (between -220 and -230 km s^{-1}).

TABLE 5.4— Epoch 2: Position offsets in right ascension $\Delta\alpha$, declination $\Delta\delta$ and peak flux S of B4 from imaging.

Date	$\Delta\alpha$ [μas]	$\Delta\delta$ [μas]	S [mJy]
2002/01/28	207	-68	3.5
2002/02/03	201	47	3.2
Mean	204±3	-11±58	

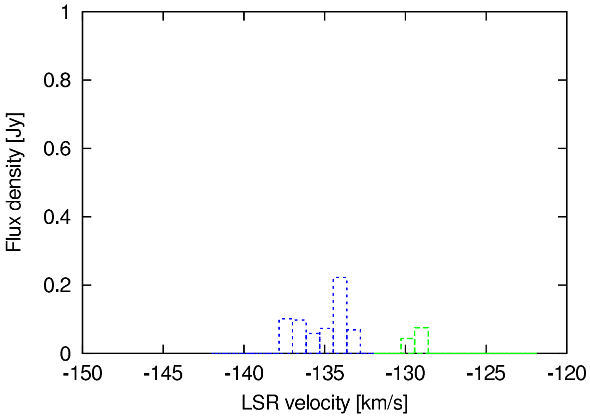

FIGURE 5.20— VLBI-spectrum of M33/19 on 2002 January 28.

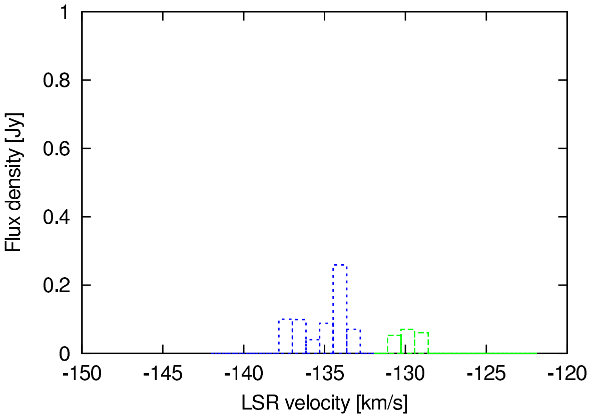

FIGURE 5.22— VLBI-spectrum of M33/19 on 2002 February 03.

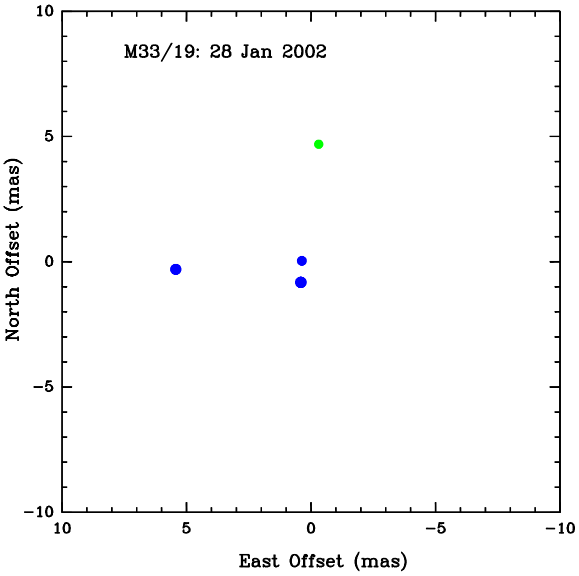

FIGURE 5.21— Composite map of the H_2O masers in M33/19. The area of the circles is proportional to the flux density of the components and the colors are as in Figure 5.20.

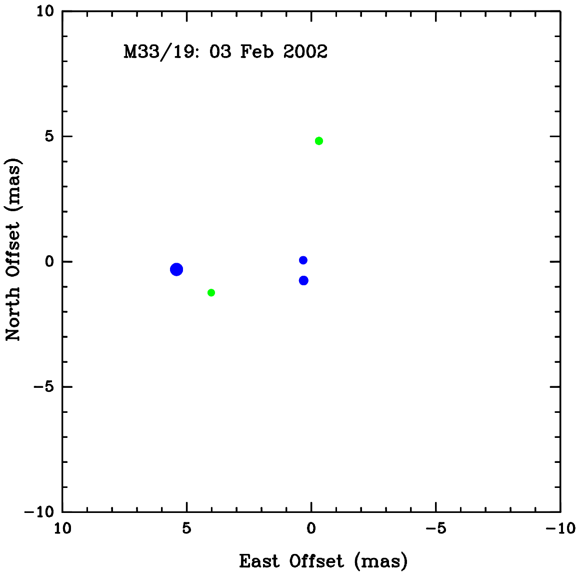

FIGURE 5.23— Composite map of the H_2O masers in M33/19. The area of the circles is proportional to the flux density of the components and the colors are as in Figure 5.22.

A single elliptical Gaussian component was fitted to the detected maser features and the positions, peak and integrated flux densities, sizes and position angles of all components are listed in Tables A.3 and A.4 for the two observations. Here most components are again unresolved.

The position differences of all components between the two observations are shown in Figure 5.19 together with the theoretical noise limit. The differences are comparable with the first epoch and most positions agree within 100 μas in right ascension and declination. The average difference in right ascension is 54 μas in right ascension and 30 μas in declination. The agreement in declination is surprisingly good despite the larger beam size in this direction. Many of the weaker features have a better agreement than the expected accuracy from the signal-to-noise ratio. This is

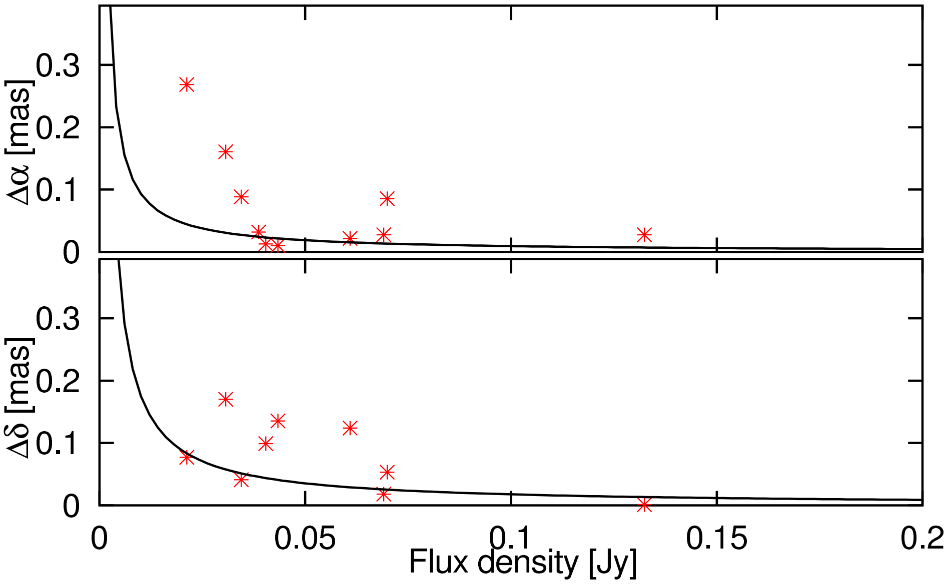

FIGURE 5.24— M33/19: Position difference between the first and second observation as a function of component flux density in right ascension (upper) and declination (lower). The solid line is the theoretical limit from Equation 5.2.

probably caused by a coincidental agreement between the two observations.

Check Source B4

The check source B4 was clearly detected in both observations. The positions and peak flux densities of B4 are given in Table 5.4. The positions agree again very good in right ascension, but disagree in declination by more than 100 μas.

M33/19

Emission in M33/19 could be detected over a range of $\approx$ 10 km s^{-1}. The spectra of M33/19 of the two observations of the second epoch are shown in Figures 5.20 and 5.22. The emission is weaker than in the first epoch, but all spectral features were also detected in the the second epoch.

The spatial distribution of the maser emission can be seen in Figures 5.21 and 5.23. Here, all components from the first epoch are also detected. The results from a fit of a Gaussian component to the detected maser features are shown in Tables A.11 and A.12. The elongated feature composed by the components M2 and M3 was in the first epoch dominated by the emission of M2. In the second epoch, M2 became significantly weaker while M3 stayed at similar flux density levels.

Figure 5.24 shows the position difference between the two observations for M1 – M3. The differences are similar to the differences in the first epoch. The large differences are again from the components M2 and M3, while the errors for M1 are always smaller than 100 μas.

5.3.3 Phase Corrections

The geodetic-like observations were used to determine a zenith delay offset and drift at each station and a clock offset and drift at each station except the reference antenna as described in section 2.3.3. The parameters of the best model-fit are given in Table 5.5 for both observations. Here Kitt Peak (KP) was the reference antenna. Since Pie Town

TABLE 5.5— Second Epoch: Zenith delay offset (τ_0) and rate ($\dot{\tau}_0$) and clock offset (Δt) and rate ($\dot{\Delta}t$) from the geodetic-like observations.

Date			BR	FD	HN	KP	LA	MK	NL	OV	PT
2002/01/28	τ_0	[cm]	3.81	0.02	6.20	-0.61	-0.23	-7.80	3.67	4.06	-2.65
	$\dot{\tau}_0$	[cm h^{-1}]	0.43	0.16	0.05	0.89	0.43	-0.17	0.28	0.28	-
	Δt	[ns]	0.26	0.29	0.68	-	0.24	-0.61	0.52	0.38	0.10
	$\dot{\Delta}t$	[ns d^{-1}]	-0.38	0.62	1.50	-	0.60	-0.31	1.34	-0.01	-
2002/02/03	τ_0	[cm]	-	-8.10	5.86	-0.21	0.72	-1.95	6.28	1.61	1.19
	$\dot{\tau}_0$	[cm h^{-1}]	-	0.10	0.41	-0.11	0.14	-0.10	0.43	0.28	0.19
	Δt	[ns]	-	-0.49	0.06	-	-0.12	-0.29	0.18	-0.19	0.00
	$\dot{\Delta}t$	[ns d^{-1}]	-	-0.34	-0.63	-	-0.56	-0.50	-0.15	-0.93	0.07

(PT) stopped observing in the middle of the first observation, the second block of geodetic-like observations at the end was not observed. Hence it was not possible to derive a zenith delay drift and clock drift for this station. The geodetic-like observations with Brewster (BR) yielded no useful data in the second observation.

The fitted values from Table 5.5 were then used to correct the uv-data of the phase-referencing observations with the AIPS task CLCOR as described in section 2.3.4. Then all sources were imaged with the corrected data. The peak-to-noise ratio for IC 133 in the channel with the strongest emission increased from 23 to 26 in the first observation and from 26.3 to 27.3 in the second observation. The results from a fit of a Gaussian component to the maser features on the corrected maps are given in Tables A.17, A.18, A.23 and A.24.

The average position difference between the the masers in IC 133 on the corrected images is 30 μas in right ascension and 72 μas in declination compared to 54 μas in right ascension and 30 μas in declination on the uncorrected images. While the agreement improved in right ascension, the differences become larger in declination. However, this larger value is a more reliable estimate of the true position error, since the good agreement on the uncorrected maps was probably caused by a coincidental agreement.

5.4 Third Epoch

5.4.1 Observations

The third epoch of M33 was observed with the VLBA on 2002 October 30 and 2002 November 12. The experimental setup was identical to the observations of the second epoch with a total observing time of 10 hours. Here also 8.5 hours were spent on the phase-referencing observations with four 8 MHz bands in right and left circular polarization while 45 minutes were spent on the geodetic-like observations with eight 8 MHz band in left circular polarization before and after the phase-referencing. All sources were observed at the best known positions listed in Table 5.2.

5.4.2 Imaging

The data reduction was identical to the data reduction in the first epochs. The amplitude was calibrated by system temperatures and gain curves. Then PCCOR was performed before a fringe fit on J0136+475 and J0152+2207 was done. Then the phase-reference J0137+312 was fringe-fitted. Again, the antenna in St. Croix yields no useful data and all data was discarded from this antenna. In the observation on 2002 November 12 no good solution could be found for one hour of the data. This is probably due to a correlation problem, since all data for all antennas were affected.

Then the sources IC 133, B4 and M33/19

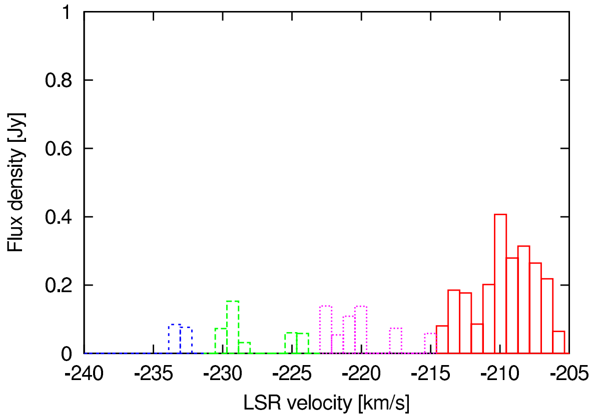

FIGURE 5.25— VLBI-spectrum of IC 133 on 2002 October 30.

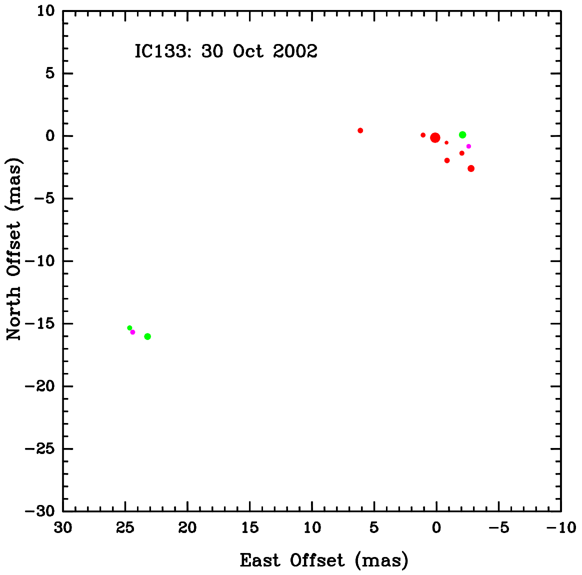

FIGURE 5.26— Composite map of the H_2O masers in IC 133. The area of the circles is proportional to the flux density of the components and the colors are as in Figure 5.25.

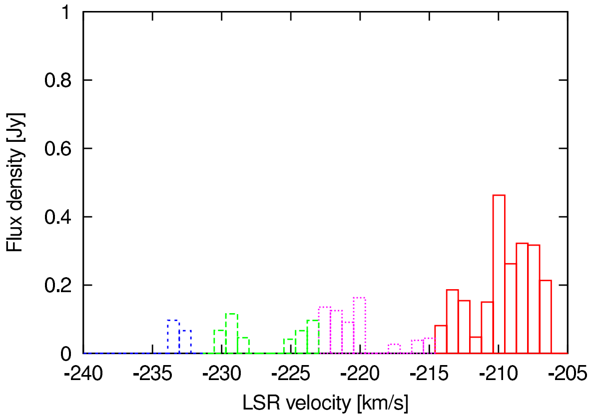

FIGURE 5.27— VLBI-spectrum of IC 133 on 2002 November 12.

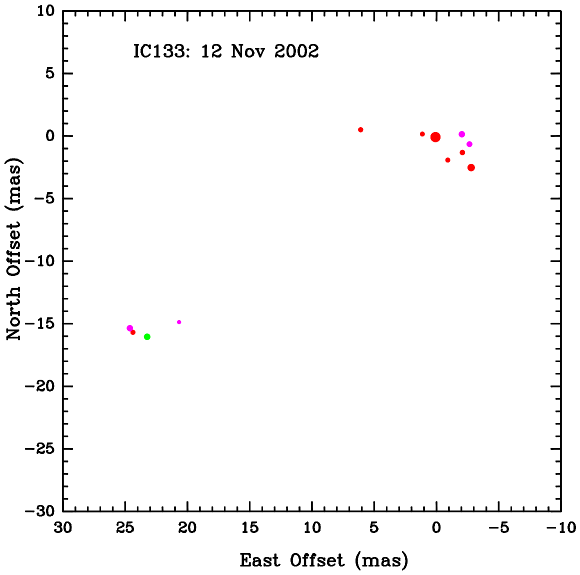

FIGURE 5.28— Composite map of the H_2O masers in IC 133. The area of the circles is proportional to the flux density of the components and the colors are as in Figure 5.27.

were imaged. The beam sizes for the two observations were 0.87×0.38 mas at a position angle of 171° and 0.84×0.36 mas at a position angle of 165°.

IC133

Maser emission could be detected in IC 133 over a range of $\approx$ 30 km s^{-1}. The spectra of the detected emission of the two observations are shown in Figure 5.25 and 5.27. The spectra are again similar to the spectra of the first two epochs.

The spatial distribution of the maser emission can be seen in Figures 5.26 and 5.28. Emission could be detected in IC 133M and IC 133SE. The components I1 – I6 in IC 133M and I12 in IC 133SE from the first two epochs can be also detected in the third epoch. Only component I5 was not detected in the second observation of the third epoch. A few

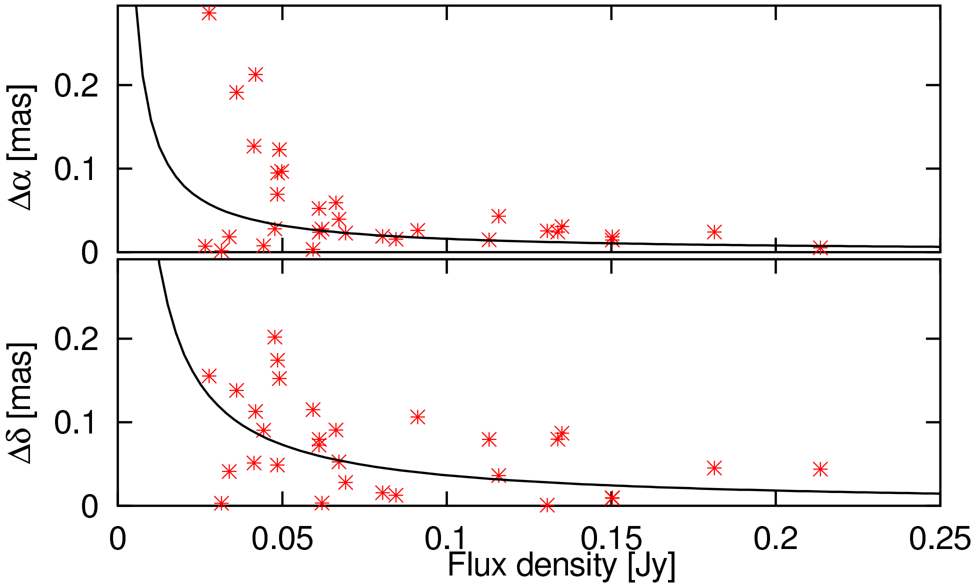

FIGURE 5.29— IC 133: Position difference between the first and second observation as a function of component flux density in right ascension (upper) and declination (lower). The solid line is the theoretical limit from Equation 5.2.

new components were detected in IC 133M and IC 133SE while other components from the old epochs were not detected anymore. The results from a fit of a Gaussian component to the detected maser features are shown in Table A.5 and A.6.

The position difference between the two observations is plotted in Figure 5.29. The agreement between the two observations is again with less than 50 μas in right ascension and 100 μas in declination for most components very good.

Check Source B4

The check source B4 was again detected in both observations. The positions and peak flux densities of B4 are given in Table 5.6. The agreement of the positions is not as good as in the previous epochs. This large deviations could be due to changes in the source structure of B4 itself, since this large displacement is not seen in the masers in IC 133 and M33/19.

TABLE 5.6— Epoch 3: Position offsets in right ascension $\Delta\alpha$, declination $\Delta\delta$ and peak flux S of B4 from imaging.

Date	$\Delta\alpha$ [μas]	$\Delta\delta$ [μas]	S [mJy]
2002/10/30	98	-127	4.6
2002/11/12	143	50	4.3
Mean	121±23	−39±89	

M33/19

Emission im M33/19 could be detected over a range of ≈ 10 km s^{-1}. The spectra of M33/19 during the two observations of the third epoch are shown in Figures 5.30 and 5.32. The emission is much stronger in the third epoch compared to the second epoch with an increase of ≈ 200% in the -134 km s^{-1} line. The emission in the other channels became also much brighter than in the second epoch.

The spatial distribution of the maser emission can be seen in Figures 5.31 and 5.33. All components from the previous epochs (M1 –

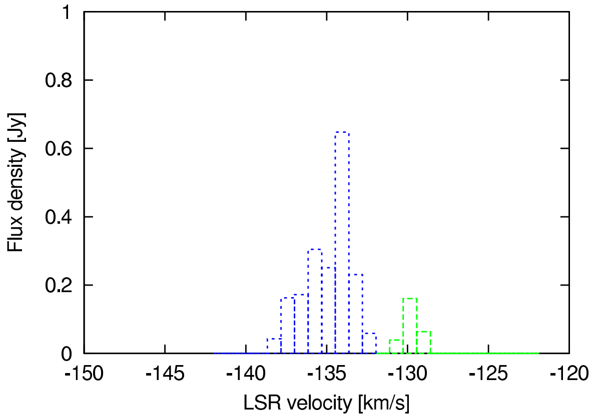

FIGURE 5.30— VLBI-spectrum of M33/19 on 2002 October 30.

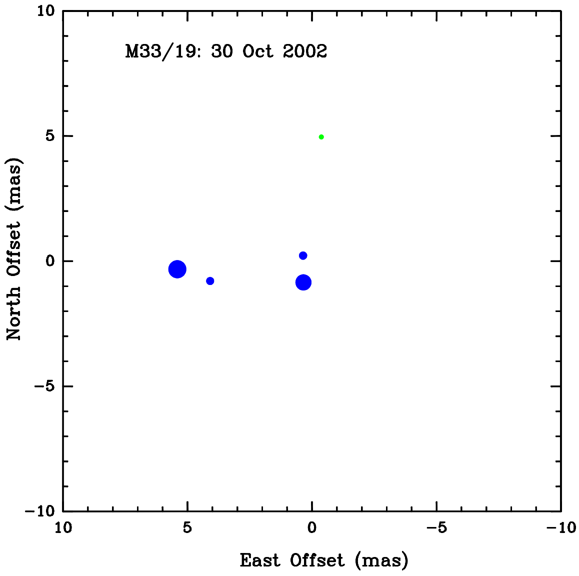

FIGURE 5.31— Composite map of the H_2O masers in M33/19. The area of the circles is proportional to the flux density of the components and the colors are as in Figure 5.30.

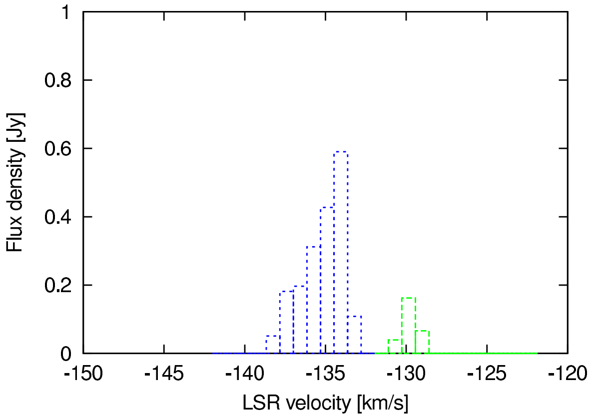

FIGURE 5.32— VLBI-spectrum of M33/19 on 2002 November 12.

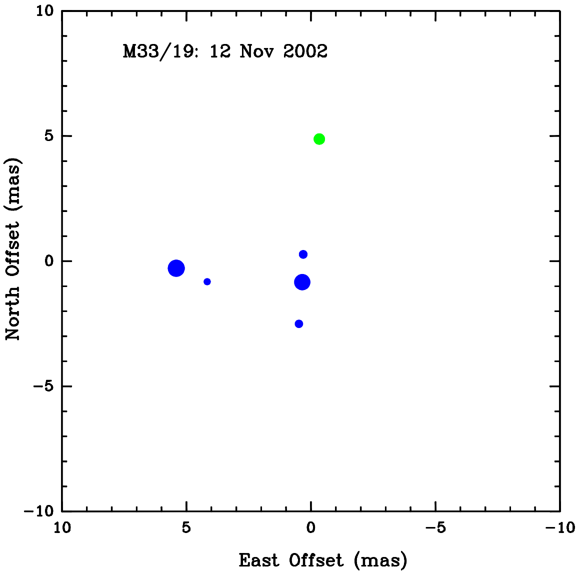

FIGURE 5.33— Composite map of the H_2O masers in M33/19. The area of the circles is proportional to the flux density of the components and the colors are as in Figure 5.32.

M5) were also detected. A new component (M6) was detected in the second observation. This component appears as an extension to the elongated structure with components M2 and M3.

The results from a fit of a Gaussian component to the maser features are given in Tables A.13 and A.14. The component M3 dominates the emission of the elongated structure composed by M2 and M3. The position differences of the maser components between the two observations are shown in Figure 5.34. The differences are smaller than in the previous epoch and the agreement is in general better than 50 μas in right ascension and 100 μas in declination. This better agreement is not surprising, since the maser features became much stronger in the third epoch.

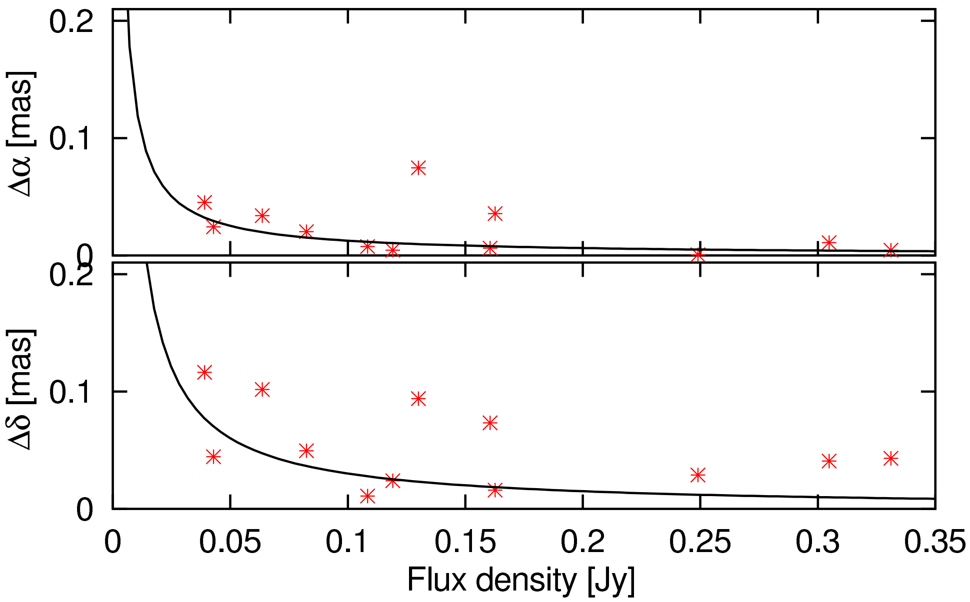

FIGURE 5.34— M33/19: Position difference between the first and second observation as a function of component flux density in right ascension (upper) and declination (lower). The solid line is the theoretical limit from Equation 5.2.

TABLE 5.7— Third Epoch: Zenith delay offset (τ_0) and rate ($\dot{\tau}_0$) and clock offset (Δt) and rate ($\dot{\Delta t}$) from the geodetic-like observations.

Date			BR	FD	HN	KP	LA	MK	NL	OV	PT
2002/10/30	τ_0	[cm]	5.56	3.81	4.87	2.99	0.72	-1.51	2.06	4.13	2.09
	$\dot{\tau}_0$	[cm h^{-1}]	-0.13	0.06	0.22	0.05	0.27	0.57	0.49	0.15	0.08
	Δt	[ns]	-0.05	0.31	0.29	0.07	-0.04	-0.75	0.01	0.07	–
	$\dot{\Delta t}$	[ns d^{-1}]	-1.13	1.35	1.45	0.09	0.42	-1.39	0.62	-0.03	-
2002/11/12	τ_0	[cm]	-2.54	1.71	1.00	2.13	1.12	-2.13	4.41	-2.50	1.17
	$\dot{\tau}_0$	[cm h^{-1}]	-0.28	0.01	0.59	0.15	0.24	0.15	0.01	0.20	0.23
	Δt	[ns]	-0.37	0.45	-0.40	0.08	-0.70	0.27	-0.35	0.02	-
	$\dot{\Delta t}$	[ns d^{-1}]	-1.30	2.33	-1.46	0.86	-1.70	0.88	-0.57	0.45	-

5.4.3 Phase Corrections

The geodetic-like observations were used to determine a zenith delay offset and drift at each station and a clock offset and drift at each station except the reference antenna as described in section 2.3.3. The parameters of the best model-fit are given in Table 5.7 for both observations. The reference antenna in both observations was Pie Town (PT).

The fitted values from Table 5.7 were then used to correct the uv-data of the phase-referencing observations with the AIPS task CLCOR as described in section 2.3.4. Then all sources were imaged with the corrected data. The peak-to-noise ratio for IC 133 in the channel with the strongest emission increased from 33.7 to 36.4 in the first observation and from 32.4 to 36.1 in the second observation. The

TABLE 5.8— Fourth Epoch: Zenith delay offset (τ_0) and rate ($\dot{\tau}_0$) and clock offset (Δt) and rate ($\dot{\Delta t}$) from the geodetic-like observations.

Date		BR	FD	HN	KP	LA	MK	NL	OV	PT
2003/12/14	τ_0 [cm]	-	3.83	7.12	1.44	0.44	-2.64	5.74	2.78	0.17
	$\dot{\tau}_0$ [cm h^{-1}]	-	0.16	0.08	-0.05	0.00	-0.43	-0.31	0.04	0.18
	Δt [ns]	-	0.13	0.37	0.04	-	-0.29	0.28	0.09	0.02
	$\dot{\Delta t}$ [ns d^{-1}]	-	0.12	-0.66	-0.27	-	-3.58	0.19	0.06	0.44
2004/01/08	τ_0 [cm]	-	0.50	-	1.70	0.37	-0.59	2.48	-1.71	0.30
	$\dot{\tau}_0$ [cm h^{-1}]	-	0.29	-	0.09	-0.05	0.20	-0.15	0.42	-0.03
	Δt [ns]	-	-0.10	-	-	-0.06	-0.15	0.06	-0.16	-0.13
	$\dot{\Delta t}$ [ns d^{-1}]	-	-1.13	-	-	-0.92	-1.40	0.40	0.38	-1.99

results from a fit of a Gaussian component to the maser features on the corrected maps are given in Tables A.19, A.20, A.25 and A.26.

The average position difference between the the masers in IC 133 on the corrected images is 33 μas in right ascension and 108 μas in declination compared to 54 μas in right ascension and 121 μas in declination on the uncorrected images. Here, the agreement improved in both right ascension and declination.

5.5 Fourth Epoch

A fourth epoch of M33 has been observed recently with the VLBA. The observations were made on 2003 December 14 and 2004 January 08. The setup of the experiments were very similar to the observations of the second and third epoch, but the total observing time was 12 hours. A third block of geodetic-like observation was added in the middle of the observation. The results of these observations will be also included in the next sections of this work.

The observations in the fourth epoch suffer from similar problems as the third epoch of IC 10. The flux density of the phase calibrator has decreased since the third epoch and a fringe fit yielded not enough good solutions. Hence the signal-to-noise cutoff was lowered from 5 to 4. The antenna in St. Croix yielded no good data and the antennas in Brewster and Hancock yielded no good data in the second observation. The beam sizes for the two observations were 0.85 × 0.36 mas at a position angle of 159° and 1.15 × 0.47 mas at a position angle of 164°.

The components I1 – I4 and I6 in IC 133 were all detected in both observations. Component I5, which has been seen in all previous epochs, was detected only in the first observation. In M33/19, the components M1, M2 and M3 were detected in both observations, while M4 was only seen in the second observation. The results from a fit of a Gaussian component to the maser features on the maps are given in Tables A.7, A.8, A.15 and A.16.

The geodetic-like observations yielded useful corrections only in the first observation. The parameters of the best model-fit for the zenith delays and clock offsets are given in Table 5.8. Here, the peak-to-noise ratio in the corrected maps of the strongest maser component increased from 35.3 to 43.9. In the second observations, the zenith delay offsets were all less than 2 cm and the corrections did not improve the phase-referenced image. However, the peak-to-noise ratio in the uncorrected images was already very high with 49.2. The results from a fit of a Gaussian component to the maser features on the corrected maps are given in Tables A.21, A.22, A.27 and A.28.

The average position difference between the two observations was 38 μas in right ascension and 193 μas in declination on the uncorrected images. This improved to 24 μas in right ascension and 58 μas in declination on the corrected images.

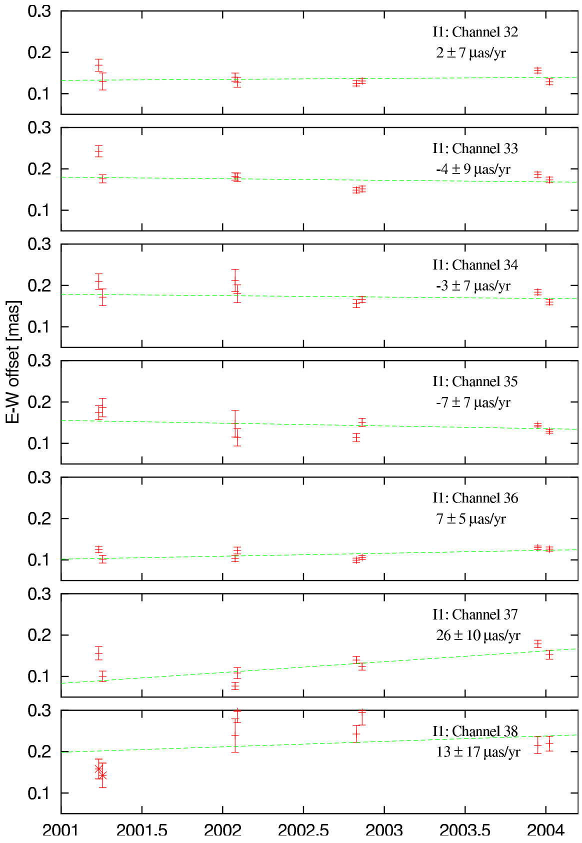

FIGURE 5.35— East-West position offsets of component I1 in each frequency channel together with the best fit linear motion.

5.6 Discussion

5.6.1 Astrometric accuracy

The astrometric accuracy of the observations is given by the position differences of the masers components in two closely spaced observations. The average position difference of all maser components between the two observations of each epoch in the uncorrected images of IC 133 is 50 μas in right ascension and 112 μas in declination. After the correction of the uv-data the average error decreased by 40% to 30 μas in right ascension and by 25% to 84 μas in declination.

Because of this significant improvement of the astrometric accuracy by the correction of the uv-data, we will consider here only the results from the corrected images.

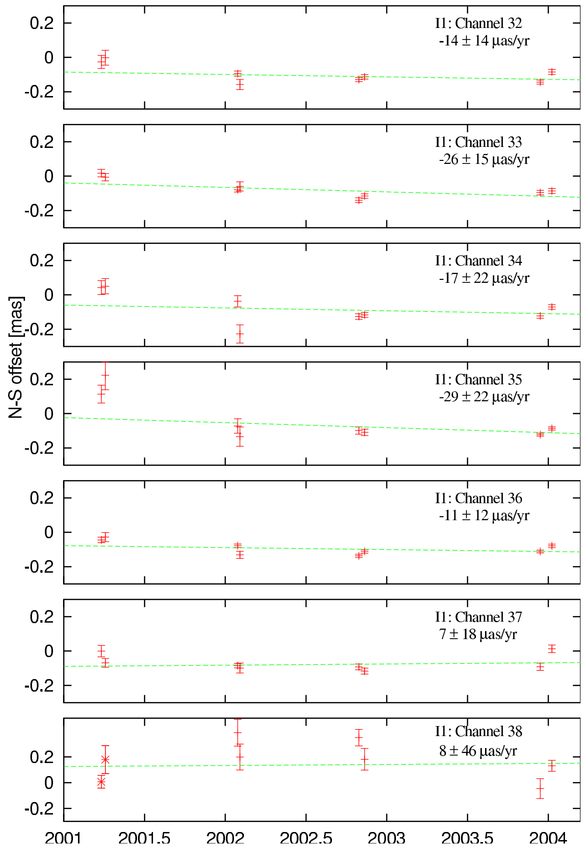

FIGURE 5.36— North-South position offsets of component I1 in each frequency channel together with the best fit linear motion.

5.6.2 Proper Motion of IC 133

A total of 29 different components could be detected in the four epochs of IC 133. Most components were detected in only a few observations. However, six components (I1 – I6) in IC 133 were detected in all four epochs. Since the accuracy of proper motion measurements depends strongly on the number of observations and the spanned time-range, we will focus here only on the six stable components which could be detected in all epochs.

I1

Component I1 is the strongest maser component in IC 133 and was present in at least 7 frequency channels in each observation. The positions of the maser component I1 in the observations of the four epochs are plotted in Figures 5.35 and 5.36 together with the best

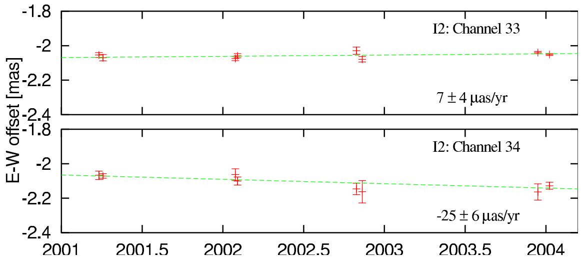

FIGURE 5.37— East-West position offsets of component I2 in each frequency channel together with the best fit linear motion.

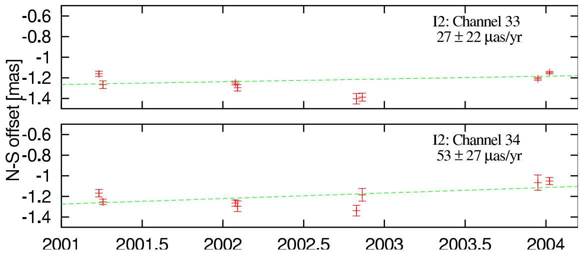

FIGURE 5.38— North-South position offsets of component I2 in each frequency channel together with the best fit linear motion.

variance weighted fit of a rectilinear motion to the data. The motions in all except one channel agree within their joint errors. Only the emission in channel 37 shows a different ($\approx 2.5\sigma$) behavior.

The weighted average motion of component I1 over all channels is 3±3 μas yr^{-1} in right ascension and -14±6 μas yr^{-1} in declination.

I2

The component I2 could be detected in two frequency channels in all four epochs. The positions in the two channels are shown in Figures 5.37 and 5.38 together with the best variance weighted fit of a rectilinear motion to the data.

The fitted motions in right ascension are different in both channels. While the motion of I2 in channel 33 is in good agreement with the average motion of component I1, the motion in channel 34 is different. However, channel 34 was in most observations weaker and sometimes slightly resolved.

The motions in declination of I2 in the two frequency channels agree within their large errors. However, the first three epochs show a clear trend towards lower declinations. Hence, it is possible that the emission in the fourth epoch is associated with a different physical region. This hypothesis is supported by the strong rise in flux density of component I2 in the last epoch.

The weighted average motion of the two channels is -3±3 μas yr^{-1} in right ascension 37±17 μas yr^{-1} in declination.

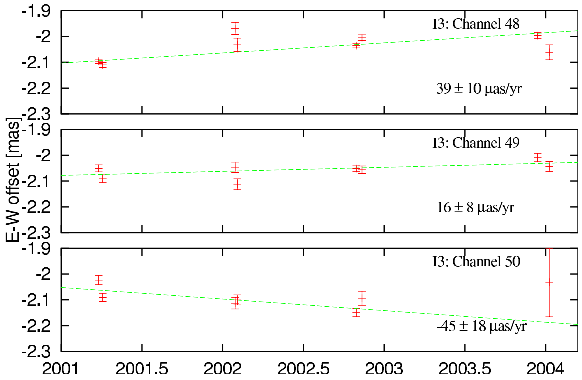

FIGURE 5.39— East-West position offsets of component I3 in each frequency channel together with the best fit linear motion.

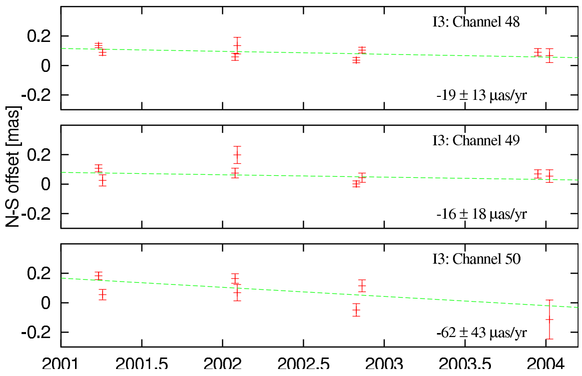

FIGURE 5.40— North-South position offsets of component I3 in each frequency channel together with the best fit linear motion.

I3

Component I3 was detected in three frequency channels in all epochs. The positions of I3 are shown in Figures 5.39 and 5.40 together with the best variance weighted fit of a rectilinear

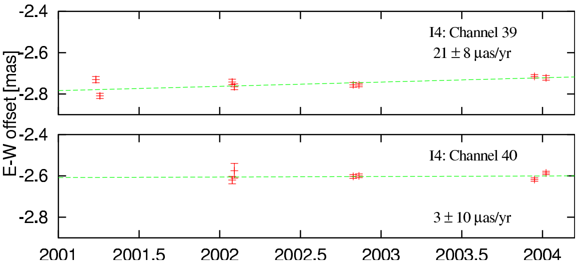

FIGURE 5.41— East-West position offsets of component I4 in each frequency channel together with the best fit linear motion.

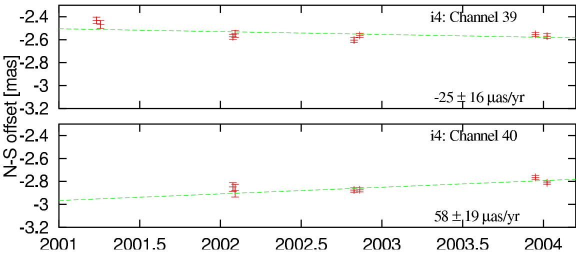

FIGURE 5.42— North-South position offsets of component I4 in each frequency channel together with the best fit linear motion.

motion to the data.

Here, channels 48 and 49 agree within their joint errors, but channel 50 shows a very different behaviour. However, channel 50 is the weakest channel with large errors and just barely detected in one observation of the fourth epoch.

The weighted average motion of I3 is 18±6 μas yr^{-1} in right ascension and -21±10 μas yr^{-1} in declination.

I4

Emission of component I4 could be detected in two frequency channels. The positions of component I2 in the two channels are shown in Figures 5.41 and 5.42 together with the best variance weighted fit of a rectilinear motion to the data.

Here, the motions in right ascension are consistent for the two channels while the motions in declination disagree. Since the emission in channel 40 is not detected in the first epoch, we will adopt the motion of channel 39 which is 21±8 μas yr^{-1} in right ascension and -25±16 μas yr^{-1} in declination.

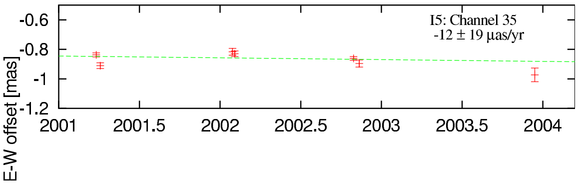

FIGURE 5.43— East-West position offsets of component I5 in each frequency channel together with the best fit linear motion.

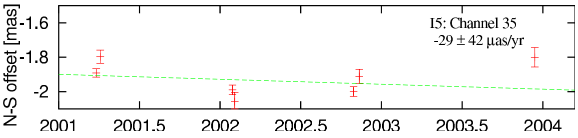

FIGURE 5.44— North-South position offsets of component I5 in each frequency channel together with the best fit linear motion.

I5

Component I5 was detected only in one frequency channel. The positions of component I5 are shown in Figures 5.43 and 5.44 together with the best variance weighted fit of a rectilinear motion to the data. This best fit gives a motion of -12±19 μas yr^{-1} in right ascension and -29±42 μas yr^{-1} in declination.

I6

Finally, component I6 was detected in three frequency channels. The positions of I6 are shown in Figures 5.45 and 5.46 together with the best variance weighted fit of a rectilinear motion to the data. The motions in channels 34 and 35 agree within their joint errors, while the motion in channel 36 is different. However, the emission in channel 36 is very weak and not detected in one observation of the first and fourth epoch.

The average weighted motion of component I6 is 1±2 μas yr^{-1} in right ascension and -45±13 μas yr^{-1} in declination.

Average Motion

The fitted motions of the components I1 – I6 are summarized in Table 5.9. The mo-

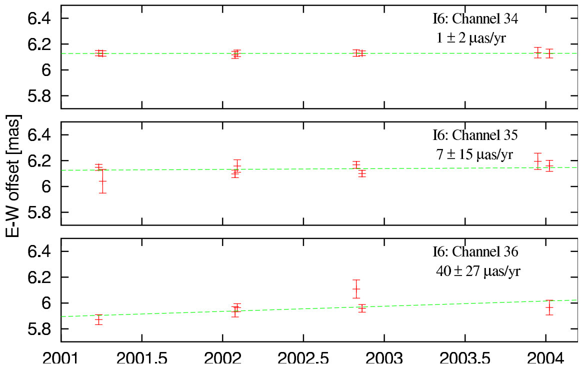

Figure 5.45— East-West position offsets of component I6 in each frequency channel together with the best fit linear motion.

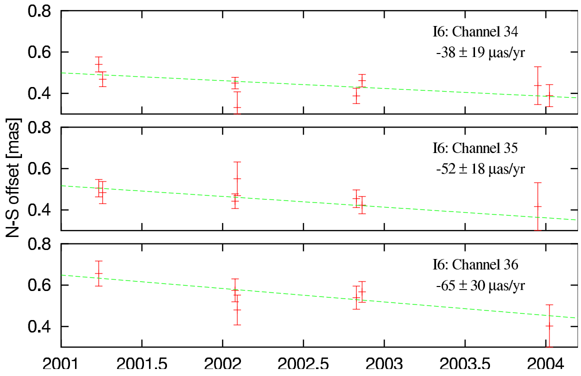

Figure 5.46— North-South position offsets of component I6 in each frequency channel together with the best fit linear motion.

Table 5.9— Motions of all six stable components in IC 133.

	$\dot{\alpha}$ [μas yr^{-1}]	$\dot{\delta}$ [μas yr^{-1}]
I1	3±3	-14±6
I2	-3±3	37±17
I3	18±6	-21±10
I4	21±8	-25±16
I5	-12±19	-29±42
I6	1±2	-45±13

tions of most components agree within their joint errors. The differences could be caused by measurement errors, different intrinsic motions or a combination of both. The motions in right ascension of components I3 and I4 are larger than the motions of the other components. These two components were already seen in G90, and they show a motion of ≈ 6-7 μas yr^{-1} in right ascension relative to I1 (see section 5.3.2). The motions in declination of all components except I2 agree within their joint errors. However, as described earlier, this deviation of I2 can be explained by the last epoch, where probably a different physical region is seen.

If one assumes a random distribution of intrinsic motions in IC 133, the average motion of many maser features would represent the true motion of IC 133. The weighted average of the motions in right ascension would be completely dominated by component I6 due to the extremely small error on the motion of this component. Since this small error probably underestimates the true error, we will adopt a minimum error of 5 μas yr^{-1} for the weighted average. This leads then to a motion of IC 133 of:

$$\begin{aligned} \dot{\bar{\alpha}}_{IC\,133} &= \quad 5 \pm 3 \qquad \mu\text{as yr}^{-1} \\ \dot{\bar{\delta}}_{IC\,133} &= \; -17 \pm 4 \qquad \mu\text{as yr}^{-1} \end{aligned} \tag{5.3}$$

If the components have different intrinsic motions, the weighted average would lead to a bias towards the motion of the component with the smallest error, which does not necessarily represent the total motion of IC 133. In this case, an arithmetic average over all components would give more reliable results. However, this would yield here the same results, only with larger errors. Thus, we will neglect the effects of different internal motions. These effects will become more important when additional observations further reduce the measurement errors. Then, more sophisticated model of the internal structure and motions of IC 133 will be necessary.

5.6.3 Proper Motion of M33/19

Four components (M1 – M4) in M33/19 were detected in all four epochs. Their motions will be the subject of this section.

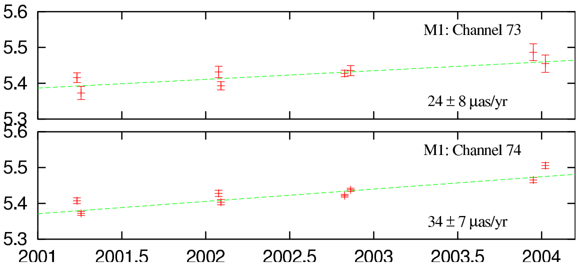

FIGURE 5.47— East-West position offsets of component M1 in each frequency channel together with the best fit linear motion.

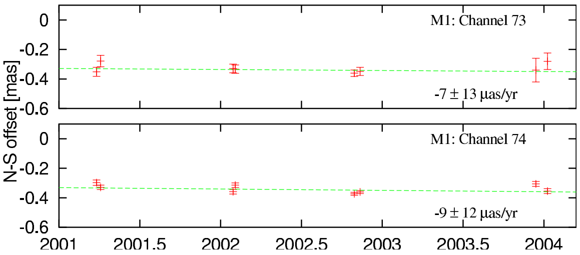

FIGURE 5.48— North-South position offsets of component M1 in each frequency channel together with the best fit linear motion.

M1

The component M1 can be seen in two different frequency channels. The positions of component M1 in these channels are shown in Figures 5.47 and 5.48 together with the best variance weighted fit of a rectilinear motion to the data. The motion in the two channels are in excellent agreement and the weighted average motion is 30±5 μas yr^{-1} in right ascension and -8±9 μas yr^{-1} in declination.

M2

Component M2 could be detected in two frequency channels in all epochs. The positions of component M2 are shown in Figures 5.49 and 5.50 together with the best variance weighted fit of a rectilinear motion to the data. The motion in right ascension in the two channels is again in very good agreement. The positions in declination show large variations between the different epochs. This is caused by the elongated structure represented by components M2 and M3. Hence, a reliable fit of a motion in declination is not possible.

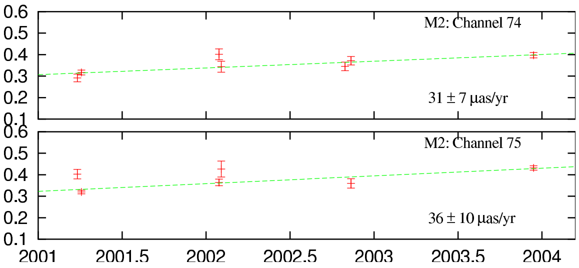

FIGURE 5.49— East-West position offsets of component M2 in each frequency channel together with the best fit linear motion.

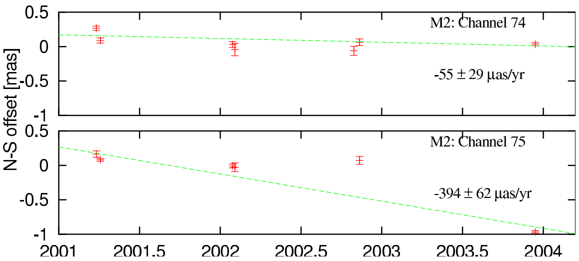

FIGURE 5.50— North-South position offsets of component M2 in each frequency channel together with the best fit linear motion. The large errors are caused by the elongated structure of M2 and M3 (see text) and these data will be discarded in the analysis.

The weighted average motion in right ascension is 33±6 μas yr^{-1}.

M3

M3 could be detected in six frequency channels. The positions of component M3 are shown in Figures 5.51 and 5.52 together with the best variance weighted fit of a rectilinear motion to the data. The motions in right ascension in the six channels are again in excellent agreement and the weighted average motion is 39±4 μas yr^{-1} in right ascension. The positions in declination are also strongly affected by the elongated structure and a reliable estimate of the motion in declination is not possible.

M4

Component M4 could be detected in two frequency channels. While emission in channel 68 could be detected in the first three epochs,

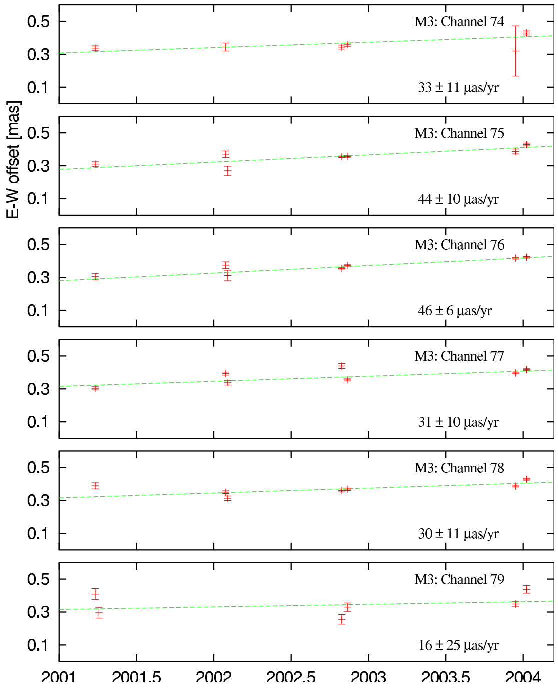

FIGURE 5.51— East-West position offsets of component M3 in each frequency channel together with the best fit linear motion.

TABLE 5.10— Motions of all four stable components in M33/19.

	$\dot{\alpha}$ [μas yr^{-1}]	$\dot{\delta}$ [μas yr^{-1}]
M1	30± 5	-8± 9
M2	33± 6	–
M3	39± 4	–
M4	39±10	3±30

the emission in channel 69 was detected only in the last three epochs. The positions of component M4 are shown in Figures 5.53 and 5.54 together with the best variance weighted fit of a rectilinear motion to the data. The motion in both channels agree within their joint errors and the weighted average motion is 30±10 μas yr^{-1} in right ascension and 3±30 μas yr^{-1} in declination.

Average Motion

The fitted motions of the components M1 – M4 are summarized in Table 5.10. The motions of M2 and M3 in declination were dis-

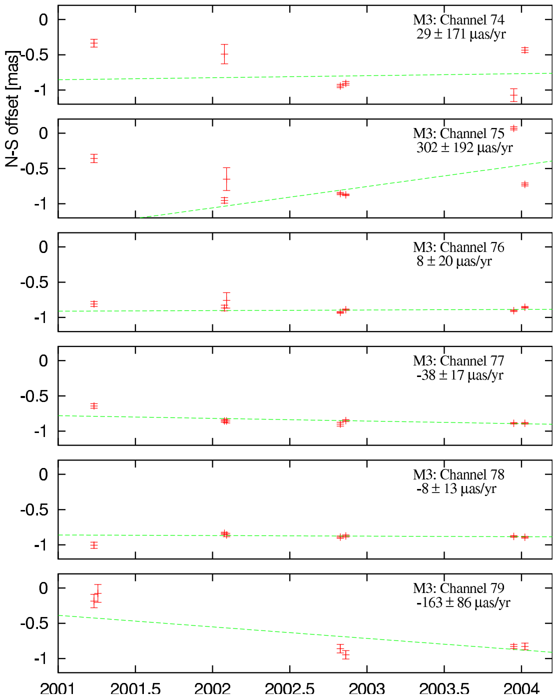

FIGURE 5.52— North-South position offsets of component M3 in each frequency channel together with the best fit linear motion. The large errors are caused by the elongated structure of M2 and M3 (see text) and these data will be discarded in the analysis.

carded here, due to the large uncertainty in the component identification caused by the elongated structure of both components. The motions of all four components are in excellent agreement. The weighted average motion of all components in M33/19 is then:

$$
\begin{aligned}
\dot{\alpha}_{M33/19} &= \quad 35 \pm 3 \quad \mu\text{as yr}^{-1} \\
\dot{\delta}_{M33/19} &= \quad -7 \pm 9 \quad \mu\text{as yr}^{-1}
\end{aligned}
\tag{5.4}
$$

This is a clear (12σ) detection of motion in right ascension for M33/19.

5.6.4 Internal rotation of M33

The measured proper motions $\tilde{v}_{prop}$ of IC 133 and M33/19 can be decomposed into a sum of several contributions:

$$\tilde{\boldsymbol{v}}_{prop} = \boldsymbol{v}_{rot} + \boldsymbol{v}_{pec} + \boldsymbol{v}_{\odot} + \boldsymbol{v}_{prop} \tag{5.5}$$

Here $\boldsymbol{v}_{rot}$ is the motion of the masers due to the internal galactic rotation of M33, $\boldsymbol{v}_{pec}$

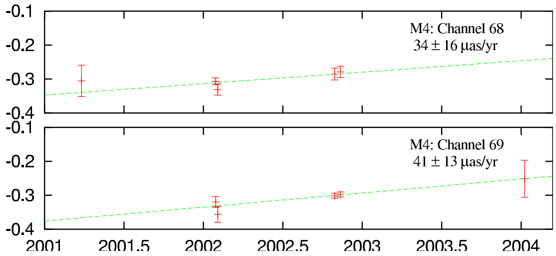

FIGURE 5.53— East-West position offsets of component M4 in each frequency channel together with the best fit linear motion.

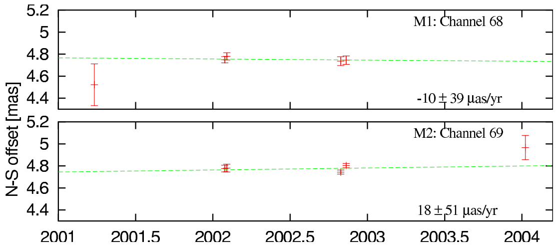

FIGURE 5.54— North-South position offsets of component M4 in each frequency channel together with the best fit linear motion.

is the deviation of the motion of the masers from this rotation, and $\boldsymbol{v}_\odot$ is the apparent motion of M33 caused by the rotation of the Sun around the Galactic Center. The last contribution $\boldsymbol{v}_{prop}$ is the true proper motion of M33 itself. The components $\boldsymbol{v}_{prop}$ and $\boldsymbol{v}_\odot$ are the same for M33/19 and IC 133. If one assumes that the deviation of the motion of the masers from the rotation of M33 is negligible ($\boldsymbol{v}_{pec} \ll \boldsymbol{v}_{rot}$), the relative motion of IC 133 towards M33/19 is determined only by the rotation of M33. This assumption is probably justified, since the maser emission originates in large regions of star formation that should rotate with the galaxy.

The H I distribution and velocity field of M33 has been observed with the Arecibo telescope by Corbelli, Schneider, & Salpeter (1989) and Corbelli & Schneider (1997). The second paper models the H I distribution and velocity field with a warped disk model. Their basic model (Equations 4 & 5) yield an inclination angle i of $49.0° \pm 3.5°$ and a position angle PA of $21.1° \pm 2.0°$ for the inner 20 arcminutes of M33. The rotation velocity of IC 133 at a distance of 22.7 arcminutes from the center of M33 is according to their model 106±11 km s^{-1}. For M33/19, at a distance of 9.7 arcminutes from the center of M33, one gets a rotation velocity 87±9 km s^{-1}. Applying Equations 4.4 – 4.7 to IC 133, one gets velocities of -59.4±6 km s^{-1} in right ascension, -81.0±8 km s^{-1} in declination and a radial velocity of 34±3 km s^{-1} relative to the center of M33. The same calculation gives for M33/19 velocities of 39.4±4 km s^{-1} in right ascension, -47.3±5 km s^{-1} in declination and a radial velocity of -61.9±6 km s^{-1}. The relative motion of IC 133 and M33/19 (in the sense of M33/19-IC 133) is then:

$$\begin{aligned} v_\alpha &= \quad 98.8 \pm 7 \text{ km s}^{-1} \\ v_\delta &= \quad 33.7 \pm 9 \text{ km s}^{-1} \\ v_{rad} &= -96.1 \pm 7 \text{ km s}^{-1} \end{aligned} \tag{5.6}$$

The difference in radial velocities agrees with the observed radial velocities of the masers (≈ 220 - 135 km s^{-1}≈ 85 km s^{-1}). The agreement between the radial velocity of the masers with the radial velocity expected from the rotation of the galaxy is evidence that the deviation of the motion of the masers from the rotation of the H I gas in M33 is small compared to the rotation velocity ($\boldsymbol{v}_{pec} \ll \boldsymbol{v}_{rot}$).

Distance to M33

The values of v_α and v_δ can be compared to the measured proper motions. The measured motion of M33/19 relative to IC 133 (in the sense M33/19-IC 133) is 30±4 μas yr^{-1} in right ascension and 10±10 μas yr^{-1} in declination. This leads to an estimate of the geometric distance to M33 of:

$$D = 695 \pm 105 \text{ kpc.} \tag{5.7}$$

Freedman et al. (2001) derive in the HST Key Project a distance to M33 of 840 kpc based on measurements of Cepheids. Recent distance estimates using Cepheids and Tip of the Red Giant Branch (TRGB) analysis, yield a distance to M33 of 802 ± 51 kpc (Lee et al. 2002) and 794 ± 23 kpc (McConnachie et al. 2004). Other measurements using TRGB and Red Clump (RC) (Kim et al. 2002) favor a larger distance of 916 ± 55 kpc and 912 ± 59 kpc respectively.

Hence, our geometric distance estimate of 695±105 kpc is slightly smaller than the Cepheid distances. This can be compared to the case of NGC 4258. Here, maser emission in a Keplerian circumnuclear disk that orbit a super-massive black hole in the center of the galaxy (Miyoshi et al. 1995) were used to measure a direct geometric distance to NGC 4258. This distance of 7.2±0.5 Mpc (Herrnstein et al. 1999) is also slightly shorter than the distance estimate using Cepheids by Newman et al. (2001) who derive a value of 7.8±0.3 Mpc.

Recently, Tammann, Sandage, & Reindl (2003) and Sandage, Tammann, & Reindl (2004) find differences in the slopes of the Period - Luminosity (P-L) relations of Cepheids in the Galaxy, LMC and SMC. This "weakens the hope of using Cepheids to attain good accuracies in measuring galaxy distances" until the reasons for the differences in the P-L relations are understood. This has been also confirmed by Ngeow & Kanbur (2004).

Further VLBI observations over the next two years have the potential to decrease the measurement error of the motion in right ascension to 2 μas yr^{-1}. This would decrease the error in the distance estimation to ≈ 68 kpc or ≈ 10%. Then a more sophisticated model of the internal rotation of M33 is needed to increase the accuracy of the geometric distance to M33.

5.6.5 Space velocity of M33

The rotation of the Sun about the Galactic Center causes an apparent motion of M33. Using the Galactic rotation described in section 4.5.3, one gets for M33 ($l = 188.96°; b = -3.32°$) at the distance of 695±105 kpc an apparent proper motion $\boldsymbol{v}_\odot$ of 62±10 μas yr^{-1} in right ascension and -15±3 μas yr^{-1} in declination.

The expected motions from the internal rotation of M33 $\boldsymbol{v}_{rot}$ at a distance of 695±105 kpc are -18±3 μas yr^{-1} in right ascension and -25±4 μas yr^{-1} in declination for IC 133 and 12±2 μas yr^{-1} in right ascension and -14±3 μas yr^{-1} in declination for M33/19.

This gives then the true proper motion of M33:

$$\begin{aligned}
\dot{\alpha}_{prop} &= \dot{\tilde{\alpha}}_{prop} - \dot{\alpha}_{rot} - \dot{\alpha}_\odot \\
&= (5 \pm 3 + 18 \pm 3 - 62 \pm 10)\frac{\mu\text{as}}{\text{yr}} \\
&= -39 \pm 11\frac{\mu\text{as}}{\text{yr}} = -128 \pm 41\frac{km}{s} \\
\text{and} & \qquad\qquad (5.8) \\
\dot{\delta}_{prop} &= \dot{\tilde{\delta}}_{prop} - \dot{\delta}_{rot} - \dot{\delta}_\odot \\
&= (-17 \pm 4 + 25 \pm 4 + 15 \pm 3)\frac{\mu\text{as}}{\text{yr}} \\
&= 23 \pm 6\frac{\mu\text{as}}{\text{yr}} = 76 \pm 23\frac{km}{s}.
\end{aligned}$$

The measured systematic velocity of M33 (-181±2 km s^{-1}) is the sum of the radial motion of the of M33 towards the Sun and the component of the solar rotation about the Galactic center towards M33 which is -130±13 km s^{-1}. Hence, M33 is moving with 51±13 km s^{-1} towards the sun.

The proper motion and the radial velocity combined give the three dimensional space velocity of M33. The total velocity is 157±49 km s^{-1}relative to the Milky Way and shown in Figure 5.55.

5.6.6 Motion relative to M31

As described in section 4.5.4, M31 is moving with a velocity of 125±15 km s^{-1} towards the Sun if we assume a zero tangential motion. Then, the motion of M33 relative to M31 is directed almost completely towards M31, if the distances to M31 and M33 are correct and M31 has a negligible tangential velocity and one can conclude that M33 is on a highly eccentric orbit around M31. Gottesman, Hunter, & Boonyasait (2002) consider the effects of dynamical friction of M31 on IC 10 and M33. They conclude that M31 cannot have a very massive halo unless the orbits of IC 10 and M33 have low eccentricity. Otherwise, this friction would have lead to

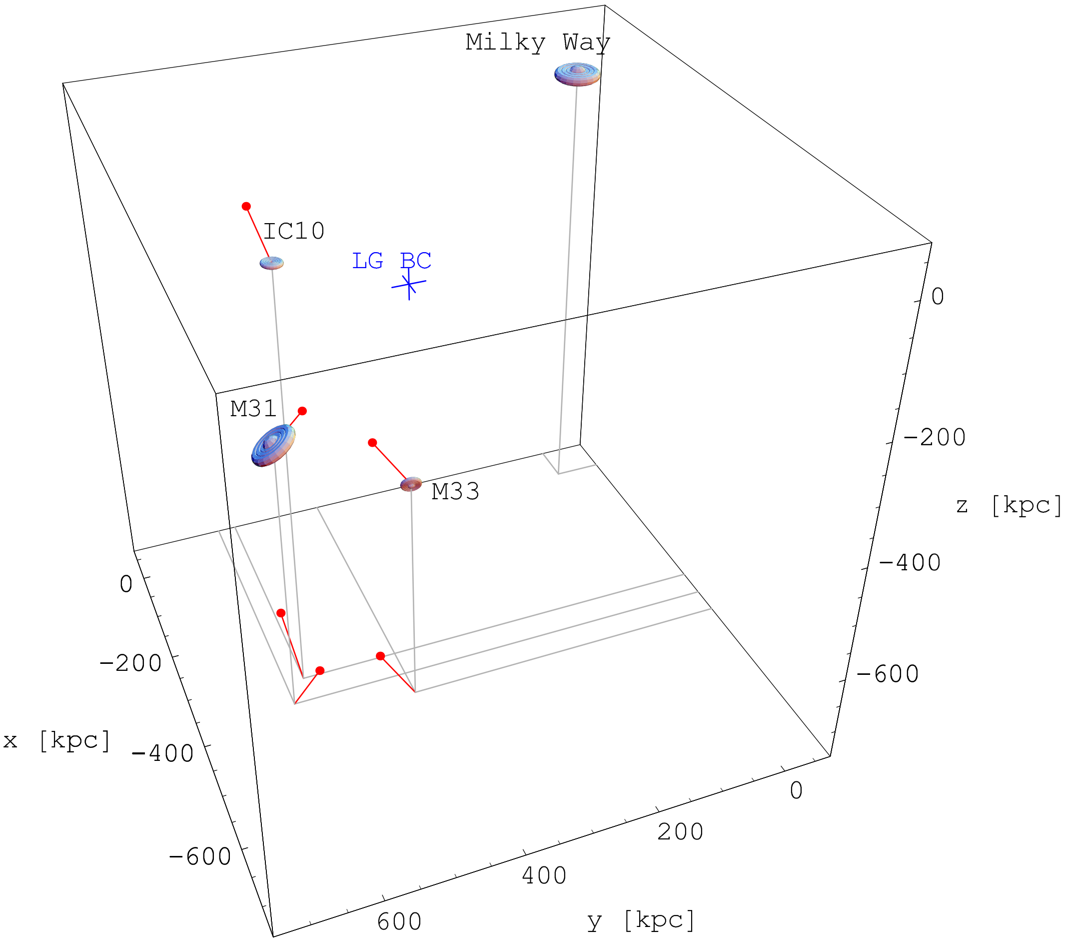

FIGURE 5.55— Schematic view of the Local Group of Galaxies. The Sun is located at (0,0,0), the Galactic Center at (8,0,0). Plotted are also the velocities of IC 10, M33 and M31 and the position of the Local Group barycenter (LGBC), taken from van den Bergh (1999).

a decay of M33s orbit over a Hubble time, which is obviously not the case. If this is correct, then the high eccentricity of the orbit of M33 would lead to the conclusion that the total mass of M31 cannot be much larger than $\approx 10^{12}$ M$_\odot$. This is in good agreement with Evans & Wilkinson (2000) and Evans et al. (2003), but lower than our estimate from IC 10. However, as pointed out earlier, this estimate was based on the assumption that IC 10 is on a circular orbit about M31 and not a free-floating member of the Local Group.

6

III Zw 2

In the previous chapters, the phase-referencing technique was used to estimate accurate relative positions of radio sources on the sky. Although this technique is very powerful, it has two disadvantages:

- Reference and target source have different line of sights through the atmosphere
- More than 50 % of the observing time is lost for the calibrator and source changes.

However, if one can use a calibrator which is close enough to the target source and in the primary beam of the telescopes, one can observe both sources through the same line of sight and does not have to move the antennas. This *in-beam* astrometry can be used to measure motions of components in jets of Active Galactic Nuclei (AGN) with high accuracy.

In this chapter we will discuss high resolution VLBI observations of the Seyfert I galaxy III Zw 2. Some results of this were published in Brunthaler et al. (2000) and Brunthaler et al. (2003).

6.1 Introduction

The radio properties of quasars with otherwise very similar optical properties can be markedly different. There is a clear dichotomy between radio-loud and radio-quiet quasars in optically selected samples. The radio-loudness is usually characterized by the radio-to-optical flux ratio. In the PG quasar sample, which is probably the best studied quasar sample in the radio and optical (Kellermann et al. 1989; Boroson & Green 1992), radio-loud and radio-weak quasars separate cleanly in two distinct populations (e.g. Kellermann et al. 1989).

It is known that radio-loud AGN almost never reside in late type, i.e. spiral galaxies (e.g. Kirhakos et al. 1999; Bahcall, Kirhakos, & Schneider 1995) whereas radio-quiet quasars appear both in spiral and in elliptical host galaxies. Furthermore, all relativistically boosted jets with superluminal motion and typical blazars have been detected in early type galaxies (e.g. Scarpa et al. 2000). It is still unclear, why AGN in spiral galaxies, at the same optical luminosity as their elliptical counterparts, should not be able to produce the powerful, relativistic jets seen in radio galaxies.

However, a few sources with intermediate radio-to-optical ratios appear to be neither radio-loud nor radio-quiet. They form a distinct subclass with very similar radio morphological and spectral properties. They all have a compact core at VLA scales and a flat and variable spectrum in common. These properties are very similar to the ones of radio cores in radio-loud quasars, but their low radio-to-optical ratio and their low extended steep-spectrum emission is atypical for radio-loud quasars. Miller, Rawlings, & Saunders (1993), Falcke, Malkan, & Biermann (1995), Falcke, Patnaik, & Sherwood (1996), and Falcke, Sherwood, & Patnaik (1996)) have identified a number of these sources, called “radio-intermediate quasars” (RIQs), and suggested that they might be relativistically boosted radio-weak quasars or “radio-weak blazars”.

This would imply that most, if not all, radio-quiet quasars also have relativistic jets. In fact, VLBI observations of radio-quiet quasars already have shown high-brightness temperature radio cores and jets (Blundell & Beasley 1998). A crucial test of the relativistic jet hypothesis is the search for apparent superluminal motion in these sources. A prime candidate for detecting this is the brightest radio source in the RIQ sample, III Zw 2, which we discuss in this chapter.

III Zw 2 (PG 0007+106, Mrk 1501, $z = 0.089$) was discovered by Zwicky (1967), classified as a Seyfert I galaxy (e.g., Arp 1968; Khachikian & Weedman 1974; Osterbrock 1977), and later also included in the PG quasar sample (Schmidt & Green 1983). The host galaxy was classified as a spiral (e.g. Hutchings & Campbell 1983) and a disk model was later confirmed by fitting of model isophotes to near-IR images (Taylor et al. 1996). A spiral arm was claimed (Hutchings 1983) but recent observations suggest a tidal arm with several knots of star forming regions (Surace, Sanders, & Evans 2001). III Zw 2 is the brightest member of a group of galaxies and an extended low surface brightness emission surrounding all the galaxies suggests that there are perhaps interactions between the galaxies (Surace, Sanders, & Evans 2001).

The source has shown extreme variability at radio wavelengths with at least 20-fold increases in radio flux density within 4 years (Aller et al. 1985). III Zw 2 is also known to be variable in the optical (Lloyd 1984; Clements et al. 1995) and X-ray (Kaastra & de Korte 1988).

III Zw 2 is a core-dominated flat-spectrum AGN with only a faint extended structure (see Unger et al. 1987 and Section 6.3.1). The weak extended radio emission and the host galaxy is quite typical for a Seyfert galaxy. Its [OIII] luminosity is a mere factor three brighter than that of a bright Seyfert galaxy like Mrk 3 (e.g. Alonso-Herrero, Ward, & Kotilainen 1997) which explains why it has been classified as either a Seyfert galaxy or a quasar. In this luminosity region a distinction between the two may not be of much significance.

TABLE 6.1— Total observing time t_{obs}, fraction of observing time on III Zw 2 at 43 GHz f_{43} and 15 GHz f_{15} and fraction of observing time on phase-reference quasar f_{quasar} for the VLBA observations.

Epoch	t_{obs}	f_{43}	f_{15}	f_{quasar}
1998.13	8 h	0.75	0.25	–
1998.45	9 h	0.75	0.25	–
1998.70	8 h	0.75	0.25	–
1998.94	8 h	0.75	0.25	–
1999.53	6 h	0.75	0.25	–
1999.86	8 h	0.33	0.33	0.33
2000.55	6 h	0.33	0.33	0.33
2000.65	8 h	0.33	0.33	0.33
2000.68	8 h	0.33	0.33	0.33

Earlier VLBI observations of the source have only shown a high-brightness temperature core (Falcke, Sherwood, & Patnaik 1996, Kellermann et al. 1998) and recent Millimeter-VLBI observations by Falcke et al. (1999) just barely resolved the source into two very compact components. A broadband radio spectrum was well explained by Synchrotron Self-Absorption.

The unique and simple structure and timescales of such outbursts within 5 years makes III Zw 2 and ideal source to study radio-jet evolution relevant also to radio galaxies.

6.2 Observations

In 1997 III Zw 2 started a new major radio outburst and we initiated a target of opportunity program to monitor the spectral evolution of the burst with the VLA and its structural evolution with the VLBA with excellent relative astrometry of the component separation.

We observed III Zw 2 with the VLA 41 times from 1998 September until September 2001 in intervals of roughly one month. The observations were made at six frequencies ranging from 1.4 GHz to 43 GHz. Results from an observation on 1998 May 21 at 350 MHz and on 1999 July 7 at 327.5 MHz are also presented here. The source 3C48 was used as the primary flux density calibrator, and III Zw 2 was self-calibrated and mapped with the Astronomical Image Processing System (AIPS).

We also used the monitoring data at 8 and 15 GHz obtained with the Michigan 26 m telescope, and at 22 and 37 GHz from the Metsähovi radio telescope. These long term radio light curves combined with our VLA monitoring are shown in Fig. 6.4.

We observed III Zw 2 with the VLBA nine times over a period of 2.5 years at 15 and 43 GHz. Details of this observations are given in Table 6.1. In the last four epochs we included the background quasar J0011+0823 at 15 GHz as phase-reference source. For the second epoch, we used the Effelsberg 100 m telescope in combination with the VLBA. We observed four 8 MHz bands, each at right and left circular polarization. The initial calibration was performed with the AIPS package. A priori amplitude calibration was applied using system temperature measurements and standard gain curves. Fringes were found in the III Zw 2 data on all baselines. The data were self-calibrated and mapped using the software package DIFMAP (Shepherd, Pearson, & Taylor 1994). We started with phase-only self-calibration and later included phase-amplitude self-calibration with solution intervals slowly decreasing down to one minute.

6.3 Results

6.3.1 Extended emission of III Zw 2

Unger et al. (1987) discovered a weak component 15.4″ (23 kpc, with an angular size distance of $d_A \sim 307.4$ Mpc; $H_0 = 75\ km\ sec^{-1}\ Mpc^{-1}$, $q_0 = 0.5$ as used in this chapter) southwest of the nucleus. This detection was confirmed later (Kukula et al. 1998; Falcke et al. 1999), but no additional extended emission was found.

To study the extended structure in more detail, we combined the raw data of eleven VLA observations. In the combined data we used data from the VLA in A, B, C and D configuration. Since the nucleus is highly variable, we subtracted it from the uv-data before combining the data. The combined data set was then self-calibrated and mapped. The combined VLA maps at 1.4, 4.8, 8.4 and 15 GHz are shown in Fig. 6.1 and 6.2. The 4.8, 8.4 and 15 GHz maps were convolved with a large beam of 5.98×5.47 arcseconds to detect faint extended structure. We detected the southwestern component at all four frequencies. This radio lobe or hotspot is connected to the nucleus with a jet-like structure visible at 1.4, 4.8 and 8.4 GHz. At 1.4 GHz one sees an indication that the jet is ejected in northwestern direction and gets deflected by almost 90° towards the southwestern lobe. This is also in accordance with the direction of the jet on sub-parsec scales (see section 6.3.4).

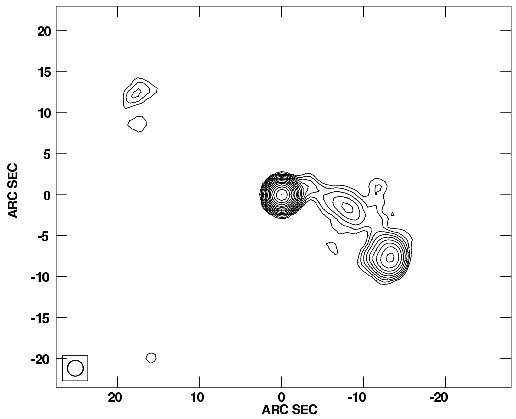

FIGURE 6.1— Combined VLA map of 11 epochs (A,B,C and D-array) of III Zw 2 at 1.4 GHz.

We also discovered a weaker secondary radio lobe 21.9″ (32.6 kpc) on the opposite side of the galaxy at 1.4 to 8.4 GHz. If one assumes equal expansion velocities for both lobes, a simple time travel argument (e.g., Ryle & Longair 1967) would suggest that the weaker northeastern lobe is approaching and the brighter southwestern lobe is receding. However, this scenario can not explain the differences in flux density between the two lobes. One would expect the approaching lobe to be brighter due to relativistic boosting of the emission.

Hence it is more likely that the armlength difference is explained by an asymmetric expansion of the the two lobes due to different intrinsic velocities or differences in the ambi-

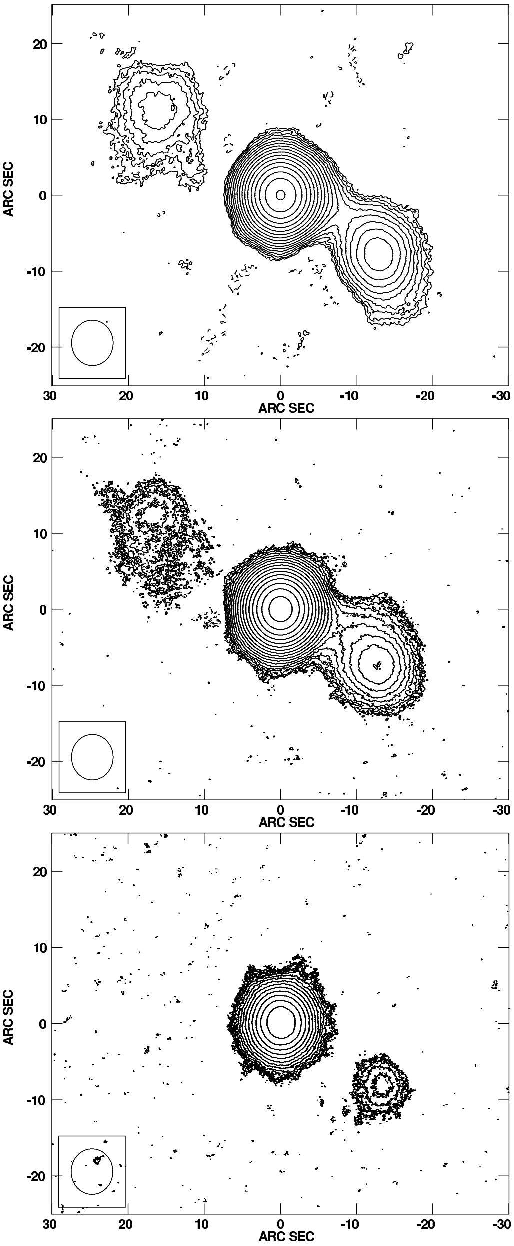

FIGURE 6.2— Combined VLA map of 11 epochs (A,B,C and D-array) of III Zw 2 at 4.8 GHz (top), 8.4 GHz (middle) and 15 GHz (bottom). All maps were convolved with a large beam to detect faint extended emission.

ent medium, i.e. the medium in the southwest of III Zw 2 has a higher density than the medium in the northeast. This is supported by the fact that there is a close companion galaxy only $\sim 30''$ to the south.

The spectra of the two radio lobes are shown in Fig 6.3. The 350 and 327.5 MHz data were from our observations on 1998 May 21 and 1999 July 7 respectively where we also detected the southwestern component. Both radio lobes have a steep spectrum with spectral indices of $\alpha = -0.57$ to -1.15 which are typical for synchrotron emission of optically thin radio lobes of radio galaxies. There is no break or a steepening of the spectrum towards higher frequencies. This indicates that both radio lobes are still active and powered by the central engine. Otherwise, the high energy electrons would have lost most of their energy due to radiation losses. This would lead to a steepening in the spectrum at higher frequencies.

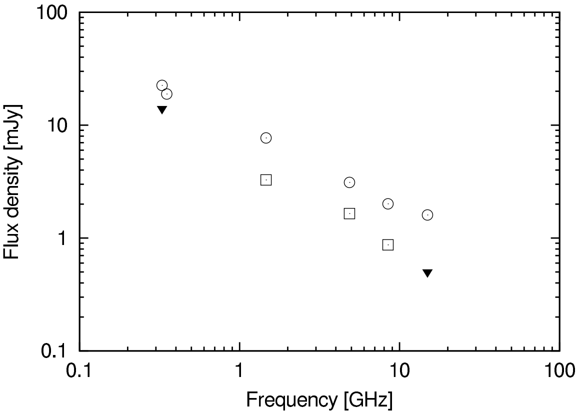

FIGURE 6.3— Spectra of the southwestern (circles) and northeastern (squares) radio lobes. The black triangles are upper limits for the northeastern lobe.

6.3.2 Variability

The core of III Zw 2 shows extreme variability at radio wavelengths. Long time radio light curves of this source spanning more than 20 years are shown in Fig. 6.4 using data from Michigan, Metsähovi and the VLA. One can see major flares with 30-fold increases in radio flux density within two years. These flares occur roughly every five years.

The outburst discussed in this chapter started in 1997 and we monitored this flare with the VLA. The good time sampling of one observation each month allowed us to study this outburst in great detail. Lightcurves at six frequencies from 1.4 to 43 GHz are shown in Fig. 6.5 and 6.6 together with our best model fits to the data. Since the Michigan

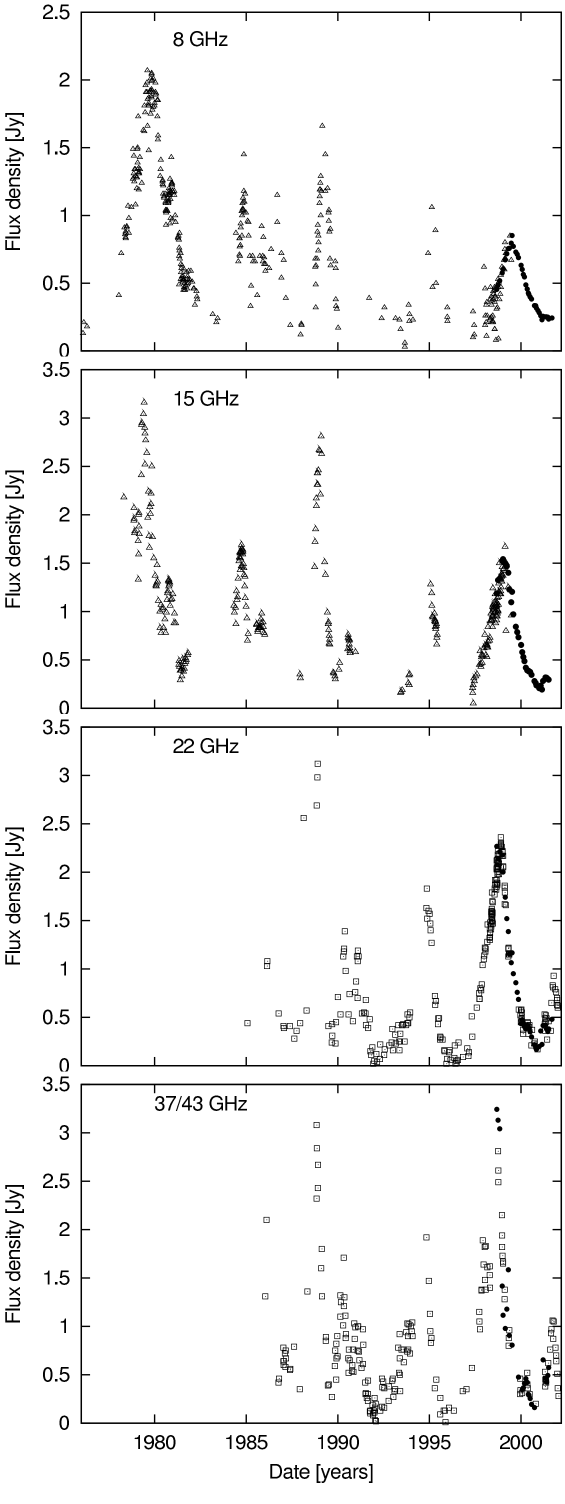

FIGURE 6.4— Radio light curves of III Zw 2. The triangles at 8 and 15 GHz are from the Michigan monitoring program, the squares at 22 and 37 GHz are from the Metsähovi monitoring program. The circles are our VLA observations at 8, 15, 22 and 43 GHz.

data is very noisy at 8.4 GHz, we used only our VLA monitoring data for the fits at this frequency. At 15, 22 and 37 GHz we used the VLA data as well as the Michigan and Metsähovi data.

First we fitted a linear increase and decrease to the flare. The increase is consistent with a linear fit at all frequencies. The decrease is also linear at 4.8 GHz. At higher frequencies, the decrease is linear only for a short time period and deviates significant from a linear behavior at later times. Thus we used only the linear part of the lightcurves for our fits.

The decay at higher frequencies can be fitted much better with an exponential decay. Thus we fitted also an exponential rise and decay,

$$S(t) = S_0 e^{(t_0 - t)/\tau_r}, \tag{6.1}$$

$$S(t) = S_0 e^{(t_0 - t)/\tau_d}, \tag{6.2}$$

to the lightcurves. The fitting parameters are S_0, the maximum amplitude of the flare and the flare rise and decay timescales τ_r and τ_d. The epochs of the flare maximum t_0 were taken from the observation with the highest flux density. The rise of the lightcurves can also be fitted by an exponential rise and the exponential decay fits the outburst until a new smaller flare starts.

The slopes of the linear rise (a_r) and decrease (a_d), the exponential rise and decay timescales τ_r and τ_d and the epoch of the flare maximum t_0 are listed in Table 6.2 for all six frequencies.

The lightcurve reaches its peak first at higher frequencies. The time-lag between the peak at 43 GHz and the peak at lower frequencies is shown in Figure 6.7 and is best fit with a $\delta t \propto \nu^{-1.1}$ power law. The increase and decrease are faster at high frequencies than at low frequencies. This behavior is typical for flares in AGN (e.g. Türler, Courvoisier, & Paltani 1999).

At 4.8 GHz the increase is slower than the decrease, while at 15, 22 and 43 GHz the increase is slower than the decrease. This is the case for the linear and the exponential fits to the flare. At 8.4 GHz the linear rise is slightly

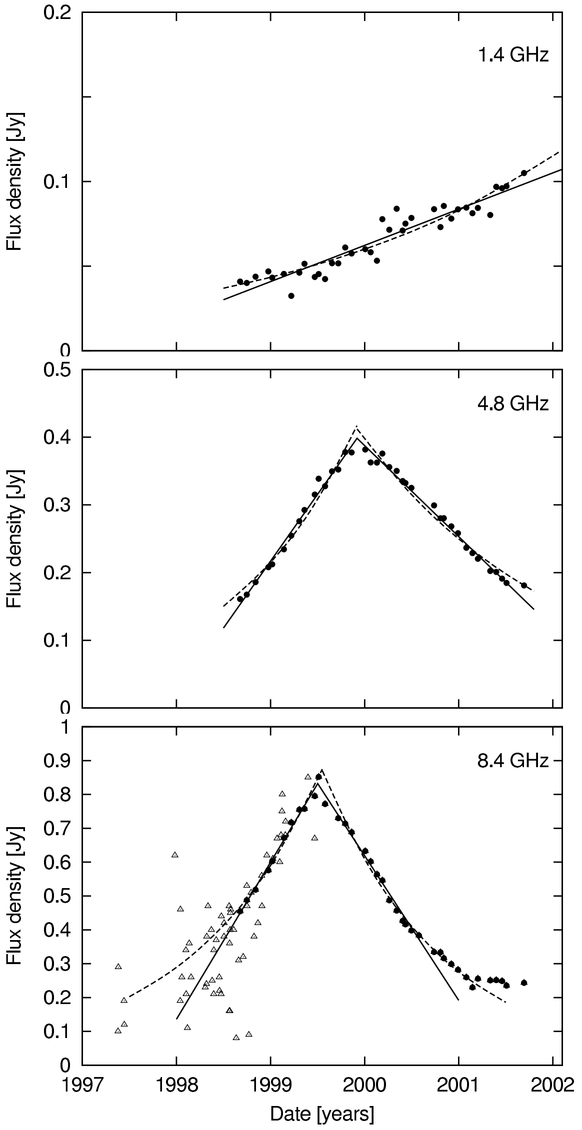

FIGURE 6.5— Radio light curves of the recent flare in III Zw 2 at 1.4, 4.8 and 8.4 GHz. The circles are our VLA observations, and the triangles are from the Michigan monitoring program. The solid lines are our linear rise and decline fits. The dashed lines are the fitted exponential rise and decay.

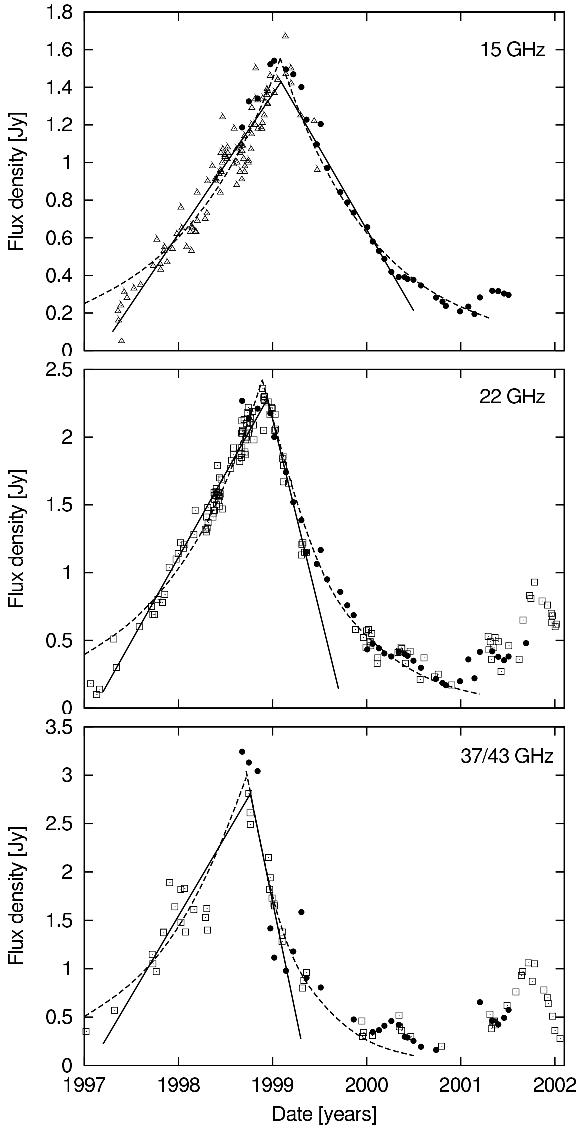

FIGURE 6.6— Radio light curves of the recent flare in III Zw 2 at 15, 22 and 37/43 GHz. The circles are our VLA observations, and the triangles are from the Michigan monitoring program and the squares are from the Metsähovi monitoring program. The solid lines are our linear rise and decline fits. The dashed lines are the fitted exponential rise and decay.

slower than the linear decay while the exponential rise slightly faster than the exponential decay is. The rise and decay timescales as a function of frequency are plotted in Figure 6.8. The data can be fitted with power laws $\tau_r \propto \nu^{-0.2}$ and $\tau_d \propto \nu^{-0.7}$. Only the rise timescale at 1.4 GHz deviates from this power law. However, the quiescence flux at 1.4 GHz is comparable to the flux density of the outburst and will affect this data point.

The small dependancy of the rise timescale on frequency indicates that optical depth effects are not very imprtant during the rise. This is in contrast to the decay, where optical depth effects are clearly important.

Valtaoja et al. (1999) modeled the radio lightcurves of flares at 22 and 37 GHz in 85 extragalactic radio sources. They fitted an exponential curve to the rise and the decay and

TABLE 6.2— Fitting information: The slopes of the linear rise (a_r) and decrease (a_d), the exponential rise and decay timescales τ_r and τ_d and the epoch of the flare maximum t_0.

ν_{obs}	a_r	a_d	τ_r	τ_d	t_0
1.4 GHz	0.02	-	3.09	-	>2002
4.8 GHz	0.20	-0.14	1.39	2.16	2000.1
8.4 GHz	0.46	-0.43	1.40	1.26	1999.5
15 GHz	0.74	-0.86	1.14	1.01	1999.1
22 GHz	1.24	-2.85	1.04	0.73	1998.9
43 GHz	1.65	-4.73	0.96	0.53	1998.7

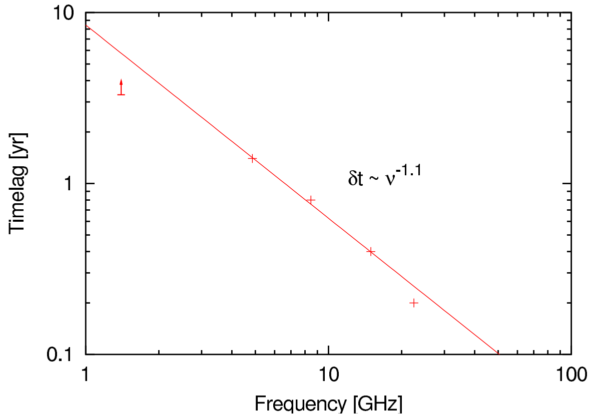

FIGURE 6.7— Time-lag between the peak at 43 GHz and the peak at the other frequencies. The data point at 1.4 GHz is a lower limit.

found that in virtually all flares a good model-fit could be obtained using a constant ratio between decay and rise timescale of $\tau_d = 1.3\tau_r$, i.e. the rise is faster than the decay. These flares can be identified with the ejection of new VLBI components in the jets.

The fact that the lightcurves of III Zw 2 at 15, 22 and 43 GHz show the opposite behavior with ratios of $\tau_d/\tau_r \approx 0.6 - 0.9$, i.e. the decay is faster than the rise, indicates that different physical processes are involved in this source.

6.3.3 Spectral evolution

During the outburst the spectrum of the source also showed variations. An almost simultaneous broadband radio spectrum from 1.4 to 660 GHz during the rise in flux density in May 1998 was presented in Falcke et al. (1999). The spectrum was highly inverted at centimeter wavelengths with a turnover frequency around 43 GHz. At frequencies above 43 GHz the spectrum became steep with a spectral index of $\alpha = -0.75 \pm 0.15$, i.e. a textbook-like synchrotron spectrum.

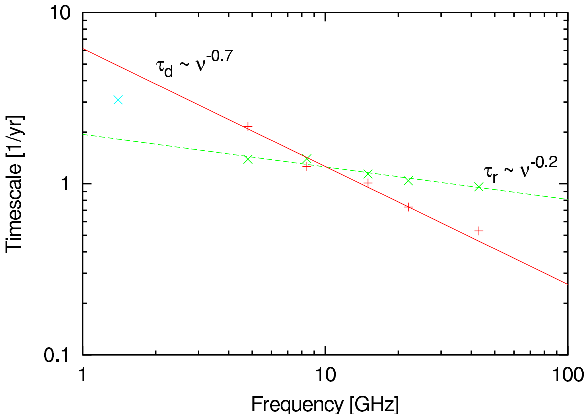

FIGURE 6.8— Rise (x) and decay (+) timescales for all frequencies.

Our VLA monitoring of the spectral evolution started in September 1998. Four of the 41 epochs yielded no or bad data due to bad weather or hardware failure. We fitted the remaining spectra with a broken power-law plus a flat and constant quiescence spectrum o,

$$S(\nu) = S_0 \left(\frac{\nu}{\nu_0}\right)^k \left(1 - e^{-\left(\frac{\nu}{\nu_0}\right)^{l-k}}\right) + o, \quad (6.3)$$

where k and l are the spectral indices of the rising and declining parts of the spectrum. S_0 and ν_0 are fitting parameters and are not exactly equal to the maximum flux density and the peak frequency of the fitted spectrum.

We assume a flat spectrum for the quiescence flux which is typical for quiescent cores in active galactic nuclei. Since we could fit all epochs with a value of 25 mJy, we adopted this value for all epochs.

The approach with a broken power-law has the disadvantage, that there are ambiguities in the parameters if the peak of the spectrum falls beyond the frequencies covered in the observations.

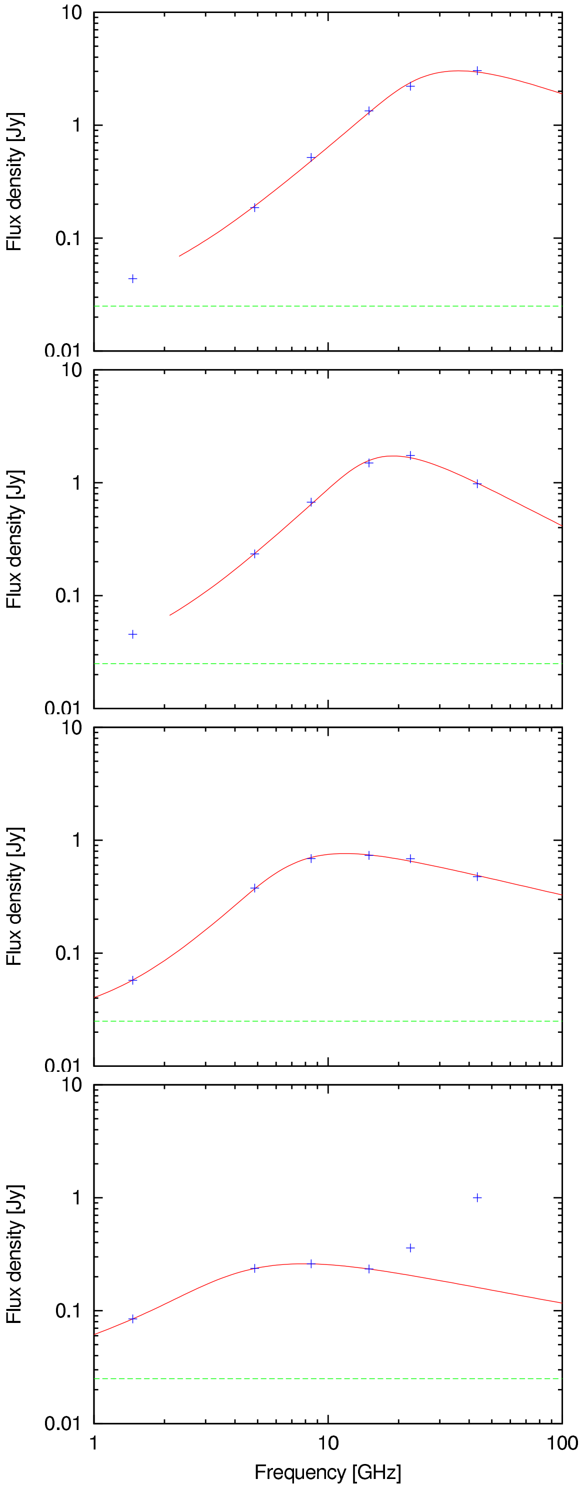

FIGURE 6.9— VLA spectra of III Zw 2 on 1998 November 04, 1999 February 22, 1999 November 12 and 2001 January 30 (from top to bottom).

This situation was the case in our first three observations in September 1998, October 1998 and November 1998. The spectral shape in these three epochs was very similar to the May 1998 spectrum. Highly inverted at centimeter wavelengths, a flattening towards higher frequencies, and possibly a turnover around 43 GHz, but with higher flux densities (see Fig. 6.9, top). Thus we assumed the spectral index of the declining part of the spectrum to be $l = -0.75$, the value of the May 1998 observation. This is a reasonable assumption since the overall spectral shape did not change significantly between May 1998 and September 1998.

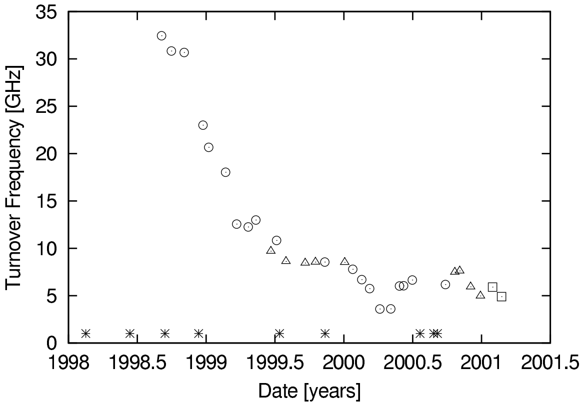

FIGURE 6.10— Evolution of the "turnover frequency" ν_0. The circles mark epochs with 6 observed frequencies (1.4-43 GHz) and the triangles epochs with 5 observed frequencies (1.4-22 GHz). In the last two epochs only 4 frequencies (1.4-15 GHz) were used because of a new outburst at high frequencies. The asterisks mark the epochs of our VLBA observations.

The temporal evolution of the fitting parameters ν_0, k and l can be seen in Fig. 6.10 and Fig 6.11. In some epochs we covered only 5 frequencies from 1.4 to 22 GHz. The absence of the 43 GHz flux density in these epochs could bias the results of the spectral fitting. Thus we marked the epochs with only 5 frequencies in Fig. 6.10 with triangles while the epochs with 6 frequencies are indicated by circles. One can see that the fits of both subsets are in good agreement.

After November 1998 the spectrum underwent a dramatic change (see also Figures B.1 – B.10). The turnover frequency ν_0 dropped from 31 GHz in November 1998 to 23 GHz in December 1998. In the following months, the turnover drops further until it reached 10

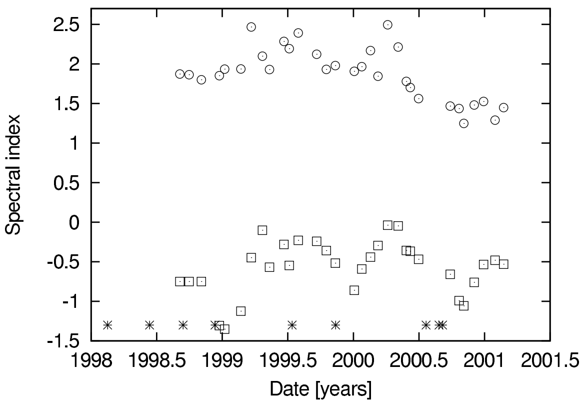

FIGURE 6.11— Evolution of the spectral indices k (circles) and l (squares). The asterisks mark the epochs of our VLBA observations.

GHz in June 1999. During the next year the turnover frequency showed only smaller and slower variations and stayed roughly constant at $\sim$ 7 GHz. The drop in turnover frequency to 4 GHz in the first months of 2000 can be explained by the onset of a new minor flare at high frequencies (see 43 GHz lightcurve in Fig. 6.6). The new flare caused a flattening of the optical thin part of the spectrum and a shift of the turnover to lower frequencies. The flattening can also be seen in Fig. 6.11 where the spectral index l changes from ~ -0.9 to ~ -0.1 during that time.

The spectral index in the optical thick part of the spectrum k stays at $\sim$ 2 and slowly flattens towards later times.

A new strong outburst started at high frequencies in January 2001 (see 22 and 43 GHz lightcurves in Fig. 6.6) and one would have to model two independent broken power-laws to the spectrum. Since one broken power-law is characterized by four parameters S_0, ν_0, k and l, our six data points in each spectrum are not sufficient to model two independent components with four parameters each. In the first two epochs of the new flare, only the 22 and 43 GHz data were affected and we fitted the broken power-law to the remaining four frequencies.

The fast change in peak frequency implies also a strong morphological change, i.e. a rapid expansion. This prediction was tested by VLBI observations which are described in the next section.

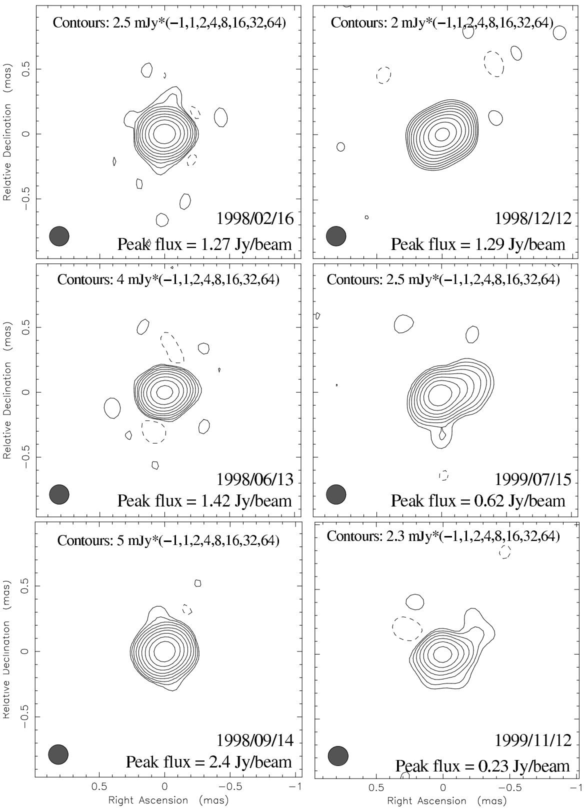

FIGURE 6.12— All six VLBA maps of III Zw 2 at 43 GHz convolved with a super-resolved circular beam of 150 μas.

6.3.4 Structural evolution

43 GHz Results

The first three VLBA observations were made during the first phase of the flare, marked by the increase in flux density and a roughly constant spectral peak above 30 GHz. The constancy of the peak frequency indicates no structural change, since the turnover is caused by synchrotron self-absorption (Falcke et al. 1999). The source is slightly resolved and the long baselines show non-zero closure phases, indicating an asymmetric structure. Two point-like components were fitted to the uv-data to represent the extent of the source. The source shows no structural change (see Fig. 6.12) and the separation of the two components during this phase of the flare stayed constant at $\sim$ 76 μas, corresponding to $\sim$ 0.11 pc. The excellent agreement within 2 μas

TABLE 6.3— Flux densities S of all, separation D and position angle P.A. of the two outermost point-like components of our model-fits to the 43 GHz uv-data.

Date	S_1 [Jy]	S_2 [Jy]	S_3 [Jy]	d [mas]	P.A.
1998.13	0.93	0.58	–	0.075	−84°
1998.45	1.03	0.65	–	0.077	−78°
1998.70	1.60	1.27	–	0.077	−72°
1998.94	0.86	0.86	–	0.106	−63°
1999.53	0.56	0.26	0.08	0.245	−71°
1999.86	0.08	0.23	0.05	0.246	−73°

TABLE 6.4— Flux densities S, separation D and position angle P.A. of the two point-like components of our model-fits to the 15 GHz uv-data.

Date	S_1 [Jy]	S_2 [Jy]	d [mas]	P.A.
1998.13	0.32	0.40	0.085	−54°
1998.45	0.45	0.48	0.114	−79°
1998.70	0.67	0.50	0.121	−70°
1998.94	0.79	0.69	0.145	−59°
1999.53	0.50	0.46	0.142	−87°
1999.86	0.43	0.25	0.195	−68°
2000.55	0.22	0.10	0.222	−61°
2000.65	0.19	0.08	0.220	−68°
2000.68	0.18	0.07	0.229	−63°

between the first three epochs shows the high quality of the data and the accuracy of the relative astrometry.

After 1998 November, the VLA monitoring shows a dramatic change in the spectrum. The peak frequency dropped quickly to 10 GHz within a few month (Fig. 6.10). In the framework of a simple equipartition jet model with a $R \propto \nu_{\rm ssa}^{-1}$ dependence (e.g., Blandford & Konigl 1979; Falcke & Biermann 1995) one would expect a rapid expansion. With a source size of 0.11 pc and a turnover frequency of 33 GHz in the first phase with no expansion one expects a source size of 0.36 pc for a self-absorption frequency of 10 GHz according to the spectral evolution.

Indeed, the fourth VLBA epoch, observed only one month after the start of the spectral evolution, shows first signs of an expansion. The fifth epoch shows a dramatic structural change (see Fig. 6.12) and a model of three point-like components is required to describe the data now. The separation between the outer components is now $\sim$ 245 μas corresponding to $\sim$ 0.37 pc. This is in good agreement with the expected value of 0.36 pc from an equipartition jet model. The structure in the sixth epoch is very similar to the fifth epoch but with lower flux density. This is again expected, since the turnover frequency stayed around 10 GHz.

The separation of the outer components for all six epochs is plotted in Fig. 6.13 (upper panel). For the first three epochs we measure an upper limit for the expansion speed of 0.04 *c*. The rapid expansion between the fourth and fifth epoch shows an apparent speed of 1.25 *c*. Between the last two epoch we detected again no expansion with an upper limit of 0.04 *c*.

Unfortunately the source was to weak at 43 GHz to be detected at the last three epochs.

15 GHz Results

At 15 GHz the picture looks completely different. The source is very compact but slightly resolved in all epochs except the first and we fitted two point-like components to the uv-data. The flux densities, separations and position angles of the two components are listed in Table 6.4. The component separation of all epochs is also plotted in Fig. 6.13. One can see a constant expansion with an apparent expansion speed of $\sim$ 0.6 *c*. Simple extrapolation backwards suggests that the expansion has started in May 1996. This is consistent with the start of the new flare in the 37 GHz lightcurve in Fig. 6.4.

One should note that the component separation of the fifth epoch shows a deviation from a constant expansion. If one splits up the separation into its north-south and east-west components (see Fig. 6.14) one can see that the scatter is larger in the north-south direction. This is expected, since the beam of

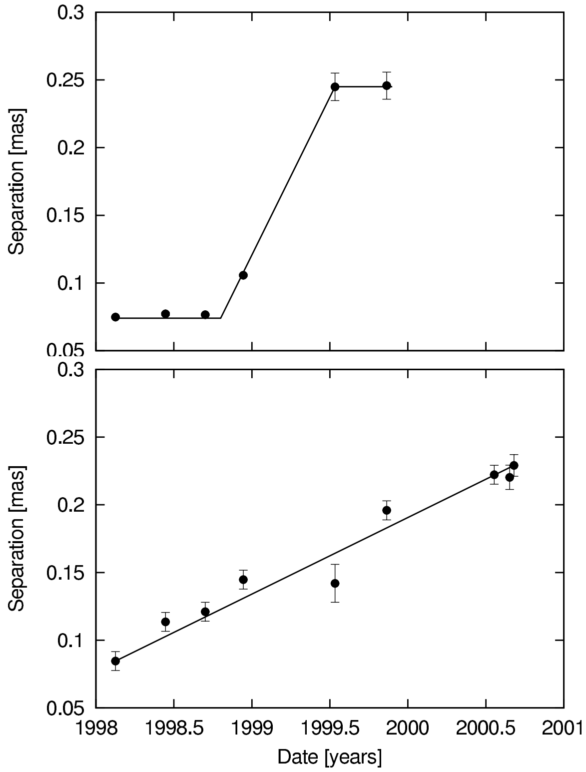

FIGURE 6.13— Component separation at 43 (upper) and 15 (lower) GHz. The apparent expansion speed is 0.6 c at 15 GHz and 1.25 c at 43 GHz.

the VLBA is elongated in the north-south direction. This relatively large scatter in north-south direction also explains the scatter in the positions angles in Table. 6.4.

Fig. 6.14 shows also that the error in the fifth epoch arises only from the large deviation in the north-south direction. The beam-size in north-south direction was significantly larger in the fifth epoch (~1.3 mas) than in the other observations (~ 0.9 mas).

In the last four observations we used the phase-referencing technique at 15 GHz to get a proper alignment of the epochs and to distinguish between moving and stationary components (i.e. jet components and the core). Unfortunately, no good maps could be obtained using phase-referencing. Hence one had to self-calibrate on III Zw 2 and the absolute position information was lost.

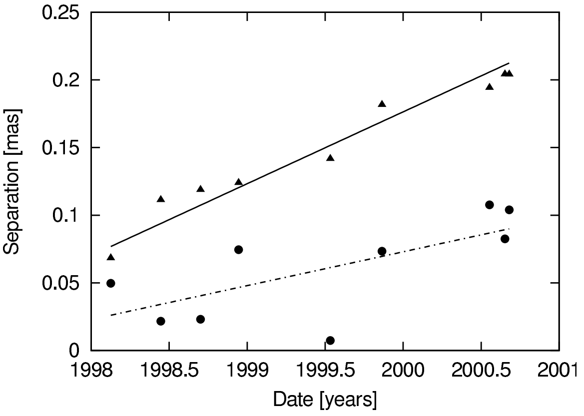

FIGURE 6.14— Component separation at 15 GHz in east-west (triangles) and north-south (circles) direction. The scatter is much smaller in east-west direction due to the smaller beamzise of the VLBA in east-west direction.

6.4 Discussion

The stop-and-go behavior and the apparent contradiction between the 43 GHz and 15 GHz data can be explained by a jet interacting with the interstellar medium in combination with optical depth effects in an 'inflating-balloon model'.

In this model, the initial phase of the flare can be explained by a relativistic jet interacting with the interstellar medium or a torus that creates a shock and gets frustrated. A relativistic shock was proposed by Falcke et al. (1999) due to synchrotron cooling times of 14-50 days which are much shorter than the duration of the outburst. The ultra-compact hotspots are pumped up, powered by the jet and responsible for the increase in flux density. The post-shock material expands with the maximum sound speed of a magnetized relativistic plasma of $c_s \approx 0.6$ c.

Since the source is optically thick at 15 GHz, one observes the outside of the source, i.e. the post-shock material expanding with sound speed. At 43 GHz, the source is optically thin and one can look inside the source and see the stationary hotspots.

The rapid expansion at 43 GHz thereafter has marked the phase where the jet breaks free and starts to propagate relativistically into a lower-density medium. Then the expansion stops again when the jet hits another cloud.

The fact that spectral and structural evolution during the outburst are closely linked demonstrates that we are dealing with a real physical expansion and not only a phase velocity. The observations described here produced a large amount of data that are all consistent with a simple Synchrotron Self-Absorbed jet model.

For the question of the nature of the radio-loud/radio-quiet dichotomy this means that radio-weak and radio-loud quasars can indeed have central engines that are in many respects very similar. Their optical properties are almost indistinguishable and both types of quasars can produce relativistic jets in their nuclei. The finding of superluminal motion supports the hypothesis of Miller, Rawlings, & Saunders (1993) and Falcke, Patnaik, & Sherwood (1996) that RIQs are relativistically boosted intrinsically radio-weak AGN. Recently, a further relativistic jet in a radio-quiet quasar was found by Blundell, Beasley, & Bicknell (2003).

However, the nature of the medium interacting with the jet remains unclear. The quasi-periodic outbursts could be explained by a precessing jet that hits a molecular torus roughly every five years. So far, no direct evidence for molecular gas in the nucleus of III Zw 2 was found.

Some Seyfert galaxies have shown H_2O maser emission associated with the nuclear jet. In these sources, the maser emission is the result from an interaction of the jet with a molecular cloud. One example is the Seyfert II galaxy Mrk 348 (see Peck et al. 2003). In this source, the ejection of a new VLBI component has lead to a flare of the radio source similar to the outburst in III Zw 2. The outburst started with a peak frequency of $\approx$ 22 GHz which gradually decreased over 20 months. During this outburst, H_2O maser emission was found. Searches for similar water maser emission in III Zw 2 with the Effelsberg 100-m telescope yielded no detection (Henkel, private communication).

Salvi et al. (2002) compare the long term radio light curves of III Zw 2 with optical, IR and X-ray light curves and find indications for correlated flux variations from radio to X-ray wavelengths. Unfortunately, the time sampling at other wavelengths than radio is very poor.

III Zw 2 remains an extremely unusual object. Future simultaneous multi-frequency observations of new outbursts would help to confirm the proposed scenario of a jet-ISM interaction.

7

Circular Polarization in M81

During some of the VLA observations of III Zw 2, the sources Mrk 348 and M81 were also observed. The results on Mrk 348 were published in Peck et al. (2003). This chapter will discuss the detection of circular polarized emission from the central radio source in the galaxy M81. This work has been published in Brunthaler et al. (2001).

7.1 Introduction

The nearby spiral galaxy M81 (NGC 3031) is very similar to our own Galaxy in many ways. It resembles the Milky Way in type, size and mass. It also contains a radio core, M81*, that is most likely associated with a super-massive black hole.

Previous VLBI (Bietenholz et al. 1996), multi-wavelength (Ho, Filippenko, & Sargent 1996) and sub-mm observations (Reuter & Lesch 1996) have shown that M81* is very similar to Sgr A*, the central radio source in our Galaxy. A comparison of the two radio sources therefore may provide interesting insights in their nature.

Especially for Sgr A* the nature of the radio emission has been debated for quite some time (see Melia & Falcke 2001, for a review). Either an origin in an accretion flow (Melia 1992, Narayan, Yi, & Mahadevan 1995) or in a jet has been proposed (Falcke, Mannheim, & Biermann 1993, Falcke & Markoff 2000). The jet model, within the context of the jet-disk symbiosis, has also been applied to M81* (Falcke 1996) where it can reproduce the radio flux density and the size of the radio core simply by changing the accretion rate. Indeed, Bietenholz, Bartel, & Rupen (2000) have discovered a one-sided, though very compact jet in M81* and they pointed out that in terms of power, jet length, and perhaps accretion rate, M81* is intermediate between radio cores of quasars and Sgr A*.

Recently, Bower, Falcke, & Backer (1999) detected circular polarization in Sgr A* in absence of linear polarization (Bower et al. 1999a & Bower et al. 1999b). This was confirmed by Sault & Macquart (1999). This result is surprising, since linear polarization usually exceeds circular by a large factor in AGN radio jets (Wardle et al. 1998; Rayner, Norris, & Sault 2000). Bower, Falcke, & Backer (1999) proposed that low-energy electrons intrinsic to the source reduce the linear polarization through Faraday de-polarization and convert linear polarization into circular polarization (Pacholczyk 1977; Jones & Odell 1977). This would provide very important information on the matter content of Sgr A*. On the other hand, it cannot be excluded that the accretion region around Sgr A* contributes to the unusual polarization (Bower et al. 1999a, Quataert & Gruzinov 2000). Less likely, but not fully excluded is the possibility that the hyperstrong scattering screen could induce the circular polarization through propagation effects (Macquart & Melrose 2000).

Since M81* is not in the direction of the Galactic Center and is likely to be observed under a very different inclination angle, observations of this closely related source are independent of the details of the geometry of Sgr A*. Here we report the results of circular and linear polarization observations of M81* which indicate that indeed M81* and Sgr A* have similar polarization properties.

7.2 Observations and Results

We observed M81* with the VLA on 2000 April 4 at 8.4 GHz in C configuration; on 2000 September 27 at 4.8 GHz and at 8.4 GHz in D configuration; and on 2000 November 4 at 4.8 GHz in A configuration with a bandwidth of 50 MHz in right circular polarization (RCP) and left circular polarization (LCP). We used 3C 48 as the primary flux density calibrator, J1044+719 as secondary calibrator and J1053+704 as check source. We went through the cycle J1044+719 - M81* - J1053+704 - J1044+719 - M81* - J1053+704 - J1044+719 once for each frequency on 2000 September 27 and twice at 4.8 GHz on 2000 November 4. The observation on 2000 April 4 was part of a polarization survey of 11 low luminosity AGNs of which M81 is the closest (Mellon et al. 2000). Here we went through the cycle J1044+719 - J1053+704 - M81* - J1044+719 five times. A detailed discussion of this survey is given in Bower, Falcke, & Mellon (2002).

Data reduction was performed with AIPS. Absolute flux densities were calibrated with the source 3C 48. Then amplitude and phase self-calibration was performed on J1044+719. This forces J1044+719 to have zero circular polarization. The amplitude calibration solutions were transfered to M81* and J1053+704. Finally each source was phase self-calibrated and imaged in Stokes I and V. Flux densities were determined by fitting a beam-sized Gaussian at the image center.

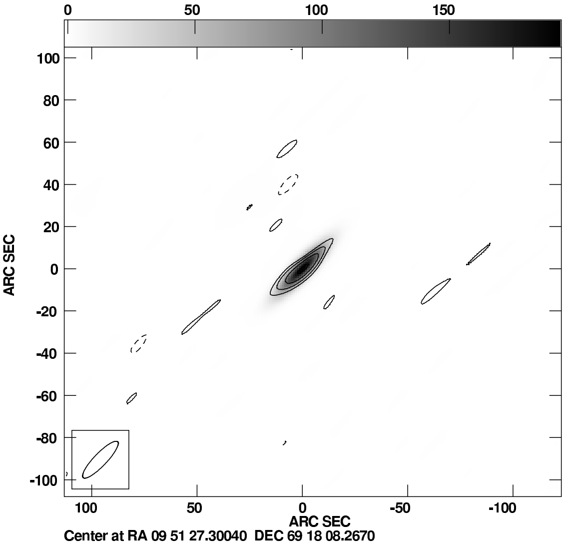

FIGURE 7.1— The Stokes V (contours) and total intensity (grey scale) map for M81 on 2000 September 27 at 8.4 GHz. The rms noise of the Stokes V map is 0.11 mJy beam^{-1}. The contours are 0.3*(-1,1,1.414,2,2.828,4,5.657) mJy and the peak flux density is 0.89 mJy/beam.

The Stokes parameter V is measured as the difference between the left- and right-handed parallel polarization correlated visibilities, LL and RR. Errors in circular polarization measurements with the VLA have numerous origins: thermal noise, gain errors, beam squint, second-order leakage corrections, unknown calibrator polarization, background noise and radio frequency interference. The thermal noise is given by the rms in each map and the values are shown in Table 7.1. The errors caused by amplitude calibration errors, beam squint and polarization leakage scale with the source strength and therefore the fractional circular polarization is a more relevant indicator for the detection of circular polarization. A detailed discussion of these errors is given in Bower, Falcke, & Backer (1999) and Bower et al. (2002). We calculated the systematic errors based on the model for VLA circular polarization from Bower et al. (2002). These values are given in Tables 7.1 and 7.2.

For the observation on 2000 April 4, 3C 48 was used to calibrate the position angle of linear polarization and the sources were also imaged in Stokes U and Q to provide linear polarization information.

The results for M81*, the calibrator J1044+719 and the check-source J1053+704 are given for 4.8 GHz in Table 7.1 and for 8.4 GHz in Table 7.2. The check source J1053+704 showed weak circular polarization at a level of 0.14% on 2000 April 04 at 8.4 GHz. At all other observations, the calibrator source and the check source showed no detectable circular polarization. The upper limits in Table 7.1 and 2 7.2 were determined

TABLE 7.1— Total flux density I, circularly polarized flux density P_c, image rms and fractional circular polarization m_c at 4.8 GHz for the calibrator J 1044+719, M81 and the check source J1053+704 with the statistical and calculated systematic errors.

Source	Date	Int. time	I [mJy]	P_c [mJy]	rms [mJy]	m_c [%]		
J1044+719	2000 Sep. 27	3m20s	1443	< 0.92	0.34	< 0.06	±0.02	-
	2000 Nov. 04	5m17s	1503	< 0.51	0.15	< 0.03	±0.01	-
M81*	2000 Sep. 27	5m03s	193.5	0.53	0.11	0.27	±0.06	±0.07
	2000 Nov. 04	12m08s	160.7	0.41	0.07	0.26	±0.04	±0.06
J1053+704	2000 Sep. 27	1m49s	355.1	< 0.53	0.17	< 0.15	±0.05	±0.07
	2000 Nov. 04	4m06s	362.1	< 0.26	0.11	< 0.07	±0.03	±0.06

by fitting a beam-sized Gaussian at the image center. M81* showed circular polarization in all observations.

We find a value of $m_c = 0.27 \pm 0.06 \pm 0.07\%$ and $m_c = 0.26 \pm 0.04 \pm 0.06\%$ for the fractional circular polarization at 4.8 GHz on 2000 September 27 and 2000 November 4 respectively. At 8.4 GHz the degree of circular polarization was $m_c = 0.25 \pm 0.02 \pm 0.05\%$ on 2000 April 4 and $m_c = 0.54 \pm 0.06 \pm 0.07\%$ on 2000 September 27. The errors are separated into statistical and systematic terms. Fig. 7.1 shows the Stokes V map (contours) and the total intensity (grey scale) of M81* on 2000 September 27 at 8.4 GHz. M81* showed no detectable linear polarization, with an upper limit of 0.1%.

At 4.8 GHz, the measured values for circular polarization in M81* are 5 and 6 times the rms in the image for the observations on 2000 September 27 and 2000 November 4, while the upper limits on circular polarization for the check source are only 3 and 2 times the image rms for the two observations. The detection is stronger in the later observation, since the observing time was more than twice as long as in the first observation.

In our observation on 2000 September 27, the measured value for circular polarization in M81* at 8.4 GHz is 10 times the rms in the image for the observation on 2000 September 27, while the upper limit on circular polarization for the check source is 4 times the rms. On 2000 April 04, we detected circular polarization in both M81* and the check source at a level of 10 times the image rms, but the fractional circular polarization is a factor of 2 higher in M81*.

If the detections would have been caused by calibration errors, beam squint, polarization leakage or unknown calibrator polarization, fractional circular polarization should have been detected in the check source with the same value.

7.3 Discussion

The mechanism for the production of circular polarization in AGN is still not known with absolute certainty and several mechanisms have been proposed. An important new parameter, that has been largely ignored so far, is the circular-to-linear polarization ratio $R_{\rm CL} = m_{\rm c}/m_{\rm l}$. For powerful blazars one typically has $R_{\rm CL} \ll 1$ (Homan & Wardle 1999) for the cores of jets. In the radio cores of very low-power AGN, M81* and Sgr A*, we now find $R_{\rm CL} \gg 1$ with limits on the linear polarization that are very low.

This first raises the question of how to reduce the linear polarization to such undetectable levels. Already Bower et al. (1999a) & Bower et al. (1999b) suggested that Faraday de-polarization in the interstellar medium, and specifically the scattering medium in the Galactic Center, could not be responsible for this. Our finding of a high $R_{\rm CL} = m_{\rm c}/m_{\rm l}$ in M81*, which is not scatter broadened, confirms this notion. This also suggests that the birefringent screen proposed by Macquart &

Table 7.2— Total flux density I, circularly polarized flux density P_c, image rms and fractional circular polarization m_c at 8.4 GHz for the calibrator J 1044+719, M81 and the check source J1053+704 with the statistical and calculated systematic errors.

Source	Date	Int. time	I [mJy]	P_c [mJy]	rms [mJy]	m_c [%]		
J1044+719	2000 Apr. 04	12m08s	1542	< 0.02	0.03	< 0.001	±0.002	-
	2000 Sep. 27	3m28s	1316	< 0.60	0.28	< 0.05	±0.02	-
M81*	2000 Apr. 04	4m59s	263.6	0.66	0.06	0.25	±0.02	±0.05
	2000 Sep. 27	5m03s	193.6	1.05	0.11	0.54	±0.06	±0.07
J1053+704	2000 Apr. 04	10m01s	467.7	0.66	0.07	0.14	±0.01	±0.05
	2000 Sep. 27	2m04s	405.0	< 0.68	0.19	< 0.17	±0.05	±0.07

Melrose (2000) is not applicable here. On the other hand, de-polarization by a hot, geometrically thick accretion flow (Agol 2000, Quataert & Gruzinov 2000) is not excluded but also does not yet explain the presence of circular polarization.

A viable mechanism could be Faraday conversion (Pacholczyk 1977; Jones & Odell 1977) of linear polarization to circular polarization caused by the lowest energy relativistic electrons. Bower, Falcke, & Backer (1999) proposed a simple model for Sgr A* in which low-energy electrons reduce linear polarization through Faraday de-polarization and convert linear polarization into circular polarization. Conversion also affects the spectral properties of circular polarization and may lead to a variety of spectral indices, including inverted spectra (Jones & Odell 1977). In inhomogeneous sources, conversion can produce relatively high fractional circular polarization (Jones 1988).

Of course, synchrotron radiation has a small intrinsic component of circular polarization (Legg & Westfold 1968) which can play an important role. However, this intrinsic circular polarization will be reduced by field reversals and optical depth effects. Finally, gyrosynchrotron emission, can also lead to high circular polarization with an inverted spectrum and low linear polarization (Ramaty 1969). All the latter mechanisms are to some degree related and require that M81* and Sgr A* both contain a rather large number of low-energy electrons.

A more detailed discussion of this issue is presented in an paper by Beckert & Falcke (2002).

7.4 Summary and Conclusion

We have presented VLA observations of M81* at 4.8 and 8.4 GHz, and circular polarization was clearly detected at both frequencies with a possible flat-to-inverted spectrum at a level of 0.25-0.5%.

In most AGN the fractional circular polarization typically is $m_c < 0.1\%$ with only a few cases where m_c approaches 0.5% (Weiler & de Pater 1983). The degree of circular polarization usually peaks near 1.4 GHz and decreases strongly with increasing frequency. Surprisingly, the fractional circular polarization in M81* is higher at 8.4 GHz than at 4.8 GHz for our observation on 2000 September 27. The value at 4.8 GHz showed no variation between two epoch separated by six weeks despite a change in total intensity.

We also found that M81* shows less than 0.1% linear polarization thus making M81* the second low-luminosity AGN radio core, after Sgr A*, with a circular-to-linear polarization $R_{\rm CL} \gg 1$. This confirms that both sources may be of similar nature and similar models may apply. It also strongly suggests that the polarization properties are indeed intrinsic to the two sources and are not caused by the Galactic scattering screen. In this respect it is important that M81* was resolved in to a jet-like structure by VLBI, indicating that jets indeed can produce an R_{CL} as high as observed here and in Sgr A*.

Since the basic mechanisms to explain circular polarization involve low-energy electrons one will need to consider their origin and their effects on the spectrum in future models. This will provide one with an important new constraint for the sub-Eddington accretion onto super-massive black holes. Even if the radio emission is produced in a jet, the composition and temperature of this plasma should reflect the plasma properties of the accretion flow very close to the black hole.

8

Summary

The goal of this work was to measure accurate proper motions of extragalactic spectral line (H_2O maser) and continuum (radio jets of AGN) objects. To achieve the very high precision astrometry at a level of a few μas needed for such a project, the technique of phase-referencing VLBI was used. Here, the interferometer is calibrated on a strong source close to the target source.

In this work, a method to improve conventional phase-referencing was developed and applied to observations of H_2O masers in IC 10 and M33. These observations yield proper motions of the two galaxies and a geometric distance to M33. Also, a textbook example of the evolution of a Synchrotron Self-Absrobed jet in the Seyfert galaxy III Zw 2 is presented. This chapter gives a short summary of the main results.

8.1 Atmosphere-Corrected Phase-Referencing

First, a method was developed to improve conventional phase-referencing. This method allows one to correct phase errors in the uv-data which are caused by an inaccurate atmospheric zenith delay in the correlator model. These errors degrade the quality of the phase-referenced image of the target source and decrease the astrometric accuracy. If the zenith delay error in the correlator model is known, the induced phase errors can be calculated and corrected. The zenith delay error can be measured by two different techniques.

If the target source is strong enough, the phase data of this target source consists of a contribution from a position offset and a contribution from the zenith delay error. It is now possible to separate the two contributions, because they have a different time behavior ($\approx \sin(t)$ and $\approx \sec(Z(t))$, where Z is the zenith angle).

If the target source is not strong enough, the phase data can not be used since it is to noisy. Then, geodetic-like observations of many quasars before and after the main observations at different elevations can be used to estimate the zenith delay error. This technique has the advantage that also a zenith delay rate, a clock offset and a clock drift can be estimated for each station.

Both methods yield consistent results and the correction of the phase data increases the quality of the phase-referenced image significantly. The noise in the image is reduced and more flux of the target source is recovered. Figure 8.1 shows the large improvement in the astrometric accuracy of this corrections. Plotted are the position differences of maser spots in IC 133 between two closely spaced observations. Here, all data from all components in all epochs was used. The upper two plots show the position differences in right ascension and declination on the uncorrected maps, while the lower two plots show the components after the corrections. Also plotted are the 1 and 3 σ theoretical limits which are expected from thermal noise. The average position difference of all components is reduced from 50 to 30 μas in right ascension and from 112 to 84 μas in declination. However, this average is dominated by the large number of

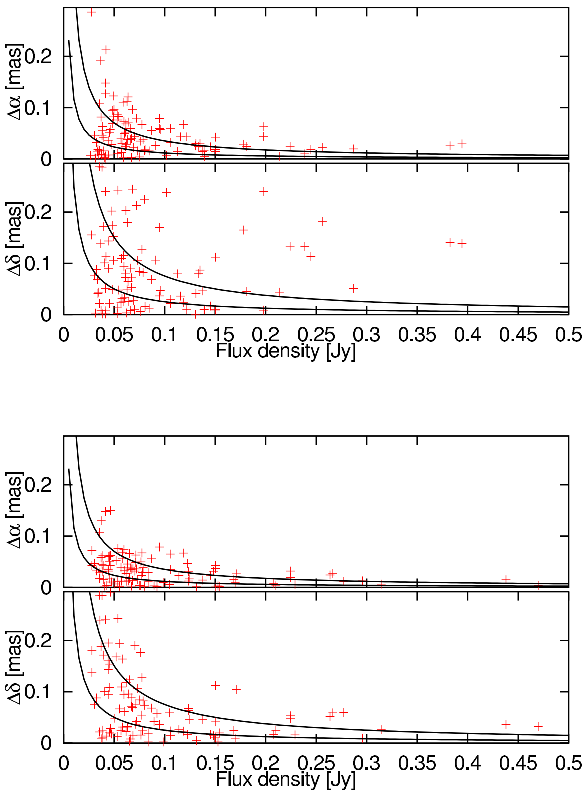

FIGURE 8.1— Astrometric accuracy of all maser spots in IC 133 before (upper) and after the correction (lower) of the phase data in right ascension and declination. The solid lines are the theoretical accuracy from the signal to noise ratio (1 and 2 σ).

weak components which have a larger error. If one looks only at the brightest components with a flux density of more than 100 mJy, the average agreement improves from 28 and 75 μas in right ascension and declination before the correction to 18 and 34 μas in declination after the correction. This astrometric accuracy almost reaches the thermal noise limit.

8.2 Proper Motions in the Local Group

This atmosphere-corrected phase-referencing was then applied to VLBI observations of water vapor masers in the two Local Group galaxies IC 10 and M33.

8.2.1 IC 10

The H_2O masers in IC 10 were observed in three epochs over 18 month. The motion of the strongest maser feature relative to a nearby background source with small angular separation on the sky is linear with time and -37±7 μas yr^{-1}in right ascension and 6±16 μas yr^{-1}in declination. This motion, corrected for the internal galactic rotation in IC 10 and the rotation of the Milky Way yields a total space motion of

$$v_{IC\,10} = 288 \pm 59 \text{ km s}^{-1}$$

relative to the Milky Way. This motion is almost completely orthogonal to the connecting line between IC 10 and M31 if one assumes that the proper motion of M31 is zero (Figure 8.2). If this is true, and IC 10 is gravitationally bound to M31 and on a circular orbit, one would get an estimate of the mass of M31 of $(3.4\pm1.9)\times10^{12}$ $M_\odot$.

8.2.2 M33

The H_2O masers in M33 were observed in four epoch over 3 years. Two regions of maser activity on opposite sides of M33 were observed. Six components in IC 133 and four components in M33/19 could be detected in all four epochs. The average motion of all components in IC 133 yield a motion of 5±3 μas yr^{-1}in right ascension and -17±4 μas yr^{-1}in declination. The average motion of M33/19 was 35±3 μas yr^{-1}in right ascension and -7±9 μas yr^{-1}in declination. These motions, corrected for the internal galactic rotation of M33 and the rotation of the Milky Way yield a total space velocity of

$$v_{M33} = 157 \pm 49 \text{ km s}^{-1}$$

relative to the Milky Way. Then the motion of M33 relative to M31 is directed almost completely towards M31 (Figure 8.2), indicating that M33 is on a highly eccentric orbit around M31 if one assumes that M31 falls towards the Milky Way.

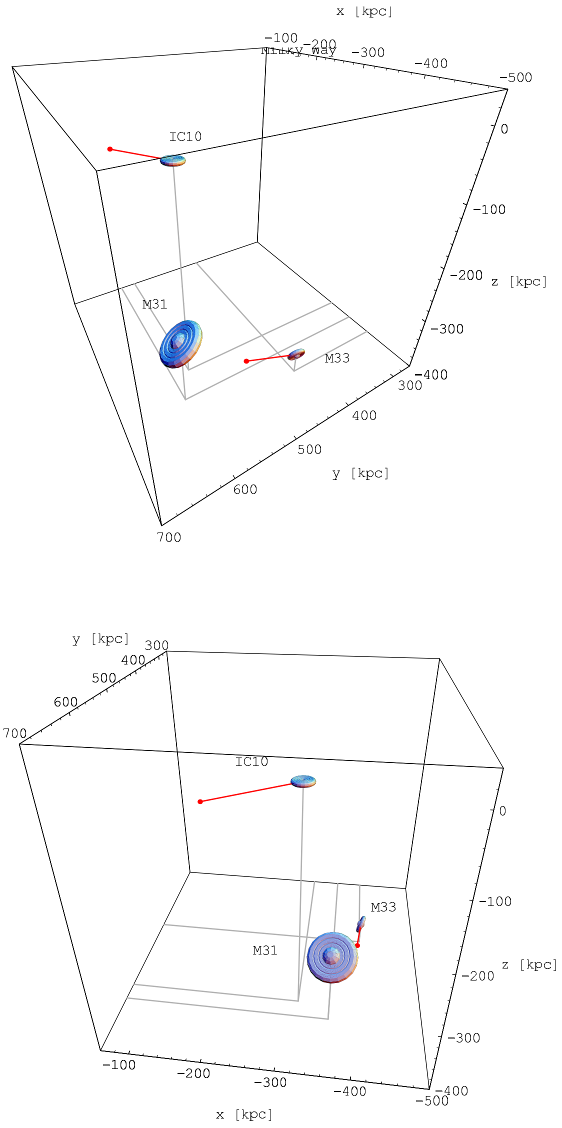

FIGURE 8.2— Schematic view of the Andromeda subgroup. Plotted are also the velocities of IC 10, M33 relative to M31, assuming that the proper motion of M31 on the plane of the sky is zero.

8.3 Geometric Distance to M33

The relative motions of the masers in IC 133 and M33/19 can be compared to the expected motion from the known inclination angle and rotation curve of H I in M33. The relative motion of 34±4 μas yr^{-1}corresponds to 99±7 km s^{-1}. This gives then a direct geometric estimate of the distance to M33 of

$$D = 695 \pm 105 \text{ kpc}.$$

The fact that the radial velocities of the masers and the H I gas are in good agreement, support the assumption that the masers are rotating with the gas in the galaxy.

8.4 III Zw 2

A very detailed monitoring of a flare in the Seyfert I galaxy III Zw 2 with the VLA and the VLBA was presented. The relative astrometry in the VLBA observations was extremely precise on a level of a few μas. These observations allowed us to study in great detail a textbook example of a Synchrotron Self-Absorbed jet that gets frustrated with no expansion before it breaks free and expands with apparent superluminal motion. A by-product of the VLA monitoring, the detection of circular polarization in M81 with striking similarities to the polarization properties of Sgr A*, the radio source at the Galactic Center, was also presented.

8.5 Outlook

Future observations within the next two years will increase the accuracy of the proper motion measurement of IC 10 and M33 even more. Then, the uncertainties form the internal rotation of IC 10 and M33 are already larger than the uncertainties from our proper motion measurements. At this point, new observations of H I in these galaxy are needed to further improve the accuracy.

More regions of maser activity are known in M33 that could be also used to improve the measurement of the rotation of M33 and allow us to measure the distance to M33, ultimately to better than 5% accuracy. The observations presented here are the first step towards an independent re-calibration of the extragalactic distance scale.

The proper motions presented here can be combined with the existing statistical approaches. This will lead to a better understanding of the kinematics and the matter distribution of the Local Group.

New surveys to search Local Group galaxies for H_2O maser emission could increase the number of possible targets. Also, new developments in VLBI using larger bandwidths will increase the sensitivity so that a detection of the nucleus of M31 might become feasible in the future, also giving us the missing proper motion of M31.

8.6 Final Words

More than 80 years after van Maanens attempt to measure the proper motion and rotation of M33, we succeeded to perform his experiment. Our measurements have provided the highest astrometric precision of phase-referencing spectral line observations to date. For the first time we are now able to measure the proper motions of external galaxies out to a distance of 800 kpc.

Bibliography

Agol E., 2000, ApJ, 538, L121

Aller H. D., Aller M. F., Latimer G. E., Hodge P. E., 1985, ApJS, 59, 513

Alonso-Herrero A., Ward M. J., Kotilainen J. K., 1997, MNRAS, 288, 977

Argon A. L., Greenhill L. J., Moran J. M., Reid M. J., Menten K. M., 1998, Proper Motions and the Distance to a Water Vapor Maser in the Galaxy M33, in ASP Conf. Ser. 144: IAU Colloq. 164: Radio Emission from Galactic and Extragalactic Compact Sources, p. 235

Argon A. L., Greenhill L. J., Moran J. M., et al., 1994, ApJ, 422, 586

Arp H., 1968, ApJ, 152, 1101

Baan W. A., Haschick A., 1994, ApJ, 424, L33

Backer D. C., Sramek R. A., 1999, ApJ, 524, 805

Bahcall J. N., Kirhakos S., Schneider D. P., 1995, ApJ, 450, 486

Beasley A. J., Conway J. E., 1995, VLBI Phase-Referencing, in ASP Conf. Ser. 82: Very Long Baseline Interferometry and the VLBA, p. 328

Becker R., Henkel C., Wilson T. L., Wouterloot J. G. A., 1993, A&A, 268, 483

Beckert T., Falcke H., 2002, A&A, 388, 1106

Bietenholz M. F., Bartel N., Rupen M. P., 2000, ApJ, 532, 895

Bietenholz M. F., Bartel N., Rupen M. P., et al., 1996, ApJ, 457, 604

Blandford R. D., Konigl A., 1979, ApJ, 232, 34

Blundell K. M., Beasley A. J., 1998, MNRAS, 299, 165

Blundell K. M., Beasley A. J., Bicknell G. V., 2003, ApJ, 591, L103

Boroson T. A., Green R. F., 1992, ApJS, 80, 109

Bottinelli L., Gouguenheim L., Heidmann J., 1972, A&A, 18, 121

Bower G. C., Backer D. C., Zhao J., Goss M., Falcke H., 1999a, ApJ, 521, 582

Bower G. C., Falcke H., Backer D. C., 1999, ApJ, 523, L29

Bower G. C., Falcke H., Mellon R. R., 2002, ApJ, 578, L103

Bower G. C., Falcke H., Sault R. J., Backer D. C., 2002, ApJ, 571, 843

Bower G. C., Wright M. C. H., Backer D. C., Falcke H., 1999b, ApJ, 527, 851

Brunthaler A., Bower G. C., Falcke H., Mellon R. R., 2001, ApJ, 560, L123

Brunthaler A., Falcke H., Bower G. C., et al., 2003, Publications of the Astronomical Society of Australia, 20, 126

Brunthaler A., Falcke H., Bower G. C., et al., 2000, A&A, 357, L45

Churchwell E., Witzel A., Pauliny-Toth I., et al., 1977, A&A, 54, 969

Clark B. G., 1980, A&A, 89, 377

Clements S. D., Smith A. G., Aller H. D., Aller M. F., 1995, AJ, 110, 529

Cohen R. J., 1979, MNRAS, 187, 839

Corbelli E., Schneider S. E., 1997, ApJ, 479, 244

Corbelli E., Schneider S. E., Salpeter E. E., 1989, AJ, 97, 390

Cornwell T., Fomalont E., 1999, Self-Calibration, in ASP Conf. Ser. 180: Synthesis Imaging in Radio Astronomy II, p. 187

Courteau S., van den Bergh S., 1999, AJ, 118, 337

de Vaucouleurs G., de Vaucouleurs A., Corwin H. G., et al., 1991, Third Reference Catalogue of Bright Galaxies. Volume 1-3, XII, 2069 pp. 7 figs.. Springer-Verlag Berlin Heidelberg New York

Dehnen W., Binney J. J., 1998, MNRAS, 298, 387

Eckart A., Genzel R., 1996, Nat., 383, 415

Eisenhauer F., Schödel R., Genzel R., et al., 2003, ApJ, 597, L121

Evans N. W., Wilkinson M. I., 2000, MNRAS, 316, 929

Evans N. W., Wilkinson M. I., Perrett K. M., Bridges T. J., 2003, ApJ, 583, 752

Falcke H., 1996, ApJ, 464, L67

Falcke H., Biermann P. L., 1995, A&A, 293, 665

Falcke H., Bower G. C., Lobanov A. P., et al., 1999, ApJ, 514, L17

Falcke H., Körding E., Markoff S., 2004, A&A, 414, 895

Falcke H., Malkan M. A., Biermann P. L., 1995, A&A, 298, 375

Falcke H., Mannheim K., Biermann P. L., 1993, A&A, 278, L1

Falcke H., Markoff S., 2000, A&A, 362, 113

Falcke H., Patnaik A. R., Sherwood W., 1996, ApJ, 473, L13

Falcke H., Sherwood W., Patnaik A. R., 1996, ApJ, 471, 106

Fender R. P., 2001, MNRAS, 322, 31

Fich M., Tremaine S., 1991, ARA&A, 29, 409

Fomalont E., 1999, Astrometry and Geodesy, in ASP Conf. Ser. 180: Synthesis Imaging in Radio Astronomy II, p. 463

Freedman W. L., 2000, Phys. Rep., 333, 13

Freedman W. L., Madore B. F., Gibson B. K., et al., 2001, ApJ, 553, 47

Garrett M. A., Wrobel J. M., Morganti R., 2003, New Astronomy Review, 47, 385

Ghez A. M., Duchêne G., Matthews K., et al., 2003, ApJ, 586, L127

Gottesman S. T., Hunter J. H., Boonyasait V., 2002, MNRAS, 337, 34

Greenhill L. J., Moran J. M., Reid M. J., et al., 1990, ApJ, 364, 513

Greenhill L. J., Moran J. M., Reid M. J., Menten K. M., Hirabayashi H., 1993, ApJ, 406, 482

Guinan E. F., Fitzpatrick E. L., Dewarf L. E., et al., 1998, ApJ, 509, L21

Högbom J. A., 1974, A&AS, 15, 417

Hartwick F. D. A., Sargent W. L. W., 1978, ApJ, 221, 512

Henkel C., Wouterloot J. G. A., Bally J., 1986, A&A, 155, 193

Herrnstein J. R., Moran J. M., Greenhill L. J., et al., 1999, Nat., 400, 539

Ho L. C., Filippenko A. V., Sargent W. L. W., 1996, ApJ, 462, 183

Hodge P., Lee M. G., 1990, PASP, 102, 26

Homan D. C., Wardle J. F. C., 1999, AJ, 118, 1942

Hubble E. P., 1936, Yale University Press

Huchra J. P., Vogeley M. S., Geller M. J., 1999, ApJS, 121, 287

Huchtmeier W. K., 1979, A&A, 75, 170

Hutchings J. B., 1983, PASP, 95, 799

Hutchings J. B., Campbell B., 1983, Nat., 303, 584

Jones B. F., Klemola A. R., Lin D. N. C., 1994, AJ, 107, 1333

Jones T. W., 1988, ApJ, 332, 678

Jones T. W., Odell S. L., 1977, ApJ, 214, 522

Kaastra J. S., de Korte P. A. J., 1988, A&A, 198, 16

Kahn F. D., Woltjer L., 1959, ApJ, 130, 705

Kellermann K. I., Sramek R., Schmidt M., Shaffer D. B., Green R., 1989, AJ, 98, 1195

Kellermann K. I., Vermeulen R. C., Zensus J. A., Cohen M. H., 1998, AJ, 115, 1295

Kerr F. J., Lynden-Bell D., 1986, MNRAS, 221, 1023

Khachikian E. Y., Weedman D. W., 1974, ApJ, 192, 581

Kim M., Kim E., Lee M. G., Sarajedini A., Geisler D., 2002, AJ, 123, 244

Kirhakos S., Bahcall J. N., Schneider D. P., Kristian J., 1999, ApJ, 520, 67

Kobayashi H., Ishiguro M., Chikada Y., et al., 1989, PASJ, 41, 141

Kobayashi H., Sasao T., Kawaguchi N., et al., 2001, VERA (VLBI Exploration of Radio Astrometry) system (invited), in 2001 Asia-Pacific Radio Science Conference AP-RASC '01, p. 243

Kochanek C. S., 1996, ApJ, 457, 228

Kukula M. J., Dunlop J. S., Hughes D. H., Rawlings S., 1998, MNRAS, 297, 366

Kulessa A. S., Lynden-Bell D., 1992, MNRAS, 255, 105

Lee M. G., Kim M., Sarajedini A., Geisler D., Gieren W., 2002, ApJ, 565, 959

Legg M. P. C., Westfold K. C., 1968, ApJ, 154, 499

Lloyd C., 1984, MNRAS, 209, 697

Macquart J.-P., Melrose D. B., 2000, ApJ, 545, 798

Massey P., Armandroff T. E., Conti P. S., 1992, AJ, 103, 1159

Mayall N. U., 1935, PASP, 47, 317

McConnachie A. W., Irwin M. J., Ferguson A. M. N., et al., 2004, MNRAS, in press, astro-ph/0401453

Melia F., 1992, ApJ, 387, L25

Melia F., Falcke H., 2001, ARA&A, 39, 309

Mellon R. R., Bower G. C., Brunthaler A., Falcke H., 2000, Bulletin of the American Astronomical Society, 32, 1456

Michelson A. A., Pease F. G., 1921, ApJ, 53, 249

Miller P., Rawlings S., Saunders R., 1993, MNRAS, 263, 425

Miyoshi M., Moran J., Herrnstein J., et al., 1995, Nat., 373, 127

Mould J. R., Huchra J. P., Freedman W. L., et al., 2000, ApJ, 529, 786

Narayan R., Yi I., Mahadevan R., 1995, Nat., 374, 623

Newman J. A., Ferrarese L., Stetson P. B., et al., 2001, ApJ, 553, 562

Ngeow S., Kanbur S., 2004, MNRAS, in press, astro-ph/0401038

Niell A. E., 1996, J. Geophys. Res., 101, 3227

Osterbrock D. E., 1977, ApJ, 215, 733

Pacholczyk A. G., 1977, Oxford Pergamon Press International Series on Natural Philosophy, 89

Peck A. B., Henkel C., Ulvestad J. S., et al., 2003, ApJ, 590, 149

Quataert E., Gruzinov A., 2000, ApJ, 545, 842

Ramaty R., 1969, ApJ, 158, 753

Rayner D. P., Norris R. P., Sault R. J., 2000, MNRAS, 319, 484

Reid M. J., 1993, ARA&A, 31, 345

Reid M. J., Argon A. L., Masson C. R., Menten K. M., Moran J. M., 1995, ApJ, 443, 238

Reid M. J., Brunthaler A., 2004, ApJ, submitted

Reid M. J., Readhead A. C. S., Vermeulen R. C., Treuhaft R. N., 1999, ApJ, 524, 816

Reuter H.-P., Lesch H., 1996, A&A, 310, L5

Richer M. G., Bullejos A., Borissova J., et al., 2001, A&A, 370, 34

Roberts M. S., 1962, AJ, 67, 431

Ryle M. S., Longair M. S., 1967, MNRAS, 136, 123

Sakai S., Madore B. F., Freedman W. L., 1999, ApJ, 511, 671

Salvi N. J., Page M. J., Stevens J. A., et al., 2002, MNRAS, 335, 177

Sandage A., Tammann G. A., 1974, ApJ, 194, 559

Sandage A., Tammann G. A., Reindl B., 2004, A&A, submitted, astro-ph/0402424

Sault R. J., Macquart J.-P., 1999, ApJ, 526, L85

Scarpa R., Urry C. M., Falomo R., Pesce J. E., Treves A., 2000, ApJ, 532, 740

Schödel R., Ott T., Genzel R., et al., 2003, ApJ, 596, 1015

Schödel R., Ott T., Genzel R., et al., 2002, Nat., 419, 694

Schmidt M., Green R. F., 1983, ApJ, 269, 352

Schwab F. R., 1984, AJ, 89, 1076

Schweitzer A. E., Cudworth K. M., Majewski S. R., Suntzeff N. B., 1995, AJ, 110, 2747

Shepherd M. C., Pearson T. J., Taylor G., 1994, BAAS, 26, 987

Shostak G. S., Skillman E. D., 1989, A&A, 214, 33

Stanek K. Z., Zaritsky D., Harris J., 1998, ApJ, 500, L141

Steigman G., Tkachev I., 1999, ApJ, 522, 793

Surace J. A., Sanders D. B., Evans A. S., 2001, AJ, 122, 2791

Türler M., Courvoisier T. J.-L., Paltani S., 1999, A&A, 349, 45

Tammann G. A., Sandage A., Reindl B., 2003, A&A, 404, 423

Taylor G. B., Carilli C. L., Perley R. A. (eds.), 1999, Synthesis Imaging in Radio Astronomy II

Taylor G. L., Dunlop J. S., Hughes D. H., Robson E. I., 1996, MNRAS, 283, 930

Thompson A. R., Moran J. M., Swenson G. W., 1986, Interferometry and synthesis in radio astronomy. New York, Wiley-Interscience, 1986, 554 p.

Udalski A., Pietrzyński G., Woźniak P., et al., 1998, ApJ, 509, L25

Unger S. W., Lawrence A., Wilson A. S., Elvis M., Wright A. E., 1987, MNRAS, 228, 521

Valtaoja E., Lähteenmäki A., Teräsranta H., Lainela M., 1999, ApJS, 120, 95

van den Bergh S., 1991, PASP, 103, 609

van den Bergh S., 1999, A&A Rev., 9, 273

van Maanen A., 1923, ApJ, 57, 264

Walker R. C., Burke B. F., Johnston K. J., Spencer J. H., 1977, ApJ, 211, L135

Wardle J. F. C., Homan D. C., Ojha R., Roberts D. H., 1998, Nat., 395, 457

Weiler K. W., de Pater I., 1983, ApJS, 52, 293

Wilcots E. M., Miller B. W., 1998, AJ, 116, 2363

Zensus J. A., Diamond P. J., Napier P. J. (eds.), 1995, Very Long Baseline Interferometry and the VLBA

Zwicky F., 1967, Adv. Astron. Astrophys., 5, 267

A

VLBA observations of M33: Tables

A.1 Uncorrected Positions

A.1.1 IC 133: First epoch

Table A.1— IC 133: Component name, LSR velocity v_r, peak and integrated flux densities S_p and S_I, position offsets from phase center $\Delta\alpha$ and $\Delta\delta$, component size and position angle (PA) of all detected components on 2001 March 27 from the fit to the maps.

	$v_{\rm r}$ [km s^{-1}]	S$_p$ [$\frac{\rm mJy}{\rm beam}$]	S$_I$ [mJy]	$\Delta\alpha$ [mas]	$\Delta\delta$ [mas]	Size [mas]	PA [°]
I1$_?$	-206.6	74 ± 7	78 ± 12	0.169 ± 0.015	-0.026 ± 0.038	1×0.4	177
I1$_a$	-207.5	119 ± 7	137 ± 14	0.243 ± 0.014	0.018 ± 0.022	0.9×0.5	159
I1$_a$	-208.3	66 ± 7	73 ± 13	0.209 ± 0.019	0.042 ± 0.041	0.9×0.4	174
I1$_?$	-209.2	75 ± 7	129 ± 17	0.174 ± 0.017	0.113 ± 0.052	1.4×0.4	1
I1$_b$	-210.0	192 ± 8	227 ± 15	0.125 ± 0.008	-0.044 ± 0.016	1×0.4	173
I1$_b$	-210.8	87 ± 7	124 ± 15	0.156 ± 0.016	0 ± 0.033	1×0.5	173
I1$_b$	-211.7	53 ± 7	62 ± 13	0.158 ± 0.024	0.007 ± 0.049	1×0.4	170
I2	-207.5	100 ± 7	103 ± 13	-2.054 ± 0.014	-1.161 ± 0.025	0.8×0.4	165
I2	-208.3	75 ± 7	115 ± 15	-2.067 ± 0.025	-1.169 ± 0.036	1.1×0.5	153
I3$_a$	-216.7	34 ± 6	47 ± 14	-2.454 ± 0.046	-0.011 ± 0.069	0.9×0.6	174
I3$_a$	-217.6	50 ± 7	63 ± 13	-2.278 ± 0.027	0.021 ± 0.055	1×0.4	169
I3$_a$	-218.4	31 ± 6	74 ± 20	-2.33 ± 0.053	-0.059 ± 0.114	1.3×0.6	0
I3$_b$	-219.2	67 ± 7	85 ± 13	-2.105 ± 0.023	0.148 ± 0.034	0.8×0.5	167
I3$_b$	-220.1	180 ± 7	221 ± 14	-2.096 ± 0.008	0.136 ± 0.015	0.9×0.5	174
I3$_b$	-220.9	103 ± 7	114 ± 13	-2.051 ± 0.013	0.108 ± 0.024	0.9×0.5	172
I3$_b$	-221.8	87 ± 7	99 ± 13	-2.024 ± 0.018	0.183 ± 0.025	0.8×0.5	162
I4	-212.5	98 ± 6	142 ± 14	-2.73 ± 0.015	-2.432 ± 0.029	1×0.5	167
I5	-209.2	91 ± 7	81 ± 11	-0.837 ± 0.014	-1.891 ± 0.025	0.8×0.4	169
I5	-210.0	167 ± 8	193 ± 15	-0.835 ± 0.011	-1.898 ± 0.017	0.9×0.4	157
I6	-208.3	67 ± 7	73 ± 12	6.13 ± 0.021	0.540 ± 0.036	0.9×0.4	164
I6	-209.2	60 ± 7	73 ± 13	6.148 ± 0.024	0.505 ± 0.042	0.9×0.5	177
I6	-210.0	49 ± 8	68 ± 16	5.871 ± 0.039	0.656 ± 0.061	1×0.5	158
I7	-211.7	46 ± 6	65 ± 14	0.277 ± 0.038	0.75 ± 0.065	1.2×0.4	155
I8	-213.4	39 ± 6	51 ± 13	-2.342 ± 0.036	-0.813 ± 0.065	0.9×0.5	171
I8	-214.2	46 ± 7	48 ± 12	-2.454 ± 0.027	-1.201 ± 0.065	1.1×0.3	165
I8	-215.0	41 ± 7	44 ± 12	-2.531 ± 0.027	-0.906 ± 0.078	1.1×0.3	171
I9	-217.6	50 ± 7	49 ± 11	-2.633 ± 0.030	-0.529 ± 0.047	0.9×0.4	154
I10	-221.8	44 ± 7	39 ± 11	0.264 ± 0.022	0.136 ± 0.062	0.9×0.3	178
I11	-225.1	24 ± 6	101 ± 31	23.452 ± 0.168	-15.993 ± 0.102	1.6×0.9	76
I12	-229.3	46 ± 6	64 ± 14	23.193 ± 0.027	-16.011 ± 0.071	1.2×0.4	171
I12	-230.2	53 ± 7	48 ± 11	23.213 ± 0.026	-15.901 ± 0.042	0.9×0.4	157
I13	-230.2	58 ± 6	97 ± 16	24.108 ± 0.023	-14.737 ± 0.060	1.3×0.5	172
I13	-231.0	64 ± 6	106 ± 16	24.077 ± 0.025	-14.674 ± 0.050	1.2×0.5	164
I14	-231.0	56 ± 6	81 ± 14	2.961 ± 0.022	-6.267 ± 0.058	1.2×0.4	175
I15	-235.2	53 ± 7	65 ± 13	23.169 ± 0.023	-16.130 ± 0.057	1.1×0.4	170
I15	-236.0	44 ± 6	65 ± 14	23.149 ± 0.042	-15.988 ± 0.047	0.8×0.7	0
I16	-236.0	39 ± 6	55 ± 14	24.307 ± 0.032	-15.669 ± 0.079	1.1×0.5	0
I16	-236.9	39 ± 7	37 ± 11	24.235 ± 0.033	-15.362 ± 0.062	0.9×0.4	161
I16	-237.7	54 ± 7	51 ± 11	24.299 ± 0.023	-15.570 ± 0.044	0.9×0.4	165

Table A.2— IC 133: LSR velocity v_r, peak and integrated flux densities S_p and S_I, position offsets from phase center $\Delta\alpha$ and $\Delta\delta$, size and position angle (PA) of all detected components on 2001 April 05. The components marked with an asterisk are new detected.

	v_r [km s^{-1}]	S$_p$ [$\frac{\mathrm{mJy}}{\mathrm{beam}}$]	S$_I$ [mJy]	$\Delta\alpha$ [mas]	$\Delta\delta$ [mas]	Size [mas]	PA [°]
I1$_?$	-206.6	57 ± 7	49 ± 12	0.130 ± 0.021	-0.002 ± 0.043	0.8×0.4	1
I1$_a$	-207.5	125 ± 8	105 ± 12	0.176 ± 0.010	-0.006 ± 0.021	0.8×0.3	171
I1$_a$	-208.3	70 ± 8	83 ± 15	0.171 ± 0.020	0.050 ± 0.044	0.9×0.4	179
I1$_?$	-209.2	57 ± 7	105 ± 20	0.186 ± 0.022	0.223 ± 0.084	1.5×0.4	2
I1$_b$	-210.0	145 ± 8	181 ± 17	0.102 ± 0.009	-0.028 ± 0.027	1.1×0.4	177
I1$_b$	-210.8	109 ± 8	105 ± 14	0.100 ± 0.013	-0.069 ± 0.026	0.8×0.4	177
I1$_b$	-211.7	40 ± 7	55 ± 16	0.143 ± 0.030	0.179 ± 0.109	1.4×0.3	8
I2	-207.5	73 ± 8	70 ± 13	-2.070 ± 0.019	-1.267 ± 0.037	0.8×0.4	170
I2	-208.3	104 ± 8	96 ± 13	-2.071 ± 0.013	-1.253 ± 0.027	0.9×0.4	166
I3$_a$	-217.6	42 ± 7	57 ± 16	-2.426 ± 0.043	-0.219 ± 0.064	0.9×0.5	21
I3$_b$	-219.2	45 ± 7	42 ± 12	-2.156 ± 0.029	0.169 ± 0.072	1.1×0.3	163
I3$_b$	-220.1	138 ± 8	145 ± 14	-2.110 ± 0.010	0.089 ± 0.021	0.9×0.4	173
I3$_b$	-220.9	79 ± 7	83 ± 13	-2.089 ± 0.016	0.025 ± 0.038	1×0.4	172
I3$_b$	-221.8	77 ± 7	73 ± 13	-2.091 ± 0.016	0.056 ± 0.036	0.9×0.4	170
I4	-212.5	95 ± 8	97 ± 14	-2.809 ± 0.013	-2.468 ± 0.034	1×0.3	171
I4	-213.4	29 ± 7	30 ± 13	-2.685 ± 0.041	-2.508 ± 0.127	1.2×0.3	169
I5	-209.2	60 ± 8	43 ± 11	-0.911 ± 0.019	-1.797 ± 0.038	0.7×0.3	175
I5	-210.0	150 ± 8	122 ± 13	-0.877 ± 0.009	-2.010 ± 0.018	0.8×0.3	172
I6	-208.3	67 ± 8	57 ± 12	6.127 ± 0.021	0.468 ± 0.036	0.7×0.4	164
I6	-209.2	35 ± 7	64 ± 20	6.040 ± 0.092	0.484 ± 0.054	1×0.6	79
I8	-213.4	43 ± 7	35 ± 11	-2.300 ± 0.021	-1.205 ± 0.069	1×0.3	174
I8	-214.2	38 ± 7	32 ± 11	-2.409 ± 0.023	-1.488 ± 0.079	1×0.3	178
I12	-229.3	40 ± 7	37 ± 12	23.196 ± 0.030	-16.112 ± 0.078	1×0.3	165
I12	-230.2	33 ± 7	62 ± 19	23.245 ± 0.059	-15.989 ± 0.118	1.4×0.5	20
I13	-231.0	35 ± 7	81 ± 22	24.094 ± 0.034	-14.962 ± 0.171	2×0.4	176
I15	-235.2	56 ± 8	43 ± 11	23.158 ± 0.019	-16.143 ± 0.044	0.8×0.3	175
I15	-236.0	46 ± 7	42 ± 12	23.113 ± 0.030	-16.131 ± 0.049	0.7×0.4	172
I16	-236.0	31 ± 7	29 ± 13	24.261 ± 0.035	-15.745 ± 0.102	1×0.3	174
I16	-237.7	54 ± 8	73 ± 17	24.224 ± 0.029	-15.813 ± 0.062	1×0.4	11
I17*	-207.5	49 ± 8	43 ± 13	1.122 ± 0.022	0.186 ± 0.064	0.9×0.3	177
I17*	-208.3	41 ± 8	30 ± 11	1.134 ± 0.027	0.229 ± 0.067	0.8×0.3	168
I18*	-220.9	39 ± 7	41 ± 13	-2.733 ± 0.034	-0.361 ± 0.070	0.9×0.4	168

A.1.2 IC 133: Second epoch

TABLE A.3— IC 133: LSR velocity v_r, peak and integrated flux densities S_p and S_I, position offsets from phase center $\Delta\alpha$ and $\Delta\delta$, size and position angle (PA) of all detected components on 2002 January 28. The components marked with an asterisk are new detected.

	v_r [km s^{-1}]	S$_p$ [$\frac{\mathrm{mJy}}{\mathrm{beam}}$]	S$_I$ [mJy]	$\Delta\alpha$ [mas]	$\Delta\delta$ [mas]	Size [mas]	PA [°]
I1$_?$	-206.6	106 ± 7	154 ± 16	0.150 ± 0.013	-0.039 ± 0.019	0.7×0.4	176
I1$_a$	-207.5	131 ± 8	186 ± 17	0.194 ± 0.011	-0.046 ± 0.016	0.7×0.4	178
I1$_a$	-208.3	59 ± 7	149 ± 24	0.267 ± 0.038	-0.012 ± 0.038	0.9×0.6	44
I1$_?$	-209.2	54 ± 7	115 ± 21	0.188 ± 0.035	-0.031 ± 0.041	0.8×0.5	33
I1$_b$	-210.0	198 ± 8	311 ± 19	0.132 ± 0.009	-0.038 ± 0.011	0.7×0.5	9
I1$_b$	-210.8	142 ± 7	203 ± 16	0.107 ± 0.009	-0.021 ± 0.015	0.7×0.4	7
I1$_?$	-211.7	34 ± 7	104 ± 26	0.254 ± 0.043	0.350 ± 0.101	1.2×0.5	8
I2	-207.5	106 ± 8	158 ± 17	-2.053 ± 0.013	-1.206 ± 0.022	0.7×0.4	5
I2	-208.3	65 ± 7	94 ± 16	-2.004 ± 0.024	-1.192 ± 0.029	0.6×0.5	154
I2	-209.2	33 ± 7	57 ± 18	-2.169 ± 0.058	-1.211 ± 0.060	0.8×0.4	136
I3$_b$	-220.1	72 ± 7	139 ± 19	-1.983 ± 0.025	0.117 ± 0.027	0.7×0.6	159
I3$_b$	-220.9	64 ± 7	89 ± 15	-2.040 ± 0.019	0.106 ± 0.033	0.7×0.4	3
I3$_b$	-221.8	58 ± 7	87 ± 16	-2.124 ± 0.022	0.146 ± 0.038	0.7×0.4	11
I4	-212.5	98 ± 7	181 ± 19	-2.709 ± 0.015	-2.507 ± 0.024	0.8×0.5	167
I4	-213.4	60 ± 7	90 ± 16	-2.571 ± 0.022	-2.817 ± 0.035	0.7×0.4	168
I5	-209.2	79 ± 7	76 ± 13	-0.835 ± 0.015	-1.963 ± 0.022	0.5×0.4	179
I5	-210.8	35 ± 7	59 ± 18	-0.850 ± 0.050	-1.763 ± 0.057	0.7×0.5	144
I6	-208.3	63 ± 7	99 ± 17	6.164 ± 0.026	0.521 ± 0.031	0.7×0.5	154
I6	-209.2	60 ± 7	80 ± 15	6.059 ± 0.022	0.543 ± 0.035	0.7×0.4	162
I6	-210.0	41 ± 8	56 ± 18	5.894 ± 0.041	0.680 ± 0.058	0.8×0.4	152
I12	-229.3	53 ± 7	77 ± 15	23.243 ± 0.026	-16.056 ± 0.035	0.6×0.5	8
I14	-231.0	37 ± 7	56 ± 16	2.975 ± 0.038	-6.465 ± 0.052	0.7×0.5	163
I19*	-219.2	47 ± 7	64 ± 15	0.246 ± 0.025	-0.056 ± 0.044	0.7×0.4	174
I19*	-220.1	122 ± 7	170 ± 16	0.135 ± 0.011	-0.033 ± 0.016	0.6×0.4	179
I19*	-220.9	42 ± 7	50 ± 14	0.175 ± 0.029	-0.050 ± 0.044	0.6×0.4	179
I20*	-220.1	42 ± 7	36 ± 12	24.694 ± 0.025	-15.277 ± 0.041	0.6×0.3	13
I21*	-222.6	30 ± 6	97 ± 26	-2.422 ± 0.073	-0.393 ± 0.100	1.3×0.5	32
I22*	-222.6	41 ± 7	66 ± 16	24.658 ± 0.036	-15.543 ± 0.047	0.7×0.5	157
I23*	-226.0	37 ± 7	53 ± 15	24.174 ± 0.040	-14.569 ± 0.046	0.6×0.5	155

Table A.4— IC 133: LSR velocity v_r, peak and integrated flux densities S_p and S_I, position offsets from phase center $\Delta\alpha$ and $\Delta\delta$, size and position angle (PA) of all detected components on 2002 February 03. The components marked with an asterisk are new detected.

	v_r [km s^{-1}]	S$_p$ [$\frac{\mathrm{mJy}}{\mathrm{beam}}$]	S$_I$ [mJy]	$\Delta\alpha$ [mas]	$\Delta\delta$ [mas]	Size [mas]	PA [°]
I1$_?$	-206.6	117 ± 7	141 ± 14	0.091 ± 0.010	-0.017 ± 0.019	0.7×0.4	0
I1$_a$	-207.5	138 ± 8	172 ± 15	0.164 ± 0.009	-0.005 ± 0.018	0.8×0.4	174
I1$_a$	-208.3	89 ± 7	108 ± 14	0.156 ± 0.013	-0.037 ± 0.028	0.8×0.4	8
I1$_?$	-209.2	65 ± 7	96 ± 16	0.105 ± 0.018	0.017 ± 0.042	0.9×0.4	6
I1$_b$	-210.0	220 ± 8	284 ± 17	0.088 ± 0.006	-0.047 ± 0.012	0.8×0.4	179
I1$_b$	-210.8	139 ± 7	211 ± 17	0.090 ± 0.009	-0.011 ± 0.020	0.9×0.4	180
I1$_?$	-211.7	36 ± 7	86 ± 22	0.262 ± 0.036	0.306 ± 0.103	1.3×0.4	2
I2	-207.5	112 ± 8	119 ± 14	-2.085 ± 0.009	-1.176 ± 0.023	0.8×0.3	177
I2	-208.3	63 ± 7	85 ± 15	-2.116 ± 0.020	-1.144 ± 0.039	0.8×0.4	169
I2	-209.2	41 ± 7	73 ± 18	-2.183 ± 0.035	-1.142 ± 0.063	0.9×0.5	168
I2	-210.0	40 ± 8	64 ± 19	-2.255 ± 0.049	-1.093 ± 0.071	1×0.4	150
I3$_b$	-220.1	64 ± 7	85 ± 16	-2.055 ± 0.025	0.092 ± 0.033	0.7×0.5	20
I3$_b$	-220.9	66 ± 7	66 ± 13	-2.161 ± 0.015	0.042 ± 0.034	0.7×0.3	1
I3$_b$	-221.8	63 ± 7	83 ± 14	-2.154 ± 0.017	0.114 ± 0.040	0.9×0.4	6
I4	-211.7	31 ± 7	53 ± 17	-2.674 ± 0.040	-2.859 ± 0.118	1.3×0.3	166
I4	-212.5	96 ± 7	177 ± 19	-2.767 ± 0.015	-2.461 ± 0.032	1.1×0.4	166
I4	-213.4	49 ± 7	84 ± 18	-2.653 ± 0.025	-2.711 ± 0.059	1×0.4	179
I5	-209.2	76 ± 7	75 ± 13	-0.870 ± 0.014	-1.957 ± 0.029	0.7×0.3	175
I5	-210.0	96 ± 8	128 ± 17	-0.887 ± 0.012	-1.910 ± 0.034	1×0.3	178
I6	-207.5	40 ± 8	30 ± 11	6.095 ± 0.024	0.492 ± 0.052	0.6×0.3	171
I6	-208.3	60 ± 7	74 ± 15	6.114 ± 0.022	0.488 ± 0.035	0.7×0.4	173
I6	-209.2	38 ± 7	58 ± 17	6.122 ± 0.035	0.542 ± 0.074	1×0.4	164
I6	-210.0	46 ± 8	63 ± 17	5.888 ± 0.040	0.681 ± 0.055	0.8×0.4	150
I7	-212.5	35 ± 7	68 ± 20	0.253 ± 0.034	0.726 ± 0.112	1.3×0.3	9
I12	-229.3	64 ± 7	64 ± 12	23.157 ± 0.015	-16.054 ± 0.034	0.7×0.3	4
I17	-207.5	42 ± 8	43 ± 14	1.223 ± 0.029	0.334 ± 0.051	0.7×0.4	5
I17	-208.3	38 ± 7	51 ± 15	1.257 ± 0.030	0.374 ± 0.067	0.8×0.4	179
I19	-220.1	167 ± 8	209 ± 15	0.092 ± 0.008	-0.023 ± 0.014	0.7×0.4	4
I19	-220.9	43 ± 7	71 ± 17	0.175 ± 0.039	-0.058 ± 0.050	0.7×0.5	163
I20	-220.9	33 ± 7	47 ± 16	24.575 ± 0.035	-15.275 ± 0.081	0.9×0.4	174
I23	-225.1	44 ± 7	41 ± 12	24.056 ± 0.023	-14.561 ± 0.054	0.8×0.3	13
I23	-226.0	50 ± 7	38 ± 10	24.093 ± 0.018	-14.578 ± 0.038	0.6×0.3	5
I24*	-221.8	34 ± 7	48 ± 15	0.178 ± 0.036	0.196 ± 0.067	0.8×0.4	8
I25*	-229.3	36 ± 7	46 ± 14	-2.616 ± 0.035	-0.489 ± 0.057	0.7×0.4	14

A.1.3 IC 133: Third epoch

TABLE A.5— IC 133: LSR velocity v_r, peak and integrated flux densities S_p and S_I, position offsets from phase center $\Delta\alpha$ and $\Delta\delta$, size and position angle (PA) of all detected components on 2002 October 30. The components marked with an asterisk are new detected.

	v_r [km s^{-1}]	S$_p$ [$\frac{\mathrm{mJy}}{\mathrm{beam}}$]	S$_I$ [mJy]	$\Delta\alpha$ [mas]	$\Delta\delta$ [mas]	Size [mas]	PA [°]
I1$_?$	-205.8	65 ± 8	46 ± 11	0.042 ± 0.017	-0.077 ± 0.038	0.7×0.3	173
I1$_a$	-206.6	218 ± 9	241 ± 16	0.106 ± 0.008	-0.100 ± 0.014	0.8×0.4	170
I1$_a$	-207.5	202 ± 9	216 ± 16	0.144 ± 0.008	-0.103 ± 0.015	0.8×0.4	171
I1$_a$	-208.3	150 ± 9	157 ± 15	0.152 ± 0.012	-0.091 ± 0.018	0.7×0.5	166
I1$_?$	-209.2	131 ± 8	157 ± 16	0.103 ± 0.012	-0.063 ± 0.025	0.9×0.4	175
I1$_b$	-210.0	315 ± 10	361 ± 18	0.098 ± 0.006	-0.116 ± 0.011	0.8×0.4	170
I1$_b$	-210.8	162 ± 8	197 ± 16	0.131 ± 0.010	-0.068 ± 0.018	0.8×0.5	178
I1$_?$	-211.7	57 ± 8	118 ± 22	0.230 ± 0.030	0.365 ± 0.073	1.3×0.5	1
I1$_?$	-212.5	43 ± 8	44 ± 15	0.162 ± 0.032	0.075 ± 0.070	0.8×0.4	180
I2	-207.5	62 ± 9	92 ± 20	-2.069 ± 0.035	-1.307 ± 0.063	1.1×0.4	157
I2	-208.3	53 ± 8	93 ± 21	-2.217 ± 0.038	-1.177 ± 0.074	1.2×0.5	164
I3$_b$	-220.1	138 ± 8	143 ± 15	-2.059 ± 0.012	0.085 ± 0.020	0.8×0.4	167
I3$_b$	-220.9	109 ± 8	120 ± 15	-2.050 ± 0.014	0.017 ± 0.025	0.8×0.4	172
I3$_b$	-221.8	54 ± 8	46 ± 12	-2.166 ± 0.018	0.022 ± 0.061	1×0.3	178
I3$_b$	-222.6	79 ± 8	78 ± 14	-2.198 ± 0.017	0.086 ± 0.037	0.9×0.4	173
I4	-211.7	29 ± 7	85 ± 28	-2.720 ± 0.099	-2.824 ± 0.123	1.2×0.8	31
I4	-212.5	134 ± 8	184 ± 18	-2.767 ± 0.013	-2.585 ± 0.026	1×0.4	165
I4	-213.4	136 ± 8	156 ± 16	-2.599 ± 0.012	-2.868 ± 0.021	0.8×0.4	169
I5	-209.2	94 ± 8	92 ± 14	-0.860 ± 0.014	-1.893 ± 0.033	0.9×0.4	177
I5	-210.0	50 ± 10	44 ± 16	-0.822 ± 0.036	-0.508 ± 0.056	0.7×0.4	173
I5	-210.8	40 ± 8	46 ± 16	-0.829 ± 0.044	-1.946 ± 0.065	0.7×0.5	6
I6	-208.3	77 ± 8	117 ± 19	6.143 ± 0.026	0.417 ± 0.042	0.9×0.5	165
I6	-209.2	54 ± 8	74 ± 17	6.128 ± 0.033	0.520 ± 0.056	0.9×0.5	170
I6	-210.0	42 ± 9	66 ± 22	6.063 ± 0.073	0.539 ± 0.076	1×0.5	138
I12	-228.5	32 ± 7	78 ± 24	23.209 ± 0.106	-16.081 ± 0.073	1.1×0.7	78
I12	-229.3	153 ± 8	158 ± 14	23.192 ± 0.009	-15.996 ± 0.020	0.9×0.4	173
I12	-230.2	73 ± 8	73 ± 14	23.233 ± 0.019	-16.045 ± 0.036	0.8×0.4	2
I12	-232.7	76 ± 8	105 ± 16	23.064 ± 0.018	-16.039 ± 0.045	1.1×0.4	175
I12	-233.5	85 ± 8	103 ± 16	23.083 ± 0.021	-16.046 ± 0.030	0.8×0.5	177
I17	-208.3	34 ± 8	94 ± 29	1.008 ± 0.083	0.061 ± 0.129	1.4×0.6	25
I22	-222.6	59 ± 8	66 ± 15	24.614 ± 0.020	-15.493 ± 0.065	1.1×0.3	5
I22	-224.3	58 ± 8	48 ± 12	24.688 ± 0.020	-15.268 ± 0.043	0.8×0.4	176
I22	-225.1	61 ± 8	93 ± 18	24.607 ± 0.025	-15.329 ± 0.061	1.2×0.4	8
I26*	-213.4	49 ± 8	54 ± 16	24.409 ± 0.027	-15.729 ± 0.071	1×0.4	180
I26*	-214.2	81 ± 8	81 ± 14	24.387 ± 0.016	-15.656 ± 0.039	0.9×0.4	174
I26*	-215.0	58 ± 8	50 ± 13	24.382 ± 0.021	-15.666 ± 0.047	0.8×0.4	172
I27*	-217.6	73 ± 9	72 ± 16	-2.593 ± 0.021	-0.823 ± 0.045	0.8×0.4	175

TABLE A.6— IC 133: LSR velocity v_r, peak and integrated flux densities S_p and S_I, position offsets from phase center $\Delta\alpha$ and $\Delta\delta$, size and position angle (PA) of all detected components on 2002 November 12. The components marked with an asterisk are new detected.

	$v_{\rm r}$ [km s^{-1}]	S$_p$ [$\frac{\rm mJy}{\rm beam}$]	S$_I$ [mJy]	$\Delta\alpha$ [mas]	$\Delta\delta$ [mas]	Size [mas]	PA [°]
I1$_a$	-206.6	214 ± 8	246 ± 15	0.101 ± 0.007	-0.056 ± 0.013	0.9×0.4	165
I1$_a$	-207.5	181 ± 8	234 ± 16	0.120 ± 0.008	-0.058 ± 0.016	0.9×0.4	166
I1$_a$	-208.3	160 ± 7	189 ± 14	0.137 ± 0.009	-0.082 ± 0.018	0.9×0.4	164
I1$_a$	-209.2	131 ± 7	183 ± 16	0.129 ± 0.011	-0.064 ± 0.022	0.9×0.5	171
I1$_b$	-210.0	287 ± 8	372 ± 17	0.078 ± 0.006	-0.065 ± 0.011	0.9×0.4	167
I1$_b$	-210.8	150 ± 7	229 ± 17	0.112 ± 0.010	-0.059 ± 0.020	1×0.5	169
I1$_?$	-211.7	48 ± 7	149 ± 26	0.258 ± 0.03	0.163 ± 0.107	1.9×0.5	1
I2	-207.5	82 ± 8	97 ± 15	-2.097 ± 0.017	-1.303 ± 0.035	0.9×0.4	165
I2	-208.3	49 ± 7	166 ± 29	-2.148 ± 0.071	-1.129 ± 0.057	1.3×0.8	121
I2	-209.2	34 ± 7	82 ± 23	-2.216 ± 0.079	-1.256 ± 0.069	0.9×0.8	88
I2	-210.0	39 ± 8	80 ± 23	-2.258 ± 0.052	-1.163 ± 0.115	1.4×0.4	162
I3$_b$	-220.1	113 ± 7	143 ± 14	-2.045 ± 0.011	0.164 ± 0.024	1×0.4	170
I3$_b$	-220.9	91 ± 7	114 ± 14	-2.076 ± 0.013	0.124 ± 0.030	0.9×0.4	176
I3$_b$	-221.8	49 ± 7	83 ± 17	-2.043 ± 0.040	0.174 ± 0.042	0.7×0.7	16
I3$_?$	-222.6	69 ± 7	77 ± 13	-2.220 ± 0.019	0.058 ± 0.036	0.9×0.4	163
I4	-212.5	155 ± 7	190 ± 14	-2.791 ± 0.009	-2.506 ± 0.019	1×0.4	162
I4	-213.4	135 ± 7	175 ± 15	-2.63 ± 0.010	-2.781 ± 0.021	1×0.4	166
I6	-208.3	61 ± 7	75 ± 15	6.119 ± 0.027	0.496 ± 0.041	0.9×0.4	157
I6	-209.2	36 ± 7	77 ± 21	6.319 ± 0.077	0.382 ± 0.057	0.9×0.7	77
I6	-210.0	50 ± 8	62 ± 17	5.851 ± 0.036	0.652 ± 0.059	0.9×0.4	158
I12	-228.5	46 ± 7	49 ± 13	23.211 ± 0.031	-16.078 ± 0.049	0.8×0.4	159
I12	-229.3	116 ± 7	141 ± 14	23.235 ± 0.012	-16.032 ± 0.022	0.9×0.4	165
I12	-230.2	67 ± 7	84 ± 14	23.193 ± 0.019	-15.992 ± 0.041	1×0.4	166
I12	-232.7	66 ± 7	83 ± 14	23.005 ± 0.017	-15.948 ± 0.050	1.2×0.3	167
I12	-233.5	97 ± 7	112 ± 13	23.067 ± 0.012	-16.058 ± 0.027	0.9×0.4	173
I17	-207.5	53 ± 7	124 ± 23	0.873 ± 0.055	0.043 ± 0.049	1.1×0.7	52
I17	-208.3	53 ± 7	100 ± 19	1.026 ± 0.042	0.102 ± 0.049	1×0.6	36
I22	-221.8	38 ± 7	64 ± 17	24.711 ± 0.053	-15.392 ± 0.057	0.9×0.6	143
I22	-222.6	66 ± 7	138 ± 19	24.611 ± 0.027	-15.378 ± 0.043	1×0.6	169
I22	-223.4	48 ± 7	90 ± 18	24.561 ± 0.038	-15.399 ± 0.055	0.9×0.6	14
I22	-224.3	28 ± 7	84 ± 26	24.974 ± 0.129	-15.113 ± 0.103	1.5×0.6	54
I22	-225.1	41 ± 6	61 ± 15	24.734 ± 0.033	-15.277 ± 0.061	0.9×0.5	1
I24	-221.8	38 ± 7	38 ± 12	0.200 ± 0.026	0.147 ± 0.070	0.9×0.3	172
I26	-213.4	51 ± 7	62 ± 14	24.314 ± 0.024	-15.554 ± 0.066	1.1×0.3	168
I26	-214.2	81 ± 7	89 ± 13	24.368 ± 0.014	-15.671 ± 0.033	0.9×0.4	168
I26	-215.0	44 ± 7	50 ± 13	24.374 ± 0.037	-15.756 ± 0.043	0.7×0.5	149
I26	-215.9	38 ± 7	35 ± 11	24.395 ± 0.028	-15.602 ± 0.068	0.9×0.3	167
I27	-217.6	27 ± 6	80 ± 24	-2.600 ± 0.079	-0.399 ± 0.128	1.3×0.7	160
I28*	-220.1	50 ± 7	50 ± 12	20.658 ± 0.017	-14.905 ± 0.063	1.1×0.3	175
I29*	-223.4	48 ± 7	65 ± 15	-2.207 ± 0.031	-0.068 ± 0.052	0.9×0.5	168
I29*	-224.3	39 ± 7	34 ± 12	-1.812 ± 0.031	0.308 ± 0.061	0.8×0.3	164

A.1.4 IC 133: Fourth epoch

TABLE A.7— IC 133: LSR velocity v_r, peak and integrated flux densities S_p and S_I, position offsets from phase center $\Delta\alpha$ and $\Delta\delta$, size and position angle (PA) of all detected components on 2003 December 14. The components marked with an asterisk are new detected.

	v_r [km s^{-1}]	S$_p$ [$\frac{\mathrm{mJy}}{\mathrm{beam}}$]	S$_I$ [mJy]	$\Delta\alpha$ [mas]	$\Delta\delta$ [mas]	Size [mas]	PA [°]
I1	-206.6	224 ± 9	236 ± 17	0.104 ± 0.007	0.049 ± 0.016	1×0.3	163
I1	-207.5	256 ± 10	300 ± 20	0.151 ± 0.008	0.096 ± 0.017	1×0.3	163
I1	-208.3	239 ± 9	274 ± 18	0.150 ± 0.007	0.062 ± 0.017	1×0.3	163
I1	-209.2	383 ± 11	402 ± 19	0.104 ± 0.005	0.054 ± 0.011	1×0.3	162
I1	-210.0	394 ± 11	445 ± 21	0.097 ± 0.005	0.060 ± 0.012	1×0.3	164
I1	-210.8	140 ± 9	220 ± 21	0.157 ± 0.012	0.023 ± 0.030	1.2×0.4	172
I1	-211.7	70 ± 8	178 ± 28	0.176 ± 0.023	0.121 ± 0.084	1.7×0.5	3
I2	-207.5	245 ± 11	253 ± 19	-2.070 ± 0.008	-1.037 ± 0.017	1×0.3	161
I2	-208.3	62 ± 9	174 ± 33	-2.060 ± 0.081	-0.849 ± 0.071	1.7×0.5	130
I3	-220.1	102 ± 9	114 ± 16	-2.054 ± 0.016	0.305 ± 0.038	1.1×0.3	162
I3	-220.9	80 ± 9	92 ± 16	-2.060 ± 0.019	0.279 ± 0.045	1×0.3	165
I4	-211.7	68 ± 9	73 ± 16	-2.661 ± 0.031	-2.523 ± 0.057	1.2×0.3	154
I4	-212.5	178 ± 8	230 ± 18	-2.750 ± 0.010	-2.404 ± 0.022	1.1×0.3	160
I4	-213.4	198 ± 9	227 ± 17	-2.649 ± 0.009	-2.572 ± 0.019	1.1×0.3	161
I6	-208.3	46 ± 10	44 ± 16	6.069 ± 0.044	0.710 ± 0.089	1.1×0.3	156
I6	-209.2	38 ± 11	46 ± 21	6.103 ± 0.074	0.703 ± 0.147	1.4×0.3	155
I26	-213.4	37 ± 9	77 ± 25	24.435 ± 0.065	-15.816 ± 0.197	2.1×0.3	163
I26	-214.2	95 ± 8	94 ± 15	24.408 ± 0.015	-15.508 ± 0.035	1×0.3	165
I26	-215.0	94 ± 8	92 ± 14	24.420 ± 0.017	-15.588 ± 0.036	1×0.3	159
I26	-215.9	58 ± 9	53 ± 14	24.424 ± 0.022	-15.490 ± 0.065	1.1×0.3	167
I29	-224.3	63 ± 8	73 ± 16	-1.800 ± 0.026	0.278 ± 0.055	1×0.3	161

TABLE A.8— IC 133: LSR velocity v_r, peak and integrated flux densities S_p and S_I, position offsets from phase center $\Delta\alpha$ and $\Delta\delta$, size and position angle (PA) of all detected components on 2004 January 08. The components marked with an asterisk are new detected.

	$v_{\rm r}$ [km s^{-1}]	S$_p$ [$\frac{\rm mJy}{\rm beam}$]	S$_I$ [mJy]	$\Delta\alpha$ [mas]	$\Delta\delta$ [mas]	Size [mas]	PA [°]
I1	-205.8	39 ± 9	95 ± 28	0.099 ± 0.106	-0.005 ± 0.105	1.2×1.1	52
I1	-206.6	345 ± 10	425 ± 19	0.129 ± 0.007	-0.085 ± 0.014	1.3×0.5	164
I1	-207.5	413 ± 11	509 ± 22	0.173 ± 0.007	-0.086 ± 0.014	1.3×0.5	165
I1	-208.3	377 ± 10	441 ± 19	0.160 ± 0.007	-0.071 ± 0.013	1.2×0.5	164
I1	-209.2	603 ± 11	690 ± 22	0.129 ± 0.005	-0.086 ± 0.009	1.2×0.5	164
I1	-210.0	580 ± 11	727 ± 23	0.126 ± 0.005	-0.079 ± 0.010	1.3×0.5	165
I1	-210.8	235 ± 9	342 ± 21	0.152 ± 0.011	0.013 ± 0.022	1.3×0.6	167
I1	-211.7	139 ± 9	252 ± 24	0.219 ± 0.018	0.131 ± 0.042	1.5×0.6	176
I1	-212.5	46 ± 9	134 ± 34	0.137 ± 0.074	0.018 ± 0.147	1.8×0.9	5
I2	-206.6	57 ± 9	106 ± 25	-2.108 ± 0.064	-1.056 ± 0.087	1.4×0.7	150
I2	-207.5	529 ± 11	620 ± 22	-2.051 ± 0.006	-1.151 ± 0.011	1.3×0.5	161
I2	-208.3	163 ± 10	288 ± 25	-2.128 ± 0.020	-1.052 ± 0.035	1.5×0.7	159
I3	-220.1	105 ± 9	219 ± 25	-2.061 ± 0.029	0.067 ± 0.047	1.4×0.8	4
I3	-220.9	114 ± 9	161 ± 19	-2.044 ± 0.020	0.054 ± 0.043	1.4×0.6	168
I3	-221.8	37 ± 8	128 ± 36	-2.032 ± 0.134	-0.114 ± 0.132	1.5×1.2	133
I3	-222.6	60 ± 9	100 ± 21	-1.885 ± 0.053	0.013 ± 0.068	1.2×0.7	150
I4	-211.7	84 ± 9	199 ± 29	-2.565 ± 0.046	-2.768 ± 0.068	1.7×0.8	152
I4	-212.5	240 ± 9	317 ± 20	-2.722 ± 0.011	-2.569 ± 0.021	1.3×0.5	160
I4	-213.4	282 ± 9	301 ± 17	-2.586 ± 0.008	-2.812 ± 0.015	1.2×0.5	163
I6	-208.3	91 ± 10	135 ± 22	6.127 ± 0.034	0.389 ± 0.053	1.2×0.6	159
I6	-209.2	75 ± 11	118 ± 26	6.159 ± 0.043	0.254 ± 0.087	1.4×0.6	164
I6	-210.0	63 ± 11	121 ± 30	5.965 ± 0.057	0.402 ± 0.102	1.4×0.7	170
I19	-220.1	49 ± 9	83 ± 22	0.120 ± 0.057	0.138 ± 0.097	1.3×0.7	168
I19	-220.9	49 ± 8	112 ± 26	0.258 ± 0.062	-0.053 ± 0.105	1.5×0.8	170
I26	-213.4	54 ± 9	83 ± 21	24.426 ± 0.045	-15.473 ± 0.096	1.4×0.6	169
I26	-214.2	121 ± 9	185 ± 21	24.468 ± 0.023	-15.678 ± 0.041	1.4×0.6	160
I26	-215.0	72 ± 9	96 ± 18	24.50 ± 0.033	-15.801 ± 0.061	1.2×0.6	165
I27	-216.7	36 ± 8	99 ± 30	-2.476 ± 0.090	-1.021 ± 0.175	1.8×0.8	167
I27	-217.6	57 ± 9	97 ± 22	-2.538 ± 0.040	-0.655 ± 0.097	1.5×0.6	172
I29	-224.3	65 ± 9	96 ± 20	-1.762 ± 0.039	0.098 ± 0.068	1.2×0.6	165

A.1.5 M33/19: First epoch

TABLE A.9— M33/19: LSR velocity v_r, peak and integrated flux densities S_p and S_I, position offsets from phase center $\Delta\alpha$ and $\Delta\delta$, size and position angle (PA) of all detected components on 2001 March 27.

	$v_{\rm r}$ [km s^{-1}]	S$_p$ [$\frac{\rm mJy}{\rm beam}$]	S$_I$ [mJy]	$\Delta\alpha$ [mas]	$\Delta\delta$ [mas]	Size [mas]	PA [°]
M1	-133.2	86 ± 7	101 ± 13	5.416 ± 0.014	-0.352 ± 0.031	1×0.4	172
M1	-134.0	162 ± 8	177 ± 14	5.407 ± 0.008	-0.298 ± 0.018	0.9×0.4	170
M2	-133.2	25 ± 7	12 ± 7	0.176 ± 0.046	0.402 ± 0.075	0.7×0.2	151
M2	-134.0	79 ± 8	64 ± 11	0.291 ± 0.018	0.267 ± 0.031	0.8×0.3	157
M2	-134.9	60 ± 7	78 ± 14	0.403 ± 0.022	0.165 ± 0.046	1×0.4	169
M2	-135.7	155 ± 7	188 ± 14	0.338 ± 0.008	0.111 ± 0.02	1×0.4	171
M2	-136.6	186 ± 8	200 ± 14	0.351 ± 0.008	0.191 ± 0.017	1×0.4	166
M2?	-137.4	71 ± 6	144 ± 18	0.341 ± 0.017	0.025 ± 0.054	1.5×0.5	178
M3	-133.2	41 ± 6	83 ± 18	0.377 ± 0.024	-0.166 ± 0.116	1.8×0.4	179
M3	-134.0	86 ± 7	157 ± 19	0.337 ± 0.014	-0.336 ± 0.056	1.6×0.4	178
M3	-134.9	78 ± 6	148 ± 18	0.31 ± 0.014	-0.358 ± 0.059	1.7×0.4	176
M3	-135.7	85 ± 7	96 ± 13	0.304 ± 0.019	-0.808 ± 0.035	1.1×0.4	157
M3	-136.6	136 ± 8	205 ± 17	0.304 ± 0.009	-0.643 ± 0.033	1.4×0.4	173
M3?	-137.4	59 ± 7	52 ± 10	0.389 ± 0.018	-1.005 ± 0.044	1×0.3	165
M3?	-138.2	39 ± 6	78 ± 18	0.409 ± 0.034	-0.186 ± 0.095	1.4×0.5	175
M4	-129.0	26 ± 6	67 ± 20	-0.305 ± 0.046	4.522 ± 0.189	2×0.4	175
M5	-130.7	33 ± 6	75 ± 18	4.146 ± 0.04	-0.935 ± 0.107	1.4×0.5	177

TABLE A.10— M33/19: LSR velocity v_r, peak and integrated flux densities S_p and S_I, position offsets from phase center $\Delta\alpha$ and $\Delta\delta$, size and position angle (PA) of all detected components on 2001 April 05.

	$v_{\rm r}$ [km s^{-1}]	S$_p$ [$\frac{\rm mJy}{\rm beam}$]	S$_I$ [mJy]	$\Delta\alpha$ [mas]	$\Delta\delta$ [mas]	Size [mas]	PA [°]
M1	-133.2	51 ± 7	27 ± 9	5.373 ± 0.018	-0.279 ± 0.039	0.7×0.3	164
M1	-134.0	207 ± 8	180 ± 13	5.372 ± 0.006	-0.329 ± 0.015	0.9×0.3	172
M2	-133.2	39 ± 7	33 ± 12	0.306 ± 0.024	0.036 ± 0.073	0.9×0.3	178
M2	-134.0	109 ± 8	127 ± 16	0.317 ± 0.011	0.089 ± 0.036	1.1×0.3	173
M2	-134.9	144 ± 8	132 ± 13	0.32 ± 0.009	0.08 ± 0.02	0.9×0.3	168
M2	-135.7	140 ± 8	112 ± 12	0.316 ± 0.008	0.082 ± 0.02	0.9×0.3	167
M2	-136.6	222 ± 9	198 ± 14	0.314 ± 0.006	0.125 ± 0.014	0.9×0.3	167
M2	-137.4	86 ± 8	75 ± 12	0.32 ± 0.012	0.189 ± 0.033	0.9×0.3	175
M3	-134.9	60 ± 8	63 ± 14	0.104 ± 0.037	-0.715 ± 0.048	1×0.3	144
M3	-135.7	51 ± 8	63 ± 16	0.096 ± 0.049	-0.693 ± 0.057	1.1×0.3	140
M3	-136.6	97 ± 9	116 ± 17	0.039 ± 0.028	-0.609 ± 0.034	1.1×0.3	142
M3	-137.4	57 ± 8	66 ± 14	0.181 ± 0.034	-0.746 ± 0.054	1.1×0.3	151
M3?	-138.2	36 ± 7	62 ± 18	0.296 ± 0.033	-0.076 ± 0.126	1.5×0.4	5
M3?	-139.1	38 ± 7	40 ± 13	0.321 ± 0.027	-0.266 ± 0.084	1×0.3	179
M3?	-139.9	35 ± 7	32 ± 12	0.294 ± 0.028	-0.334 ± 0.085	0.9×0.3	179

A.1.6 M33/19: Second epoch

Table A.11— M33/19: LSR velocity v_r, peak and integrated flux densities S_p and S_I, position offsets from phase center $\Delta\alpha$ and $\Delta\delta$, size and position angle (PA) of all detected components on 2002 January 28.

	v_r [km s^{-1}]	S$_p$ [$\frac{\mathrm{mJy}}{\mathrm{beam}}$]	S$_I$ [mJy]	$\Delta\alpha$ [mas]	$\Delta\delta$ [mas]	Size [mas]	PA [°]
M1	-133.2	69 ± 7	97 ± 15	5.426 ± 0.015	-0.318 ± 0.031	0.7×0.4	1
M1	-134	132 ± 8	182 ± 17	5.432 ± 0.010	-0.294 ± 0.016	0.6×0.4	178
M2	-134.0	31 ± 8	32 ± 14	0.491 ± 0.056	0.221 ± 0.050	0.6×0.3	51
M2	-134.9	34 ± 7	32 ± 12	0.419 ± 0.038	0.157 ± 0.044	0.6×0.3	38
M3	-134.0	59 ± 7	151 ± 25	0.360 ± 0.021	-0.16 ± 0.067	1.3×0.4	176
M3	-134.9	39 ± 7	128 ± 28	0.325 ± 0.030	-0.311 ± 0.113	1.6×0.4	175
M3	-135.7	58 ± 7	74 ± 15	0.338 ± 0.019	-0.854 ± 0.037	0.7×0.3	169
M3	-136.6	98 ± 7	191 ± 20	0.406 ± 0.015	-0.807 ± 0.025	0.8×0.5	4
M3	-137.4	102 ± 7	183 ± 20	0.375 ± 0.015	-0.809 ± 0.022	0.7×0.5	13
M4	-129.0	75 ± 7	133 ± 18	-0.312 ± 0.015	4.699 ± 0.035	0.9×0.4	172
M4	-129.8	43 ± 7	104 ± 22	-0.304 ± 0.041	4.699 ± 0.051	0.9×0.5	31

Table A.12— M33/19: LSR velocity v_r, peak and integrated flux densities S_p and S_I, position offsets from phase center $\Delta\alpha$ and $\Delta\delta$, size and position angle (PA) of all detected components on 2002 February 03.

	v_r [km s^{-1}]	S$_p$ [$\frac{\mathrm{mJy}}{\mathrm{beam}}$]	S$_I$ [mJy]	$\Delta\alpha$ [mas]	$\Delta\delta$ [mas]	Size [mas]	PA [°]
M1	-133.2	71 ± 7	79 ± 13	5.399 ± 0.013	-0.300 ± 0.036	0.8×0.3	177
M1	-134.0	202 ± 8	239 ± 16	5.404 ± 0.006	-0.295 ± 0.014	0.8×0.3	176
M2	-134.0	57 ± 8	93 ± 19	0.331 ± 0.025	0.051 ± 0.054	0.9×0.4	169
M2	-134.9	35 ± 7	46 ± 15	0.331 ± 0.041	0.117 ± 0.082	1×0.3	157
M2	-136.6	29 ± 7	48 ± 17	0.383 ± 0.052	0.361 ± 0.138	1.4×0.3	162
M3	-134.9	53 ± 7	78 ± 16	0.293 ± 0.018	-0.765 ± 0.055	1×0.3	1
M3	-135.7	40 ± 7	85 ± 22	0.325 ± 0.027	-0.755 ± 0.113	1.5×0.3	174
M3	-136.6	70 ± 7	98 ± 16	0.320 ± 0.014	-0.754 ± 0.042	1×0.3	177
M3	-137.4	79 ± 7	141 ± 18	0.302 ± 0.012	-0.67 ± 0.046	1.2×0.3	4
M3	-137.4	21 ± 7	35 ± 17	0.643 ± 0.109	-0.732 ± 0.065	0.8×0.5	86
M4	-129.0	61 ± 7	102 ± 17	-0.333 ± 0.017	4.823 ± 0.049	1×0.4	180
M4	-129.8	70 ± 7	95 ± 15	-0.314 ± 0.017	4.835 ± 0.031	0.7×0.4	180
M5	-130.7	52 ± 7	74 ± 15	4.010 ± 0.019	-1.241 ± 0.051	0.9×0.3	175

A.1.7 M33/19: Third epoch

TABLE A.13— M33/19: LSR velocity v_r, peak and integrated flux densities S_p and S_I, position offsets from phase center $\Delta\alpha$ and $\Delta\delta$, size and position angle (PA) of all detected components on 2002 October 30.

	v_r [km s^{-1}]	S$_p$ [$\frac{\mathrm{mJy}}{\mathrm{beam}}$]	S$_I$ [mJy]	$\Delta\alpha$ [mas]	$\Delta\delta$ [mas]	Size [mas]	PA [°]
M1	-133.2	139 ± 9	146 ± 15	5.391 ± 0.009	-0.250 ± 0.025	1×0.3	172
M1	-134.0	406 ± 12	448 ± 22	5.401 ± 0.005	-0.317 ± 0.012	1×0.4	173
M2	-134.0	82 ± 12	90 ± 22	0.349 ± 0.021	0.241 ± 0.062	1×0.3	175
M2	-136.6	42 ± 9	86 ± 26	0.250 ± 0.030	0.033 ± 0.178	2×0.3	0
M3	-132.4	20 ± 7	69 ± 31	0.876 ± 0.141	-0.464 ± 0.264	1.9×0.6	25
M3	-133.2	49 ± 8	75 ± 19	0.326 ± 0.047	-0.780 ± 0.054	0.8×0.6	19
M3	-134.0	160 ± 12	172 ± 22	0.338 ± 0.014	-0.821 ± 0.025	0.8×0.4	169
M3	-134.9	251 ± 9	422 ± 24	0.338 ± 0.006	-0.782 ± 0.021	1.3×0.4	175
M3	-135.7	305 ± 10	376 ± 19	0.336 ± 0.005	-0.868 ± 0.014	1×0.4	173
M3	-136.6	130 ± 9	153 ± 18	0.400 ± 0.016	-0.872 ± 0.022	0.7×0.5	168
M3	-137.4	163 ± 8	194 ± 16	0.368 ± 0.010	-0.824 ± 0.019	0.9×0.4	172
M3	-138.2	43 ± 8	52 ± 16	0.314 ± 0.034	-0.810 ± 0.07	0.9×0.4	1
M4	-129.0	64 ± 8	84 ± 17	-0.285 ± 0.023	4.756 ± 0.061	1.2×0.4	168
M4	-129.8	161 ± 9	176 ± 16	-0.337 ± 0.009	4.832 ± 0.021	0.9×0.4	172
M4	-130.7	39 ± 8	32 ± 12	-0.390 ± 0.026	4.992 ± 0.074	0.9×0.3	171
M5	-133.2	43 ± 8	92 ± 24	4.260 ± 0.079	-0.793 ± 0.054	1×0.7	82
M5	-132.4	38 ± 7	82 ± 22	4.071 ± 0.054	-1.233 ± 0.083	1×0.6	9

TABLE A.14— M33/19: LSR velocity v_r, peak and integrated flux densities S_p and S_I, position offsets from phase center $\Delta\alpha$ and $\Delta\delta$, size and position angle (PA) of all detected components on 2002 November 12.

	v_r [km s^{-1}]	S$_p$ [$\frac{\mathrm{mJy}}{\mathrm{beam}}$]	S$_I$ [mJy]	$\Delta\alpha$ [mas]	$\Delta\delta$ [mas]	Size [mas]	PA [°]
M1	-133.2	108 ± 7	119 ± 14	5.383 ± 0.012	-0.261 ± 0.026	0.9×0.3	164
M1	-134.0	331 ± 9	403 ± 18	5.406 ± 0.005	-0.274 ± 0.011	1×0.4	168
M2	-134.0	83 ± 9	66 ± 13	0.329 ± 0.014	0.290 ± 0.037	0.8×0.3	170
M2	-134.9	95 ± 8	100 ± 15	0.304 ± 0.012	0.290 ± 0.035	1×0.3	175
M3	-134.0	119 ± 9	142 ± 17	0.342 ± 0.011	-0.797 ± 0.034	1.1×0.3	172
M3	-134.9	249 ± 8	290 ± 16	0.338 ± 0.006	-0.811 ± 0.012	0.9×0.4	165
M3	-135.7	312 ± 9	368 ± 17	0.347 ± 0.005	-0.827 ± 0.011	1×0.4	165
M3	-136.6	197 ± 8	236 ± 15	0.325 ± 0.007	-0.778 ± 0.015	0.9×0.4	167
M3	-137.4	182 ± 8	240 ± 16	0.332 ± 0.008	-0.808 ± 0.017	1×0.4	165
M3	-138.2	51 ± 7	63 ± 14	0.339 ± 0.024	-0.855 ± 0.057	1×0.4	168
M4	-129.0	66 ± 7	79 ± 14	-0.319 ± 0.022	4.858 ± 0.048	1.1×0.3	161
M4	-129.8	162 ± 8	179 ± 14	-0.344 ± 0.007	4.905 ± 0.019	1×0.3	170
M4	-130.7	39 ± 7	61 ± 16	-0.345 ± 0.023	5.108 ± 0.116	1.6×0.3	176
M6	-134.0	57 ± 9	67 ± 17	0.545 ± 0.026	-2.508 ± 0.070	1.1×0.3	167
M6	-134.9	83 ± 8	103 ± 16	0.476 ± 0.016	-2.466 ± 0.042	1×0.4	170

A.1.8 M33/19: Fourth epoch

TABLE A.15— M33/19: LSR velocity v_r, peak and integrated flux densities S_p and S_I, position offsets from phase center $\Delta\alpha$ and $\Delta\delta$, size and position angle (PA) of all detected components on 2003 December 14.

	v_r [km s^{-1}]	S$_p$ [$\frac{\mathrm{mJy}}{\mathrm{beam}}$]	S$_I$ [mJy]	$\Delta\alpha$ [mas]	$\Delta\delta$ [mas]	Size [mas]	PA [°]
M1	-133.2	44 ± 8	69 ± 20	5.443 ± 0.031	-0.037 ± 0.119	1.5×0.3	171
M1	-134.0	207 ± 10	204 ± 17	5.432 ± 0.008	-0.112 ± 0.018	0.9×0.3	166
M2	-134.0	124 ± 10	125 ± 17	0.377 ± 0.014	0.175 ± 0.030	0.9×0.3	161
M2	-134.9	100 ± 9	270 ± 32	0.404 ± 0.019	-0.278 ± 0.074	2×0.4	171
M3	-134.0	52 ± 9	115 ± 28	0.459 ± 0.097	-0.86 ± 0.089	1.7×0.4	132
M3	-134.9	99 ± 10	56 ± 12	0.301 ± 0.017	-0.717 ± 0.026	0.7×0.2	150
M3	-135.7	265 ± 10	273 ± 18	0.391 ± 0.006	-0.709 ± 0.016	1×0.3	167
M3	-136.6	272 ± 10	294 ± 18	0.365 ± 0.007	-0.687 ± 0.015	1×0.3	161
M3	-137.4	220 ± 10	222 ± 17	0.363 ± 0.007	-0.695 ± 0.018	1×0.3	164
M3	-138.2	82 ± 9	78 ± 14	0.329 ± 0.018	-0.656 ± 0.040	0.9×0.3	162
M5	-132.4	40 ± 8	83 ± 24	4.153 ± 0.037	-1.351 ± 0.122	1.4×0.4	179
M7	-134.9	52 ± 9	96 ± 25	4.401 ± 0.030	0.084 ± 0.104	1.4×0.4	177

TABLE A.16— M33/19: LSR velocity v_r, peak and integrated flux densities S_p and S_I, position offsets from phase center $\Delta\alpha$ and $\Delta\delta$, size and position angle (PA) of all detected components on 2004 January 08.

	v_r [km s^{-1}]	S$_p$ [$\frac{\mathrm{mJy}}{\mathrm{beam}}$]	S$_I$ [mJy]	$\Delta\alpha$ [mas]	$\Delta\delta$ [mas]	Size [mas]	PA [°]
M1	-133.2	80 ± 9	82 ± 16	5.455 ± 0.024	-0.280 ± 0.056	1.2×0.4	163
M1	-134.0	281 ± 10	294 ± 18	5.506 ± 0.008	-0.355 ± 0.017	1.2×0.4	162
M1	-134.9	144 ± 11	181 ± 22	4.459 ± 0.018	-0.029 ± 0.037	1.2×0.5	166
M3	-134.0	189 ± 9	361 ± 26	0.429 ± 0.012	-0.434 ± 0.035	1.7×0.5	175
M3	-134.9	327 ± 11	547 ± 26	0.429 ± 0.008	-0.726 ± 0.022	1.6×0.5	169
M3	-135.7	567 ± 12	707 ± 24	0.422 ± 0.005	-0.856 ± 0.011	1.3×0.5	163
M3	-136.6	504 ± 11	574 ± 22	0.417 ± 0.005	-0.889 ± 0.012	1.2×0.4	165
M3	-137.4	414 ± 11	486 ± 21	0.429 ± 0.006	-0.891 ± 0.013	1.2×0.5	165
M3	-138.2	111 ± 9	190 ± 22	0.437 ± 0.023	-0.828 ± 0.048	1.5×0.6	164
M3	-139.1	49 ± 9	41 ± 14	0.425 ± 0.038	-0.739 ± 0.073	0.9×0.4	168
M4	-129.8	43 ± 8	71 ± 21	-0.251 ± 0.055	4.967 ± 0.110	1.4×0.6	166
M4	-130.7	32 ± 9	64 ± 26	-0.244 ± 0.098	4.899 ± 0.141	1.2×0.8	178
M5	-131.5	64 ± 9	87 ± 19	4.141 ± 0.036	-1.295 ± 0.074	1.3×0.5	164
M5	-132.4	70 ± 9	109 ± 20	4.274 ± 0.029	-1.24 ± 0.069	1.3×0.6	179

A.2 Corrected Positions

A.2.1 IC 133: Second epoch

TABLE A.17— IC 133: LSR velocity v_r, peak and integrated flux densities S_p and S_I, position offsets from phase center $\Delta\alpha$ and $\Delta\delta$, size and position angle (PA) of all detected components on 2002 January 28. The components marked with an asterisk are new detected.

	$v_{\rm r}$ [km s^{-1}]	S$_p$ [$\frac{\rm mJy}{\rm beam}$]	S$_I$ [mJy]	$\Delta\alpha$ [mas]	$\Delta\delta$ [mas]	Size [mas]	PA [°]
I1	-206.6	136 ± 8	160 ± 15	0.140 ± 0.010	-0.094 ± 0.015	0.6×0.4	170
I1	-207.5	154 ± 8	177 ± 15	0.182 ± 0.009	-0.079 ± 0.013	0.6×0.4	174
I1	-208.3	70 ± 7	144 ± 21	0.212 ± 0.027	-0.037 ± 0.033	0.8×0.5	29
I1	-209.2	60 ± 7	129 ± 22	0.148 ± 0.032	-0.072 ± 0.042	0.9×0.5	27
I1	-210.0	225 ± 8	329 ± 19	0.103 ± 0.008	-0.078 ± 0.010	0.7×0.5	1
I1	-210.8	162 ± 8	211 ± 16	0.077 ± 0.009	-0.085 ± 0.013	0.6×0.4	177
I1	-211.7	37 ± 7	117 ± 28	0.239 ± 0.040	0.387 ± 0.104	1.3×0.5	0
I2	-207.5	124 ± 8	180 ± 17	-2.075 ± 0.012	-1.251 ± 0.019	0.7×0.4	172
I2	-208.3	63 ± 7	111 ± 19	-2.063 ± 0.034	-1.265 ± 0.030	0.8×0.5	127
I2	-209.2	28 ± 7	59 ± 22	-2.209 ± 0.079	-1.368 ± 0.100	1.1×0.4	144
I3	-220.1	82 ± 7	140 ± 19	-1.970 ± 0.023	0.059 ± 0.024	0.6×0.6	162
I3	-220.9	65 ± 7	86 ± 15	-2.046 ± 0.020	0.075 ± 0.033	0.7×0.4	169
I3	-221.8	64 ± 7	95 ± 17	-2.113 ± 0.023	0.164 ± 0.032	0.7×0.5	0
I4	-212.5	114 ± 7	203 ± 19	-2.742 ± 0.013	-2.575 ± 0.023	0.9×0.4	164
I4	-213.4	63 ± 7	81 ± 15	-2.620 ± 0.018	-2.848 ± 0.038	0.8×0.3	169
I5	-209.2	68 ± 8	88 ± 16	-0.816 ± 0.023	-1.989 ± 0.027	0.6×0.5	9
I5	-210.0	105 ± 8	154 ± 19	-0.845 ± 0.017	-2.018 ± 0.022	0.7×0.5	153
I5	-210.8	37 ± 8	48 ± 16	-0.834 ± 0.050	-1.991 ± 0.047	0.7×0.4	131
I6	-208.3	65 ± 7	97 ± 17	6.117 ± 0.027	0.45 ± 0.028	0.6×0.6	154
I6	-209.2	60 ± 8	99 ± 19	6.098 ± 0.029	0.442 ± 0.035	0.7×0.5	152
I6	-210.0	45 ± 8	62 ± 18	5.932 ± 0.040	0.575 ± 0.055	0.8×0.4	151
I12	-229.3	64 ± 7	81 ± 15	23.164 ± 0.021	-16.021 ± 0.030	0.6×0.4	165
I14	-231.0	26 ± 7	59 ± 22	2.894 ± 0.072	-6.355 ± 0.100	1×0.5	152
I19	-219.2	45 ± 7	65 ± 16	0.160 ± 0.031	-0.07 ± 0.048	0.7×0.4	171
I19	-220.1	123 ± 8	177 ± 17	0.134 ± 0.013	-0.044 ± 0.017	0.7×0.5	165
I19	-220.9	47 ± 7	62 ± 15	0.153 ± 0.033	-0.049 ± 0.044	0.7×0.4	150
I20	-220.1	43 ± 8	38 ± 13	24.608 ± 0.028	-15.376 ± 0.042	0.6×0.3	14
I21	-222.6	34 ± 7	94 ± 25	-2.571 ± 0.055	-0.507 ± 0.099	1.3×0.5	22
I22	-222.6	46 ± 7	69 ± 16	24.568 ± 0.038	-15.587 ± 0.038	0.6×0.5	135
I23	-226.0	38 ± 7	73 ± 19	24.113 ± 0.047	-14.622 ± 0.060	0.9×0.5	149

TABLE A.18— IC 133: LSR velocity v_r, peak and integrated flux densities S_p and S_I, position offsets from phase center $\Delta\alpha$ and $\Delta\delta$, size and position angle (PA) of all detected components on 2002 February 03. The components marked with an asterisk are new detected.

	$v_{\rm r}$ [km s^{-1}]	S$_p$ [$\frac{\rm mJy}{\rm beam}$]	S$_I$ [mJy]	$\Delta\alpha$ [mas]	$\Delta\delta$ [mas]	Size [mas]	PA [°]
I1	-206.6	123 ± 9	123 ± 15	0.128 ± 0.012	-0.158 ± 0.029	1×0.4	168
I1	-207.5	159 ± 9	183 ± 18	0.18 ± 0.01	-0.06 ± 0.027	1.1×0.4	169
I2	-207.5	127 ± 9	126 ± 16	-2.059 ± 0.012	-1.297 ± 0.032	1×0.3	167
I17	-207.5	39 ± 9	63 ± 22	1.329 ± 0.071	0.062 ± 0.106	1.2×0.4	150
I6	-207.5	46 ± 9	53 ± 18	6.123 ± 0.03	0.485 ± 0.109	1.3×0.3	173
I1	-208.3	85 ± 9	127 ± 20	0.18 ± 0.022	-0.227 ± 0.053	1.3×0.4	166
I2	-208.3	74 ± 9	97 ± 18	-2.1 ± 0.024	-1.296 ± 0.052	1.1×0.4	168
I17	-208.3	48 ± 9	46 ± 15	1.223 ± 0.03	0.336 ± 0.091	1.2×0.3	167
I6	-208.3	62 ± 9	85 ± 19	6.129 ± 0.025	0.331 ± 0.076	1.3×0.4	170
I1	-209.2	76 ± 9	93 ± 18	0.114 ± 0.021	-0.134 ± 0.056	1.2×0.4	169
I2	-209.2	53 ± 9	76 ± 19	-2.166 ± 0.039	-1.23 ± 0.067	1×0.5	161
I5	-209.2	68 ± 9	58 ± 14	-0.83 ± 0.019	-2.058 ± 0.054	1×0.3	171
I6	-209.2	46 ± 9	78 ± 22	6.159 ± 0.048	0.55 ± 0.081	1×0.6	166
I1	-210.0	227 ± 10	288 ± 20	0.123 ± 0.008	-0.131 ± 0.021	1.1×0.4	168
I2	-210.0	57 ± 10	67 ± 19	-2.124 ± 0.045	-1.295 ± 0.061	0.9×0.4	149
I5	-210.0	107 ± 10	121 ± 19	-0.84 ± 0.014	-1.959 ± 0.05	1.3×0.3	171
I6	-210.0	68 ± 10	87 ± 20	5.964 ± 0.031	0.48 ± 0.072	1.2×0.4	163
I1	-210.8	148 ± 9	204 ± 20	0.108 ± 0.013	-0.099 ± 0.029	1.1×0.4	165
I1	-211.7	50 ± 8	83 ± 20	0.297 ± 0.027	0.199 ± 0.1	1.5×0.4	177
I4	-211.7	39 ± 8	45 ± 16	-2.752 ± 0.04	-2.841 ± 0.112	1.2×0.3	166
I7	-212.5	35 ± 8	55 ± 20	0.255 ± 0.055	0.399 ± 0.111	1.1×0.5	166
I4	-212.5	135 ± 9	183 ± 18	-2.765 ± 0.014	-2.549 ± 0.03	1.2×0.4	163
I4	-213.4	64 ± 9	90 ± 19	-2.575 ± 0.035	-2.88 ± 0.056	1.1×0.4	153
I19	-220.1	185 ± 9	236 ± 18	0.088 ± 0.01	-0.061 ± 0.023	1.1×0.4	165
I3	-220.1	72 ± 9	99 ± 19	-2.032 ± 0.026	0.135 ± 0.056	1.1×0.4	168
I19	-220.9	64 ± 9	95 ± 20	0.143 ± 0.031	-0.032 ± 0.068	1.2×0.4	162
I3	-220.9	69 ± 9	71 ± 16	-2.112 ± 0.021	0.198 ± 0.059	1.1×0.3	168
I20	-220.9	44 ± 9	58 ± 18	24.475 ± 0.048	-15.058 ± 0.103	1.3×0.4	160
I24	-221.8	30 ± 8	67 ± 25	0.174 ± 0.077	0.265 ± 0.132	1.2×0.7	171
I3	-221.8	77 ± 8	91 ± 17	-2.1 ± 0.019	0.069 ± 0.055	1.2×0.3	168
I23	-225.1	42 ± 8	46 ± 15	24.121 ± 0.028	-14.692 ± 0.111	1.3×0.3	173
I23	-226.0	58 ± 8	46 ± 12	24.083 ± 0.019	-14.597 ± 0.057	0.9×0.3	173
I12	-229.3	55 ± 8	80 ± 18	23.167 ± 0.033	-15.954 ± 0.085	1.4×0.4	164
I15	-229.3	27 ± 8	49 ± 21	-2.708 ± 0.095	-0.635 ± 0.117	1×0.6	149

A.2.2 IC 133: Third epoch

TABLE A.19— IC 133: LSR velocity v_r, peak and integrated flux densities S_p and S_I, position offsets from phase center $\Delta\alpha$ and $\Delta\delta$, size and position angle (PA) of all detected components on 2002 October 30. The components marked with an asterisk are new detected.

	v_{r} [km s^{-1}]	S$_p$ [$\frac{\mathrm{mJy}}{\mathrm{beam}}$]	S$_I$ [mJy]	$\Delta\alpha$ [mas]	$\Delta\delta$ [mas]	Size [mas]	PA [°]
I1	-205.8	55 ± 8	54 ± 14	0.06 ± 0.03	-0.1 ± 0.042	0.7×0.5	6
I1	-206.6	253 ± 9	264 ± 16	0.125 ± 0.006	-0.129 ± 0.012	0.8×0.4	173
I1	-207.5	231 ± 9	232 ± 16	0.149 ± 0.007	-0.14 ± 0.014	0.8×0.4	174
I2	-207.5	77 ± 9	91 ± 17	-2.029 ± 0.021	-1.403 ± 0.05	1×0.4	171
I1	-208.3	170 ± 9	166 ± 15	0.156 ± 0.01	-0.126 ± 0.017	0.8×0.4	172
I2	-208.3	60 ± 9	79 ± 18	-2.146 ± 0.033	-1.339 ± 0.052	0.9×0.5	166
I17	-208.3	43 ± 8	71 ± 21	1.19 ± 0.052	0.098 ± 0.074	0.9×0.6	173
I6	-208.3	81 ± 9	105 ± 18	6.131 ± 0.025	0.388 ± 0.037	0.9×0.5	162
I1	-209.2	151 ± 8	168 ± 15	0.114 ± 0.01	-0.099 ± 0.021	0.9×0.4	174
I5	-209.2	106 ± 8	98 ± 14	-0.861 ± 0.012	-1.999 ± 0.028	0.9×0.4	174
I6	-209.2	65 ± 8	75 ± 16	6.167 ± 0.027	0.454 ± 0.043	0.8×0.5	176
I1	-210.0	352 ± 10	366 ± 17	0.099 ± 0.005	-0.137 ± 0.01	0.8×0.4	172
I6	-210.0	46 ± 9	76 ± 23	6.108 ± 0.071	0.539 ± 0.056	0.8×0.7	103
I5	-210.0	46 ± 9	59 ± 19	-0.847 ± 0.037	-0.503 ± 0.089	1×0.4	3
I1	-210.8	182 ± 8	203 ± 16	0.139 ± 0.008	-0.092 ± 0.017	0.9×0.4	1
I2	-210.8	30 ± 8	29 ± 14	-0.777 ± 0.06	-1.94 ± 0.086	0.8×0.4	25
I1	-211.7	71 ± 8	125 ± 20	0.243 ± 0.02	0.349 ± 0.064	1.4×0.4	6
I4	-211.7	50 ± 8	62 ± 16	-2.708 ± 0.033	-2.764 ± 0.066	1×0.4	164
I4	-212.5	151 ± 8	183 ± 17	-2.756 ± 0.011	-2.604 ± 0.022	1×0.4	165
I1	-212.5	60 ± 8	57 ± 14	0.186 ± 0.021	-0.009 ± 0.054	0.9×0.4	2
I4	-213.4	160 ± 8	161 ± 14	-2.603 ± 0.009	-2.875 ± 0.019	0.9×0.4	167
I26	-213.4	55 ± 8	56 ± 14	24.382 ± 0.026	-15.803 ± 0.055	0.9×0.4	171
I26	-214.2	101 ± 8	83 ± 13	24.375 ± 0.012	-15.701 ± 0.027	0.8×0.3	177
I26	-215.0	70 ± 8	48 ± 11	24.435 ± 0.019	-15.707 ± 0.033	0.7×0.3	164
I27	-217.6	83 ± 10	77 ± 16	-2.588 ± 0.02	-0.848 ± 0.038	0.8×0.4	172
I3	-220.1	154 ± 8	139 ± 13	-2.035 ± 0.009	0.037 ± 0.018	0.8×0.4	172
I3	-220.9	134 ± 8	131 ± 14	-2.052 ± 0.011	0.002 ± 0.02	0.8×0.4	177
I3	-221.8	68 ± 8	54 ± 12	-2.149 ± 0.016	-0.049 ± 0.042	0.9×0.3	175
I3	-222.6	92 ± 8	87 ± 14	-2.201 ± 0.016	0.036 ± 0.03	0.8×0.4	170
I22	-222.6	71 ± 8	81 ± 15	24.621 ± 0.019	-15.499 ± 0.05	1×0.4	7
I22	-224.3	65 ± 8	52 ± 12	24.731 ± 0.018	-15.367 ± 0.04	0.8×0.3	176
I22	-225.1	63 ± 8	80 ± 16	24.642 ± 0.021	-15.336 ± 0.06	1.1×0.4	4
I12	-228.5	37 ± 7	90 ± 24	23.06 ± 0.096	-16.128 ± 0.06	1.2×0.7	81
I12	-229.3	179 ± 8	162 ± 13	23.23 ± 0.007	-16.066 ± 0.017	0.9×0.4	174
I12	-230.2	80 ± 8	73 ± 13	23.25 ± 0.016	-16.096 ± 0.033	0.8×0.4	1
I12	-232.7	91 ± 8	119 ± 16	23.083 ± 0.015	-16.075 ± 0.037	1×0.4	180
I12	-233.5	98 ± 8	116 ± 16	23.071 ± 0.017	-16.067 ± 0.028	0.8×0.5	177

TABLE A.20— IC 133: LSR velocity v_r, peak and integrated flux densities S_p and S_I, position offsets from phase center $\Delta\alpha$ and $\Delta\delta$, size and position angle (PA) of all detected components on 2002 November 12. The components marked with an asterisk are new detected.

	$v_{\rm r}$ [km s^{-1}]	S$_p$ [$\frac{\rm mJy}{\rm beam}$]	S$_I$ [mJy]	$\Delta\alpha$ [mas]	$\Delta\delta$ [mas]	Size [mas]	PA [°]
I1	-205.8	30 ± 7	63 ± 20	0.41 ± 0.099	-0.037 ± 0.064	1×0.7	97
I1	-206.6	229 ± 8	270 ± 15	0.131 ± 0.007	-0.113 ± 0.013	0.9×0.4	167
I1	-207.5	210 ± 8	245 ± 15	0.151 ± 0.007	-0.116 ± 0.013	0.9×0.4	166
I2	-207.5	85 ± 8	101 ± 15	-2.079 ± 0.016	-1.388 ± 0.039	1×0.3	166
I17	-207.5	40 ± 7	123 ± 28	0.948 ± 0.102	0.037 ± 0.054	1.3×0.7	84
I1	-208.3	183 ± 8	198 ± 14	0.166 ± 0.008	-0.117 ± 0.015	0.9×0.4	165
I2	-208.3	46 ± 7	134 ± 27	-2.162 ± 0.065	-1.185 ± 0.061	1.1×0.8	129
I17	-208.3	45 ± 7	86 ± 20	1.186 ± 0.055	0.084 ± 0.049	0.8×0.7	116
I6	-208.3	80 ± 8	84 ± 14	6.129 ± 0.019	0.461 ± 0.03	0.8×0.4	162
I1	-209.2	150 ± 7	198 ± 15	0.15 ± 0.01	-0.109 ± 0.019	0.9×0.4	171
I5	-209.2	67 ± 7	88 ± 15	-0.896 ± 0.024	-1.911 ± 0.041	0.9×0.4	160
I6	-209.2	58 ± 7	63 ± 14	6.1 ± 0.025	0.423 ± 0.042	0.8×0.4	162
I1	-210.0	314 ± 8	396 ± 17	0.106 ± 0.005	-0.111 ± 0.01	0.9×0.4	167
I5	-210.0	101 ± 9	106 ± 15	-0.89 ± 0.015	-1.974 ± 0.032	0.9×0.4	166
I2	-210.0	37 ± 8	78 ± 24	-2.322 ± 0.068	-1.185 ± 0.13	1.5×0.4	156
I6	-210.0	60 ± 8	70 ± 16	5.959 ± 0.03	0.567 ± 0.05	0.9×0.4	158
I1	-210.8	169 ± 8	217 ± 15	0.124 ± 0.009	-0.117 ± 0.017	0.9×0.4	168
I1	-211.7	52 ± 7	142 ± 24	0.295 ± 0.031	0.181 ± 0.084	1.5×0.6	2
I4	-212.5	169 ± 7	211 ± 15	-2.756 ± 0.008	-2.563 ± 0.018	1×0.4	164
I4	-213.4	153 ± 7	184 ± 14	-2.6 ± 0.009	-2.873 ± 0.018	0.9×0.4	166
I26	-213.4	46 ± 7	54 ± 14	24.32 ± 0.029	-15.509 ± 0.075	1.2×0.3	165
I26	-214.2	84 ± 7	81 ± 12	24.386 ± 0.015	-15.72 ± 0.031	0.9×0.3	162
I26	-215.0	56 ± 7	69 ± 14	24.433 ± 0.031	-15.9 ± 0.036	0.7×0.5	147
I26	-215.9	40 ± 7	32 ± 11	24.455 ± 0.025	-15.781 ± 0.063	0.9×0.3	166
I27	-217.6	36 ± 7	68 ± 18	-2.616 ± 0.041	-0.608 ± 0.091	1.1×0.5	177
I3	-220.1	124 ± 7	143 ± 14	-2.005 ± 0.011	0.104 ± 0.02	0.8×0.4	166
I28	-220.1	51 ± 7	57 ± 13	20.71 ± 0.02	-14.992 ± 0.072	1.2×0.3	171
I3	-220.9	90 ± 7	117 ± 15	-2.056 ± 0.015	0.044 ± 0.031	0.9×0.4	1
I3	-221.8	58 ± 7	79 ± 15	-2.094 ± 0.027	0.115 ± 0.04	0.8×0.5	175
I24	-221.8	42 ± 7	41 ± 12	0.243 ± 0.029	0.009 ± 0.054	0.8×0.4	175
I22	-221.8	35 ± 7	53 ± 16	24.675 ± 0.053	-15.419 ± 0.079	1×0.5	153
I3	-222.6	78 ± 7	91 ± 14	-2.172 ± 0.017	0.012 ± 0.033	0.9×0.4	168
I22	-222.6	83 ± 7	140 ± 17	24.67 ± 0.019	-15.462 ± 0.035	1×0.5	169
I29	-223.4	46 ± 7	73 ± 17	-2.115 ± 0.036	-0.123 ± 0.059	0.9×0.5	10
I22	-223.4	39 ± 7	133 ± 29	24.612 ± 0.079	-15.479 ± 0.099	1.6×0.7	36
I29	-224.3	45 ± 7	41 ± 12	-1.786 ± 0.032	0.213 ± 0.055	0.8×0.3	157
I22	-224.3	28 ± 7	77 ± 25	24.803 ± 0.119	-15.187 ± 0.085	1.2×0.7	68
I22	-225.1	39 ± 7	83 ± 19	24.704 ± 0.046	-15.326 ± 0.073	1×0.6	175
I12	-228.5	55 ± 7	51 ± 12	23.189 ± 0.026	-16.12 ± 0.039	0.7×0.4	158
I12	-229.3	132 ± 7	148 ± 14	23.231 ± 0.01	-16.061 ± 0.02	0.9×0.4	164
I12	-230.2	77 ± 7	82 ± 13	23.227 ± 0.016	-16.042 ± 0.033	0.8×0.4	170
I12	-232.7	62 ± 7	87 ± 15	23.056 ± 0.024	-16.052 ± 0.059	1.3×0.3	163
I12	-233.5	117 ± 7	116 ± 12	23.08 ± 0.009	-16.064 ± 0.022	0.9×0.3	169

A.2.3 IC 133: Fourth epoch

Table A.21— IC 133: LSR velocity v_r, peak and integrated flux densities S_p and S_I, position offsets from phase center $\Delta\alpha$ and $\Delta\delta$, size and position angle (PA) of all detected components on 2003 December 14. The components marked with an asterisk are new detected.

	$v_{\rm r}$ [km s^{-1}]	S$_p$ [$\frac{\rm mJy}{\rm beam}$]	S$_I$ [mJy]	$\Delta\alpha$ [mas]	$\Delta\delta$ [mas]	Size [mas]	PA [°]
I1	-206.6	266 ± 9	250 ± 15	0.156 ± 0.006	-0.144 ± 0.012	0.9×0.3	161
I1	-207.5	296 ± 10	310 ± 18	0.186 ± 0.006	-0.096 ± 0.013	0.9×0.3	162
I2	-207.5	277 ± 10	266 ± 17	-2.04 ± 0.007	-1.21 ± 0.014	0.9×0.3	160
I1	-208.3	264 ± 9	280 ± 17	0.184 ± 0.007	-0.122 ± 0.014	1×0.3	162
I2	-208.3	69 ± 9	157 ± 28	-2.164 ± 0.047	-1.067 ± 0.075	1.5×0.5	150
I6	-208.3	51 ± 9	71 ± 20	6.133 ± 0.041	0.437 ± 0.091	1.2×0.3	161
I1	-209.2	438 ± 11	408 ± 17	0.144 ± 0.004	-0.123 ± 0.008	0.9×0.3	160
I5	-209.2	86 ± 10	120 ± 22	-0.973 ± 0.047	-1.8 ± 0.057	1.4×0.3	141
I6	-209.2	44 ± 10	53 ± 20	6.195 ± 0.063	0.416 ± 0.116	1.3×0.3	153
I1	-210.0	470 ± 11	462 ± 18	0.13 ± 0.004	-0.111 ± 0.008	0.9×0.3	163
I1	-210.8	171 ± 9	203 ± 17	0.179 ± 0.009	-0.091 ± 0.021	1×0.4	169
I1	-211.7	76 ± 8	186 ± 27	0.215 ± 0.021	-0.046 ± 0.077	1.7×0.4	4
I4	-211.7	84 ± 9	84 ± 15	-2.594 ± 0.024	-2.765 ± 0.041	1×0.3	152
I4	-212.5	208 ± 8	239 ± 16	-2.714 ± 0.009	-2.553 ± 0.016	1×0.4	158
I4	-213.4	225 ± 9	244 ± 16	-2.618 ± 0.008	-2.765 ± 0.016	1×0.3	158
I26	-213.4	45 ± 9	68 ± 20	24.366 ± 0.047	-15.668 ± 0.099	1.3×0.4	159
I26	-214.2	92 ± 8	108 ± 16	24.466 ± 0.015	-15.737 ± 0.043	1.1×0.3	167
I26	-215.0	110 ± 8	100 ± 13	24.464 ± 0.014	-15.759 ± 0.028	0.9×0.3	158
I26	-215.9	69 ± 9	49 ± 12	24.479 ± 0.018	-15.765 ± 0.041	0.8×0.3	163
I3	-220.1	125 ± 8	117 ± 14	-1.996 ± 0.012	0.09 ± 0.025	0.9×0.3	161
I3	-220.9	106 ± 9	103 ± 15	-2.009 ± 0.016	0.069 ± 0.028	0.9×0.3	158
I29	-224.3	73 ± 8	68 ± 14	-1.779 ± 0.021	0.095 ± 0.041	0.9×0.3	161

Table A.22— IC 133: LSR velocity v_r, peak and integrated flux densities S_p and S_I, position offsets from phase center $\Delta\alpha$ and $\Delta\delta$, size and position angle (PA) of all detected components on 2004 January 08. The components marked with an asterisk are new detected.

	v_r [km s^{-1}]	S$_p$ [$\frac{\mathrm{mJy}}{\mathrm{beam}}$]	S$_I$ [mJy]	$\Delta\alpha$ [mas]	$\Delta\delta$ [mas]	Size [mas]	PA [°]
I1	-205.8	39 ± 9	95 ± 28	0.099 ± 0.106	-0.005 ± 0.105	1.2×1.1	52
I1	-206.6	345 ± 10	425 ± 19	0.129 ± 0.007	-0.085 ± 0.014	1.3×0.5	164
I2	-206.6	57 ± 9	106 ± 25	-2.108 ± 0.064	-1.056 ± 0.087	1.4×0.7	150
I1	-207.5	413 ± 11	509 ± 22	0.173 ± 0.007	-0.086 ± 0.014	1.3×0.5	165
I2	-207.5	529 ± 11	620 ± 22	-2.051 ± 0.006	-1.151 ± 0.011	1.3×0.5	161
I1	-208.3	377 ± 10	441 ± 19	0.16 ± 0.007	-0.071 ± 0.013	1.2×0.5	164
I2	-208.3	163 ± 10	288 ± 25	-2.128 ± 0.02	-1.052 ± 0.035	1.5×0.7	159
I6	-208.3	91 ± 10	135 ± 22	6.127 ± 0.034	0.389 ± 0.053	1.2×0.6	159
I1	-209.2	603 ± 11	690 ± 22	0.129 ± 0.005	-0.086 ± 0.009	1.2×0.5	164
I6	-209.2	75 ± 11	118 ± 26	6.159 ± 0.043	0.254 ± 0.087	1.4×0.6	164
I1	-210.0	580 ± 11	727 ± 23	0.126 ± 0.005	-0.079 ± 0.01	1.3×0.5	165
I6	-210.0	63 ± 11	121 ± 30	5.965 ± 0.057	0.402 ± 0.102	1.4×0.7	170
I1	-210.8	235 ± 9	342 ± 21	0.152 ± 0.011	0.013 ± 0.022	1.3×0.6	167
I1	-211.7	139 ± 9	252 ± 24	0.219 ± 0.018	0.131 ± 0.042	1.5×0.6	176
I4	-211.7	84 ± 9	199 ± 29	-2.565 ± 0.046	-2.768 ± 0.068	1.7×0.8	152
I1	-212.5	46 ± 9	134 ± 34	0.137 ± 0.074	0.018 ± 0.147	1.8×0.9	5
I4	-212.5	240 ± 9	317 ± 20	-2.722 ± 0.011	-2.569 ± 0.021	1.3×0.5	160
I4	-213.4	282 ± 9	301 ± 17	-2.586 ± 0.008	-2.812 ± 0.015	1.2×0.5	163
I26	-213.4	54 ± 9	83 ± 21	24.426 ± 0.045	-15.473 ± 0.096	1.4×0.6	169
I26	-214.2	121 ± 9	185 ± 21	24.468 ± 0.023	-15.678 ± 0.041	1.4×0.6	160
I26	-215.0	72 ± 9	96 ± 18	24.5 ± 0.033	-15.801 ± 0.061	1.2×0.6	165
I27	-216.7	36 ± 8	99 ± 30	-2.476 ± 0.09	-1.021 ± 0.175	1.8×0.8	167
I27	-217.6	57 ± 9	97 ± 22	-2.538 ± 0.04	-0.655 ± 0.097	1.5×0.6	172
I3	-220.1	105 ± 9	219 ± 25	-2.061 ± 0.029	0.067 ± 0.047	1.4×0.8	4
I19	-220.1	49 ± 9	83 ± 22	0.12 ± 0.057	0.138 ± 0.097	1.3×0.7	168
I3	-220.9	114 ± 9	161 ± 19	-2.044 ± 0.02	0.054 ± 0.043	1.4×0.6	168
I19	-220.9	49 ± 8	112 ± 26	0.258 ± 0.062	-0.053 ± 0.105	1.5×0.8	170
I3	-221.8	37 ± 8	128 ± 36	-2.032 ± 0.134	-0.114 ± 0.132	1.5×1.2	133
I3	-222.6	60 ± 9	100 ± 21	-1.885 ± 0.053	0.013 ± 0.068	1.2×0.7	150
I29	-224.3	65 ± 9	96 ± 20	-1.762 ± 0.039	0.098 ± 0.068	1.2×0.6	165

A.2.4 M33/19: Second epoch

Table A.23— M33/19: LSR velocity v_r, peak and integrated flux densities S_p and S_I, position offsets from phase center $\Delta\alpha$ and $\Delta\delta$, size and position angle (PA) of all detected components on 2002 January 28.

	v_r [km s^{-1}]	S$_p$ [$\frac{\mathrm{mJy}}{\mathrm{beam}}$]	S$_I$ [mJy]	$\Delta\alpha$ [mas]	$\Delta\delta$ [mas]	Size [mas]	PA [°]
M4	-129.0	114 ± 7	128 ± 14	-0.307 ± 0.01	4.749 ± 0.028	1.1×0.3	169
M4	-129.8	76 ± 7	69 ± 12	-0.32 ± 0.016	4.776 ± 0.03	0.8×0.4	169
M1	-133.2	82 ± 7	87 ± 13	5.432 ± 0.016	-0.329 ± 0.029	0.8×0.4	163
M1	-134.0	174 ± 8	179 ± 14	5.428 ± 0.009	-0.359 ± 0.015	0.8×0.4	163
M3	-134.0	51 ± 7	140 ± 27	0.344 ± 0.025	-0.491 ± 0.138	2.2×0.4	177
M2	-134.0	58 ± 8	48 ± 12	0.401 ± 0.025	0.03 ± 0.041	0.7×0.3	156
M3	-134.9	61 ± 7	53 ± 12	0.37 ± 0.02	-0.953 ± 0.039	0.8×0.3	165
M2	-134.9	88 ± 7	91 ± 13	0.364 ± 0.016	-0.007 ± 0.028	0.8×0.4	162
M3	-135.7	70 ± 8	83 ± 15	0.374 ± 0.02	-0.866 ± 0.041	0.9×0.4	173
M3	-136.6	156 ± 8	192 ± 15	0.393 ± 0.009	-0.856 ± 0.017	0.9×0.4	169
M3	-137.4	165 ± 8	181 ± 14	0.35 ± 0.008	-0.836 ± 0.016	0.8×0.4	171

Table A.24— M33/19: LSR velocity v_r, peak and integrated flux densities S_p and S_I, position offsets from phase center $\Delta\alpha$ and $\Delta\delta$, size and position angle (PA) of all detected components on 2002 February 03.

	v_r [km s^{-1}]	S$_p$ [$\frac{\mathrm{mJy}}{\mathrm{beam}}$]	S$_I$ [mJy]	$\Delta\alpha$ [mas]	$\Delta\delta$ [mas]	Size [mas]	PA [°]
M4	-129.0	77 ± 7	92 ± 14	-0.331 ± 0.017	4.78 ± 0.033	0.8×0.4	171
M4	-129.8	71 ± 7	101 ± 16	-0.356 ± 0.023	4.781 ± 0.035	0.9×0.5	157
M5	-130.7	53 ± 7	78 ± 16	4.067 ± 0.029	-1.327 ± 0.05	0.9×0.5	166
M1	-133.2	91 ± 7	82 ± 12	5.393 ± 0.011	-0.333 ± 0.028	0.8×0.3	170
M1	-134.0	202 ± 9	232 ± 16	5.403 ± 0.007	-0.314 ± 0.015	0.9×0.4	168
M2	-134.0	58 ± 8	128 ± 25	0.344 ± 0.026	-0.044 ± 0.09	1.5×0.4	174
M3	-134.9	36 ± 7	74 ± 20	0.27 ± 0.027	-0.651 ± 0.162	2×0.3	176
M2	-134.9	38 ± 7	33 ± 12	0.427 ± 0.037	-0.028 ± 0.063	0.9×0.3	153
M3	-135.7	41 ± 8	79 ± 21	0.311 ± 0.032	-0.758 ± 0.109	1.4×0.4	172
M2	-136.6	33 ± 8	36 ± 14	0.376 ± 0.039	0.356 ± 0.075	0.8×0.4	167
M3	-136.6	96 ± 8	113 ± 15	0.338 ± 0.014	-0.856 ± 0.028	0.9×0.4	168
M3	-137.4	43 ± 8	50 ± 14	0.392 ± 0.031	0.141 ± 0.071	1×0.3	164
M3	-137.4	100 ± 8	117 ± 14	0.313 ± 0.014	-0.86 ± 0.025	0.8×0.4	169

A.2.5 M33/19: Third epoch

Table A.25— M33/19: LSR velocity v_r, peak and integrated flux densities S_p and S_I, position offsets from phase center $\Delta\alpha$ and $\Delta\delta$, size and position angle (PA) of all detected components on 2002 October 30.

	$v_{\rm r}$ [km s^{-1}]	S$_p$ [$\frac{\rm mJy}{\rm beam}$]	S$_I$ [mJy]	$\Delta\alpha$ [mas]	$\Delta\delta$ [mas]	Size [mas]	PA [°]
M4	-129.0	79 ± 8	90 ± 16	-0.285 ± 0.017	4.736 ± 0.04	0.9×0.4	174
M4	-129.8	190 ± 9	199 ± 16	-0.302 ± 0.007	4.744 ± 0.018	0.9×0.4	173
M4	-130.7	39 ± 8	34 ± 12	-0.353 ± 0.03	4.847 ± 0.07	0.8×0.3	172
M5	-132.4	35 ± 8	64 ± 20	4.051 ± 0.051	-1.259 ± 0.096	1.1×0.5	10
M1	-132.4	15 ± 7	73 ± 43	0.647 ± 0.297	-0.504 ± 0.281	1.7×0.9	48
M1	-133.2	151 ± 9	157 ± 16	5.427 ± 0.009	-0.361 ± 0.022	0.9×0.4	171
M5	-133.2	51 ± 8	104 ± 24	4.292 ± 0.048	-0.893 ± 0.07	1.1×0.6	26
M3	-133.2	47 ± 9	57 ± 17	0.249 ± 0.039	-0.859 ± 0.061	0.8×0.5	2
M1	-134.0	456 ± 12	486 ± 21	5.422 ± 0.004	-0.373 ± 0.01	0.9×0.4	175
M2	-134.0	86 ± 12	105 ± 23	0.345 ± 0.02	-0.062 ± 0.065	1.2×0.3	1917
M3	-134.0	167 ± 12	166 ± 20	0.343 ± 0.012	-0.943 ± 0.024	0.8×0.4	166
M3	-134.9	295 ± 9	443 ± 21	0.355 ± 0.005	-0.856 ± 0.016	1.2×0.4	178
M3	-135.7	361 ± 10	403 ± 18	0.354 ± 0.004	-0.929 ± 0.011	1×0.4	174
M3	-136.6	121 ± 9	152 ± 19	0.439 ± 0.015	-0.901 ± 0.027	0.8×0.5	6
M7	-136.6	87 ± 9	67 ± 14	0.251 ± 0.016	-0.758 ± 0.038	0.9×0.3	165
M3	-137.4	182 ± 9	209 ± 16	0.361 ± 0.008	-0.891 ± 0.017	0.8×0.4	177
M3	-138.2	52 ± 8	66 ± 17	0.256 ± 0.029	-0.86 ± 0.061	0.9×0.4	2

Table A.26— M33/19: LSR velocity v_r, peak and integrated flux densities S_p and S_I, position offsets from phase center $\Delta\alpha$ and $\Delta\delta$, size and position angle (PA) of all detected components on 2002 November 12.

	$v_{\rm r}$ [km s^{-1}]	S$_p$ [$\frac{\rm mJy}{\rm beam}$]	S$_I$ [mJy]	$\Delta\alpha$ [mas]	$\Delta\delta$ [mas]	Size [mas]	PA [°]
M4	-129.0	74 ± 7	71 ± 12	-0.279 ± 0.017	4.746 ± 0.038	0.9×0.3	162
M4	-129.8	172 ± 8	194 ± 15	-0.297 ± 0.007	4.803 ± 0.019	1×0.3	169.000
M4	-130.7	33 ± 7	52 ± 17	-0.308 ± 0.029	4.971 ± 0.152	1.7×0.3	174
M1	-133.2	104 ± 7	120 ± 14	5.435 ± 0.014	-0.349 ± 0.028	1×0.3	160
M8	-133.2	20 ± 7	132 ± 52	4.643 ± 0.252	-0.661 ± 0.285	2.5×0.8	41
M1	-134.0	354 ± 9	402 ± 17	5.438 ± 0.004	-0.361 ± 0.01	0.9×0.3	168
M6	-134.0	49 ± 9	52 ± 16	0.497 ± 0.032	-2.443 ± 0.077	1×0.3	163
M2	-134.0	78 ± 9	74 ± 15	0.372 ± 0.02	0.063 ± 0.048	1×0.3	163
M3	-134.0	138 ± 9	138 ± 16	0.358 ± 0.01	-0.905 ± 0.025	0.9×0.3	169
M2	-134.9	74 ± 8	115 ± 19	0.36 ± 0.022	0.071 ± 0.058	1.3×0.3	165
M3	-134.9	274 ± 8	284 ± 15	0.356 ± 0.005	-0.873 ± 0.011	0.9×0.3	165
M6	-134.9	85 ± 8	108 ± 17	0.463 ± 0.014	-2.454 ± 0.046	1.1×0.3	172
M3	-135.7	334 ± 9	380 ± 17	0.372 ± 0.005	-0.89 ± 0.01	0.9×0.3	166
M3	-136.6	214 ± 8	235 ± 14	0.355 ± 0.006	-0.851 ± 0.014	0.9×0.4	166
M3	-137.4	196 ± 8	232 ± 15	0.368 ± 0.007	-0.874 ± 0.014	0.9×0.4	164
M3	-138.2	48 ± 7	56 ± 14	0.33 ± 0.025	-0.946 ± 0.06	0.9×0.4	169

A.2.6 M33/19: Fourth epoch

TABLE A.27— M33/19: LSR velocity v_r, peak and integrated flux densities S_p and S_I, position offsets from phase center $\Delta\alpha$ and $\Delta\delta$, size and position angle (PA) of all detected components on 2003 December 14.

	v_r [km s^{-1}]	S$_p$ [$\frac{\mathrm{mJy}}{\mathrm{beam}}$]	S$_I$ [mJy]	$\Delta\alpha$ [mas]	$\Delta\delta$ [mas]	Size [mas]	PA [°]
M5	-132.4	52 ± 8	72 ± 18	4.149 ± 0.027	-1.419 ± 0.072	1×0.4	0
M1	-133.2	55 ± 9	67 ± 17	5.487 ± 0.023	-0.34 ± 0.08	1.2×0.3	170
M1	-134.0	222 ± 9	230 ± 17	5.465 ± 0.008	-0.306 ± 0.017	1×0.3	162
M3	-134.0	37 ± 9	150 ± 43	0.32 ± 0.152	-1.072 ± 0.091	1.6×0.7	113
M2	-134.0	141 ± 9	139 ± 16	0.397 ± 0.013	0.035 ± 0.024	0.9×0.3	159
M8	-134.9	90 ± 9	63 ± 13	4.414 ± 0.016	-0.044 ± 0.031	0.8×0.3	158
M2	-134.9	165 ± 9	169 ± 16	0.432 ± 0.01	-0.965 ± 0.021	0.9×0.3	160
M3	-134.9	154 ± 9	180 ± 18	0.387 ± 0.015	0.068 ± 0.022	1×0.3	149
M3	-135.7	302 ± 10	287 ± 16	0.416 ± 0.005	-0.904 ± 0.012	0.9×0.3	165
M3	-136.6	331 ± 9	304 ± 15	0.397 ± 0.005	-0.888 ± 0.01	0.9×0.3	158
M3	-137.4	279 ± 9	245 ± 15	0.387 ± 0.006	-0.88 ± 0.012	0.9×0.3	160
M3	-138.2	98 ± 9	83 ± 13	0.349 ± 0.014	-0.829 ± 0.03	0.8×0.3	164

TABLE A.28— M33/19: LSR velocity v_r, peak and integrated flux densities S_p and S_I, position offsets from phase center $\Delta\alpha$ and $\Delta\delta$, size and position angle (PA) of all detected components on 2004 January 08.

	v_r [km s^{-1}]	S$_p$ [$\frac{\mathrm{mJy}}{\mathrm{beam}}$]	S$_I$ [mJy]	$\Delta\alpha$ [mas]	$\Delta\delta$ [mas]	Size [mas]	PA [°]
M4	-129.8	43 ± 8	71 ± 21	-0.251 ± 0.055	4.967 ± 0.11	1.4×0.6	166
M4	-130.7	32 ± 9	64 ± 26	-0.244 ± 0.098	4.899 ± 0.141	1.2×0.8	178
M9	-131.5	64 ± 9	87 ± 19	4.141 ± 0.036	-1.295 ± 0.074	1.3×0.5	164
M9	-132.4	70 ± 9	109 ± 20	4.274 ± 0.029	-1.24 ± 0.069	1.3×0.6	179
M1	-133.2	80 ± 9	82 ± 16	5.455 ± 0.024	-0.28 ± 0.056	1.2×0.4	163
M1	-134.0	281 ± 10	294 ± 18	5.506 ± 0.008	-0.355 ± 0.017	1.2×0.4	162
M3	-134.0	189 ± 9	361 ± 26	0.429 ± 0.012	-0.434 ± 0.035	1.7×0.5	175
M1	-134.9	144 ± 11	181 ± 22	4.459 ± 0.018	-0.029 ± 0.037	1.2×0.5	166
M3	-134.9	327 ± 11	547 ± 26	0.429 ± 0.008	-0.726 ± 0.022	1.6×0.5	169
M3	-135.7	567 ± 12	707 ± 24	0.422 ± 0.005	-0.856 ± 0.011	1.3×0.5	163
M3	-136.6	504 ± 11	574 ± 22	0.417 ± 0.005	-0.889 ± 0.012	1.2×0.4	165
M3	-137.4	414 ± 11	486 ± 21	0.429 ± 0.006	-0.891 ± 0.013	1.2×0.5	165
M3	-138.2	111 ± 9	190 ± 22	0.437 ± 0.023	-0.828 ± 0.048	1.5×0.6	164
M3	-139.1	49 ± 9	41 ± 14	0.425 ± 0.038	-0.739 ± 0.073	0.9×0.4	168

B

VLA Spectra of III Zw 2

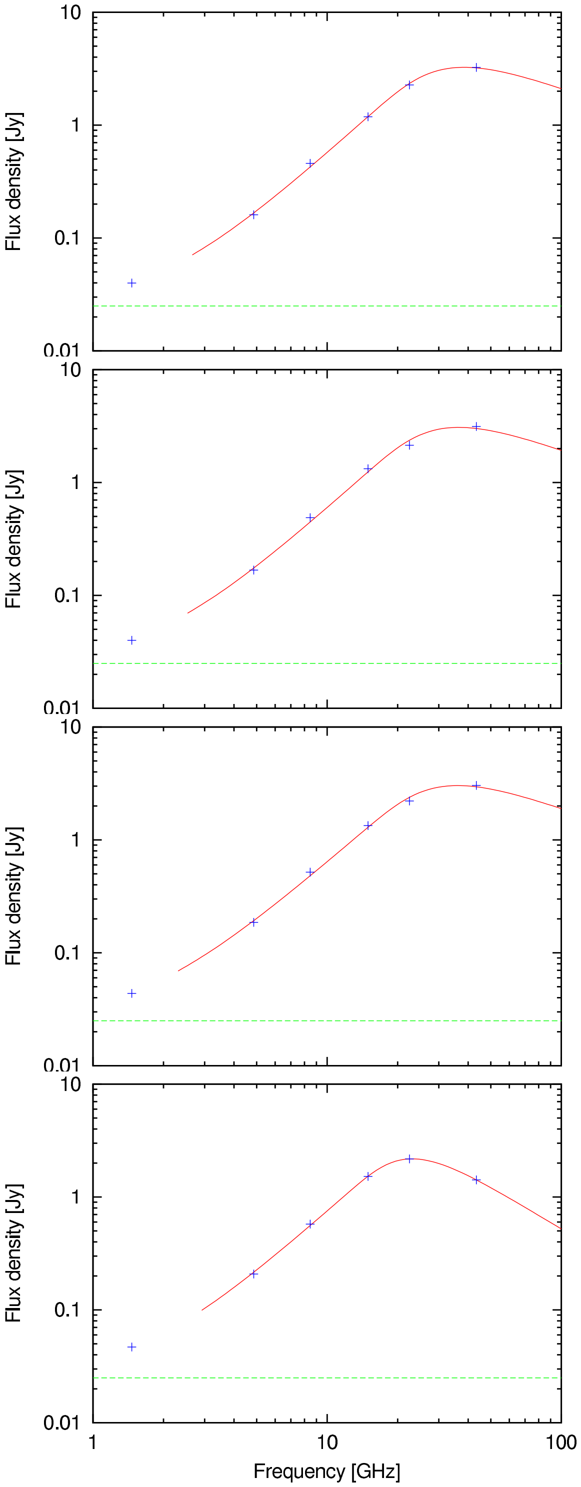

FIGURE B.1— Spectra of III Zw 2 on 1998 September 05, 1998 October 01, 1998 November 04 and 1998 December 24 (from top to bottom).

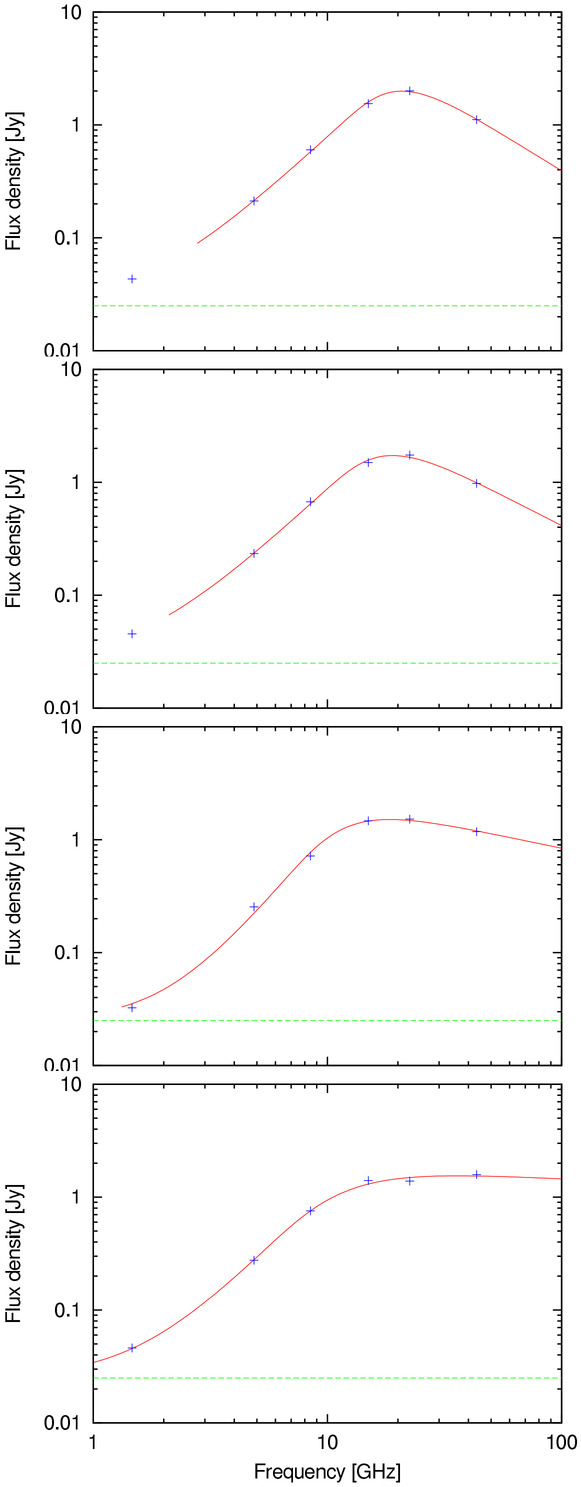

FIGURE B.2— Spectra of III Zw 2 on 1999 January 08, 1999 February 22, 1999 March 23 and 1999 April 23 (from top to bottom).

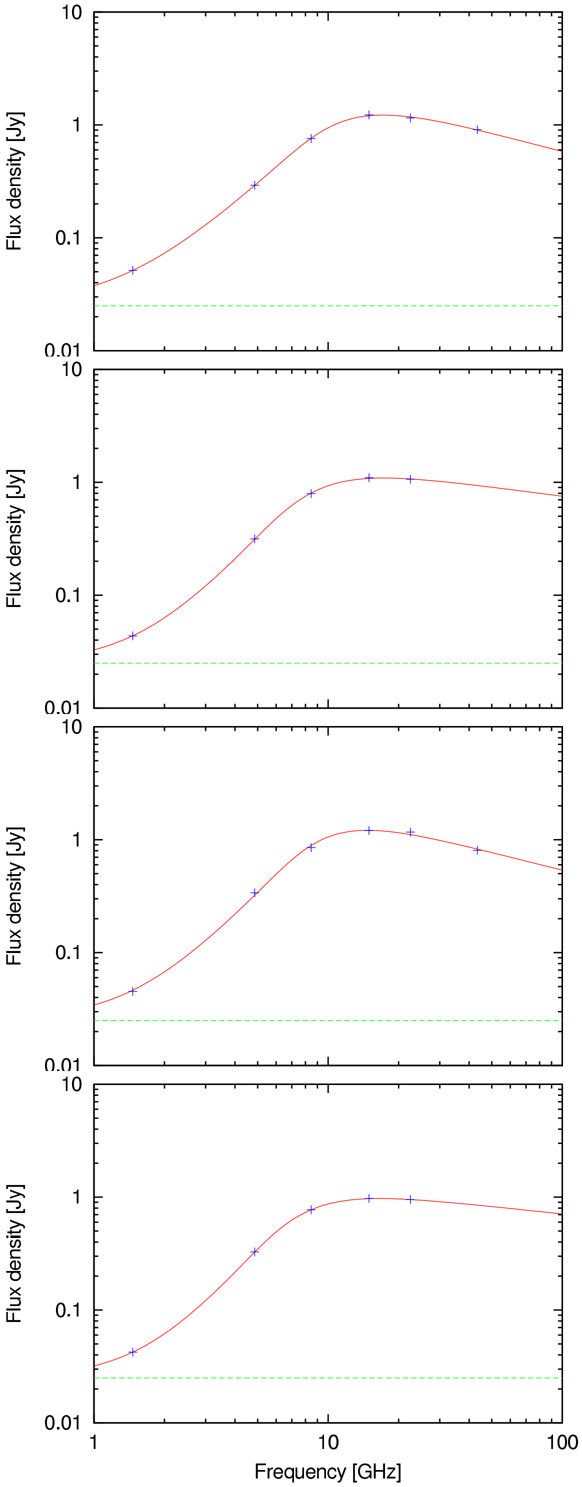

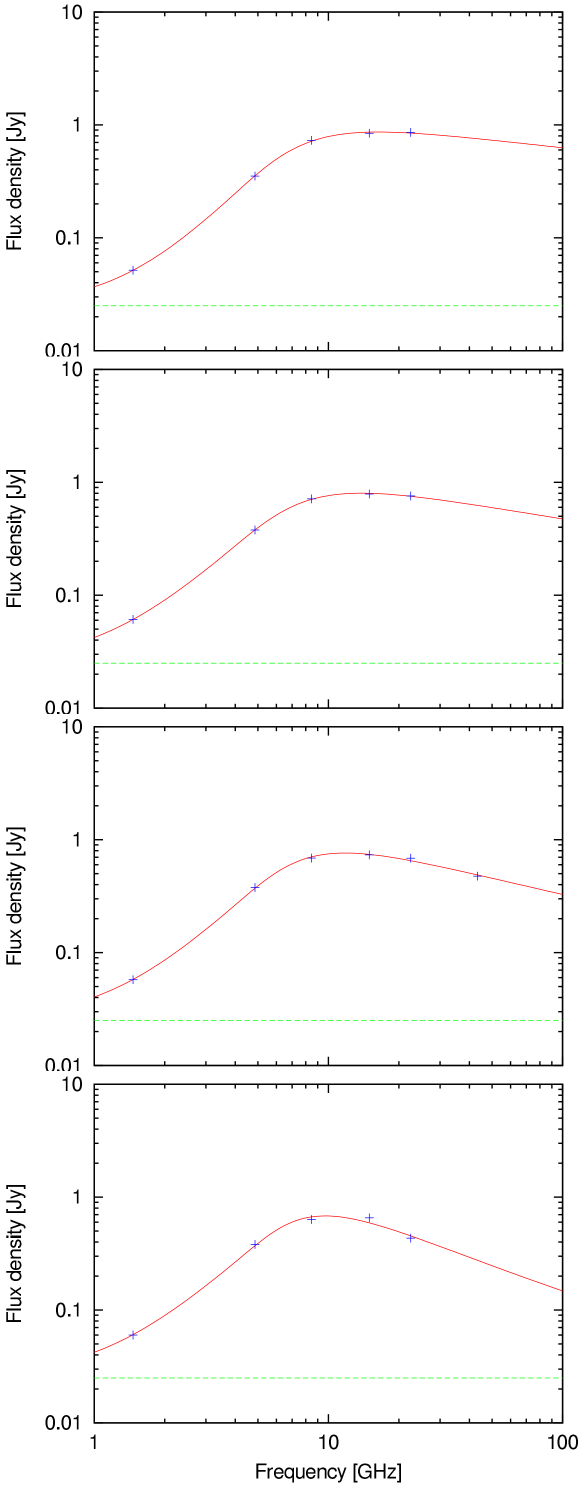

FIGURE B.3— Spectra of III Zw 2 on 1999 May 13, 1999 June 22, 1999 July 07 and 1999 August 01 (from top to bottom).

FIGURE B.4— Spectra of III Zw 2 on 1999 September 21, 1999 October 18, 1999 November 12 and 2000 January 04 (from top to bottom).

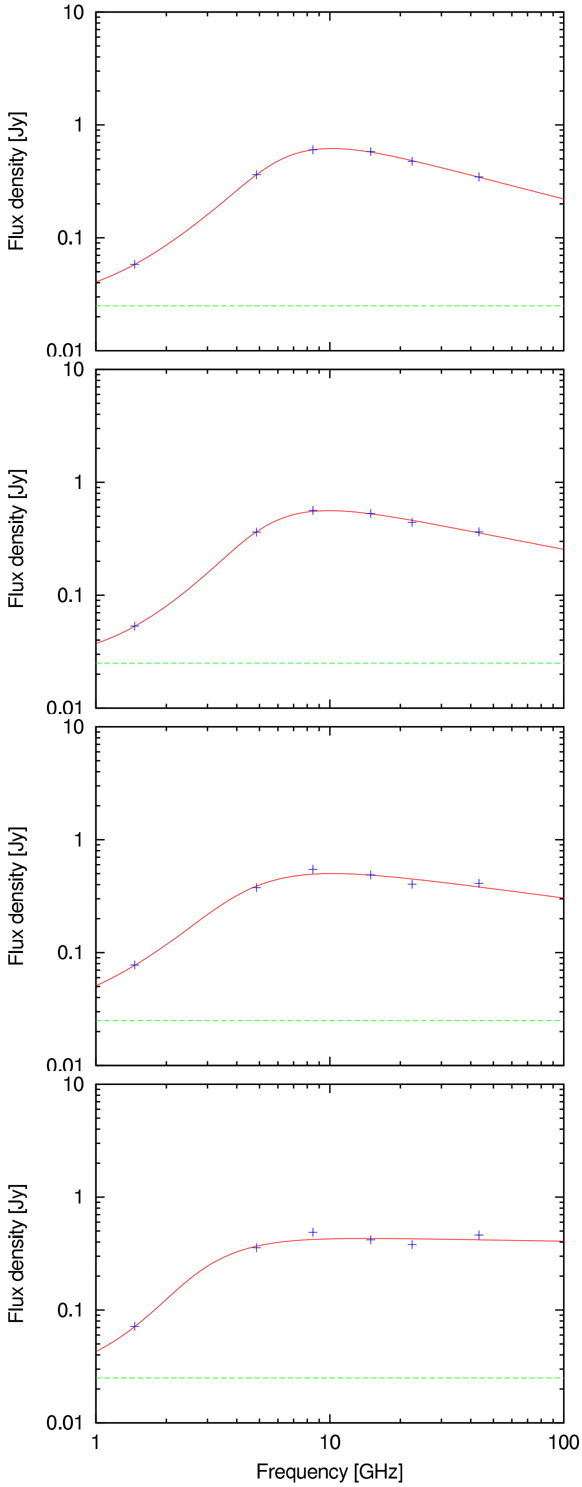

FIGURE B.5— Spectra of III Zw 2 on 2000 January 25, 2000 February 18, 2000 March 10 and 2000 April 06 (from top to bottom).

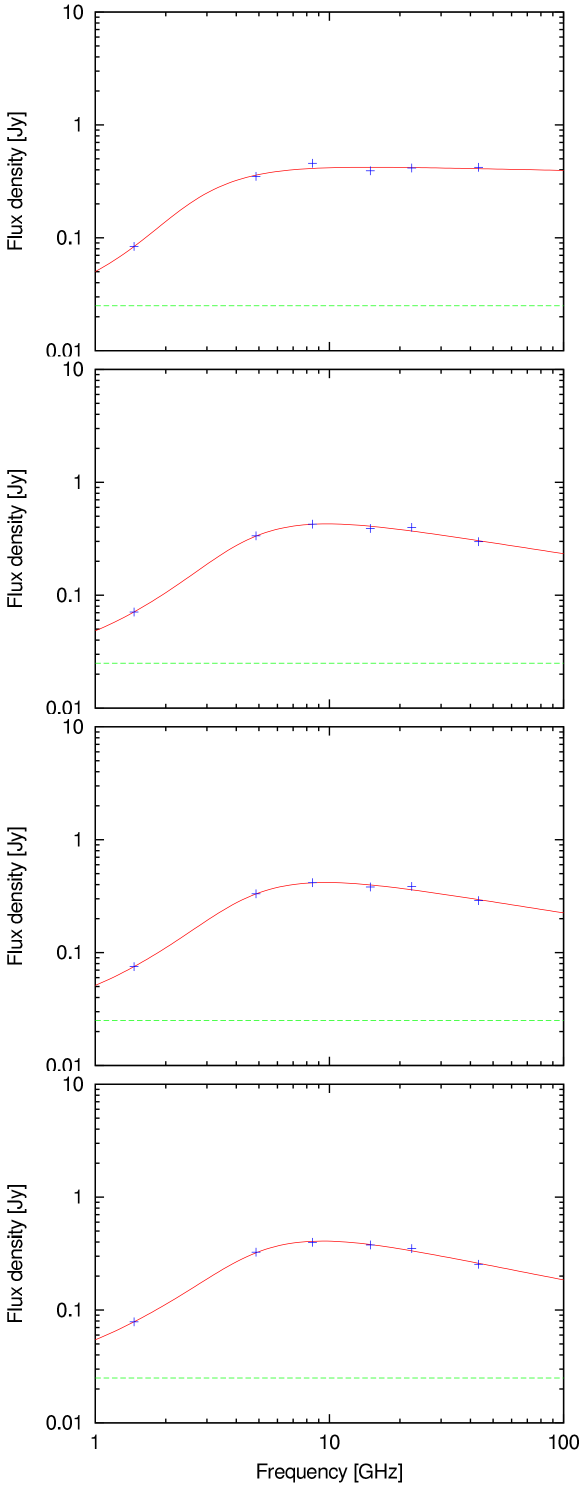

FIGURE B.6— Spectra of III Zw 2 on 2000 May 05, 2000 May 28, 2000 June 08 and 2000 July 01 (from top to bottom).

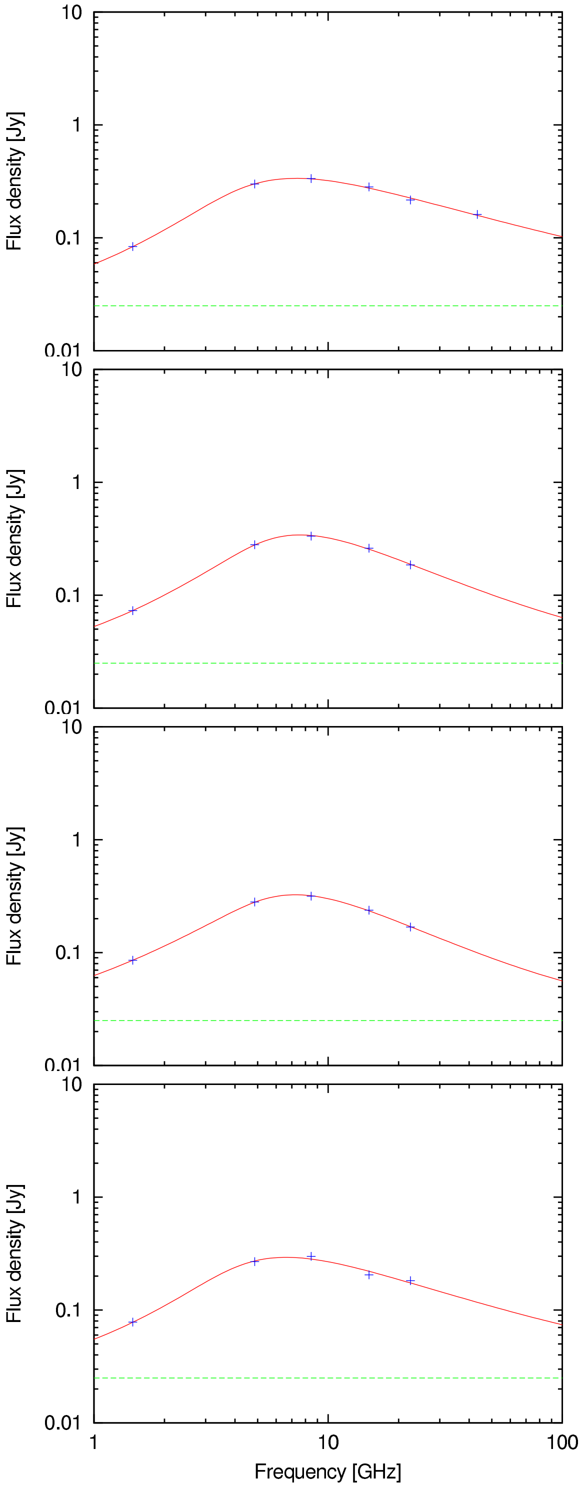

FIGURE B.7— Spectra of III Zw 2 on 2000 September 27, 2000 October 22, 2000 November 04 and 2000 December 03 (from top to bottom).

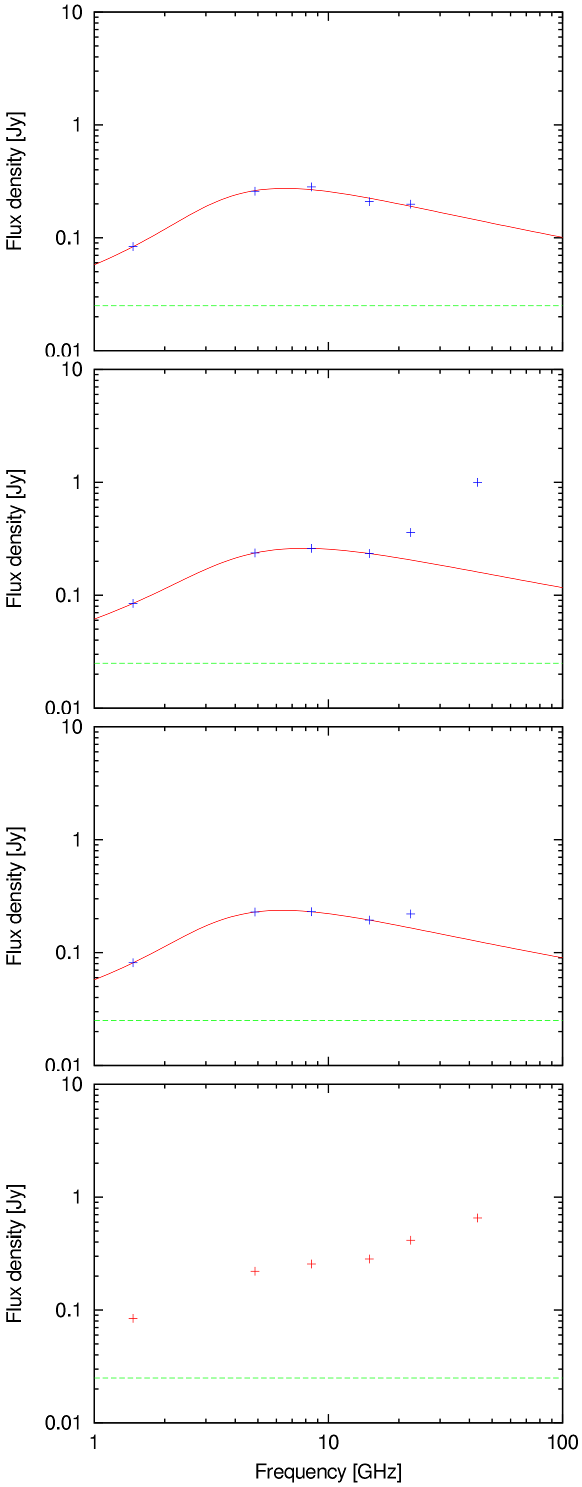

FIGURE B.8— Spectra of III Zw 2 on 2000 December 29, 2001 January 30, 2001 February 23 and 2001 March 16 (from top to bottom).

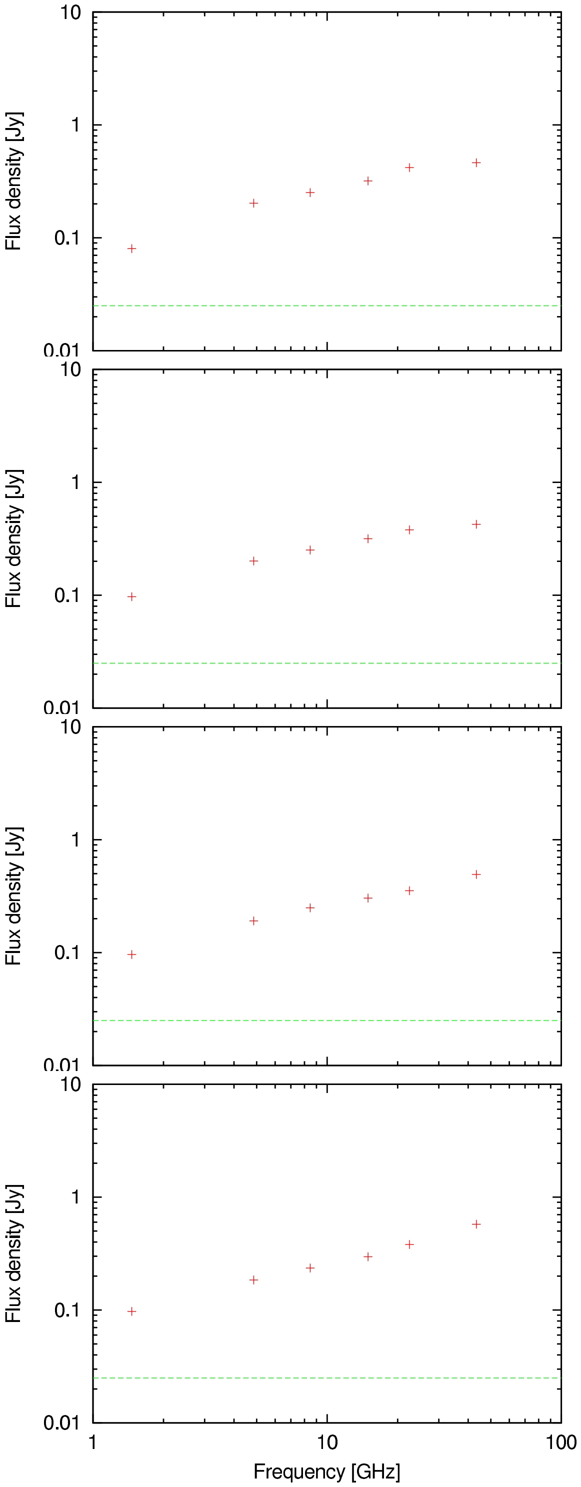

FIGURE B.9— Spectra of III Zw 2 on 2001 May 03, 2001 May 26, 2001 June 18 and 2001 July 05 (from top to bottom).

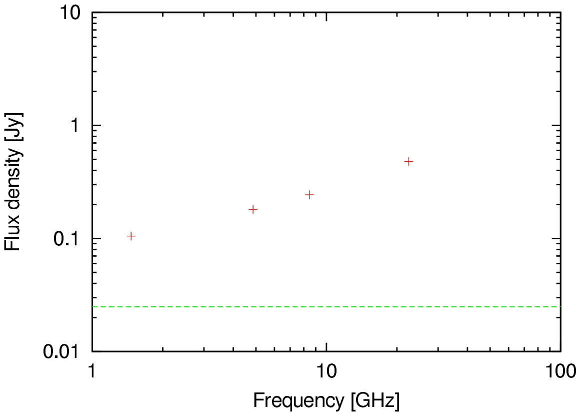

FIGURE B.10— Spectra of III Zw 2 on 2001 September 13.

Danksagung

Diese Doktorarbeit wäre ohne die Hilfe Anderer nicht möglich gewesen. Daher ist es nun an der Zeit mich bei allen zu bedanken, die zum Gelingen dieser Arbeit beigetragen haben.

Zunächst möchte ich den Referenten Prof. Dr. Heino Falcke und Prof. Dr. Ulrich Klein für die Betreuung und die zahlreichen Anregungen zur Verbesserung dieser Arbeit danken.

Herrn Dr. Anton Zensus, Direktor der VLBI-Gruppe am Max-Planck-Institut für Radioastronomie in Bonn, danke ich für die Möglichkeit diese Arbeit am MPIfR anzufertigen und die Gelegenheit die Ergebnisse auf internationalen Konferenzen präsentieren zu können.

Grosser Dank gilt auch Dr. Mark J. Reid vom Harvard-Smithsonian Center for Astrophysics (CfA) für seine Betreuung und persönliche Hilfe während meiner Zeit als *predoctoral fellow* am CfA. Ohne seine wertvollen Anregungen wäre die Arbeit in dieser Form nicht möglich gewesen.

Ferner danke ich allen Mitgliedern der VLBI-Gruppe am Max-Planck-Institut für die vielen lehrreichen und hilfreichen Diskussionen. Hiermit möchte ich mich ebenfalls bei Violetta, Krisztina, Rupal und Matthias dafür entschuldigen, dass ich ihre Computer mit unzähligen *fringe-fits* auf meinen grossen Datensätzen gequält und lahmgelegt habe. Andreas, Elmar und Tim danke ich für das hervorragende Arbeitsklima in der *VLBI-Aussenstelle*.

Ausserdem danke ich Dr. Michael Garrett und Dr. Bob Campbell vom Joint Institute for VLBI in Europe für die Nachsicht in den letzten Monaten und die Gelegenheit meine Arbeit zügig zu beenden.

Besonderer Dank gilt natürlich meiner Familie für die Unterstützung während des ganzen Studiums, insbesondere meiner Mutter für die vielen Hilfen in allen Bereichen während der letzten Jahre.

Den grössten Dank schulde ich jedoch Maria für ihr Verständniss und die grosse Unterstützung seit wir uns kennen. Vorallem für ihre Liebe und die schöne Zeit neben der Astronomie möchte ich mich aus ganzem Herzen bedanken.

List of publications:

"HST and VLA Observations of the H_2O Gigamaser Galaxy TXS2226-184"
Falcke H., Wilson A.S., Henkel C., Brunthaler A., Braatz J.A. 2000, ApJ 530, L13

"III Zw 2, the first superluminal jet in a Seyfert galaxy"
Brunthaler A., Falcke H., Bower G.C., Aller M.F., Aller H.D., Teräsranta H., Lobanov A.P., Krichbaum T.P., Patnaik A.R. 2000, A&A Letters 357, L45-L48

"Detection of Circular Polarization in M81*"
Brunthaler A., Bower, G.C., Falcke, H., Mellon, R.R. 2001, ApJ Letters 560, L123-L126

"III Zw 2: Evolution of a Radio Galaxy in a Nutshell"
Brunthaler A., Falcke H., Bower G.C., Aller M.F., Aller, H.D., Teräsranta H., Krichbaum T.P. 2003, PASA 20, 126-128

"The Flaring H_2O Megamaser and Compact Radio Source in Mrk 348"
Peck A.B., Henkel C., Ulvestad J.S., Brunthaler A., Falcke H., Elitzur M., Menten K.M., Gallimore J.F. 2003, ApJ 590, 149-161

"The Proper Motion of Sgr A*: II. The Mass of Sgr A*"
Reid M.J. and Brunthaler A. 2004, ApJ, submitted